UNIVERSITY OF
BIRMINGHAM

Synthesis and Characterisation of Novel Materials for Energy Applications

By

Abbey Jarvis

Supervisor: Professor Peter Slater

A thesis submitted to The University of Birmingham for the degree of Doctor of Philosophy

The School of Chemistry
College of Engineering and Physical Sciences
The University of Birmingham
October 2020

Abstract

In this thesis a range of different systems have been investigated including perovskite phases and perovskite type phases such as Ruddlesden-Popper materials. In addition apatite materials have also been investigated. These materials have been of particular interest due to appealing properties for energy applications, in particular for solid oxide fuel cells. A particular focus has been on iron oxide systems due to the low cost and high natural abundance of iron. Oxyanion doping and fluorination has been investigated for the perovskite related systems, while exsolution of Cu has been investigated for apatite systems, with the aim to improve the properties of these materials.

Perovskite ($SrFeO_{3-\delta}$, $Sr_{0.5}Ba_{0.5}FeO_{3-\delta}$ and $BaFeO_{3-\delta}$,) and Ruddlesden-Popper materials ($Sr_4Fe_3O_{10-\delta}$ and $Sr_4Fe_2(Cu/Co)O_{10-\delta}$) were doped with various oxyanions (sulfate, borate, phosphate, chromate and carbonate). It was found that a range of oxyanions could be successfully incorporated into these perovskite and Ruddlesden-Popper phases. Interestingly, X-ray diffraction and thermogravimetric analysis suggests carbonate stabilises the cubic perovskite Ba-Fe-O system at low synthesis temperatures. The perovskite systems, $SrFeO_{3-\delta}$ and $Sr_{0.5}Ba_{0.5}FeO_{3-\delta}$ and all Ruddlesden-Popper systems were tested in dry and wet N_2, and conductivity measurements were performed in order to test suitability for use as cathodes in solid oxide fuel cells. Following the successful incorporation of oxyanions into perovskite phases, oxyanion incorporation into Ruddlesden-Popper materials also showed oxyanions could be successfully incorporated into the structure. The Ruddlesden-Popper phases showed promising results when heating in wet N_2 indicating potential for future studies into the use in conjunction with a proton conducting electrolyte. However, low conductivity values were reported for these Ruddlesden-Popper phases, which could be improved by replacing some Fe

for Cu/ Co. The most promising oxyanion doped Ruddlesden-Popper material was found to be $Sr_4Fe_{3-x}S_xO_{10-\delta}$, therefore further doping strategies (Cu/ Co doping) were carried out for these materials. Cu/ Co incorporation successfully improved the stability and conductivity of these materials for SOFC applications.

Further oxyanion studies were investigated to prepare "0201-1201" type layered oxide phases with this doping strategy allowing the successful synthesis of new phases, $Sr_{4.5}Fe_2(S/Cr)_{0.5}O_{9\pm\delta}$. Neutron diffraction indicated successful incorporation of SO_4^{2-} and CrO_4^{2-} with X-ray absorption spectroscopy additionally supporting the incorporation of tetrahedral Cr^{6+} as observed for $Sr_4Fe_{3-x}(S/Cr)_xO_{10-\delta}$ phases. Although low conductivity, the stability of materials in dry and wet N_2 indicates potential for use as SOFC cathode materials particularly for proton conducting SOFCs if further optimised.

In addition to doping on the cation sites, fluorination of the Ruddlesden-Popper phases, $Sr_4Fe_{2.75}(S/Cr)_{0.25}O_{10-\delta}$ was investigated. Successful fluorination of $Sr_4Fe_{3-x}(S/Cr)_xO_{10-\delta}$ was shown through X-ray diffraction with a large cell expansion with increased F content. $Sr_4Fe_{2.75}Cr_{0.25}O_{10-\delta}$ was found to incorporate higher F contents than the sulfate doped analogues attributed to the ability to reduce not only iron, but also chromium. Using a low temperature synthesis method, fluorinated Ruddlesden-Popper materials are not only successfully synthesised, but also have the additional ability to incorporate a range of F contents. This work highlights interesting materials with the potential for use in fluoride-ion batteries.

Potential solid oxide fuel cell electrolyte materials were also investigated following the successful incorporation of oxyanions into perovskite and perovskite type electrode materials. These materials include oxyanion doped perovskite type $Ba_3(Y/Tm)_2Ti_{1-x}(S/P)_xO_{8+y}$ phases. $Ba_3(Y/Tm)_2Ti_{1-x}(S/P)_xO_{8+y}$ phases were successfully prepared, showing stabilisation

of the cubic perovskite structure for $Ba_3Tm_2Ti_{1-x}(S/P)_xO_{8+y}$ phases. These oxyanion doped systems were found to have improved conductivities compared with the undoped phases.

Following the successful stabilisation of potential SOFC materials through oxyanion doping, an alternate doping strategy was considered. Exsolution was used in order to exsolve copper nanoparticles onto the surface of apatite materials. Due to the appealing properties of apatite phases as electrolyte materials for solid oxide fuel cell applications, a selection of Si/Ge/P apatite phases were investigated. All apatite phases were doped with Cu and heated in 10% H_2/ 90% N_2. After heat treatment, materials were analysed with X-ray diffraction and scanning electron microscopy showing the successful exsolution of Cu particles on the surface of the apatite structure. Future studies will investigate the potential of such phases for use as anodes in solid oxide fuel cells.

Acknowledgements

Firstly I would like to thank my supervisor Professor Peter Slater for taking me on and supporting me throughout my PhD. Not only with all of your help with the project, but also for the much needed coffee trips, pub sessions and team days out. I would also like to thank EPSRC and the School of Chemistry for funding my PhD.

Thanks to Dr Alex Gibbs and Dr Giannantonio Cibin for their help with running Neutron data and X-ray absorption spectroscopy data respectively. Additionally, thank you to Dr José F. Marco and Dr María Sánchez-Arenillas at the Instituto de Química Física and in particular Professor Frank Berry for your help with running ^{57}Fe Mössbauer data. For help with Neutron data analysis I would like to thank Dr Oliver Clemens.

Thank you to all of the Slater group and everyone on Floor 5 past and present for keeping me sane and fuelled by coffee and cider.

A big thank you to my friends and family for putting up with me and being so supportive through my many years at University. Finally, a massive thank you to Daniel for always being so supporting and encouraging me to keep going.

Table of Contents

Abbreviations

BSCF	$Ba_{0.5}Sr_{0.5}Co_{0.8}Fe_{0.2}O_{3-\delta}$
CGO	Cerium doped with Gadolinium
CHP	Combined Heat and Power
DTA	Differential Thermal Analysis
EDX	Energy Dispersive X-ray spectroscopy
GSAS	General Structure Analysis System
LSC	$La_{1-x}Sr_xCoO_3$
LSCF	$La_{1-x}Sr_xCo_{1-y}Fe_yO_{3-\delta}$
LSGM	$La_{0.8}Sr_{0.2}Ga_{0.8}Mg_{0.2}O_3$
ND	Neutron Diffraction
PVDF	Poly(vinylidene Fluoride)
SCO	Samarium doped Ceria
SEM	Scanning Electron Microscopy
SOFC	Solid Oxide Fuel Cell
TGA	Thermogravimetric Analysis
TOF NPD	Time of Flight Neutron Powder Diffraction
XAS	X-ray Absorption Spectroscopy
XRD	X-ray Diffraction
YSZ	Yttria stabilised Zirconia

1 Introduction

The majority of the world's energy is supplied through fossil fuels, nuclear power and renewable energy sources. Increasing concerns about the effect of global warming have been fuelled by the rise in greenhouse gas emissions as a result of continued fossil fuel usage. With an increasing population, energy demand is also increasing, therefore putting further pressure on current sources of energy.

Many renewable energy resources such as solar and wind are currently being used to relieve pressure from fossil fuel usage. Although renewable energy has been found to play an important role in reducing greenhouse gas emissions, there are also issues with these sources. As these sources of energy typically rely on intermittent weather, constant supply is not always possible. Furthermore, when an excess of electricity is produced it cannot be stored and used at a later date. Therefore a more reliable and consistent power source as well as large scale efficient energy storage are required to overcome these current issues.

1.1 Solid Oxide Fuel Cells

While electricity production through combustion of fossil fuels is a mature technology, its efficiency of electricity production is not ideal. A more environmentally friendly solution could be the use of solid oxide fuel cells (SOFCs). SOFCs offer high efficiency for the conversion of the chemical energy from the fuel oxidation to electricity, and therefore stationary power applications with commercial systems are already being developed. In comparison with combustion based power planets which operate with efficiencies at ≈ 30%, SOFCs have higher efficiencies of above 60% with combined heat and power systems having a higher efficiency of up to 85-90%. [1,2]

The first SOFC was developed in 1937 by E. Baur and H. Preis, operating at 1000 °C.[3] The high temperature operation allows the use of a range of fuels including hydrogen, carbon

monoxide and hydrocarbons. Additionally, high temperatures allow the use of cheaper catalysts rather than expensive materials such as platinum required for low temperature polymer electrolyte fuel cells. Although there are advantages to high temperature operation, there are also issues with the degradation of materials, cracking due to thermal expansion mismatch between components, as well as issues with sealing cells. Consequently, research into materials for lower temperature operation (500-700°C) is being performed.

Fuel cells have three main components; an anode, cathode and electrolyte. The fuel and air are continuously supplied to produce electricity and water, with the addition of CO_2 production if fossil fuels are used as the fuel. Oxygen molecules from the air diffuse into the cathode where reduction of oxygen to O^{2-} ions occurs via Equation 1. The oxide ions pass through the oxide ion conducting electrolyte and react with the fuel at the anode (Equation 2). Here electrons are released which then flow around the external circuit producing electricity.

Equation 1 $O_{2\,(g)} + 4e^- \longrightarrow 2\,O^{2-}$

Equation 2 $2H_{2\,(g)} + 2O^{2-} \longrightarrow 2H_2O_{\,(g)} + 4e^-$

Equation 3 $2H_{2\,(g)} + O_{2\,(g)} \longrightarrow 2H_2O_{\,(g)}$

Additionally, water is produced in the form of steam which can either be used in heating, or combined with a turbine can produce more electricity to improve the overall efficiency of the fuel cell. These former systems are called combined heat and power (CHP) systems. In addition to SOFCs based on oxide ion conducting electrolytes, other systems using proton conducting electrolytes can be used (Figure 1).

Traditionally, oxide ion electrolytes have been most widely researched, where the most commonly used system is yttria stabilised zirconia (YSZ) as seen in the first SOFC in 1937[3]. More recently research into proton conducting electrolytes has occurred due to the

higher conductivity at lower temperatures and the advantage of water being produced at the cathode (rather than anode for an oxide ion conducting electrolyte) and therefore dilution of the fuel does not occur under operation (Figure 1).

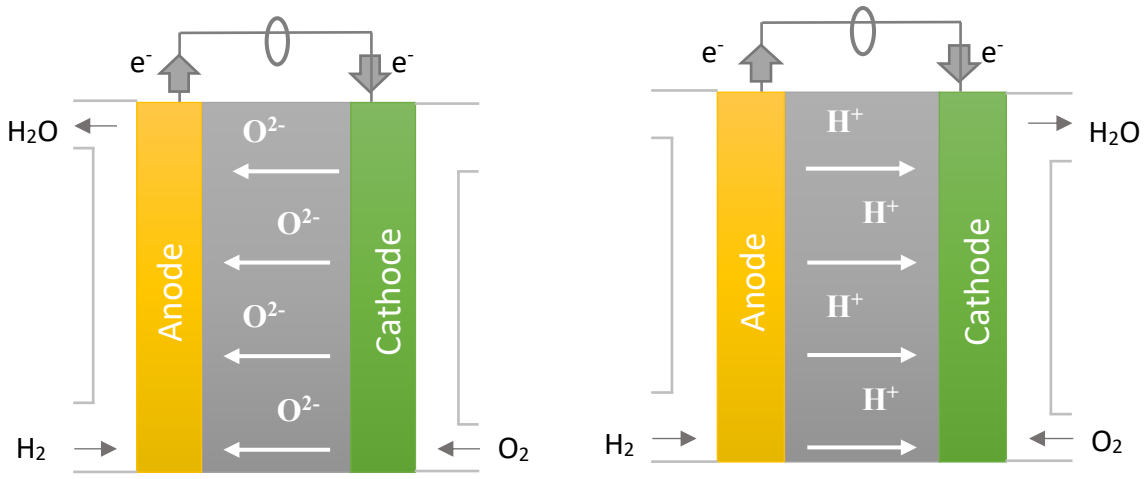

Figure 1. SOFC diagram for an oxide ion conducting electrolyte (left) and proton conducting electrolyte (right)

Although hydrogen is the common fuel source, alternative fuels can be used such as ammonia, methane and higher hydrocarbons. For SOFC systems which use fuels other than hydrogen, an additional step is needed to reform these more complex fuels e.g. steam reformation of methane (Equation 4).

Equation 4 $CH_4 + H_2O \longrightarrow CO + 3H_2$

As shown in Equation 4, methane is combined with steam to produce carbon monoxide and hydrogen. Due to the natural gas network which is already in place, methane as a fuel is a feasible solution for stationary power applications. Additionally, for high

temperature operating SOFCs, steam reformation can be carried out within the cell rather than being externally performed.

However, due to the issues related to high temperature operation of SOFCs, ongoing research is being carried out on the development of new materials in order to lower operating temperatures, reduce cost and improve overall performance. Examples of such materials will be further discussed in the following sections: Electrolyte Materials, Cathode Materials and Anode Materials.

1.1.1 Electrolyte Materials

Electrolytes in SOFCs require high ionic (oxide ion or proton) conductivity and low electronic conductivity, in addition to being stable in both oxidising and reducing conditions. Equally important is the necessity for all materials in the fuel cell to be chemically compatible and have similar thermal expansion coefficients.

The first operating SOFC[3] used yttria stabilised zirconia (YSZ) which has the fluorite, AO_2 structure. Apart from fluorite systems, the other most widely studied electrolyte systems possess the perovskite structure, suitably doped to introduce oxide ion vacancies. For the fluorite systems the highest conductivity is seen for doped bismuth oxide systems, but it has been found these systems can only operate below 400°C, due to issues with instability towards H_2 at higher temperature.[4–7] Consequently, the practical use of the bismuth oxide systems is limited.

The most commonly used fluorite system for electrolytes in SOFCs is YSZ. Pure ZrO_2 is found to have a monoclinic structure which undergoes phase transitions upon increasing temperature.[8] In addition, pure ZrO_2 is found to have low ionic conductivity and therefore is not suitable as an oxide ion electrolyte. Therefore in order to stabilise the highly conducting cubic fluorite structure and improve conductivity, ZrO_2 is doped with various oxides such as

scandium and yttrium oxides.[9] By doping ZrO_2 with Y_2O_3 the cubic fluorite structure is stabilised with the incorporation of oxygen vacancies.[10–13] As a result conductivity is improved compared to the undoped system.[11,14] Additionally, scandium doped systems are also widely studied due to the observed higher conductivity compared to the Y_2O_3 doped system.[10] However, due to the higher cost for scandium doped systems and aging effects on the conductivity, of these Sc doped ZrO_2 systems, YSZ is more favoured.

For the ZrO_2 systems, high operating temperatures (typically > 700 °C) are required which, as previously described, results in numerous issues for SOFCs. To overcome issues related to high temperature operation, electrolyte materials which are compatible with lower temperature operation have been investigated including doped ceria[15–19]. More specifically, gadolinium or samarium doped ceria (CGO or SCO) have been found to be the most promising electrolyte materials for intermediate temperature fuel cell operation (500-600°C).[20,21] By doping ceria with Gd_2O_3, oxygen vacancies are incorporated into the structure via Equation 5. The introduction of oxygen vacancies is vital to improve oxide ion mobility.

Equation 5 $$Gd_2O_3 + 2Ce_{Ce}^{X} + 4O_O^X \longrightarrow 2Gd'_{Ce} + V_O^{\cdot\cdot} + 3O_O^X + 2CeO_2$$

The operating temperatures for doped ceria systems are, however, limited to below 600 °C due to electronic conduction introduced by partial reduction of Ce^{4+} to Ce^{3+} in reducing conditions above this temperature. In addition to studies of fluorite systems, research into perovskite materials has been carried out, including research into doped lanthanum gallate systems. These systems were first reported in 1994 by Ishihara et al.[22], where Sr and Mg co-doped $LaGaO_3$ (LSGM) was reported to have high ionic conductivity and low electronic conductivity. By doping with Sr^{2+} on the La^{3+} site and Mg^{2+} on the Ga^{3+} site, the

formation of oxygen vacancies within the structure occurs. As seen for the Gd_2O_3 doped ceria systems, the incorporation of oxygen vacancies results in improved ionic conductivity. Additionally, operation at temperatures higher than 600 °C can occur when using these perovskite materials, overcoming the temperature limits of the ceria doped system.

Apatite materials have also shown promise as SOFC electrolyte materials with Ge/Si based systems exhibiting high ionic conductivity. Further details are discussed in section 1.4.

Potential electrolyte materials for SOFCs has been dominated by research into oxide ion conducting materials with proton conducting electrolyte materials being less widely studied despite their great promise.[23–29] A range of perovskite materials have been investigated as proton conducting electrolytes including doped $BaCeO_3$[23,27,30] and $AZrO_3$ where A = Ca[28], Sr[25,29], Ba[25]. These systems are found to incorporate water into oxygen vacancies according to Equation 6.

Equation 6 $$H_2O + V_O^{\cdot\cdot} + O_O^X \longrightarrow 2OH_O^{\cdot}$$

Proton conductivity occurs due to the formation of hydroxyl groups, with movement of protons between hydroxyl and oxide groups via the Grotthus mechanism.[31]

Although $BaCeO_3$ systems have been found to have the highest proton conductivity, there are issues related to chemical stability of these systems in CO_2.[32,33] To overcome this issue, anionic doping strategies have been utilised where substitution of O^{2-} for F^-, Cl^- or Br^- has been investigated. Wang et al.[34] reported improved chemical stability upon doping $BaCe_{0.8}Sm_{0.2}O_{3-\delta}$ with Cl^- while also maintaining high proton conductivity as typically seen for $BaCeO_3$ systems. Further to these studies additional anionic doping of $BaCe_{0.8}Sm_{0.2}O_{3-\delta}$[35] and $BaCe_{0.9}Gd_{0.1}O_{3-\delta}$ [36] has been examined. Overall, Br doped $BaCe_{0.9}Gd_{0.1}O_{3-\delta}$ resulted in

better chemical stability with comparable conductivity to the undoped system.[36] The most effective way to improve the stability is however to co-dope with Zr. Ruy et al.[37] investigated solid solutions of $BaCeO_3$-$BaZrO_3$ finding improved stability in CO_2 and H_2O when doping with Zr. Furthermore, Katahira et al.[27] reported Zr incorporation into barium cerate system giving $BaCe_{0.9-x}Zr_xY_{0.1}O_{3-\delta}$. Again, improvements to chemical stability are reported with increasing Zr content with pure protonic conduction in a hydrogen atmosphere. Although improvements in chemical stability were observed, increasing Zr content results in a decrease in proton conductivity.

1.1.2 Cathode Materials

For SOFCs the cathode is required to catalyse the reduction of oxygen. As for electrolyte materials, there are also a number of key requirements for electrode materials. These requirements include high electronic and ionic conductivity, high catalytic activity for oxygen reduction and stability at high temperatures in oxidising conditions. In addition to these requirements, the cathode should be chemically compatible and have similar a thermal expansion coefficient to the electrolyte.

For an oxide ion electrolyte based SOFC, strontium doped lanthanum manganates (LSM) were traditionally the most commonly used cathode material. Research has shown LSM has high electronic conductivity, a good thermal expansion coefficient match with YSZ and is chemical compatible with the commonly used electrolyte YSZ.[38–40] However an issue is the poor oxide ion conductivity and issues with LSM reacting with YSZ at elevated temperatures.

For SOFC systems with CGO electrolytes, strontium doped $LaCoO_3$ systems ($La_{1-x}Sr_xCoO_3$ or mixed Co/Fe systems) have been shown to improve catalytic activity and oxide ion conductivity.[41–43] In comparison, LSC cathodes are not suitable for use with YSZ

electrolytes due to incompatible thermal expansion coefficients and issues with electrode and electrolyte materials reacting with each other at the high operating temperature.[41] Further cation doping of $LaCoO_3$ has been investigated resulting in the mixed Co/Fe perovskite, $La_{1-x}Sr_xCo_{1-y}Fe_yO_{3-\partial}$ (LSCF). LSCF is found to be the most promising mixed conducting electrode system, although it is generally used with CGO systems than YSZ systems.[44–47] For use with the latter, typically the protective CGO layer is deposited on the YSZ electrolyte.

Due to the cobalt systems reacting with YSZ, further research into alternative materials which are compatible with YSZ has been carried out. It has been found that Sr doped $LaFeO_3$ (LSF) shows promising performance with reduced reactivity with YSZ.[48,49] In addition to the La perovskite systems, the Ba system $Ba_{0.5}Sr_{0.5}Co_{0.8}Fe_{0.2}O_{3-\partial}$ (BSCF) has shown significant promise for low temperature (≈ 500 °C) solid oxide fuel cells.[50] By doping $SrCo_{0.8}Fe_{0.2}O_{3-\partial}$ with the larger Ba^{2+} vs Sr^{2+}, improved performance was achieved. [51] Wei et al.[52] and Chen et al. [53] further investigated the effect of Ba and Fe content, respectively, which showed in addition to $Ba_{0.5}Sr_{0.5}Co_{0.8}Fe_{0.2}O_{3-\partial}$, $Ba_{0.4}Sr_{0.6}Co_{0.8}Fe_{0.2}O_{3-\partial}$ was also found to be a promising cathode material.[52] Although an increase in area specific resistance was observed with increasing iron content in $Ba_{0.5}Sr_{0.5}Co_{1-y}Fe_yO_{3-\partial}$ systems, a decrease in oxygen non-stoichiometry and electrical conductivity was reported.[53] There are, however, issues with BSCF, notably an instability at SOFC operating temperatures which leads to a gradual transformation to a poorly performing hexagonal perovskite system.

Following on from research on perovskites, the perovskite related Ruddlesden-Popper systems have been investigated for potential cathode materials. Specifically, n=1 (K_2NiF_4) systems have been reported as promising cathode materials. The most widely studied system, $La_2NiO_{4+\partial}$, has been of particular interest for lower temperature operation. [54,55] $La_2NiO_{4+\partial}$ is found to be stable at intermediate temperature fuel cell operating temperatures (500-700 °C)

with high oxide ion and electronic conductivity.[56,57] However, $La_2NiO_{4+\partial}$ is found to react with CGO and YSZ. [58] Further Ruddlesden-Popper systems will be discussed in section 1.3.

1.1.3 Anode Materials

Similar properties are needed for anode materials as for cathode materials, where high electronic and ionic conductivity, chemical compatibility with other components and similar thermal expansion coefficients are required. Furthermore, anode materials must have high catalytic activity for oxidation of the fuel and high stability at high temperatures in reducing conditions.

For SOFCs which use hydrogen as the fuel, Ni/electrolyte composites such as Ni/YSZ cermets are commonly used due to the compatibility of the thermal expansion coefficients of the cermet and the electrolyte. For high temperature operation (>500 °C) with alternative fuels such as natural gas, Ni/YSZ anodes are not ideal materials. This is due to issues with catalytic cracking at high temperatures in low $p(H_2O)$, leading to the formation of carbon and thus resulting in poisoning of the anode. Alternatively, a more suitable anode material for use with hydrocarbons would be a Ni/CGO composite material although this still can also give rise to issues with carbon deposition.[59] In addition to carbon deposition, the presence of sulfur as an impurity in hydrocarbon fuels is an problem for such anode materials. Poisoning of the Ni in the anode through adsorbed suflur results in the reduction of cell performance. Furthermore on extended operation at elevated temperatures, sintering of Ni particles can occur reducing surface area and therefore catalytic performance. Therefore new anode materials are required to be more robust against carbon deposition and sulfur poisoning.

In addition to Ni electrolyte composite materials, alternate materials including perovskites such as $(La/Sr)_{1-x}TiO_{3-\delta}$ and $Sr_{1-x}Ti_{1-y}Nb_yO_3$ have been investigated.[60–64] These

materials have been shown to have respectable electronic conductivity and remain stable under reducing conditions, although the catalytic activity is lower than Ni containing anodes.

Further perovskite anode materials including lanthanum chromates have been found to be potential SOFC anode materials.[65–67] Tao et al. reported a chromate-manganate perovskite, $La_{0.75}Sr_{0.25}Cr_{0.5}Mn_{0.5}O_3$, which is stable at elevated temperatures in both oxidising and reducing conditions.[65] Catalytic activity was, however, lower than Ni based anodes.

1.2 Perovskites

The perovskite structure was first reported in 1839 by Gustav Rose who discovered the mineral form of $CaTiO_3$. The perovskite structure (Figure 2) has the ideal general formula ABX_3 where in this ideal perovskite, A is 12 coordinate and B is 6 coordinate. The perovskite structure is particularly interesting as it can accommodate a wide variety of elements and defects making it an appealing material for a range of applications.

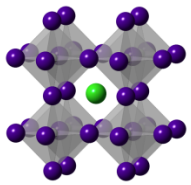

Figure 2. The perovskite structure with the general formula ABX_3 where green = A, grey = B and purple = X.

Ideally, the perovskite structure is a cubic system which can be predicted by using the Goldschmidt[68] tolerance factor as seen in Equation 7.

Equation 7 $$t = \frac{r_A + r_X}{\sqrt{2}(r_B + r_X)}$$

For ABX_3 systems, r_A is the ionic radius of cation A, r_B is the ionic radius of cation B and r_X is the ionic radius of the anion which is typically oxygen. By calculating the tolerance factor, any distortion from the ideal cubic structure can be predicted. For systems where t=1, it is predicted that the ideal cubic perovskite structure is formed. Deviation from t=1 can result in distortion from cubic symmetry. For t <1 it is predicted that the octahedra will tilt due to the B cation being too large. Values of t>1 indicate that the B cation is too small for the perovskite structure resulting in either an off-centre displacement, or the formation of alternate, so-called, hexagonal perovskites.

A range of perovskite materials have been researched as potential SOFC electrolytes or electrode materials as highlighted earlier. Commonly for perovskite systems, rare earth or alkaline earth metals are used for the A cation site and smaller transition metals are used for the B cation site. An example includes the perovskite system $LaMnO_3$ which, as described, has a larger rare earth metal, La^{3+} (ionic radius for 12-coordination: 1.36 Å[69]) on the A site, and a smaller transition metal Mn^{3+} (ionic radius for 6-coordination: 0.645 Å[69]) on the B site. Doping with strontium in $LaMnO_3$ systems introduces mixed valency (Mn^{3+}/Mn^{4+}), resulting in improved electronic conductivity as described in section 1.1.2 Cathode Materials. [38–40]

Additionally, doped $SrTiO_3$ systems have been researched as potential anode materials. While H_2 reduced $SrTiO_3$ is a moderate electronic conductor, it is a poor oxide ion conductor, and so improvements to ionic conductivity by doping have been used to enhance the performance of these potential anode materials. By doping with lanthanides or yttrium on the strontium site, or Nb on the Ti site, enhanced conductivity is reported.[70,71]

It is evident that perovskite materials show promising applications as electrode and electrolyte materials in SOFCs, and the flexibility of the structure to doping provides many potential avenues to improve material performance.

1.3 Ruddlesden-Popper Phases

Ruddlesden-Popper phases were first investigated by Ruddlesden and Popper, where a series of $Sr_{n+1}Ti_nO_{3n+1}$ materials were reported.[72,73] In 1957 Ruddlesden and Popper reported the synthesis and characterisation of Sr_2TiO_4, Ca_2MnO_4, $SrLaAlO_4$ (n=1 phases) which were found to possess the K_2NiF_4 structure which can be considered as having a single perovskite layer separated by rock salt layers.[72] A year later, $Sr_3Ti_2O_7$ (n=2) and $Sr_4Ti_3O_{10}$ (n=3) were reported by the same authors, where the structures were found to have alternating layers of double (n=2) or triple (n=3) perovskites and rock salt type SrO layers as seen in Figure 3.[73]

In general Ruddlesden-Popper structures have the formula $A_{n+1}B_nO_{3n+1}$ where n=1 ,2, 3. As n increases the number of adjacent perovskite layers increases as seen in Figure 3. The perovskite structure can be classed as the n = ∞ extreme.

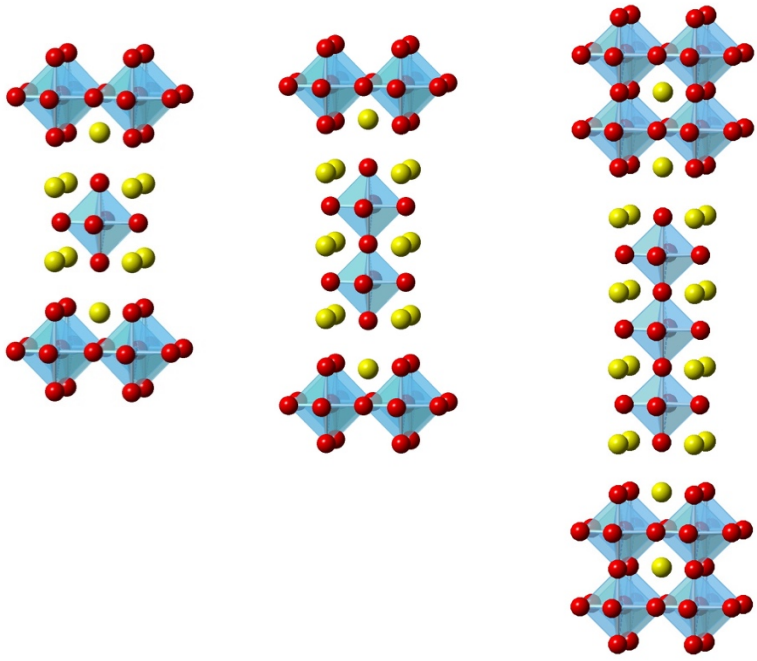

Figure 3. Ruddlesden-Popper structures with the general formula $A_{n+1}B_nO_{3n+1}$ where n=1 (left), 2 (middle), 3 (right). Yellow = A, blue = B and red = O.

As seen for perovskite systems, numerous Ruddlesden-Popper structures are also found to have applications for SOFC materials. This is related to the additional ability of such phases to incorporate excess oxide ions in interstitial sites as well as to incorporate oxide ion vacancies. Thus, there is great flexibility to move from a system containing oxide ion vacancies to one containing oxide ion interstitials through doping. The most extensively researched systems are the n=1 phases which have the K_2NiF_4 structure. In this area, $La_2NiO_{4+\delta}$ has been reported to be a good candidate cathode material.[54,55,57,74,75]

Less widely studied are the n>1 Ruddlesden-Popper phases. Higher order Ruddlesden-Popper phases $La_3Ni_2O_7$ and $La_4Ni_3O_{10}$ have been reported to display improved electronic conductivity compared to $La_2NiO_{4+\delta}$.[75–78] For the higher order Ruddlesden-Popper systems, this leads to improved electrode performance along with improved thermal stability as reported by Anow and Skinner.[75] These systems have therefore been shown to be good candidates for cathode materials operating at lower temperatures.

Additionally, $(La,Sr)_{n+1}(Fe,Co)_nO_{3n+1}$ systems have been investigated as potential cathode materials.[79–81] $LaSr_3Fe_{3-y}Co_yO_{10-\delta}$[79] was investigated by Lee and Manthiram, who showed that the electrochemical performance was comparable to the well-known perovskite $La_{0.6}Sr_{0.4}CoO_{3-\delta}$. An advantage of the n=3 Ruddlesden-Popper systems is the lower thermal expansion coefficient and improved structural stability compared with the perovskite systems.

Lee et al. have also investigated the n=2 Ruddlesden-Popper system, $Sr_{3-x}La_xFe_{2-y}Co_yO_{7-\delta}$[80], as a potential cathode material for an intermediate temperature SOFC. These materials were found to have improved electrical conductivity, thermal expansion coefficients and electrochemical performance comparable to the n=3 Ruddlesden-Popper phase and other cobalt based perovskite systems.

Thus, although the n>1 Ruddlesden-Popper phases have been not as widely studied, they do show promising results for applications as potential cathode materials in SOFCs.

1.4 Apatites

The apatite structure has the general formula $A_{10}(MO_4)_6X_{2+\delta}$ where A is a rare earth or alkaline earth metal, M is Si, Ge or P and X is OH^-, O^{2-} or halides. The structure has a hexagonal unit cell with an arrangement of MO_4 tetrahedra forming A site and oxide ion channels (Figure 4). A number of materials with the apatite structure have been found to have good oxide ion conductivity with negligible electronic conductivity therefore making them appealing electrolyte materials for SOFC applications.

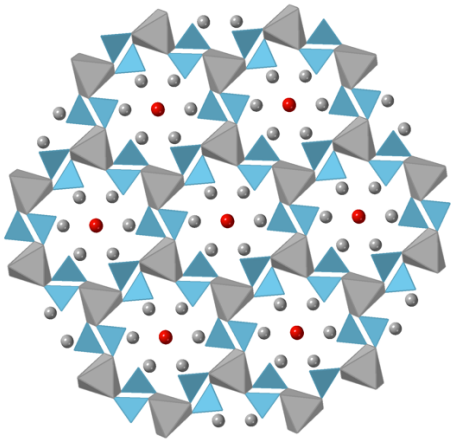

Figure 4. The apatite structure with the general formula $A_{10}(MO_4)_6X_{2+\delta}$ where grey = A, blue = MO_4, red = X.

Nakayama et al.[82,83] first reported high oxide ion conductivity in silicate apatite systems. Samson et al.[84] later investigated $La_{9.33}Si_6O_{26}$ and $La_8Sr_2Si_6O_{26}$ systems, and showed that the presence of vacancies on the cation site in $La_{9.33}Si_6O_{26}$ leads to additional displacement of channel oxygens into interstitial sites resulting in higher oxide ion conductivity. This work was the first to highlight the importance of interstitial oxygen on oxide ion conductivity. A range of Si/Ge apatite phases have also been investigated by Najib

et al.[85] showing the importance of oxygen interstitials with samples showing oxygen excess having higher conductivity. In addition, doping strategies on both La and Si sites have been investigated in order to improve properties for solid oxide fuel cell applications. McFarlane et al.[86] reported the incorporation of transition metals Co, Fe, Mn and Cr into $La_{9.33}Si_6O_{26}$ where Mn favours doping on the La site and other transition metals on the Si site. The highest conductivity was found for Co doping where an increase in oxygen content resulted in improved oxide ion conductivity.

In addition to silicate apatite systems, germanium apatite phases have been investigated. $La_{9.33}Ge_6O_{26}$ forms the hexagonal structure with high oxide ion conductivity.[87] Increasing the La content raises the conductivity by introducing oxide ion excess in interstitial sites. At very high levels of oxygen excess, e.g. $La_{10}Ge_6O_{27}$[88–90], distortions to a triclinic cell result in a reduction in conductivity. Therefore there is an optimum oxygen excess ($\delta \approx 0.5$) to ensure the hexagonal structure is retained. Although germanium apatite phases are found to have poor ionic conductivity compared with Si phases, León-Reina et al.[89] highlighted a significant proton contribution for La-Ge-O apatite phases above 600 K. Due to issues with Ge loss in Ge apatite systems, Sansom et al[91] investigated mixed Si/Ge system, $La_{9.33}Si_{6-x}Ge_xO_{26}$. The optimum Ge doping and highest conductivity was found for x=4 with higher Ge contents suffering from Ge loss at high temperatures. Further doping strategies by Orera et al.[92] found stabilisation of the hexagonal apatite structure with enhancement in conductivity at low temperature could be achieved by doping on either the La or Ge site with Y, Yb, Ti, Nb and W.

A range of dopants have been used to improve properties of apatite phases including doping on La and Si/Ge sites. Some examples include doping with Sr[84,93], Ba[91], Mg[94], B[95], Mn[86], Co[86], Fe[86] and Cu[96].

In comparison phosphate apatites are found to have poor ionic conductivity to Si/Ge apatite system which can be related to an inability to accommodate oxygen excess.

1.5 Oxyanion Doping

Traditionally SOFC materials have been doped with cations which have a similar size, but different charge. An alternate method for adapting SOFC materials such as perovskite and Ruddlesden-Popper type materials is through oxyanion doping, where a perovskite octahedral BO_6 unit is effectively replaced by a BO_4 (B=Si, P, S), or BO_3 (B= C, B, N) unit.[97] This has the effect of stabilising oxide ion vacancies around the oxyanion, allowing for the preparation of new materials.

Previous work on superconducting perovskite-type cuprate systems reported a number of examples of incorporation of oxyanions such as nitrate, phosphate, carbonate and sulfate.[98,99] Slater et al.[92] reported the successful incorporation of sulfate and phosphate into $YSr_2Cu_3O_7$ achieving superconducting phases. Subsequent work has followed on from the superconducting cuprate systems with further investigation into perovskite-type systems with transition metals other than copper. More recently oxyanion doping of materials for SOFC applications has been carried out. The first report in this latter area examined oxyanion doping of the potential electrolyte material, $Ba_2In_2O_5$.[100,101] At room temperature, $Ba_2In_2O_5$ possesses the brownmillerite structure with ordered oxide ion vacancies. The ordering of oxide ion vacancies results in low oxide ion conductivity. By increasing the temperature to approximately 930 °C a phase change occurs resulting in disorder of the oxide ion vacancies.[102,103] By doping with phosphate[101,104], sulfate[101,105] or silicate[100] the disordered cubic structure was shown to be stabilised to room temperature, resulting in improved conductivity. Not only were these systems found to have high oxide ion conductivity, they

were also shown to display high protonic contributions in wet atmospheres, along with improved stabilities. Water is incorporated into these systems by filling oxide ion vacancies as described in Equation 6. Proton conductivity occurs via the Grotthus mechanism where H^+ ions migrate between hydroxide ions. In addition to XRD and conductivity data, Raman and ^{31}P NMR analysis was carried out by Shin et al.[101] in order to confirm the incorporation of phosphate in $Ba_2In_2O_5$. Raman data indicated the presence of phosphate within the structure with increasing intensity of the phosphate band with increasing phosphate content. By combining the Raman and ^{31}P NMR data, incorporation of phosphate into $Ba_2In_2O_5$ was confirmed.

In addition to electrolyte materials, potential electrode materials have been shown to incorporate oxyanions. Examples include $SrMnO_3$[106,107] and $SrCoO_3$[106,108–110], which at room temperature both adopt a hexagonal perovskite structure. By doping these systems with silicate the disordered cubic perovskite cell is stabilised.[108] A similar result is also seen for sulfate and phosphate doping of $SrCoO_3$ where Hancock et al.[108] reported the successful incorporation of sulfate and phosphate into the cubic perovskite structure with enhanced conductivity. Additionally, oxyanion doped $SrCoO_3$ has been used for mixed ionic-electronic conducting membrane technology[110] and as an electrocatalyst for the oxygen evolution reaction in electrolytes[109]. Stabilisation of the cubic perovskite occurs for these systems due to the incorporation of higher valent oxyanions e.g. P^{5+} and S^{6+}. As tetrahedral oxyanions are incorporated on the octahedral transition metal site, oxygen vacancies are introduced. Therefore due to the creation of oxygen vacancies partial reduction of the transition metal e.g. Co^{4+} to the larger Co^{3+} occurs, resulting in a reduction in the tolerance factor.

Porras-Vazquez et al.[111] also reported that the iron oxide system, $SrFeO_{3-\delta}$ could also incorporate silicate. The undoped system, $SrFeO_{3-\delta}$ has high ionic and electronic conductivity

and therefore is appealing for use in SOFCs. However, in low $p(O_2)$, oxygen loss occurs leading to the formation of $Sr_2Fe_2O_5$ which has the brownmillerite structure, and hence ordered oxide ion vacancies and low oxide ion conductivity. As seen for other perovskite oxide systems, by doping with oxyanions the disordered cubic structure was stabilised even in low $p(O_2)$.

In addition to perovskite materials, oxyanion incorporation into the Ruddlesden-Popper system $Sr_4Fe_3O_{10-\delta}$ has been reported by Yamaura et al.[112], Bréard et al.[113] and Gonano et al.[114,115]. Carbonate and /or sulfate were successfully incorporated into $Sr_4Fe_3O_{10-\delta}$ through solid state synthesis in evacuated sealed tubes.

Overall, oxyanion doping of a range of perovskite-type materials has shown to be able to modify the structure and improve the performance for a range of SOFC materials. A key effect appears to be the stabilisation of oxide ion vacancies by the oxyanion. Although a range of materials and oxyanion dopants have been investigated, there is potential for further systems to be investigated including perovskite type materials for SOFC applications. Therefore, further work in expanding oxyanion doping into perovskite type materials will be discussed in this work.

1.6 Exsolution

Surfaces coated with metal nanoparticles are found to be appealing materials due to their attractive catalytic properties. Due to issues with dispersion of nanoparticles on the surface of these materials, in-situ exsolution has attracted considerable interest. In-situ exsolution is achieved by initially doping materials with metals such as Ni and Cu. These phases are then heated in reducing conditions e.g. H_2, in order to exsolve the metal nanoparticles onto the surface. An example equation as described by Neagu et al. [116] for exsolution of A-site deficient perovskites is given in Equation 8.

Equation 8[116] $A_{1-\alpha}BO_{3-\delta} \longrightarrow (1 - \alpha)\, ABO_{3-\delta'} + \alpha B$

This technique has already been investigated for a number of SOFC materials. Madsen et al.[117] and Kobsiriphat et al.[118,119] have successfully exsolved Ru and Ni nanoparticles on the surface of lanthanum chromite perovskite materials ($La_{0.8}Sr_{0.2}CrO_{3-\delta}$). Improvements in electrochemical performance compared with the undoped ($La_{0.8}Sr_{0.2}CrO_{3-\delta}$) due to Ni nanocluster nucleation is observed making them appealing anode materials for solid oxide fuel cells. Perovskite materials have been of particular interest for in-situ exsolution of nanoparticles. A wide range of perovskite materials have been investigated with a number of different metals including Ni[116,119–125], Fe[122] and Ru[117–119]. Nickel doped perovskite materials have been of particular interest for energy applications. Tsekouras et al.[122] successfully exsolved Ni and Fe nanoparticles onto the surface of A-site deficient perovskite, $La_{0.4}Sr_{0.4}TiO_{3-\delta}$. Under reducing conditions exsolution of metal nanoparticles with an increase in oxygen vacancy concentration occurs. In particular the Ni doped perovskite phase, $La_{0.4}Sr_{0.4}Ti_{0.94}Ni_{0.06}O_{2.94}$, is found to be the most appealing as a solid oxide electrolysis cell (SOEC) cathode material. Although studies have been dominated by B site doping, Lee et al.[126] reported exsolution from the Ca A-site in the Ni doped perovskite phase. Additionally, more than one metal dopant can be introduced and exsolved to produce metal alloys on the surface of perovskite materials under reducing conditions.[127–129] Lu et al.[127] demonstrated the in-situ exsolution of Ni/Cu alloys from the perovskite phase $(La_{0.75}Sr_{0.25})_{0.9}(Cr_{0.5}Mn_{0.5})_{0.9}(Ni_{1-x}Cu_x)_{0.1}O_{3-\delta}$ with XRD and XPS studies supporting the presence of $Ni_{1-x}Cu_x$ alloys. This method shows different synthesis techniques can be used to improve stability and performance of potential SOFC materials. While exsolution from perovskite materials has

been widely studied, similar experiments for other structure types are lacking, and so there is a need to extend this work accordingly.

2 Project Aims

The aim of this project is to apply various doping strategies to create a variety of novel materials for energy applications. A particular focus will be on perovskite and perovskite related materials due to the promising applications of these phases in SOFCs. In order to test suitability for use as cathode and electrolyte materials for SOFCs, stability in fuel cell conditions and the effect of the doping strategy on conductivity will be investigated.

Previous research has shown the successful incorporation of oxyanions in cathode and electrolyte materials. Therefore a range of oxyanions including sulfate, borate, carbonate, phosphate and chromate will be examined for these perovskite and perovskite related materials. For these materials a key focus will be on stabilising the desired structure by oxyanion incorporation and investigating the suitability of these materials for SOFCs.

Additionally, fluorination of oxyanion doped Ruddlesden-Popper phases will be investigated to analyse the effect on the Ruddlesden-Popper structure. Specifically, diffraction techniques and ^{57}Fe Mössbauer spectroscopy will be used to investigate the purity and structure of these materials with increasing F content including the effect of incorporation of anions into interstitial sites.

Finally, due to the success of metal exsolution from perovskites, the potential for in-situ exsolution from other structure types will be examined. In particular, in-situ exsolution of Cu doped apatite materials will be investigated. Here the key aim is to successfully exsolve nanoparticles on the surface of a range of apatite materials while maintaining the apatite structure.

3 Experimental

3.1 Synthesis techniques

3.1.1 Solid state synthesis

Solid state synthesis is the most commonly used method for the synthesis of solid inorganic materials. This method involves grinding the required amounts of starting materials and heating to high temperature for several hours or days in a crucible typically made from an inert material such as alumina. Regrinding and reheating of samples is commonly carried out to refresh surface contact and ensure homogeneity to aid synthesis. Mixing of materials can be carried out manually or with mechanical methods such as ball milling. By heating to high temperature large activation energies required to synthesise the thermodynamically most stable products are overcome. Due to the high temperature synthesis the most stable products are usually formed, therefore this method is not suitable for the synthesis of metastable phases.

Although there is ease of synthesis with this method, there are also issues with solid state synthesis. Although high temperature synthesis is a simple method to effectively produce single phase materials, when impurities do occur it is almost always impossible to purify materials. A number of issues can cause impurities in the synthesis of solid state materials including hygroscopic starting materials and volatility of reagents. Hygroscopic materials can lead to incorrect stoichiometry when preparing materials, therefore drying of starting materials may be needed before the preparation of materials. Additionally, due to the high temperature synthesis issues with volatility of reagents such as barium can occur. Therefore a number of additional measures can be taken. This involves using excess of reagents such as excess $BaCO_3$ in the synthesis of Ba containing compounds $BaCO_3$ and/or

additionally pressing powders into pellets to improve surface contact and reduce evaporation of materials. Further to this sacrificial powder can be placed on top of the pellet to reduce volatility with additional sanding of pellets to remove any impure Ba deficient layer.

3.1.2 Fluorination

Fluorine incorporation into materials can occur via insertion of F into vacancy/interstitial sites, substitution of O by F (either direct substitution (2F in place of 1O) or reductive substitution (1F in place of 1O), or a combination of both these processes. This can be carried out through a number of methods such as reacting samples with F_2 gas or heating with NH_4F at low temperatures.[130,131] There are, however, a number of problems such as toxicity of F_2 gas, and issues with controlling the fluorination and impurity phases. Consequently, alternative methods have been attracting attention, such as heat treatment with F-containing polymers. In this work low temperature fluorination has been carried out specifically using polyvinylidene fluoride (PVDF). This polymer has been shown to be an excellent fluorinating agent with improved purity and control over fluorination level.[132] For example synthesis of K_2NiF_4 related phases, $Sr_2TiO_3F_2$ and $Ca_2CuO_2F_2$ were successfully made using low temperature synthesis with PVDF.[132] By using this method the quality of phases were improved compared to other fluorination methods.[132] In this thesis fluorination was carried out by grinding stoichiometric amounts of PVDF and oxide materials with slow heating in a furnace to low temperature (≈ 350 °C).

3.2 Structural characterisation

X-ray diffraction (XRD) and Neutron diffraction (ND) were used in this work with XRD as the main technique to determine the purity of samples and for structural analysis.

3.2.1 Crystallography

In a crystalline solid there is a regular pattern of atoms forming a structure. This is represented by a repeating three dimensional pattern which in its simplest form can be described by its unit cell (Figure 5). The lattice parameters of a system are given by the angles (α, β and γ) and lengths (a, b and c) are used to define the unit cell. There are seven allowed shapes (Table 1) with an additional 4 types of lattice centerings. These are given as primitive (P), body centred (I) and face centred (F) and base centred (C) and can be used to describe the crystal system. Combining these 4 lattice types with the crystal systems described in Table 1, leads to a total of 14 possible Bravais lattices. Symmetry elements also need to be considered in order to fully describe the crystal structure in three dimensions. These include inversion centre, rotation axes and mirror planes (point symmetry elements) and glide planes and screw axes (translation symmetry elements). All of this information gives a total of 230 different space groups which are used to describe the full symmetry of the system.

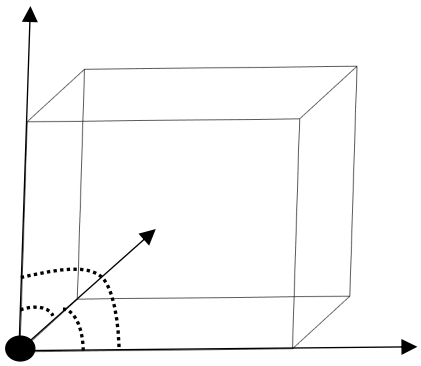

Figure 5. Lattice parameters of a unit cell

Table 1. Seven allowed crystal systems

Crystal system	Unit cell parameters
Cubic	$a = b = c$ $\alpha = \beta = \gamma = 90°$
Hexagonal	$a = b \neq c$ $\alpha = \beta = 90° \gamma = 120°$
Trigonal/ Rhombohedral	$a = b = c$ $\alpha = \beta = \gamma \neq 90°$
Tetragonal	$a = b \neq c$ $\alpha = \beta = \gamma = 90°$
Orthorhombic	$a \neq b \neq c$ $\alpha = \beta = \gamma = 90°$
Monoclinic	$a \neq b \neq c$ $\alpha = \gamma = 90° \beta \neq 90°$
Triclinic	$a \neq b \neq c$ $\alpha \neq \beta \neq \gamma$

Additionally important for powder diffraction is the lattice planes which can be described by using Miller indices (hkl). These lattice planes are determined by the points at which the lattice plane intersects the unit cell. This is given by the reciprocal of the fractional intercepts along the lattice vectors. An example of which is given in Figure 6.

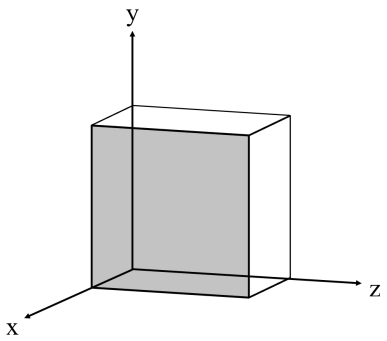

Figure 6. Cubic unit cell showing shaded lattice plane (grey) with miller indices (100)

3.2.2 X-ray diffraction

X-ray diffraction is a valuable non-destructive technique used in order to investigate the crystal structure and phase composition of a material. X-rays are used due to the wavelength being similar to the distance between atoms in a solid (approximately 1Å). Incident X-rays are scattered by electrons in atoms giving rise to a diffraction pattern. This process can be explained via Figure 7; here two adjacent lattice planes are separated by distance d with the incident X-rays interacting with the set of planes at angle θ. When waves are scattered interference occurs resulting in waves being either in phase or out of phase. When waves are out of phase there is a loss of intensity due to destructive interference. When waves are in phase a gain in intensity is observed due to constructive interference and as a result peaks in a diffraction pattern. Constructive interference can be described using Bragg's law (Equation 9). A strong peak in the diffraction pattern is observed when the law is satisfied.

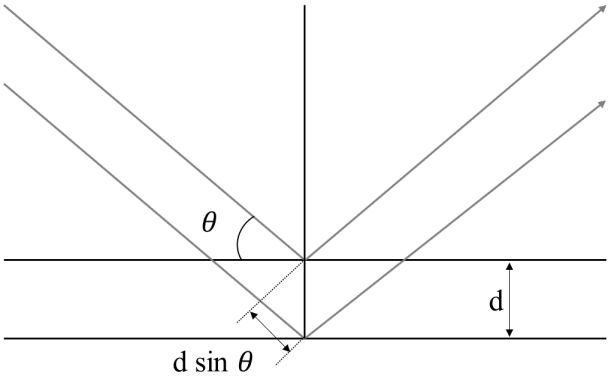

Figure 7. Schematic representation of Bragg's Law where θ is the angle of incidence, d is the distance between lattice planes and d sin θ is the path difference.

Equation 9 $2d\sin\theta = n\lambda$

In order to record such diffraction data, an X-ray diffractometer instrument is required. Laboratory based powder X-ray diffractometers have a number of components including a sample stage, an X-ray source and a detector. Two instrument orientations are commonly used. The two orientations are named Bragg-Brentano (reflection) and Debye-Scherrer (transmission). Firstly, the X-ray source commonly used is a sealed glass tube. This contains a metal target anode and a tungsten filament cathode where high energy electrons bombard the metal target resulting in an energy emission in the X-ray region of the electromagnetic spectrum. This occurs due to the ejection of a core electron resulting in the creation of a hole. Higher energy electrons will drop into the hole and release a specific amount of energy. The released X-ray has a characteristic wavelength associated with the target material. As electrons from different shells can drop to fill the hole, there is the emission of different radiation e.g. K_α, K_β as seen in Figure 8. In addition to the characteristic wavelength a continuous spectrum is produced when electrons hit the target (Bremsstrahlung radiation) see Figure 9 with sharp intensity maxima for the emission of characteristic wavelengths.

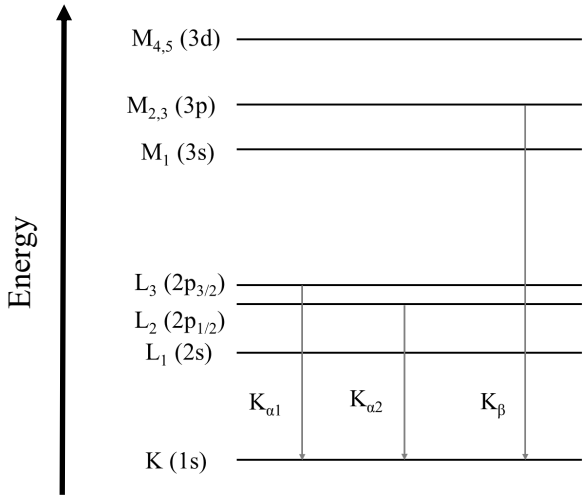

Figure 8. Energy level diagram showing electron transitions for copper

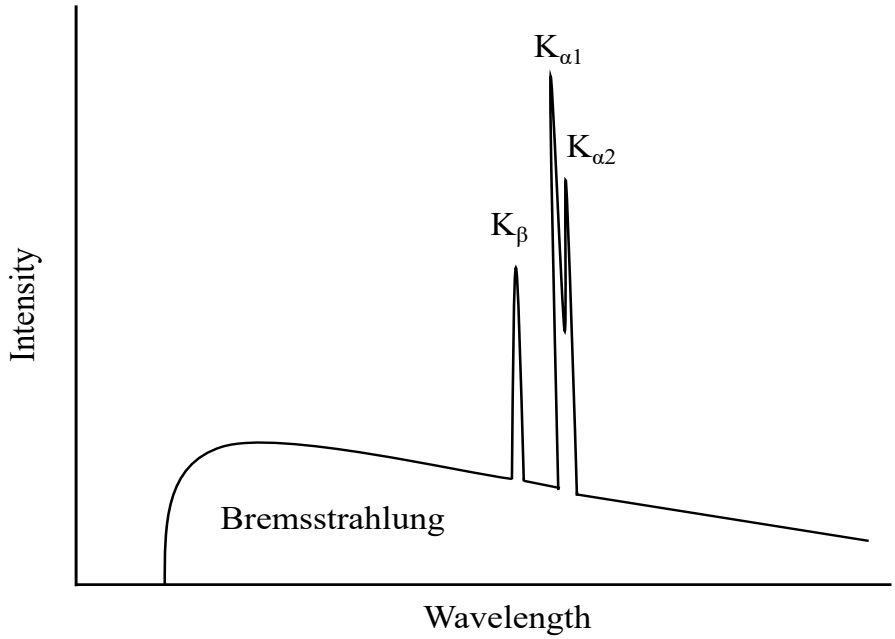

Figure 9. X-ray spectrum from a copper target

In order to remove unwanted radiation and to ensure a single wavelength of X-rays as required for diffraction, crystal monochromators or filters are used. Crystal monochromators are set at a specific orientation which ensures the Bragg equation (Equation 9) is obeyed therefore resulting in a single wavelength needed for diffraction. Alternatively a filter can be

used where the absorption edge of the filter falls between the K_α and K_β radiation. For example when using a Cu source a Ni filter is used to remove the K_β radiation.

Within this work three different diffractometers were used for XRD analysis. A Panalytical Empyrean diffractometer equipped with a Pixcel 2D detector (Cu Kα radiation) and Bruker D8 and D5005 diffractometers with Cu Kα radiation.

3.2.3 Neutron diffraction

In comparison to XRD where X-rays interact with electrons, in ND neutrons interact with the nucleus of the atoms. Therefore where X-ray scattering is dominated by heavier elements, this is not necessarily the situation for ND. As a result lighter elements can be detected through ND; furthermore, neighbouring elements can also often be readily distinguished. Additionally, neutrons have a magnetic moment which can interact with unpaired electrons giving rise to information about the magnetic structure. Therefore through combining XRD and ND data, detailed information about the structure of materials can be obtained.

Typically, there are two different methods to produce neutrons. One method involves fission of nuclear materials. An alternative method involves using high energy protons to bombard a metal target to produce a neutron beam. The latter method is called spallation. Within this thesis neutron diffraction experiments were carried out at ISIS neutron and muon source using the high resolution powder diffractometer (HRPD).[133] This facility uses a spallation source and the time of flight technique. In comparison to X-ray diffraction where a fixed wavelength is used, and θ is varied, for time of flight ND the wavelength is effectively varied while θ is fixed. Therefore the ND data can be plotted as intensity vs time of flight. Additionally, this can also be plotted as intensity vs d-spacing by combining Bragg's Law

(Equation 9), the de Broglie relationship (Equation 10) and using the relationship of velocity = length/ time. This gives the final equation given by Equation 11.

Equation 10 $$\lambda = \frac{h}{mv}$$

Equation 11 $$t_{hkl} = \frac{mL}{h} \times 2d_{hkl}\sin\theta$$

Although a powerful technique for structure characterisation, large scale central facilities are required for ND which in comparison to XRD are less easily accessible. Therefore this method was only used for selective samples.

3.2.4 Rietveld refinement

The Rietveld refinement method is used to solve structures by using a starting structural model and then refining this model to minimise the difference between calculated and experimental diffraction patterns. This technique was first described by Hugo Rietveld in the 1960s.[134,135] The measured intensities for Bragg peaks are related to the structure factor shown in Equation 12. The structure factor gives information about the scattering of incident X-ray radiation by all atoms in the unit cell and is given by Equation 13. This equation sums the scattering from all atoms in the unit cell and is dependent on the position of atoms (x_j, y_j and z_j) and the type of atom (scattering factor f_j). The sum of scattering for a given Miller plane forms a diffraction peak as given by Equation 12. Where the structure factor is zero no intensity is observed in the diffraction pattern and is a forbidden reflection.

Equation 12 $$I_{hkl} \propto F_{hkl}^2$$

Equation 13 $$F_{hkl} = \sum_{j=1}^{m} f_j \exp\left[2\pi i \left(hx_j + ky_j + lz_j\right)\right]$$

For single crystal experiments, the intensities collected are for individual Bragg peaks and these can be utilised to accurately determine the crystal structure. In comparison, for powder diffraction the measurement of individual peak intensities is hindered due to overlapping of peaks, and so structure solution is more challenging. Therefore in order to characterise powder materials, the Rietveld method is used.

The Rietveld method uses the least-squares refinement procedure in order to model a full powder diffraction pattern using information about the structure. By using a range of parameters and the least-squares method the difference between the calculated and experimental patterns can be minimised. An example fit is given in Figure 10. In order to carry out Rietveld refinement analysis of powder diffraction data a number of parameters are needed. In relation to the powder diffraction data a parameter file is needed giving information about the instrument including wavelength and monochromator/ filter. Additionally, crystallographic information (a starting structural model) is needed where typically this is given in the crystallographic information files (CIF). These files can be found on the international crystallographic structure database (ICSD) and contain the space group, cell parameters and information about the atom positions. If the material is a new phase, then a related structural model from a similar system is utilised as a starting point.

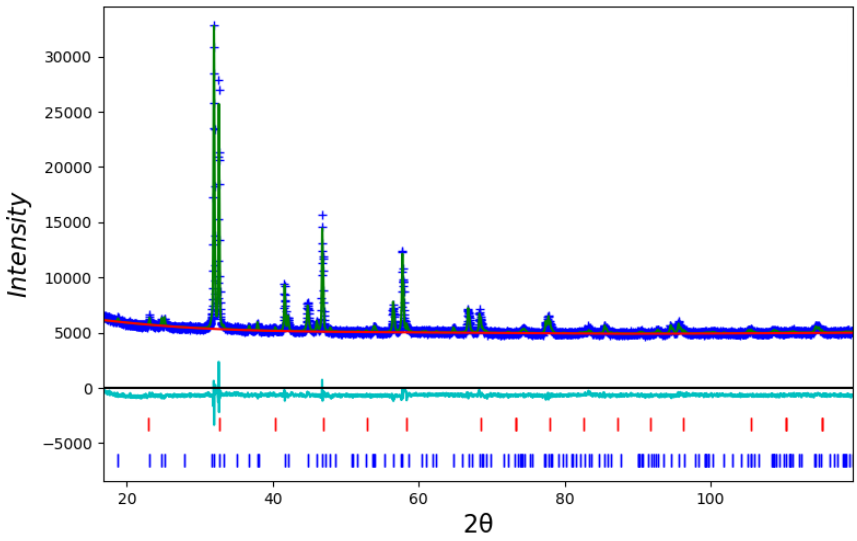

Figure 10. Example GSAS refinement profile. Observed (dotted blue line), calculated (solid green line) and difference (solid blue line) X-ray diffraction profiles.

Using all of this information the least square model can be used to minimise the difference between calculated and experimental patterns, which is measured by the residual S_y (Equation 14).

Equation 14 $$S_y = \sum_i w_i [y_i(obs) - y_i(calc)]^2$$

w_i is the weighting of each point

$y_i(obs)$ is the observed intensity to the i^{th} step

$y_i(calc)$ is the calculated intensity to the i^{th} step

In order to minimise the difference between the calculated and experimental trace, parameters are slowly added to the refinement in order to improve the fit. This includes background functions, scale factors, profile parameters, lattice parameters, zero point error

and sample displacement. Additionally, refinement of atomic positions, site occupancy and thermal parameters further improves the fit.

A measure of the quality of the fit is given by the goodness of fit (Equation 15). For a perfect fit χ^2 will be equal to 1. In addition to χ^2 a number of other factors can be used to determine the quality of fit. These are known as R factors and are given in Equation 16 to Equation 18. When analysing all of the values care needs to be taken to not over refine the data. In addition to these values, it is most important to inspect the observed, calculated and difference profiles to ensure that the fit is good. In addition it is also important to check that the refinement leads to a physically sensible structure.

Equation 15 $$\chi^2 = \left[\frac{R_{wp}}{R_{exp}}\right]^2$$

Equation 16 $$R_p = \frac{\sum \mathrm{y_i(obs) - y_i(calc)}}{\sum \mathrm{y_i(obs)}}$$

Equation 17 $$R_{wp} = \left[\frac{\sum w_i \left(\mathrm{(y_i(obs) - y_i(calc))}\right)^2}{\sum w_i \left(\mathrm{(y_i(obs))}\right)^2}\right]^{\frac{1}{2}}$$

Equation 18 $$R_{exp} = \left[\frac{N-P-C}{\sum w_i \left(\mathrm{(y_i(obs))}\right)^2}\right]^{\frac{1}{2}}$$

R_p is the R profile	N is the number of data points
R_{wp} is the weighted profile	P is the number of refined parameters
R_{exp} is the expected profile	C is the number of constraints

Within this thesis Rietveld refinements were carried out using the GSAS suite of programs[136].

3.2.5 Pawley refinement

An additional analysis technique for powder pattern analysis is the Pawley method.[137] This is a similar method as used for Rietveld refinements, but detailed structure information about the crystal system is not required, instead only the space group and unit cell parameters are needed. Hence no atoms are included in the refinement. This method uses peak intensities in order to give information on lattice parameters, size and microstrain.

3.3 X-ray absorption spectroscopy

X-ray absorption spectroscopy (XAS) uses high energy X-rays with a tuneable energy range to probe the electronic structure of materials. A monochromatic X-ray beam is used in order to utilise characteristic wavelengths specific to the element being probed. These characteristic energies correspond to the binding energies of inner-shell electrons. These energies are labelled as K, L and M edges where the edges are named according to the principle quantum number of the excited electron.

A simplified version of an XAS measurement is given in Figure 11, where measurements can be taken in either transmission or reflection mode using a monochromatic incident beam.

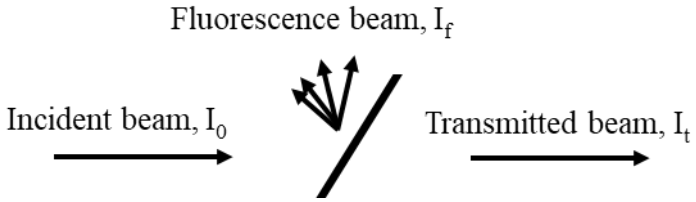

Figure 11. Schematic of an X-ray absorption measurement in transmission and fluorescence mode

Using the incident beams and the transmitted and fluorescence beams, the absorption coefficients can be calculated using Equation 19 and Equation 20 .

Equation 19 $$\mu(E) = \ln \frac{I_0}{I_t}$$

Equation 20 $$\mu(E) \propto \ln \frac{I_f}{I_0}$$

X-ray absorption spectra can be divided into two main sections: X-ray absorption near-edge structure (XANES) and the X-ray absorption fine structure (EXAFS). XANES data give information about the oxidation state and coordination environment of the element being probed. Typically XANES data can be used to fingerprint characteristic environments. Included in the XANES part of the spectrum is an area called the pre-edge. This is where core electrons are excited to higher empty orbitals giving rise to characteristic intensities. At higher energies in the EXAFS region of the spectra, information about nearby atoms including bond lengths can be investigated. An advantage to this technique is the ability to measure amorphous materials or species in solution, as well as to gain element specific information where there are more than 1 element on a particular site.

Within this work Cr K-edge X-ray absorption spectroscopy was performed at Diamond Light Source (beamline B18 at Rutherford Appleton Lab, Harwell, UK). Data processing was performed using the Athena Software package.[138]

3.4 Mössbauer spectroscopy

Mössbauer spectroscopy is used to give details about the chemical, structural and magnetic properties of materials. Mössbauer spectroscopy involves the recoilless absorption and emission of gamma rays by nuclei and was first discovered in 1958 by Rudolf

Mössbauer.[139] For Mössbauer experiments a radioactive source is used where a sample is exposed to a beam of gamma radiation and the transmitted beam measured. The gamma source used is a radioactive isotope embedded in a solid matrix. An example decay of a radioactive source is given in Figure 12. It can be seen ^{57}Co decays into an excited state ^{57}Fe state which further decays to another excited state.[140] As this process occurs gamma rays are emitted which can be subsequently absorbed by the sample. One of the challenges of Mössbauer spectroscopy is that the source is element specific, and so a different source is required for each element. In addition, not all elements have suitable sources that can be used. In this thesis ^{57}Fe Mössbauer spectroscopy for iron containing materials is discussed, however a range of elements can be probed by Mössbauer spectroscopy, with the most common other ones being ^{119}Sn, ^{129}I and ^{197}Au.

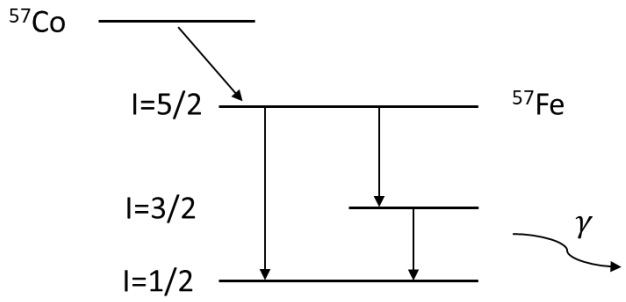

Figure 12. Schematic diagram showing the decay of ^{57}Co

During Mössbauer spectroscopy, the energy of the gamma rays must be modulated to achieve the required energy sweep. To achieve this, the source is accelerated through a range of velocities to modify the energy through the Doppler effect. By varying the velocity a shift in energy occurs, and therefore a scan over a range of energies can be performed. This shift in

energy is described using Equation 21 where v is the velocity, c is the speed of light and E_γ is the unshifted gamma ray energy.

Equation 21 $$\Delta E = (\frac{v}{c})E_\gamma$$

Using this information the transmittance can be plotted against the velocity (Figure 13). Assuming a sample with one iron environment identical to the emitting nuclei, the Mössbauer spectrum would be predicted to consist of a single line as seen in Figure 13. Realistically the environment of the absorbing nuclei is, however, likely to be different and therefore the energy for absorption will be different; thus there is a need to sweep across a range of energies exploiting the Doppler effect. A peak in the spectrum will be observed when the emitted gamma ray energy matches the energy of a nuclear transition in the absorber.

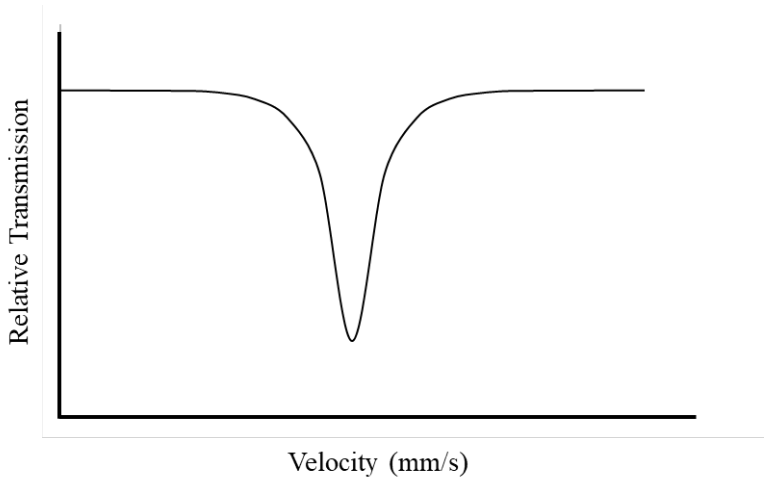

Figure 13. Example Mössbauer spectrum of Relative Transmission vs Velocity

Typically, there are three main components to a Mössbauer spectrum. They are the isomer shift, quadrupole splitting and magnetic splitting. The isomer shift (δ) is reported in the spectra relative to the known absorber where the velocity is shifted by a positive or

negative amount. The isomer shift is as a result of the difference in *s* electron density between the source and absorber. The quadrupole splitting (Δ) leads to a doublet in the spectra and is the result of a shift in nuclear energy levels induced by an electric field. Information obtained from isomer shift and quadruple splitting parameters can be used to determine the chemical environment of the species probed including oxidation states. Finally, magnetic splitting is observed due to the interaction of the nuclear spin moment with the magnetic field therefore allowing further information about the magnetic properties of the material.

In this thesis ^{57}Fe Mössbauer spectroscopy was carried out by Professor Frank Berry, Dr José F. Marco and Dr María Sánchez-Arenillas at the Instituto de Química Física "Rocasolano".

3.5 Thermogravimetric analysis

Thermogravimetric analysis (TGA) is carried out by heating a sample with a known mass and measuring any mass change. Samples can be heated in a range of gases such as N_2, Ar, H_2 and O_2 and the exhaust gas can be linked with a mass spectrometer in order to characterise the evolved gases. For example, this can be used to determine the oxygen content of a material (and hence transition metal oxidation states).

In addition to information about mass loss/ gain, most systems can also follow heat changes in a sample, measuring any differences in sample temperature with a standard such as alumina. This differential thermal analysis (DTA) profile can provide information about exothermic and endothermic events, including those in which there is no mass change, such as phase changes within a material.

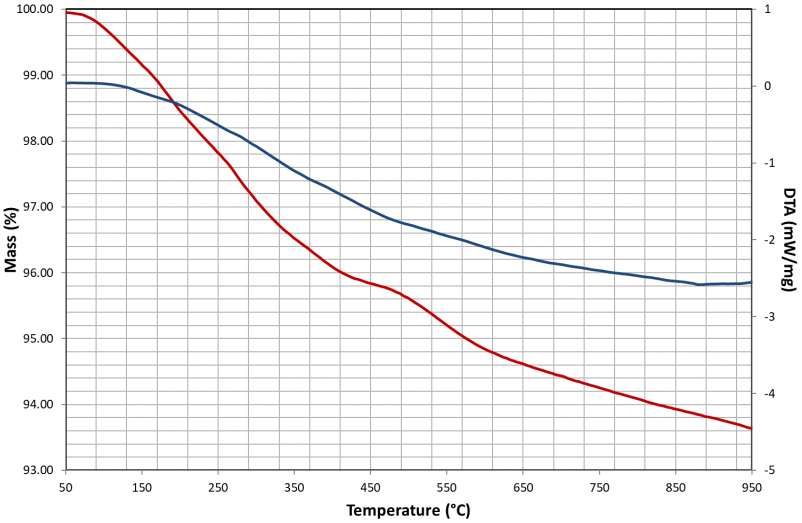

Figure 14. Example TGA plot where the red line indicates %mass and blue line indicates DTA

3.6 Raman spectroscopy

First reported in 1928 by C. V. Raman and K. S. Krishnan[141], Raman spectroscopy is a type of vibrational spectroscopy which is a useful tool used to give information about the bonding in materials. This technique can be used to identify and monitor the concentration of known components in materials.[140]

Raman spectroscopy is a non-destructive technique carried out by exposing a sample with an intense laser in the visible region of the spectrum. When the light interacts with the molecules/moieties, photons cause a transition to a virtual excited state which emits photons when the molecule/moiety relaxes. The majority of photons emitted are equal in energy to the incident photons. This can be described as elastic scattering (Rayleigh scattering). Additionally, a small number of photons have a different energy due to relaxation to a different vibrational state. This can be described as inelastic scattering. If the emitted photon relaxes to a vibrational energy level that is higher than the initial excited state this is described

as Stokes scattering. Where relaxation is to a lower energy state this can be described as anti-stokes scattering.

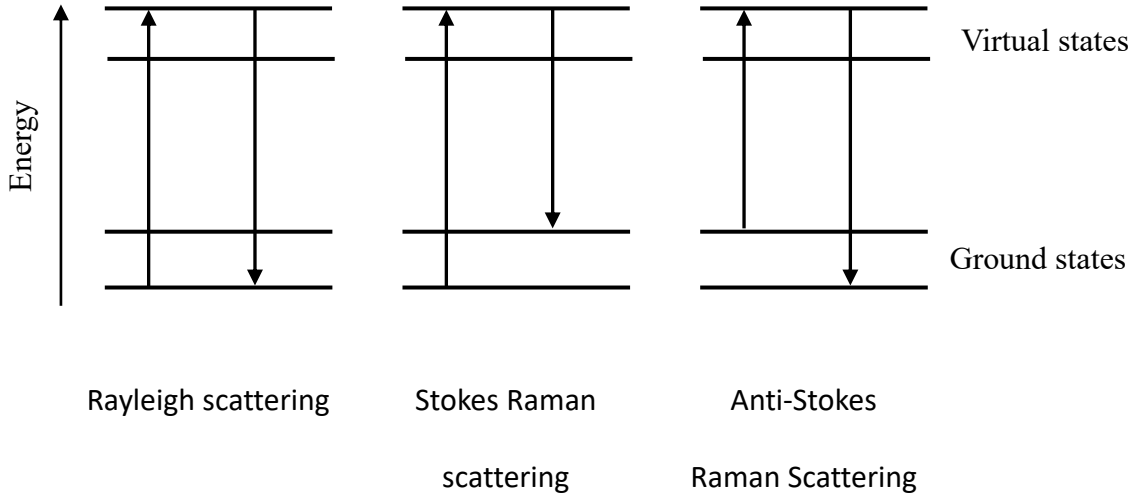

Figure 15. Energy level diagram showing Rayleigh and Raman scattering

In order for materials to be Raman active there needs to be a change in polarisation of a molecule where in comparison, infrared active materials must have a permanent dipole. The molecular symmetry combined with the use of group theory can be used to identify Raman active bands. In this work, the method was used to gain more information about the presence of oxyanion groups in the samples.

3.7 Scanning electron microscopy

Scanning electron microscopy is used in order to investigate the microstructure of samples including crystal morphology and particle size. An electron beam is scanned across a sample in order to create an image. The electron beam interacts with the sample generating a variety of signals including secondary electron and back scattered electrons in order to create an

image. In order to protect the electron source and allow collection of high resolution images, measurements are collected under vacuum.

Additionally, characteristic X-rays are collected for images which allows the investigation of the elemental distribution in a material. This occurs due to the electron beam exciting an electron in an atom resulting in excitation to a high energy leaving behind a positively charged electron hole. This positive charge attracts another electron from an outershell in order to fill the hole. The energy released from this is emitted as a characteristic X-ray. This information obtained through energy dispersive X-ray spectroscopy can be used to determine not only the type of elements present, but also the percentage of each element and their distribution across the sample (i.e. is it a uniform distribution or are there regions rich in certain elements indicative of impurities).

3.8 Electrical 4 probe conductivity measurements

Typically, direct current (dc) conductivity measurements are used to determine the conductivity of solid oxide fuel cell electrode materials due to the low resistivity of these materials. In order to investigate potential cathode materials for SOFCs, materials are pressed into dense pellets and the resistance measured. This is carried out by attaching 4 electrodes to the pellets and measuring the voltage, when a current is applied. This can be performed by using two different methods known as Van de Pauw[142] and the 4 probe DC method.[143]

Van de Pauw method

Resistance is measured in the Van de Pauw method[142] by attaching 4 platinum (or gold, silver) wires at 90° on the pellet. Two resistance measurements are taken in two

different orientations as seen in Figure 16 and used to calculate the conductivity (σ) given in Equation 22 where d is the thickness of the sample.

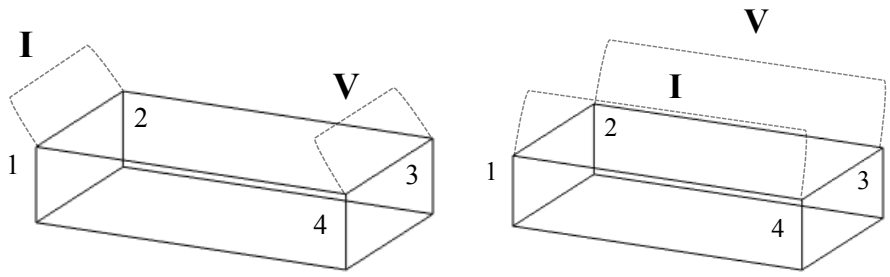

Figure 16. Diagram for Van de Pauw conductivity method

Equation 22

$$R_A = \frac{V_{34}}{I_{12}}, R_B = \frac{V_{23}}{I_{14}}$$

$$\rho = \frac{\pi d}{\ln(2)}\left(\frac{R_A + R_B}{2}\right)\left(f\left(\frac{R_A}{R_B}\right)\right) \qquad \sigma = \frac{1}{\rho}$$

4 probe DC conductivity method

In comparison the 4 probe dc method involves attaching two Pt (or Au, Ag) electrodes to the outer ends of a pellet to apply a current and two additional Pt (or Au, Ag) electrodes to the inner part of the pellet to measure voltage (Figure 17). Using the applied current and measured voltage the conductivity can be calculated using Equation 23 where A is the cross sectional area and d is the distance between voltage probes (Figure 17). For the materials investigated in this thesis the 4 probe DC method was used.

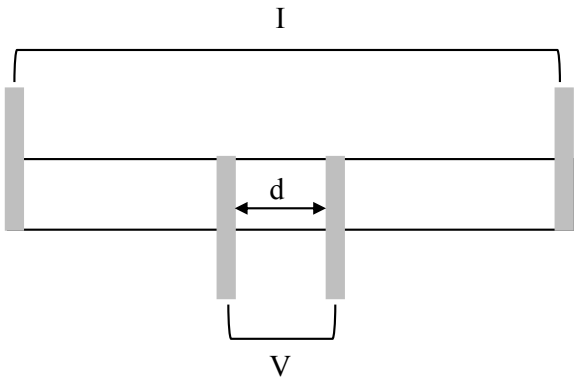

Figure 17. Diagram for 4 probe DC conductivity method

Equation 23 $$\sigma = \frac{I\,d}{V\,A}$$

Typically, the resistance is measured over a range of temperatures, in order to investigate changes with temperature. In this thesis samples were measured in a temperature range (400-800 °C) in order to analyse the potential for the materials to be used as SOFC cathode materials.

3.9 AC impedance conductivity measurements

Alternating current (AC) impedance spectroscopy is typically used for materials with high resistivity, for example electrolyte materials for solid oxide fuel cells. Measurements require dense sintered pellets coated with conducting paste (e.g. Pt, Au, Ag) and electrodes attached on both sides of the pellet. In this work impedance measurements were performed using a Hewlett Packard 4192A instrument analyser with data analysed using the programme Zview.

Impedance spectroscopy is performed by applying an oscillating voltage and measuring the oscillating current response across a range of frequencies. This information can be plotted on a Nyquist plot of Z'' vs Z' (Figure 18) as a function of frequency (ω).

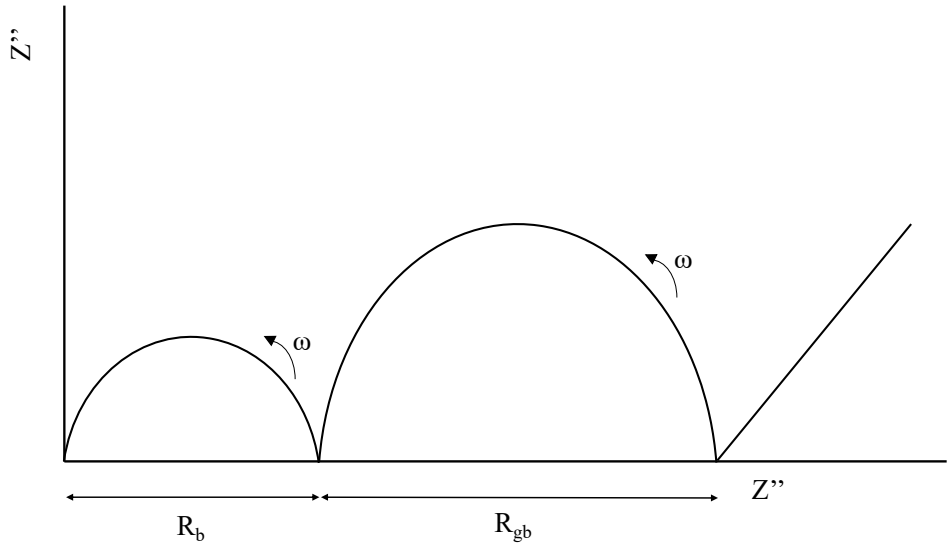

Figure 18. Example Nyquist plot showing ideal plot with bulk, grain boundary and electrode contributions

As seen in Figure 18 an example Nyquist plot is given which has two clear semi circles. Although an ideal plot is given here impedance plots can be more complex with overlapping of semicircles, although typically a particular focus is on two main components. In the example given, the two semicircle components are due to different regions of the sample, the bulk (grains) and the grain boundary between grains. Using the Nyquist plot the resistance (R) can be determined as the intercept on the Z' axis with capacitance calculated using Equation 24. The values obtained can then be assigned to relevant components depending on the capacitance. Typically Capacitance for bulk contributions are $\approx 10^{-12}$ F and for grain boundary $\approx 10^{-11}$ - 10^{-8} F.[144]

Equation 24 $$\omega_{max} RC = 1$$

These values can be calculated by fitting the data to a semi-circle to give values for R and C. In this work Zview software was used to fit equivalent circuits. An example equivalent circuit is given in Figure 19.

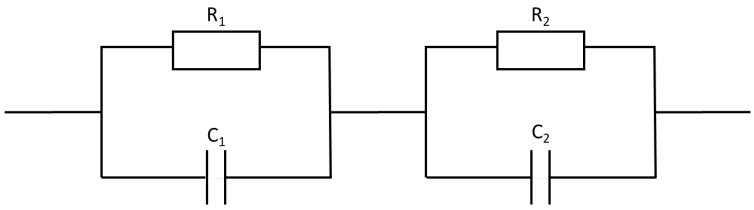

Figure 19. Example equivalent circuit for two semi circles

Using this information conductivity (σ) values for materials can be calculated using Equation 25 where R is resistance, l is sample thickness and A is the sample surface area.

Equation 25 $$\sigma = \frac{1}{R} \times \frac{l}{A}$$

Typically materials are measured over a temperature range, for example in this work materials were measured in the temperature range (400-800 °C) expected to be suitable for SOFC applications. Therefore the temperature dependence of the conductivity data can be calculated using Equation 26. By plotting a graph of $Log_{10}\sigma T$ vs 1000/ T the activation energy can be calculated from the gradient of the slope (Figure 20).

Equation 26 $$\sigma T = Ae^{\frac{-E_a}{RT}}$$

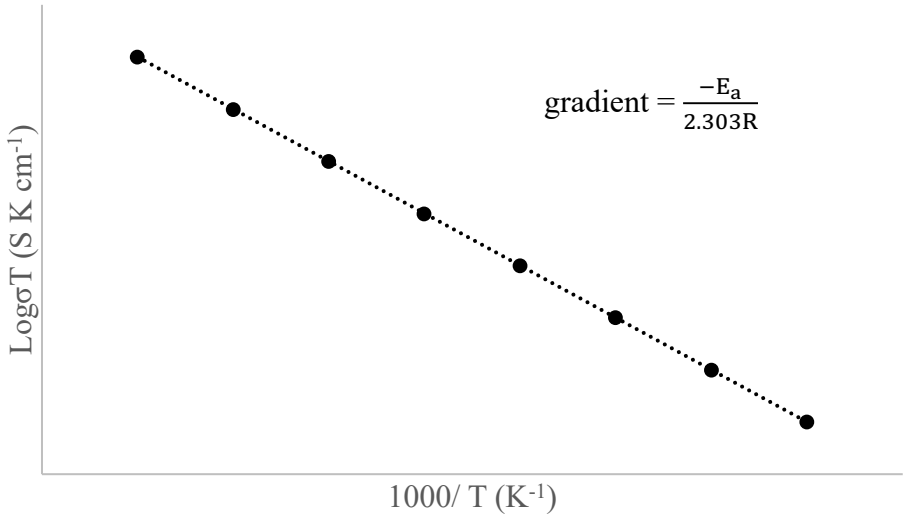

Figure 20. Arrhenius plot of Log10**σ**T vs 1000/T

4 Oxyanion incorporation into perovskite systems

4.1 Introduction

Perovskite materials are appealing for a range of applications due to their ability to accommodate a wide range of cations. Specifically, for solid oxide fuel cell applications, perovskite materials are appealing due to the ability to obtain high electronic conductivity (see review articles[145,146]). As a result, a number of properties can be explored through different dopant methods. Typically, materials are doped on the A and B sites in ABO_3 with cations of a similar size, but different charge. These doping strategies introduce oxygen vacancies into the structure. For example solid oxide fuel cell cathode material $La_{1-x}Sr_xCoO_{3-\delta}$ dopes Sr^{2+} on the La^{3+} site.[47,147] As a result the cubic perovskite structure is maintained and oxygen vacancies are introduced into the structure. Instead, oxyanion doping of solid oxide fuel cell materials has been utilised as an alternative doping strategy. Here the central ion of the oxyanion group is located on the B cation site. Previous work has shown a range of oxyanions can be incorporated into solid oxide fuel cell materials. For example sulfate, silicate and phosphate doping of $Ba_2(In/Sc)_2O_5$ electrolyte materials lead to improvements in the ionic conductivity.[100,101,104,105] Further to this a range of perovskite systems have been successfully doped with oxyanions including $SrCoO_3$[106,108,109,148], $SrCo_{0.85}Fe_{0.15}O_3$[149], $SrMnO_3$[106], $CaMnO_3$[107], $SrFeO_3$[111] with improved performance.

Although a range of oxyanions have been reported in perovskite materials, carbonate incorporation is the least reported. Previously, superconducting perovskite cuprate materials have shown to accommodate a range of oxyanions including carbonate.[98,99,150–156] Even with prior studies on cuprate materials, carbonate has been assumed to be too small to be incorporated into materials therefore has been overlooked when investigating perovskite and perovskite type materials. Deakin et al.[157] reported the synthesis of the layered perovskite

oxide $Ba_3Y_2O_5CO_3$. These materials have been found to be stabilised by carbonate at temperatures < 1000 °C, showing materials synthesised at low temperature may contain carbonate. Additionally, carbonate incorporation in perovskite type, Ba_2TiO_4 is reported by McSloy et al.[158] when annealing samples at 450 °C for 8 hours in air. Again, highlighting the importance of investigating carbonate incorporation at low synthesis temperature.

In this work the effect of oxyanion incorporation (Figure 21) in $SrFeO_{3-\delta}$, $Sr_{0.5}Ba_{0.5}FeO_{3-\delta}$ and $BaFeO_{3-\delta}$ is investigated with the view to utilise materials as solid oxide fuel cell cathode materials.[159] As discussed above, previous studies on perovskite materials has shown that oxyanions can be successfully incorporated into a range of perovskite materials. $SrFeO_{3-\delta}$ has been shown to successfully accommodate silicate with improvement in performance making them suitable for use in SOFCs. Therefore expanding on this work was a key aim by investigating not only alternate oxyanion dopants, but also further doping studies on the A site in ABO_3. Additionally, due to not only experimental, but computational work on carbonate incorporation in perovskite materials, a focus for this work was to investigate the incorporation of carbonate into these systems particularly at lower temperatures.

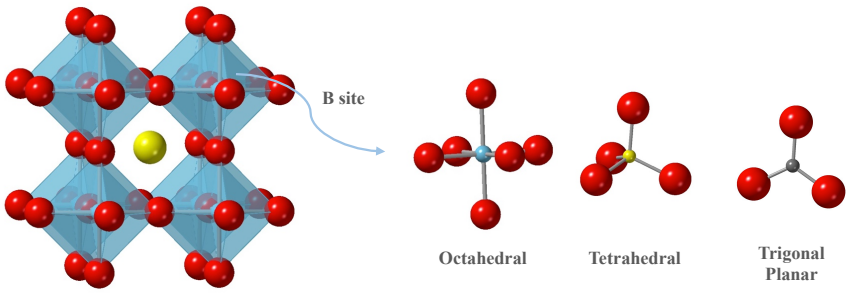

Figure 21. The perovskite structure (ABO_3), showing the incorporation of oxyanions on the B site

4.2 $SrFe_{1-x}(S/B)_xO_{3-\delta}$

4.2.1 Experimental

Stoichiometric amounts of $SrCO_3$, Fe_2O_3 and either $(NH_4)_2SO_4$ or H_3BO_3 were intimately ground and heated to 900 °C (4 °C/min) for 12 h. $SrFe_{1-x}S/B_xO_{3-\delta}$ samples were then ballmilled (350 rpm for 1 h, Fritsch Pulverisette 7 planetary Mill) and reheated to 1000 °C for 12 h. This was repeated with heat treatments at 1050 and 1100 °C for 12 h. A further heat treatment to 1200 °C was carried out for $SrFe_{1-x}B_xO_{3-\delta}$. All samples underwent a final heat treatment to 350 °C for 12 h in air to ensure maximum oxygen content.

In order to test stability under low $p(O_2)$, $SrFe_{1-x}S/B_xO_{3-\delta}$ samples were heated to 950 °C for 12 h under N_2. Additionally, sulfate doped samples were heated under O_2 to 900 °C for 12h with slow cooling at 50 °C/ h to 350 °C, with the samples then maintained at this temperature for 12 h followed by cooling at 50 °C/ h to room temperature.

Powder X-ray diffraction (XRD) data were used in order to determine lattice parameters and phase purity. Rietveld refinements were carried out using the GSAS suite of programs.[136] For $SrFe_{1-x}S_xO_{3-\delta}$ samples heated in air, XRD data were collected on a Panalytical Empyrean diffractometer equipped with a Pixcel 2D detector (Cu Kα radiation). For the remaining sulfate and borate doped samples, a Bruker D8 diffractometer with Cu Kα radiation was used.

Thermogravimetric analysis (TGA) (Netzch STA 449 F1 Jupiter Thermal Analyser with mass spectrometry attachment) were used to estimate oxygen contents. Samples were heated under N_2 to 950 °C and held for 30 min to reduce the iron oxidation state to Fe^{3+}.

Four probe dc conductivity measurements were carried out for $SrFe_{1-x}S/B_xO_{3-\delta}$ samples. Powders were initially balled milled (350 rpm for 1 h), before pressing into pellets and sintering at 1100 °C ($SrFe_{1-x}S_xO_{3-\delta}$) and 1200 °C ($SrFe_{1-x}B_xO_{3-\delta}$). Pt electrodes were attached

to the pellets with Pt paste and samples were heated to 900 °C for 1 h in air. All samples underwent a final heat treatment to 350 °C for 12 h in air to ensure maximum oxygen content.

4.2.2 $SrFe_{1-x}S_xO_{3-\delta}$

4.2.2.1 X-ray Diffraction results

As mentioned in the introduction, oxyanion doped perovskite materials have previously been investigated within the group. Here, sulfate and borate doped $SrFeO_{3-\delta}$ systems are reported. XRD data showed the undoped material, $SrFeO_{3-\delta}$, forms a tetragonal perovskite. This can be more clearly seen in Figure 22 where peak splitting in the region 2θ = 45 to 60° illustrates a tetragonal cell. Upon doping with sulfate, stabilisation of the cubic cell occurs up to x = 0.075. Above x = 0.075 single phase samples are not achieved due to the formation of $SrSO_4$ impurities.

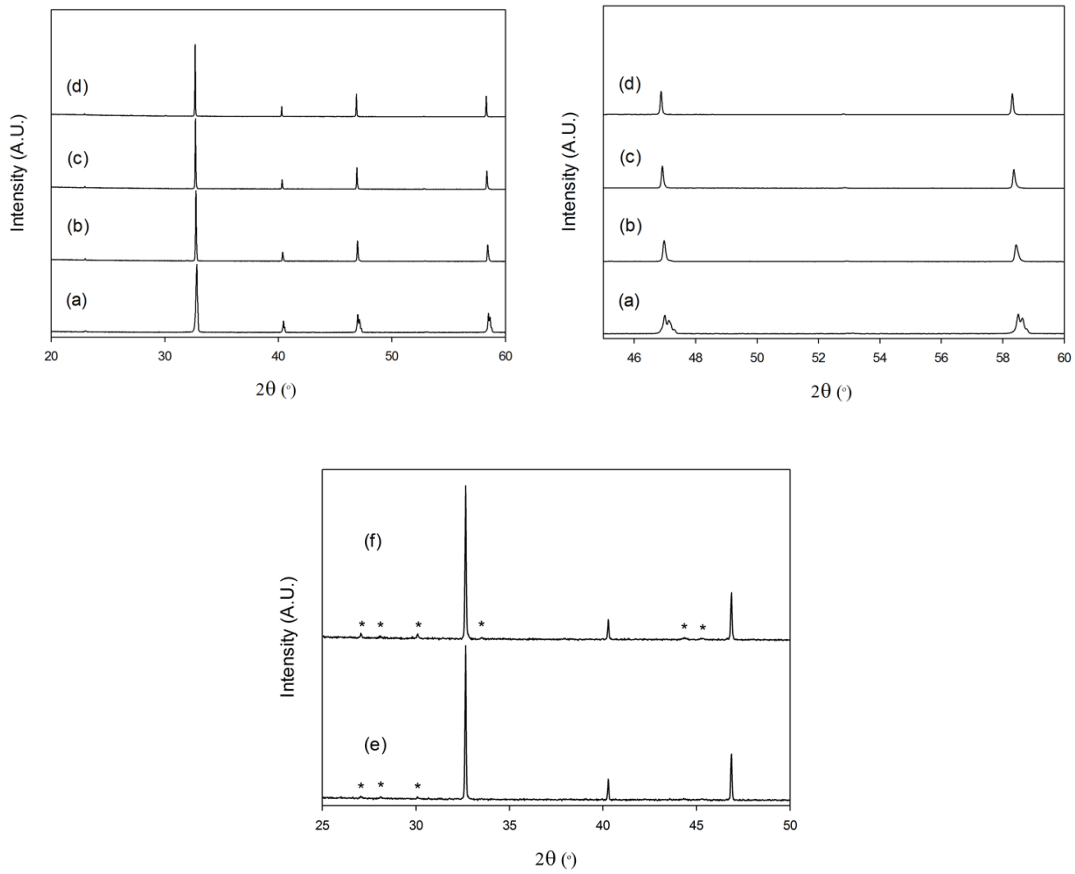

Figure 22. XRD patterns of a) $SrFeO_{3-\delta}$, b) $SrFe_{0.975}S_{0.025}O_{3-\delta}$, c) $SrFe_{0.95}S_{0.05}O_{3-\delta}$, d) $SrFe_{0.925}S_{0.075}O_{3-\delta}$, e) $SrFe_{0.9}S_{0.1}O_{3-\delta}$ and f) $SrFe_{0.85}S_{0.15}O_{3-\delta}$. Peak splitting is observed (see expanded region Figure 23 2θ = 45 to 60°) for the tetragonal cell $SrFeO_{3-\delta}$. $SrSO_4$ impurities are highlighted by an asterisk for higher sulfate contents (x = 0.1 and 0.15).

In order to further support sulfate incorporation the Fe-deficient sample, $SrFe_{0.95}O_{3-\delta}$ is unsuccessfully synthesised in the same conditions as the sulfate doped materials. For $SrFe_{0.95}O_{3-\delta}$, XRD indicates the presence of impurities with peak splitting suggesting a tetragonal unit cell. In comparison, impurities are not observed for the sulfate containing $SrFe_{0.95}S_{0.05}O_{3-\delta}$ and the cell is now cubic. This comparison provides further evidence of successful sulfate incorporation.

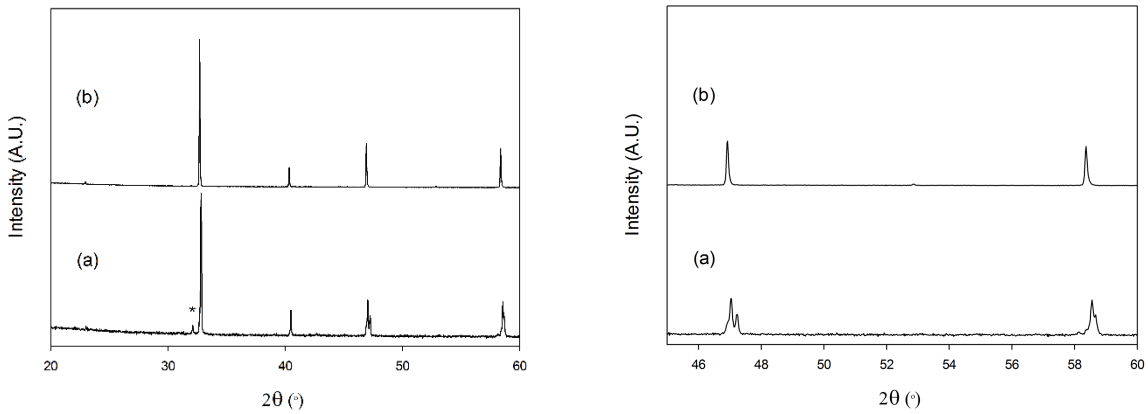

Figure 23. XRD patterns for (a) $SrFe_{0.95}O_{3-\delta}$ and (b) $SrFe_{0.95}S_{0.05}O_{3-\delta}$. The data show impurities (highlighted by an asterisk) and a tetragonal cell for $SrFe_{0.95}O_{3-\delta}$, while the sulfate-containing sample $SrFe_{0.95}S_{0.05}O_{3-\delta}$ is phase pure and cubic.

Cell parameters for the sulfate and borate doped systems were determined using the Rietveld method (an example fit is shown in Figure 24). With an increase in sulfate content a small general increase is observed for $SrFe_{1-x}S_xO_{3-\delta}$. This will be discussed in more detail in section 4.2.2.4.

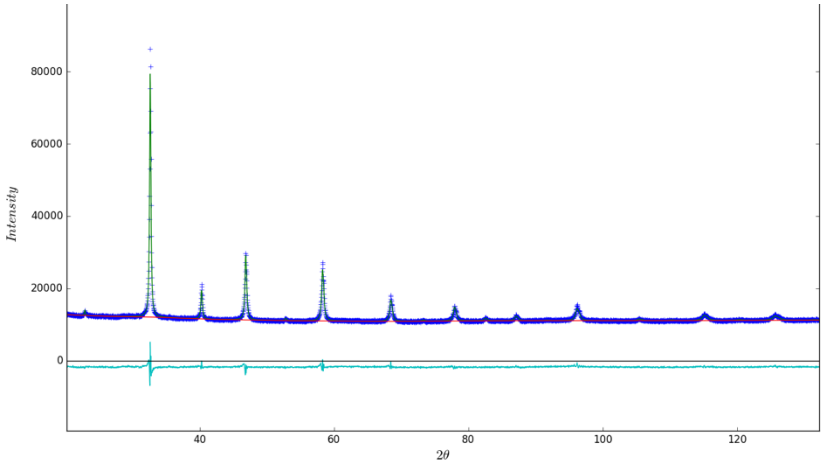

Figure 24. Observed (dark blue), calculated (green) and difference (light blue) XRD profile for $SrFe_{0.975}S_{0.025}O_{3-\delta}$

During Rietveld refinements, occupancies were also refined for Fe/S sites. The occupancies given in Table 2, were found to be in good agreement with the expected values.

Table 2. Lattice parameters and site occupancies obtained from Rietveld refinement of XRD data for $SrFe_{1-x}S_xO_{3-\delta}$. $SrFeO_{3-\delta}$ was refined in a tetragonal space group (*P4/mmm*). Doped samples were refined in a cubic space group ($Pm\bar{3}m$).

	$SrFe_{1-x}S_xO_{3-\delta}$			
S (x)	0	0.025	0.05	0.075
a (Å)	3.8648(1)	3.8723(1)	3.8776(1)	3.8766(1)
c (Å)	3.8487(1)	-	-	-
V ($Å^3$)	57.486(4)	58.066(2)	58.303(4)	58.260(4)
R_{wp} (%)	1.84	1.67	2.01	1.97
R_{exp} (%)	0.92	0.92	0.90	0.90
Fe	1	0.98(1)	0.96(1)	0.94(1)
S	-	0.02(1)	0.04(1)	0.06(1)
Fe/S Uiso	0.003(1)	0.009(1)	0.011(1)	0.008(1)

4.2.2.2 Stability under N_2

$SrFe_{1-x}S_xO_{3-\delta}$ samples were heated under N_2 to 950 °C to investigate the stability under reducing conditions. XRD data showed $SrFeO_{3-\delta}$ transforms into the oxygen vacancy ordered brownmillerite type $Sr_2Fe_2O_5$ (Figure 25 and Figure 26). Due to the reduction of Fe^{4+} to Fe^{3+} there is an increase in oxide ion vacancies resulting in an ordered perovskite structure as seen in Figure 26. This structure has layers of octahedra and tetrahedra coordination around the B cation. This is expected to be unfavorable for fuel cell applications due to the ordering of oxygen vacancies which is expected to lower oxide ion conductivity. For sulfate doped samples the disordered cubic perovskite is stabilised with the reduction of iron to Fe^{3+}. For lower sulfate

levels, x = 0.025, XRD data indicate weak peaks present due to the brownmillerite structure (Figure 25). For higher sulfate contents, x = 0.05, a single phase cubic cell is observed.

Sulfate doped samples heated in N_2 show an increase in unit cell with increasing sulfate content. This is due to the reduction of iron towards Fe^{3+} which is supported by the increase in unit cell parameters which is associated with the larger size of Fe^{3+} vs Fe^{4+}.

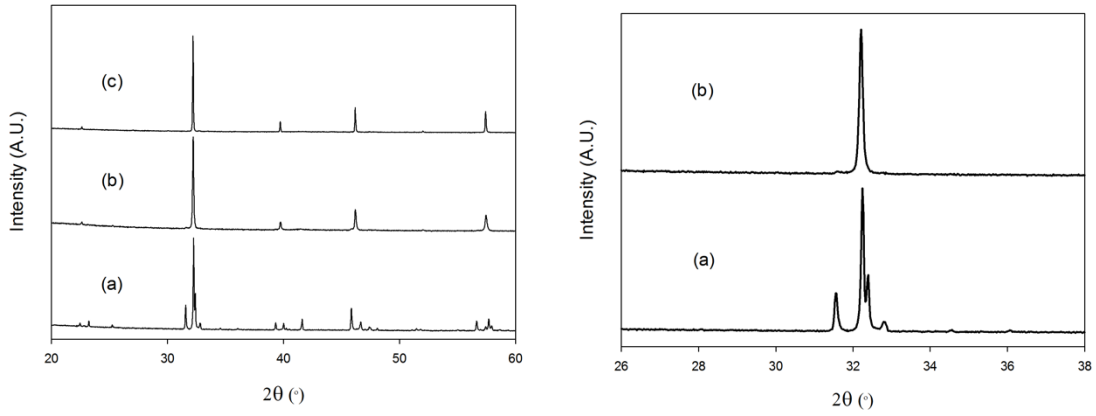

Figure 25. XRD patterns of a) $SrFeO_{3-\delta}$, b) $SrFe_{0.975}S_{0.025}O_{3-\delta}$ and c) $SrFe_{0.95}S_{0.05}O_{3-\delta}$ after heating under N_2 to 950 °C

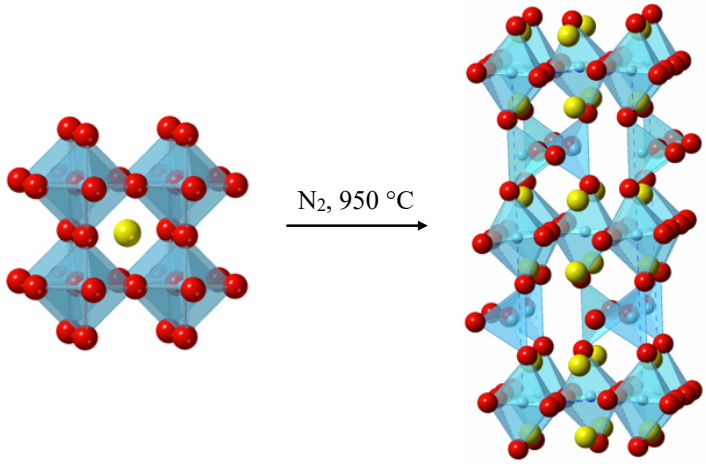

Figure 26. Diagram showing the phase change from disordered cubic perovskite structure ($SrFeO_{3-\delta}$) to ordered orthorhombic structure ($Sr_2Fe_2O_5$) after heat treatment in N_2. Yellow = Sr, blue = Fe and red = O.

Table 3. Lattice parameters for $SrFe_{1-x}S_xO_{3-\delta}$ after heating in air and N_2

$SrFe_{1-x}S_xO_{3-\delta}$						
S (x)	0.025		0.05		0.075	
	Air	Dry N_2	Air	Dry N_2	Air	Dry N_2
a (Å)	3.8723(1)	3.9231(1)	3.8776(1)	3.9256(1)	3.8766(1)	3.9280(1)
V ($Å^3$)	58.066(2)	60.379(1)	58.303(4)	60.496(1)	58.260(4)	60.606(1)
R_{wp} (%)	1.67	3.10	2.01	3.09	1.97	3.20
R_{exp} (%)	0.92	2.59	0.90	2.51	0.90	2.50

4.2.2.3 Thermogravimetric Analysis

TGA was carried out to determine oxygen contents of samples by heating samples in N_2 to reduce the iron oxidation state to Fe^{3+}. For sulfate doped samples an interesting observation is reported where a mass loss associated with CO_2 is observed. For the undoped sample, $SrFeO_{3-\delta}$, the loss of mass is associated with only oxygen as indicated by the mass spectrometry data. In order to remove carbonate from the sulfate doped samples, heat treatment in O_2 was carried out for $SrFe_{1-x}S_xO_{3-\delta}$. After heating all samples under O_2, TGA indicates oxygen has driven out any carbonate which may have been previously present within the sample. This can be seen in Figure 27 where a mass loss associated with CO_2 is not observed after heat treatment in O_2 for $SrFe_{0.95}S_{0.05}O_{3-\delta}$.

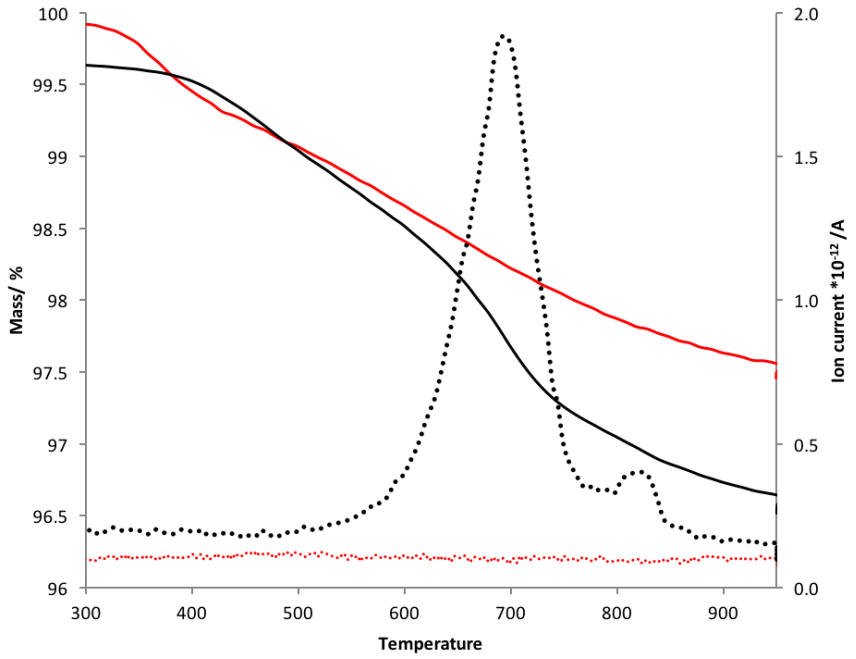

Figure 27. Plot of mass vs temperature and ion current (m/z = 44) vs temperature for $SrFe_{0.95}S_{0.05}O_{3-\delta}$ heated in air (black) and O_2 (red). Solid lines indicate %mass and dashed indicate ion current

In order to determine if the carbonate present is due to a $SrCO_3$ impurity or incorporation of carbonate in the system, TGA was carried out for $SrCO_3$. When comparing TGA data for $SrCO_3$ and $SrFe_{0.95}S_{0.05}O_{3-\delta}$ a clear difference is observed in the temperature at which CO_2 is lost. For $SrFe_{0.95}S_{0.05}O_{3-\delta}$ a significantly lower temperature of ≈ 490 °C is observed for the start of CO_2 loss compared with ≈ 760 °C for $SrCO_3$. Therefore suggesting this is a mixed sulfate/ carbonate doped sample – $SrFe_{1-x-y}S_xC_yO_{3-\delta}$. As discussed in the introduction, carbonate has been previously shown to accommodate the perovskite structure. Further work is required to investigate the possibility of a combined sulfate carbonate system.

It is not possible to reliably determine oxygen contents for these samples due to the dual mass loss from O_2 and CO_2. In addition, as detailed by Starkov et al.[160], the determination of oxygen contents in partially substituted ferrites is non-trivial without a reliable fixed reference

point. This is due to the possibility of a small amount of Fe^{4+} in the samples heated in N_2, therefore only a rough estimate of any oxygen contents can be given.

4.2.2.4 Heat treatment under O_2

As described above, samples were heated in O_2 in order to investigate carbonate incorporation. In addition to removing any included carbonate, the effect on structure could be investigated. After heating in O_2, all $SrFe_{1-x}S_xO_{3-\delta}$ samples retained their original structure (Figure 28). Where $SrFeO_{3-\delta}$ remained tetragonal and all sulfate doped retained their cubic cell.

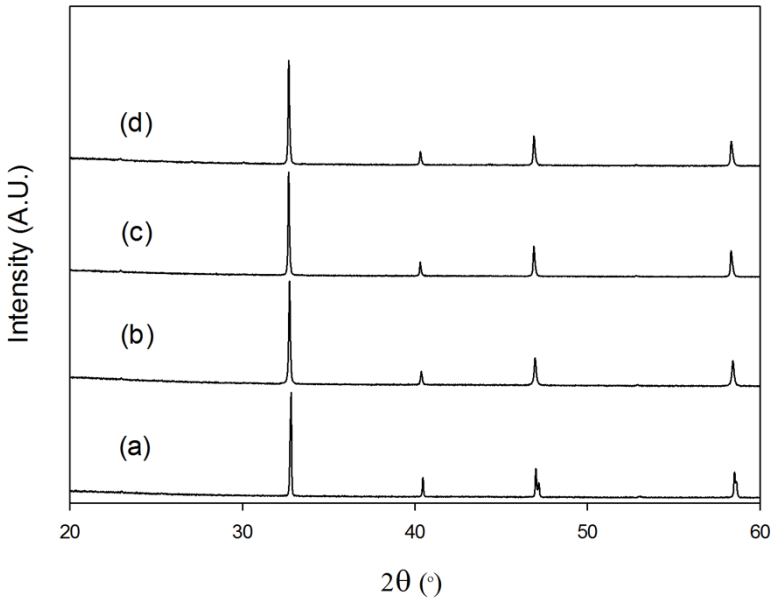

Figure 28. XRD patterns of a) $SrFeO_{3-\delta}$, b) $SrFe_{0.975}S_{0.025}O_{3-\delta}$, c) $SrFe_{0.95}S_{0.05}O_{3-\delta}$ and d) $SrFe_{0.925}S_{0.075}O_{3-\delta}$ after heating under O_2

All XRD data was analysed by the Rietveld refinement method. From the refinement data (Table 4) it can be seen there is a change in unit cell parameters upon heating in O_2. This can be more clearly seen in Figure 29 where samples heated in O_2 have a decrease in volume compared with the samples heated in air. This is expected to be due to the increase in oxygen

content which as a result gives a higher concentration of the smaller Fe^{4+}. The lattice parameters for both air and O_2 samples indicate a linear trend up to x = 0.05. This suggests the solubility limit is between x = 0.05 and 0.075.

The increase in unit cell volume for both air and O_2 samples is unexpected due to the smaller size of S^{6+} compared to $Fe^{3+/4+}$. This can possibly be explained by the changes in $Fe^{3+/4+}$ ratio on sulfate incorporation. However, this cell volume increase is also seen for N_2 treated samples where we have only Fe^{3+}. Therefore another factor must be significant to justify this trend. The unit cell volume increase may be associated with the extra oxygen associated with sulfate. Therefore if we take the case of the N_2 treated samples, we are effectively replacing $Fe(III)O_{1.5}$ with SO_3. Therefore there is the introduction of an extra 1.5 oxide ion per sulfate, which might be expected to contribute to an expanded cell size.

Table 4. Lattice parameters and Fe/S site occupancies for $SrFe_{1-x}S_xO_{3-\delta}$ after heating in O_2

	$SrFe_{1-x}S_xO_{3-\delta}$ Heated in O_2			
S(x)	0	0.025	0.05	0.075
a (Å)	3.8651(1)	3.8641(1)	3.8692(1)	3.8691(1)
c (Å)	3.8477(1)	-	-	-
V ($Å^3$)	57.349(3)	57.694(2)	57.924(2)	57.922(3)
R_{wp} (%)	4.16	3.29	3.79	3.93
R_{exp} (%)	3.71	2.81	2.73	2.79
Fe occ	1	0.97(2)	0.94(2)	0.93(2)
S occ	-	0.03(2)	0.06(2)	0.07(2)

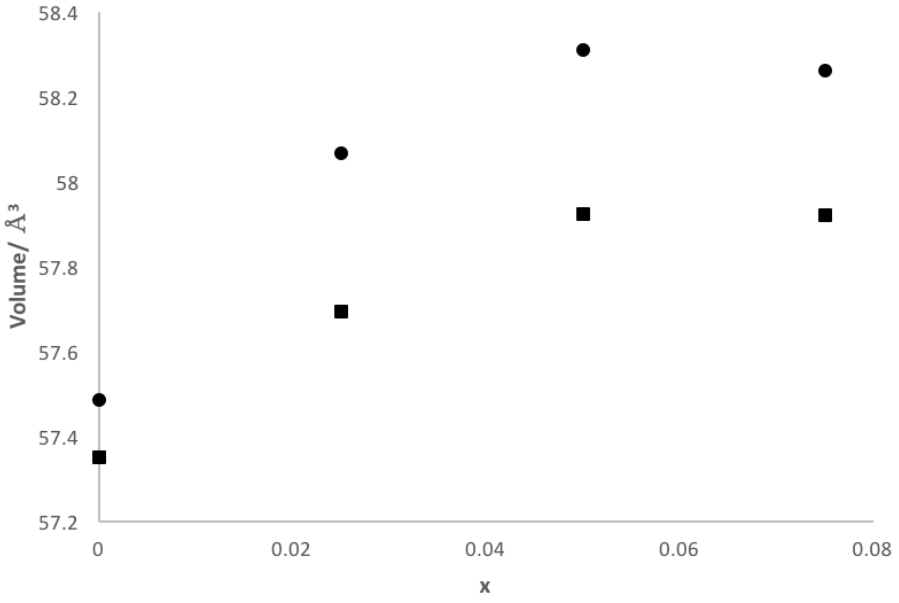

Figure 29. Plot of volume vs x for $SrFe_{1-x}S_xO_{3-\delta}$ heated in air (●) and heated in O_2 (■)

4.2.2.5 Conductivity studies

In general $SrFe_{1-x}S_xO_{3-\delta}$ samples are found to have similar conductivities when examined in air (Figure 30). At lower temperatures the higher sulfate content, x = 0.075, is found to have a notable decrease in conductivity. This decrease in conductivity at higher dopant levels has previously been reported for the silicon-doped $SrFeO_{3-\delta}$ systems.[111] At higher dopant levels it is expected the silicate disrupts the Fe-O network, resulting in a decrease in conductivity. Another factor could be low level of insulating impurities at high sulfate contents. Additionally, with increasing temperature a decrease in conductivity is observed. This is due to oxygen loss at higher temperature reducing the amount of Fe^{4+} present. This will be further discussed in section 4.2.3.4.

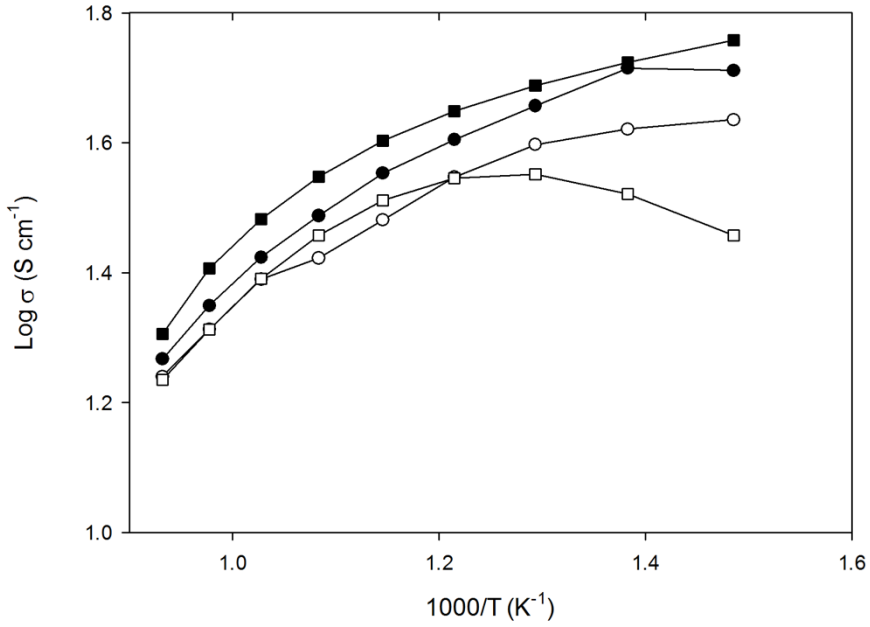

Figure 30. Plot of log σ vs. 1000/T for $SrFeO_{3-\delta}$ (●), $SrFe_{0.975}S_{0.025}O_{3-\delta}$ (○), $SrFe_{0.95}S_{0.05}O_{3-\delta}$ (■) and $SrFe_{0.925}S_{0.075}O_{3-\delta}$ (□) in air

4.2.3 $SrFe_{1-x}B_xO_{3-\delta}$

4.2.3.1 X-ray Diffraction results

In addition to sulfate incorporation, borate incorporation into $SrFeO_{3-\delta}$ was investigated. Similar results are observed for the borate doped systems compared with $SrFe_{1-x}S_xO_{3-\delta}$. For borate doped samples single phase cubic cells are reported (Figure 31). Compared with the sulfate-doped samples, single phase samples were achieved with a higher borate content ($(0 \leq x \leq 0.15)$.

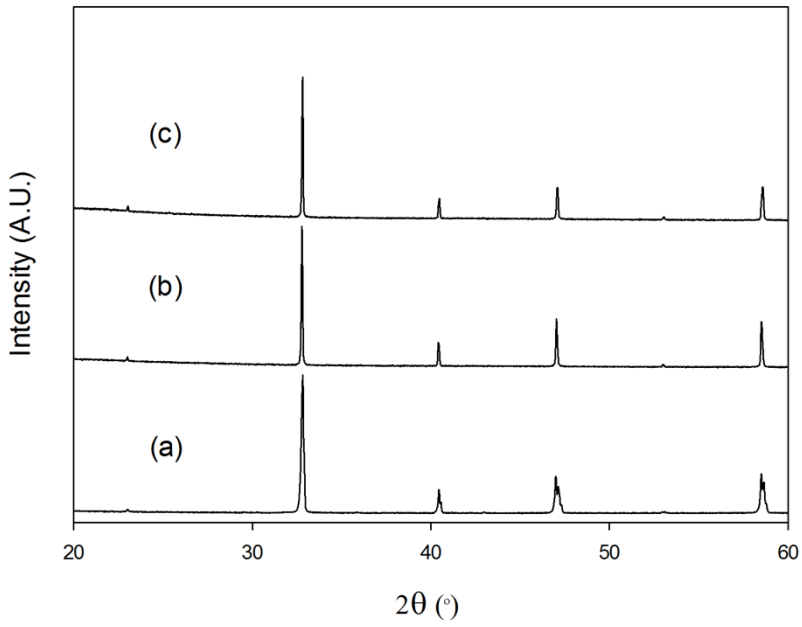

Figure 31. XRD patterns of a) $SrFeO_{3-\delta}$, b) $SrFe_{0.95}B_{0.05}O_{3-\delta}$ and c) $SrFe_{0.9}B_{0.1}O_{3-\delta}$

Rietveld refinements were carried out on XRD data (an example fit is shown in Figure 32) to determine cell parameters and site occupancies.

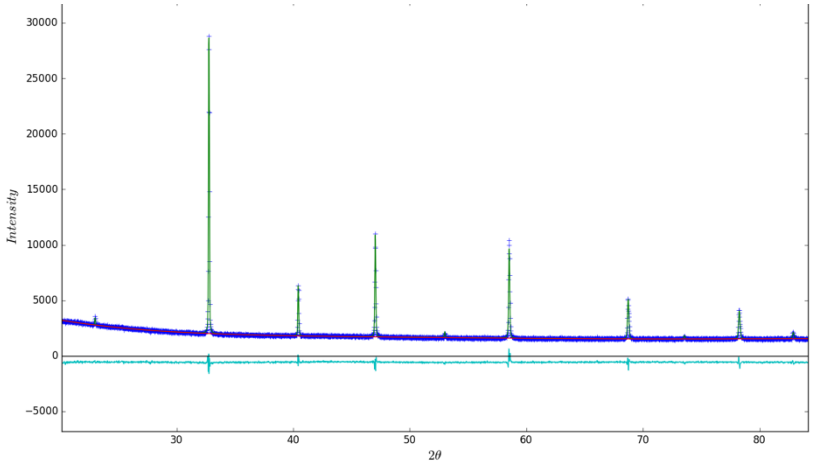

Figure 32. Observed (dark blue), calculated (green) and difference (light blue)XRD profile for $SrFe_{0.95}B_{0.05}O_{3-\delta}$

Rietveld refinements gave occupancies in good agreement with the expected values. As predicted for the sulfate doped samples, it is expected there would be a decrease in the unit cell due to the smaller size of B^{3+} compared to $Fe^{3+/4+}$. This is observed for the borate doped systems where the unit cell volume decreases with increasing borate content (Table 5). This is unlike the sulfate doped samples as there is no additional oxygen associated with the dopant (i.e., we are effectively replacing $Fe(III)O_{1.5}$ with $BO_{1.5}$).

Table 5. Lattice parameters and site occupancies obtained from XRD analysis for $SrFe_{1-x}B_xO_{3-\delta}$. $SrFeO_{3-\delta}$ was refined in a tetragonal space group (*P*4/*mmm*). Doped samples were refined in a cubic space group ($Pm\bar{3}m$).

	$SrFe_{1-x}B_xO_{3-\delta}$		
S (x)	0	0.05	0.1
a (Å)	3.8648(1)	3.8593(1)	3.8561(1)
c (Å)	3.8487(1)	-	-
V ($Å^3$)	57.486(4)	57.483(2)	57.336(4)
R_{wp} (%)	1.84	3.23	3.67

R_{exp} (%)	0.92	2.30	2.52
Fe occupancy	1(-)	0.92(1)	0.89(1)
B occupancy	-	0.08(1)	0.11(1)
Fe/B Uiso	0.003(1)	0.015(1)	0.022(1)

4.2.3.2 Stability under N_2

The same conditions (heat treatment to 950 °C under N_2) were used for the borate doped systems as for the sulfate doped systems. Similar results are observed, where the cubic cell is stabilised upon heating in nitrogen (Figure 33). The reduction of Fe^{4+} to the larger Fe^{3+} results in a shift in the XRD data indicating a larger unit cell.

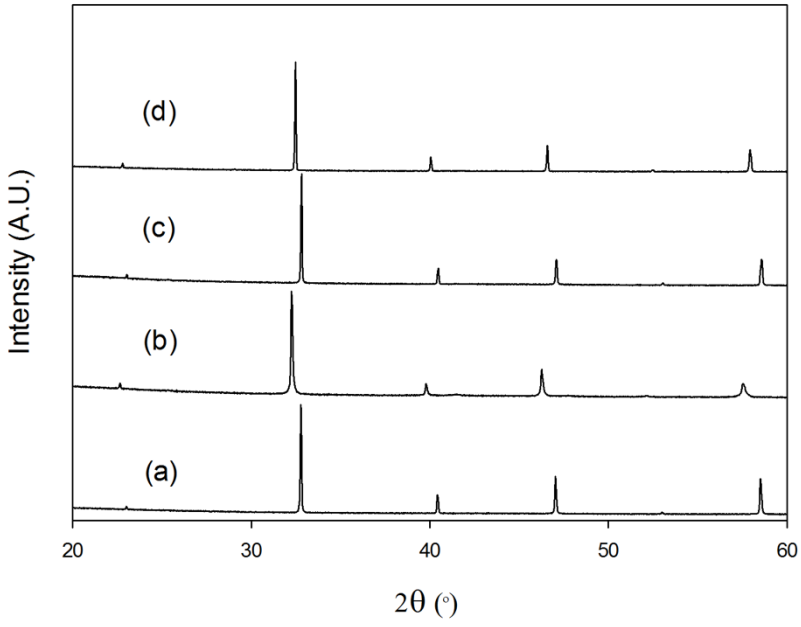

Figure 33. XRD patterns of a) $SrFe_{0.95}B_{0.05}O_{3-\delta}$, b) $SrFe_{0.95}B_{0.05}O_{3-\delta}$ after heating under N_2, c) $SrFe_{0.9}B_{0.1}O_{3-\delta}$ and d) $SrFe_{0.9}B_{0.1}O_{3-\delta}$ after heating under N_2

4.2.3.3 Thermogravimetric Analysis

These samples were analysed by TGA as reported for the sulfate doped materials. In contrast these samples have no mass loss due to CO_2. Therefore indicating no carbonate present in these materials.

4.2.3.4 Conductivity studies

At lower temperatures the $SrFe_{1-x}B_xO_{3-\delta}$ samples (x = 0.05, 0.1) showed significantly lower conductivities compared with the undoped system (Figure 34). Above 600 °C, the doped materials showed an increase in conductivity with a small improvement in conductivity for x = 0.1. Notably, these temperatures are in the range where solid oxide fuel cell cathodes operate. Additionally, for the borate doped phases and $SrFe_{0.925}S_{0.075}O_{3-\delta}$ a curved plot is observed. At low temperatures these materials have improvements in conductivity with increasing temperature due to the expected semiconducting behavior. At higher temperatures, conductivity begins to decrease due to the loss of oxygen at these temperatures resulting in the reduction of Fe^{4+} to Fe^{3+}, therefore loss of mixed valency.

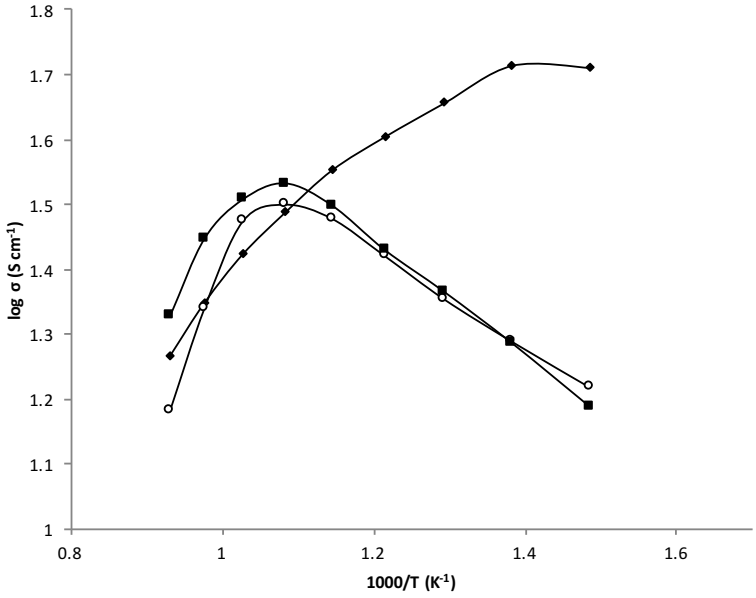

Figure 34. Plot of log σ vs. 1000/T for $SrFeO_{3-\delta}$ (●), $SrFe_{0.95}B_{0.05}O_{3-\delta}$ (○) and $SrFe_{0.9}B_{0.1}O_{3-\delta}$ (■) in air

Silicate[111], sulfate and borate-doped $SrFeO_{3-\delta}$ conductivity values (at 700 °C) are shown in Table 6. At typical solid oxide fuel cell operating temperature, similar values are shown for all samples. This data shows that by incorporating oxyanions an improvement in conductivity is achieved. This is predicted to be due to the mixed valency (Fe^{4+}/ Fe^{3+}) which is introduced when incorporating oxygen vacancies due to the presence of tetrahedral and trigonal planar oxyanions. Common SOFC cathode materials LSCF and LSM are found to have electronic conductivity of ≈ 300-400 S cm^{-1} (600 °C) and ≈ 180 S cm^{-1} (600 °C) respectively.[39,161,162] In comparison to common SOFC cathode materials, the conductivity data reported in table 6 is found to be low.

Table 6. Conductivity data in air at 700 °C for $SrFe_{1-x}M_xO_{3-\delta}$ where M = Si[111] , S and B.

	Si (x)				**S (x)**				**B (x)**	
	0	**0.05**	**0.1**	**0.15**	**0**	**0.025**	**0.05**	**0.075**	**0.05**	**0.1**
Conductivity 700 °C (S cm^{-1})	26	21	35	18	26	25	30	25	30	32

4.2.4 Conclusions

The first reports of successful incorporation of sulfate and borate into $SrFeO_{3-\delta}$ are presented in this work. The cubic cell is stabilised for sulfate and borate-doped materials with the tetragonal unit cell reported for $SrFeO_{3-\delta}$. The cubic cell is maintained even after heating under N_2, where undoped $SrFeO_{3-\delta}$ transforms to the oxygen vacancy ordered brownmillerite structure. Sulfate/ borate-doped samples have comparable conductivities (Table 6) to the undoped $SrFeO_{3-\delta}$ in the operating temperature range for solid oxide fuel cells. Further studies are warranted after these promising results to further investigate these systems as solid oxide fuel cell cathodes.

Work within this chapter has been published in Crystals *(A. Jarvis and P. R. Slater, Crystals,* ***2017****, 7(6), 169–181; https://doi.org/10.3390/cryst7060169).*

4.3 $Sr_{0.5}Ba_{0.5}Fe_{1-x}(S/P)_xO_{3-\delta}$

4.3.1 Experimental

Stoichiometric amounts of $SrCO_3$, $BaCO_3$, Fe_2O_3 and either $(NH_4)_2SO_4$ or $NH_4H_2PO_4$ were ground and heated to 900 °C (4 °C/min) for 12 h. After the initial heat treatment, $Sr_{0.5}Ba_{0.5}Fe_{1-x}(S/P)_xO_{3-\delta}$ samples were then ball milled at 350 rpm for 1 h (Fritsch Pulverisette 7 planetary Mill). Samples were then reheated to 1000 °C for 12 h before regrinding and heating to 1100 °C for 12 h. Finally, to ensure maximum oxygen content, samples were heated to 350 °C for 12 h.

In order to test stability under low $p(O_2)$, $Sr_{0.5}Ba_{0.5}Fe_{1-x}(S/P)_xO_{3-\delta}$ samples were heated to 950 °C for 12 h under N_2.

Powder XRD were collected for all samples with GSAS suite of programs used for structure refinements.[136] XRD data was used to confirm phase purity and to characterise cell parameters. For $SrFe_{1-x}S_xO_{3-\delta}$ samples heated in air, data collection was carried out on a Bruker D8 diffractometer with Cu Kα radiation. All other XRD data were collected on a Panalytical Empyrean diffractometer equipped with a Pixcel 2D detector (Cu Kα radiation).

TGA was collected using a Netzch STA 449 F1 Jupiter Thermal Analyser with mass spectrometry attachment. Samples were heated at 10 °C min^{-1} under N_2 to 1000 °C.

Four probe dc conductivity measurements were carried out for $Sr_{0.5}Ba_{0.5}Fe_{1-x}(S/P)_xO_{3-\delta}$ samples. Initially powders were balled milled at 350 rpm for 1 hour. The resulting powder was pressed into pellets and sintered at 1100 °C. Au electrodes were attached to the pellets with Au paste and fired to 800 °C for 1 h in air. To ensure full oxygenation, pellets were finally annealed at 350 °C for 12 h.

4.3.2 X-ray Diffraction results

In addition to oxyanion doped $SrFeO_{3-\delta}$ systems, doped $Sr_{0.5}Ba_{0.5}FeO_{3-\delta}$ systems have been investigated. XRD data indicates disordered cubic perovskite systems are observed for the undoped and sulfate/ phosphate doped systems (Figure 35 and Figure 36). By incorporating Ba on the A site, stabilisation of the cubic perovskite system occurs where in comparison, $SrFeO_{3-\delta}$ forms a tetragonal perovskite. Sulfate and phosphate oxyanions also stabilise the cubic perovskite system. At higher dopant levels, x = 0.05 and 0.075, small $BaSO_4$ impurities form for $Sr_{0.5}Ba_{0.5}Fe_{1-x}S_xO_{3-\delta}$. Although phosphate incorporation stabilises the cubic perovskite system, small impurities ($Sr_3(PO_4)_2$ and $Ba_3(PO_4)_2$) form for all systems.

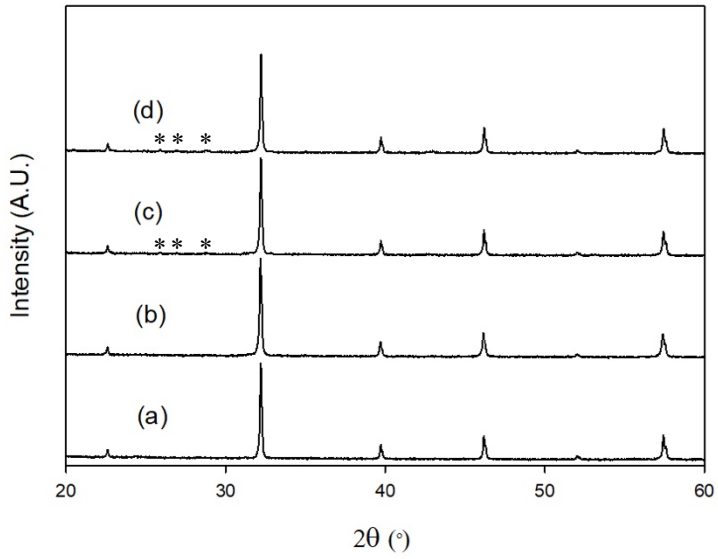

Figure 35. XRD patterns of a) $Sr_{0.5}Ba_{0.5}FeO_{3-\delta}$, b) $Sr_{0.5}Ba_{0.5}Fe_{0.975}S_{0.025}O_{3-\delta}$, c) $Sr_{0.5}Ba_{0.5}Fe_{0.95}S_{0.05}O_{3-\delta}$ and d) $Sr_{0.5}Ba_{0.5}Fe_{0.925}S_{0.075}O_{3-\delta}$. $SrSO_4$ impurities are highlighted with an asterisk (*).

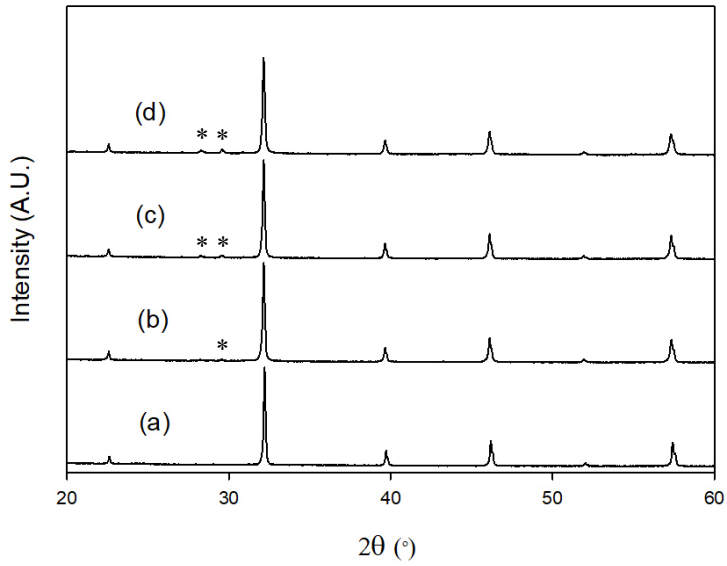

Figure 36. XRD patterns of a) $Sr_{0.5}Ba_{0.5}FeO_{3-\delta}$, b) $Sr_{0.5}Ba_{0.5}Fe_{0.975}P_{0.025}O_{3-\delta}$, c) $Sr_{0.5}Ba_{0.5}Fe_{0.95}P_{0.05}O_{3-\delta}$ and d) $Sr_{0.5}Ba_{0.5}Fe_{0.925}P_{0.075}O_{3-\delta}$. $Sr_3(PO_4)_2$ and $Ba_3(PO_4)_2$ impurities are highlighted with an asterisk (*).

Rietveld refinements were carried out on XRD data where an example fit can be found in Figure 37. Unit cell parameters and site occupancies were refined for all systems. Occupancies were found to be in good agreement with expected values (Table 7).

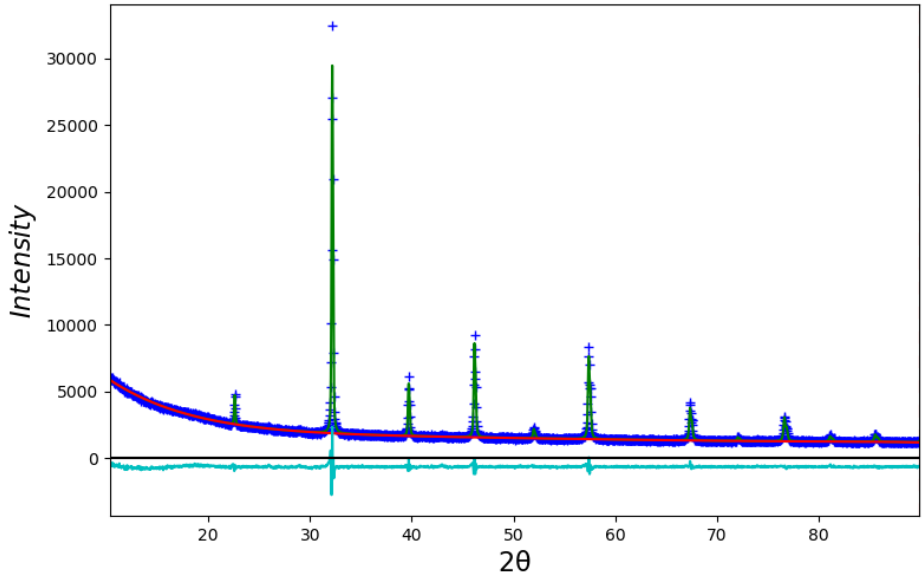

Figure 37. Observed (dark blue), calculated (green) and difference (light blue) XRD profile for $Sr_{0.5}Ba_{0.5}Fe_{0.975}S_{0.025}O_{3-\delta}$

Table 7. Lattice parameters and site occupancies obtained from XRD analysis for $Sr_{0.5}Ba_{0.5}Fe_{1-x}(S/P)_xO_{3-\delta}$ heated in air. Samples were refined in a cubic space group ($Pm\bar{3}m$).

$Sr_{0.5}Ba_{0.5}Fe_{1-x}(S/P)_xO_{3-\delta}$							
		S_x			**P_x**		
	0	0.025	0.05	0.075	0.025	0.05	0.075
a (Å)	3.9269(1)	3.9282(1)	3.9258(1)	3.9238(1)	3.9309(1)	3.9315(1)	3.9323(1)
V (Å^3)	60.554(3)	60.613(4)	60.503(4)	60.414(4)	60.740(3)	60.767(3)	60.806(4)
R_{wp} (%)	4.53	3.60	3.72	4.38	3.03	3.08	3.10
R_{exp} (%)	2.13	2.19	2.26	2.04	1.87	1.86	1.86
Fe occ	1	0.96(18)	0.93(18)	0.89(19)	0.98(13)	0.95(13)	0.93(13)
S occ	-	0.04(18)	0.07(18)	0.11(19)	0.02(13)	0.05(13)	0.07(13)

Unit cell data (Figure 38) for $Sr_{0.5}Ba_{0.5}Fe_{1-x}P_xO_{3-\delta}$ show a general increase with increasing phosphate content. This is as observed for $SrFe_{1-x}S_xO_{3-\delta}$ where it would be

predicted doping with smaller P^{6+} for Fe^{3+}/Fe^{4+} is expected to decrease the unit cell. Instead the change in Fe^{3+}/Fe^{4+} ratio upon phosphate incorporation results in an increase in unit cell. In comparison there is an initial increase upon doping with sulfate (x = 0.025) which decreases with further sulfate incorporation. The initial increase in unit cell parameters could be explained by the competing effects of doping with the smaller S^{6+} and the change in Fe^{3+}/Fe^{4+} ratio. The decrease in unit cell with increasing sulfate incorporation can be explained due to the small size of S^{6+} compared with Fe^{3+}/Fe^{4+}.

A larger unit cell is observed when doping with phosphate compared with sulfate which is as expected due to the larger ionic radii of P^{6+} compared with S^{6+}.

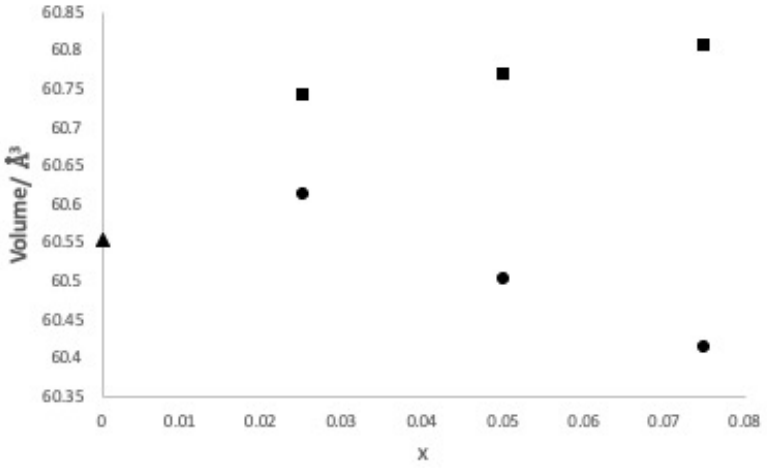

Figure 38. Plot of volume vs x for $Sr_{0.5}Ba_{0.5}FeO_{3-\delta}$ (▲), $Sr_{0.5}Ba_{0.5}Fe_{1-x}S_xO_{3-\delta}$ (●) and $Sr_{0.5}Ba_{0.5}Fe_{1-x}P_xO_{3-\delta}$ (■) heated in air

4.3.3 Stability under N_2

Upon heating in N_2 to 950 °C sulfate/ phosphate doped samples stabilise the cubic perovskite system. As observed for the annealed samples impurities are still present in sulfate doped (x =

0.05 and 0.075) and phosphate doped samples (Figure 39 and Figure 40). Weak peaks in the XRD data for the undoped ($Sr_{0.5}Ba_{0.5}FeO_{3-\delta}$) suggests possibly some oxygen vacancy ordering as observed in the brownmillerite structure. For $Sr_{0.5}Ba_{0.5}Fe_{0.975}S_{0.025}O_{3-\delta}$, asymmetry is present in the XRD data suggesting the possibility of 2 perovskite phases. This could be predicted to be due to differing oxygen contents in each phase. Additionally, broad peaks in the XRD for $Sr_{0.5}Ba_{0.5}Fe_{0.925}P_{0.075}O_{3-\delta}$ suggest multiple perovskite phases.

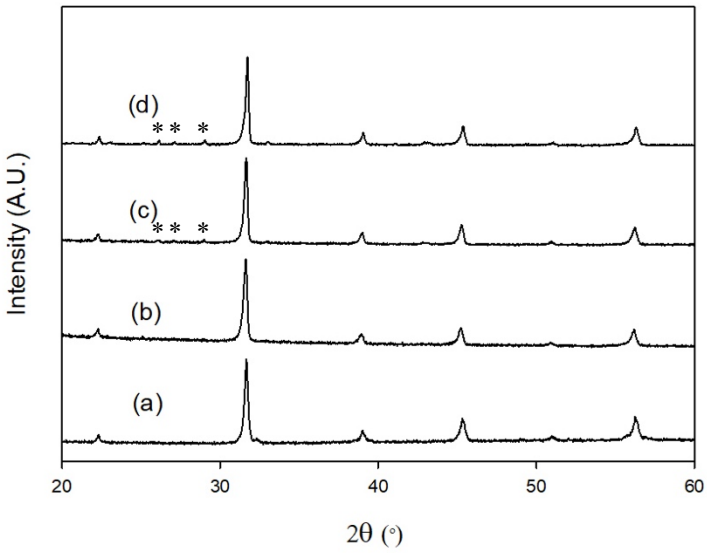

Figure 39. XRD patterns of a) $Sr_{0.5}Ba_{0.5}FeO_{3-\delta}$, b) $Sr_{0.5}Ba_{0.5}Fe_{0.975}S_{0.025}O_{3-\delta}$, c) $Sr_{0.5}Ba_{0.5}Fe_{0.95}S_{0.05}O_{3-\delta}$ and d) $Sr_{0.5}Ba_{0.5}Fe_{0.925}S_{0.075}O_{3-\delta}$ after heating under N_2 to 950 °C. $SrSO_4$ impurities are highlighted with an asterisk (*).

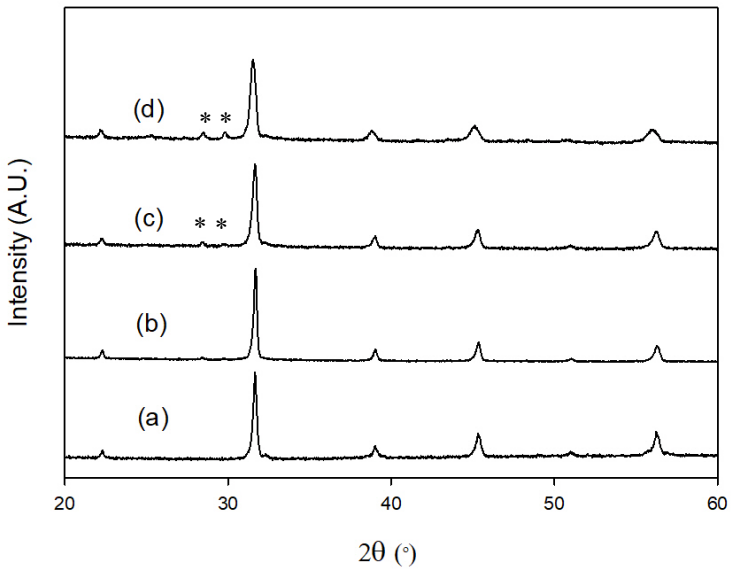

Figure 40. XRD patterns of a) $Sr_{0.5}Ba_{0.5}FeO_{3-\delta}$, b) $Sr_{0.5}Ba_{0.5}Fe_{0.975}P_{0.025}O_{3-\delta}$, c) $Sr_{0.5}Ba_{0.5}Fe_{0.95}P_{0.05}O_{3-\delta}$ and d) $Sr_{0.5}Ba_{0.5}Fe_{0.925}P_{0.075}O_{3-\delta}$ after heating under N_2 to 950 °C. $Sr_3(PO_4)_2$ and $Ba_3(PO_4)_2$ impurities are highlighted with an asterisk (*).

Rietveld refinements were carried out on $Sr_{0.5}Ba_{0.5}Fe_{1-x}S_xO_{3-\delta}$ (x = 0.05 and 0.075) and $Sr_{0.5}Ba_{0.5}Fe_{1-x}P_xO_{3-\delta}$ (x = 0.025 and 0.05). A shift in XRD data and the increase in unit cell parameters in Table 8 indicate an increase in unit cell volume when heating samples in dry N_2 to 950 °C compared with samples heated in air. This is due to the reduction of Fe^{4+} to Fe^{3+}. Refined occupancies for Fe/S/P are found to have high errors therefore occupancy of sulfate/phosphate is inconclusive. Further work would be needed to investigate this. Although issues with refined occupancies, the variation in cell parameters and stability in N_2 supports in the incorporation.

Table 8. Lattice parameters and site occupancies obtained from XRD analysis for $Sr_{0.5}Ba_{0.5}Fe_{1-x}(S/P)_xO_{3-\delta}$ heated in N_2. Samples were refined in a cubic space group ($Pm\bar{3}m$).

$Sr_{0.5}Ba_{0.5}Fe_{1-x}(S/P)_xO_{3-\delta}$				
	S_x		**P_x**	
	0.05	0.075	0.025	0.05
a (Å)	4.0161(2)	4.0130(3)	4.0097(2)	4.0182(3)
V (Å^3)	64.775(12)	64.624(14)	64.468(9)	64.878(17)
R_{wp} (%)	3.50	4.17	3.05	2.98
R_{exp} (%)	2.28	2.22	1.99	2.28
Fe occupancy	0.97(25)	0.94(31)	0.99(26)	0.97(32)
S occupancy	0.03(25)	0.06(31)	0.01(26)	0.03(32)

4.3.4 Thermogravimetric Analysis

TGA was carried out for $Sr_{0.5}Ba_{0.5}Fe_{0.975}(S/P)_{0.025}O_{3-\delta}$ samples. As well as the loss of water and oxygen, mass spectrometry data indicates the loss of a small amount of CO_2 (Figure 41) as observed for the $SrFe_{1-x}S_xO_{3-\delta}$ samples. The loss of CO_2 for all samples is found to be at lower temperature than the mass spectrometry data for $BaCO_3$ or $SrCO_3$ (Figure 42). This therefore indicates the possibility of the incorporation of carbonate. Further work would be needed to investigate this.

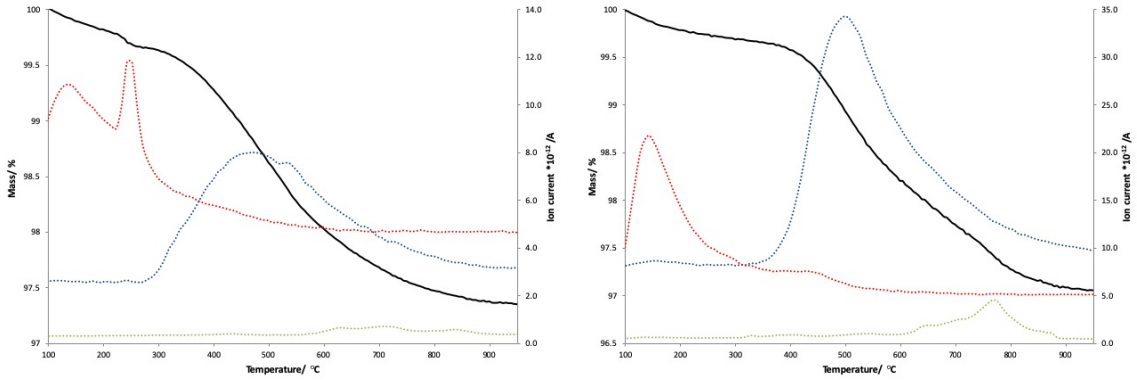

Figure 41. Plot of mass vs. temperature and ion current vs. temperature (under N_2) for a) $Sr_{0.5}Ba_{0.5}Fe_{0.975}S_{0.025}O_{3-\delta}$ and b) $Sr_{0.5}Ba_{0.5}Fe_{0.975}P_{0.025}O_{3-\delta}$ prepared in air. TGA shows mass loss associates with H_2O (red), O_2 (blue), and CO_2 (green). Solid lines indicate %mass and dashed lines indicate ion current.

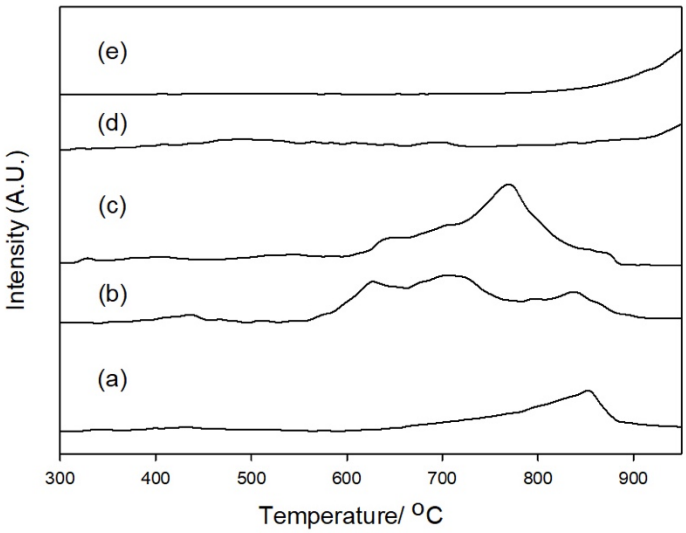

Figure 42. Ion current (m/z = 44; CO_2) vs temperature (under N_2) for a) $Sr_{0.5}Ba_{0.5}FeO_{3-\delta}$ b) $Sr_{0.5}Ba_{0.5}Fe_{0.975}S_{0.025}O_{3-\delta}$ c) $Sr_{0.5}Ba_{0.5}Fe_{0.975}P_{0.025}O_{3-\delta}$ d) $BaCO_3$ and e) $SrCO_3$

4.3.5 Conductivity studies

In order to test suitability for use as a cathode in a solid oxide fuel cell, conductivities for both sulfate and phosphate samples were examined in air. $Sr_{0.5}Ba_{0.5}Fe_{1-x}S_xO_{3-\delta}$ samples were found to decrease in conductivity with increasing temperature (Figure 43). This is as observed for the $SrFe_{1-x}S_xO_{3-\delta}$ samples. Sulfate doped materials were found to have lower conductivities than the undoped $Sr_{0.5}Ba_{0.5}FeO_{3-\delta}$ sample.

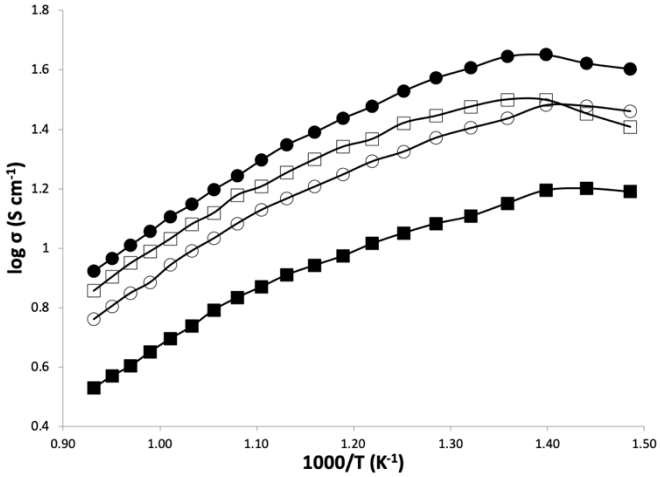

Figure 43. Plot of log σ vs. 1000/T for $Sr_{0.5}Ba_{0.5}FeO_{3-\delta}$ (●), b) $Sr_{0.5}Ba_{0.5}Fe_{0.975}S_{0.025}O_{3-\delta}$ (○), $Sr_{0.5}Ba_{0.5}Fe_{0.95}S_{0.05}O_{3-\delta}$ (■) and $Sr_{0.5}Ba_{0.5}Fe_{0.925}S_{0.075}O_{3-\delta}$ (□) in air

Compared with phosphate doped materials, sulfate doped $Sr_{0.5}Ba_{0.5}FeO_{3-\delta}$ samples were found to have higher conductivities. A similar trend is observed for $Sr_{0.5}Ba_{0.5}Fe_{1-x}P_xO_{3-\delta}$ where a decrease in conductivities with incorporation of phosphate is reported (Figure 44).

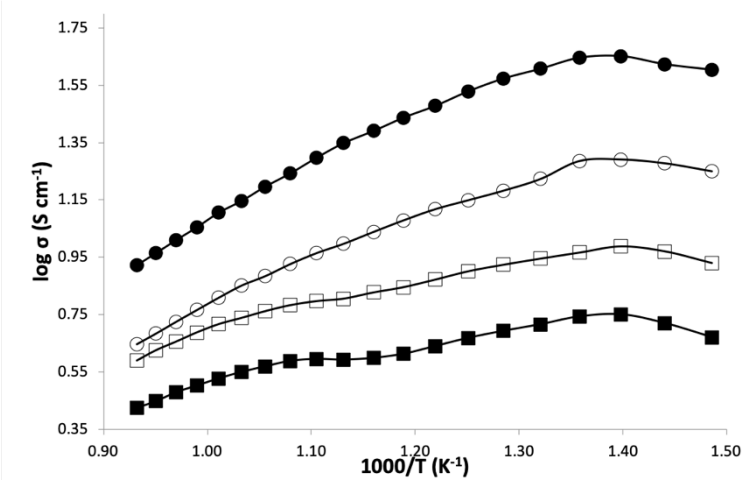

Figure 44. Plot of log σ vs. 1000/T for $Sr_{0.5}Ba_{0.5}FeO_{3-\delta}$ (●), b) $Sr_{0.5}Ba_{0.5}Fe_{0.975}P_{0.025}O_{3-\delta}$ (○), $Sr_{0.5}Ba_{0.5}Fe_{0.95}P_{0.05}O_{3-\delta}$ (■) and $Sr_{0.5}Ba_{0.5}Fe_{0.925}P_{0.075}O_{3-\delta}$ (□) in air

4.3.6 Conclusions

This work presents the successful incorporation of sulfate and phosphate into $Sr_{0.5}Ba_{0.5}FeO_{3-\delta}$. All materials including the undoped sample stabilise the cubic perovskite system with the addition of impurities in phosphate and higher sulfate levels. Higher sulfate levels and phosphate doped materials are found to be stable when heating in N_2 to 950 °C. Rietveld refinements of samples heated in N_2 provided inconclusive occupancy information. Further microscopy studies would be needed to investigate the structure and composition of these phases. Compared with the doped $SrFeO_{3-\delta}$ systems, lower conductivities are observed for $Sr_{0.5}Ba_{0.5}FeO_{3-\delta}$ doped systems. Given these initial results, further work is needed to investigate the performance of these materials as solid oxide fuel cell cathodes.

4.4 $BaFe_{1-x}S_xO_{3-\delta}$ and $BaFe_{1-y}O_{3-\delta}$

4.4.1 Experimental

Stochiometric amounts of $BaCO_3$, Fe_2O_3 and $(NH_4)_2SO_4$ were intimately ground and heated to 800 °C (4°C/ min) for 12 h. Samples were reground and split into 5 and heated to different temperatures - 800, 850 900, 950 and 1000 °C for 12 h. Samples were again reground and heated to the same temperature for 48 h.

Powder XRD (Bruker D8 and D5005 diffractometer with Cu Kα radiation) was used to confirm phase purity and to characterise cell parameters.

TGA was collected using a Netzch STA 449 F1 Jupiter Thermal Analyser with mass spectrometry attachment. Samples were heated at 10 °C min^{-1} under N_2 to 1000 °C.

4.4.2 $BaFe_{1-y}O_{3-\delta}$

4.4.2.1 X-ray Diffraction results

Following on from sulfate incorporation in $SrFeO_{3-\delta}$ and $Sr_{0.5}Ba_{0.5}FeO_{3-\delta}$, oxyanion incorporation in $BaFeO_{3-\delta}$ was investigated. The undoped sample, $BaFeO_{3-\delta}$, did not form the cubic or tetragonal perovskite at high temperature. Because of this observation a range of temperatures and times were investigated to synthesise a pure perovskite phase (Figure 45). Initially samples were heated for 12 h at various temperatures between 800 -1000 °C. In this temperature range there is difficulty in forming a pure perovskite system for $BaFeO_{3-\delta}$. When introducing a longer heating time, a hexagonal cell forms when samples are heated to 800 °C and 850 °C, but again impurities are present in these samples (Figure 45).

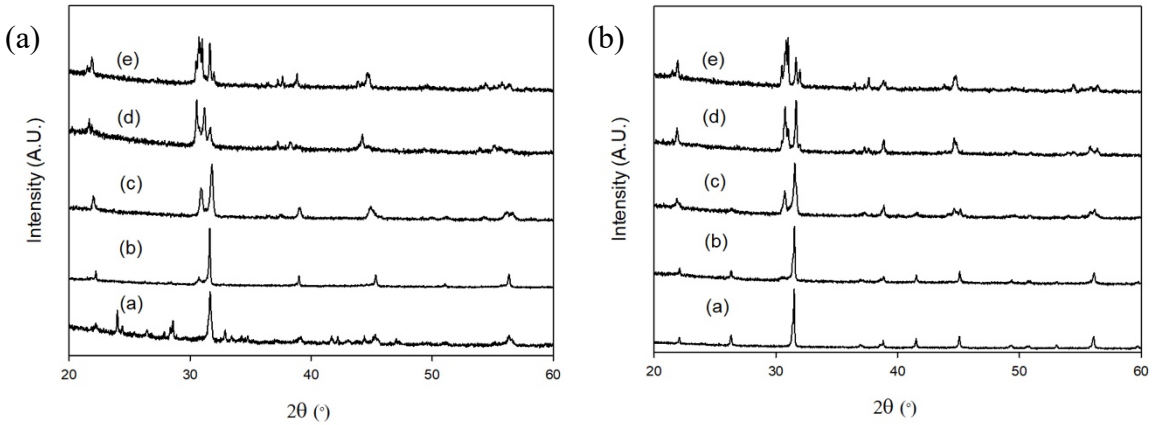

Figure 45. XRD patterns of $BaFeO_{3-\delta}$ heated for (a) 12 h and (b) 48 h to a) 800 °C, b) 850 °C, c) 900 °C, d) 950 °C and e) 1000 °C

Due to impure $BaFeO_{3-\delta}$ samples, lowering of Fe content was investigated. Here it is expected by lowering the Fe content, carbonate could be incorporated into the sample to stabilise the cubic perovskite structure. Therefore, two further samples were synthesised ($BaFe_{0.9}O_{3-\delta}$ and $BaFe_{0.8}O_{3-\delta}$).

XRD suggests both $BaFe_{0.9}O_{3-\delta}$ (Figure 46) and $BaFe_{0.8}O_{3-\delta}$ (Figure 47) form the cubic perovskite structure when heated to 900 °C for 12 hours. In addition to the cubic perovskite phase, small impurities are present for $BaFe_{0.8}O_{3-\delta}$. Synthesis of these materials at 900 °C is significantly lower compared to $Sr_{0.5}Ba_{0.5}FeO_{3-\delta}$ which is synthesised at 1100 °C. It is expected the incorporation of carbonate in the structure lowers the oxidation state of Fe which in turn stabilises the cubic perovskite. Heating these materials for longer periods of time (48 h) results in a change in structure for $BaFe_{0.9}O_{3-\delta}$ and $BaFe_{0.8}O_{3-\delta}$. Where at 900 °C a cubic cell is observed, when heating for longer the cubic structure is lost and a hexagonal cell forms at the lower temperature of 850 °C.

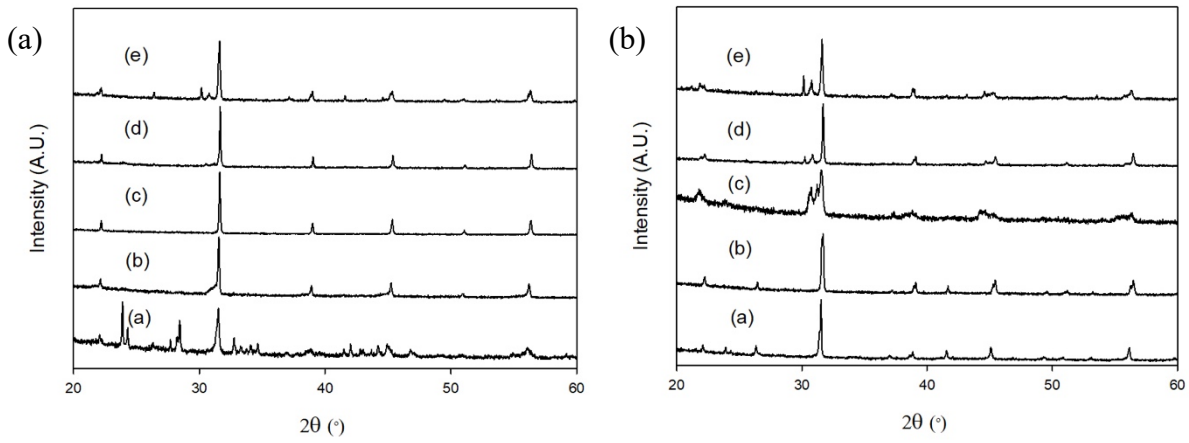

Figure 46. XRD patterns of $BaFe_{0.9}O_{3-\delta}$ heated for (a) 12 h and (b) 48 h to a) 800 °C, b) 850 °C, c) 900 °C, d) 950 °C and e) 1000 °C

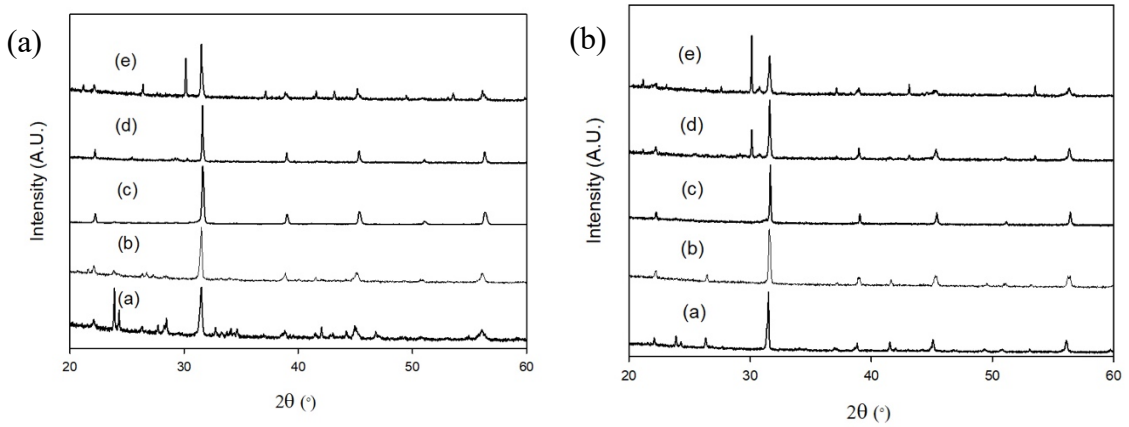

Figure 47. XRD patterns of $BaFe_{0.8}O_{3-\delta}$ heated for (a) 12 h and (b) 48 h to a) 800 °C, b) 850 °C, c) 900 °C, d) 950 °C and e) 1000 °C

Rietveld refinements were carried out on the pure cubic perovskite system $BaFe_{0.9}O_{3-\delta}$ heated to 900 °C for 12h (Figure 48). Unit cell parameters and structural information can be found in Table 9. Refinements suggest oxygen vacancies in the structure, but significant vacancies are not observed on the Fe site. Further work is needed to investigate carbonate incorporation.

Table 9. Lattice parameters and site occupancies obtained from XRD analysis for $BaFe_{0.9}O_{3-\delta}$ heated to 900 °C for 12 hours. Samples were refined in a cubic space group ($Pm\bar{3}m$).

	a/ Å		V/ Å^3	Rwp/ %	Rexp/ %
	3.9999(1)		63.998(3)	5.07	2.79
	x	**y**	**z**	**Occupancy**	**U_{iso}**
Ba	0.0000	0.0000	0.0000	1.000	
Fe	0.5000	0.5000	0.5000	0.999(4)	0.0091
O	0.5000	0.5000	0.0000	0.900(7)	

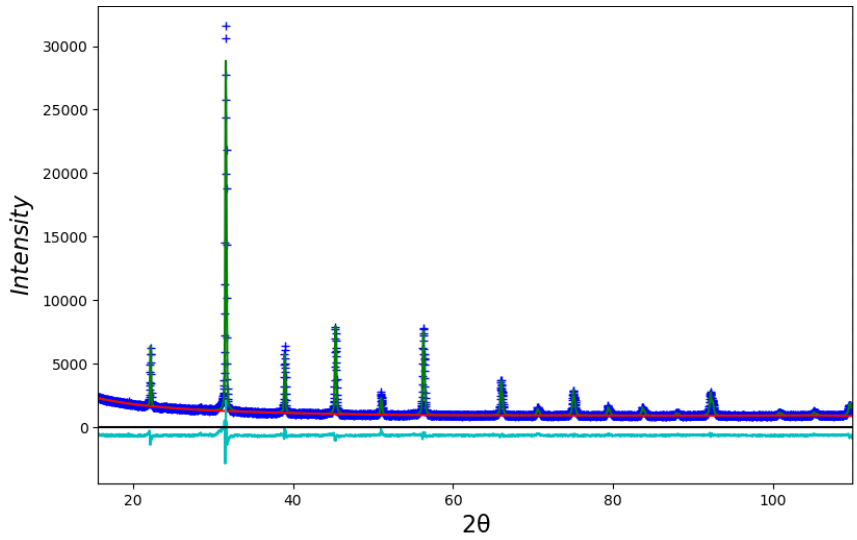

Figure 48. Observed (dark blue), calculated (green) and difference (light blue) XRD profile for $BaFe_{0.9}O_{3-\delta}$

4.4.2.2 Thermogravimetric Analysis

TGA was carried out on $BaFe_{0.9}O_{3-\delta}$ to investigate the incorporation of carbonate in the cubic perovskite system. At low temperature (50 – 200 °C) mass loss is associated water (Figure 49). Furthermore, a small mass loss at ≈ 350 – 450 °C is present with an additional mass loss from ≈ 850 °C due to the loss of CO_2. The loss of CO_2 is found to be at a lower temperature

than $BaCO_3$ where loss of CO_2 is seen from ≈ 900 °C. This suggests carbonate is incorporated into $BaFe_{0.9}O_{3-\delta}$.

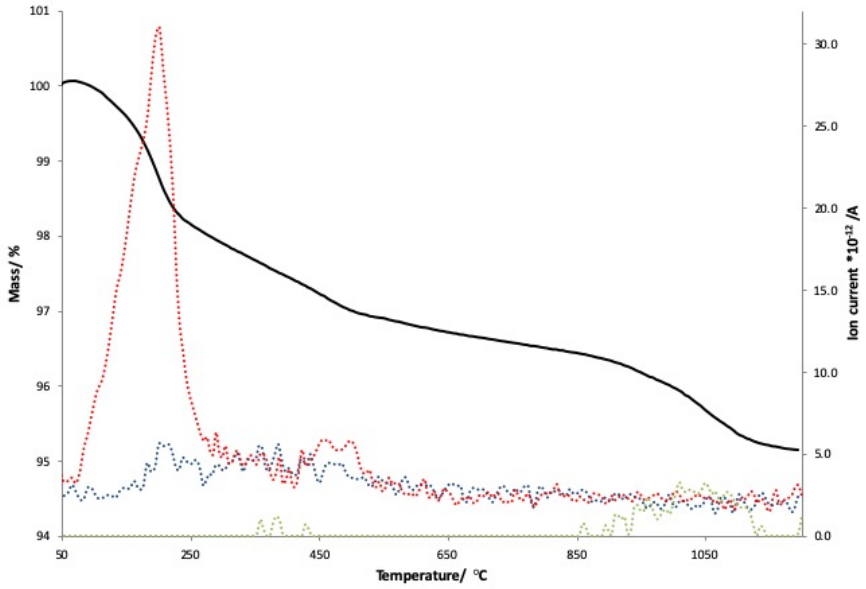

Figure 49. Plot of mass vs. temperature and ion current vs. temperature (under N_2) for a) $BaFe_{0.9}O_{3-\delta}$ prepared in air at 900 °C for 12 hours. TGA shows mass loss associates with H_2O (red), O_2 (blue), and CO_2 (green). Solid lines indicate %mass and dashed lines indicate ion current.

4.4.3 $BaFe_{1-x}S_xO_{3-\delta}$

4.4.3.1 X-ray Diffraction results

Although sulfate incorporation into $SrFeO_{3-\delta}$ and $Sr_{0.5}Ba_{0.5}FeO_{3-\delta}$ has shown to successfully stabilise the cubic perovskite, this is not observed when doping $BaFeO_{3-\delta}$. The cubic perovskite phase is synthesised at high temperatures (1100 °C) for $SrFeO_{3-\delta}$ and $Sr_{0.5}Ba_{0.5}FeO_{3-\delta}$. At this temperature it is predicted $BaFe_{1-x}S_xO_{3-\delta}$ systems form a mixture of phases including the cubic perovskite and monoclinic $Ba_2Fe_2O_5$ phase (Figure 50 and Figure 51).

As observed for $BaFe_{1-y}O_{3-\delta}$, when heating to 800 and 850 °C for 48 h the hexagonal perovskite is formed. At higher sulfate doping levels (x = 0.075) $BaSO_4$ impurities begin to form. Additionally, when heating to 850 °C for 48 h $BaSO_4$ impurities begin to form for $BaFe_{0.95}S_{0.05}O_{3-\delta}$.

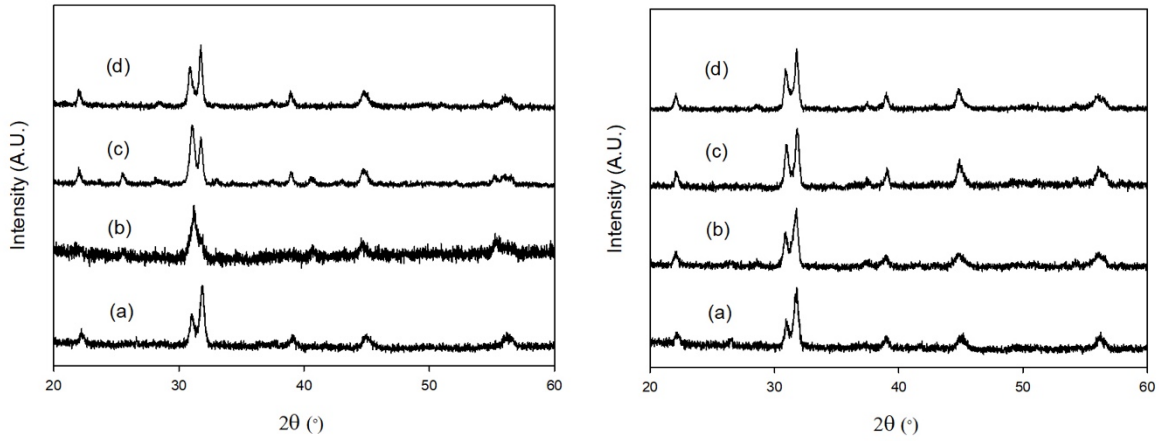

Figure 50. XRD patterns for (a) $BaFe_{0.975}S_{0.025}O_{3-\delta}$ and (b) $BaFe_{0.95}S_{0.05}O_{3-\delta}$ heated in air to a) 900 °C, b) 1000 °C, c) 1050 °C and d) 1100 °C for 12 hours

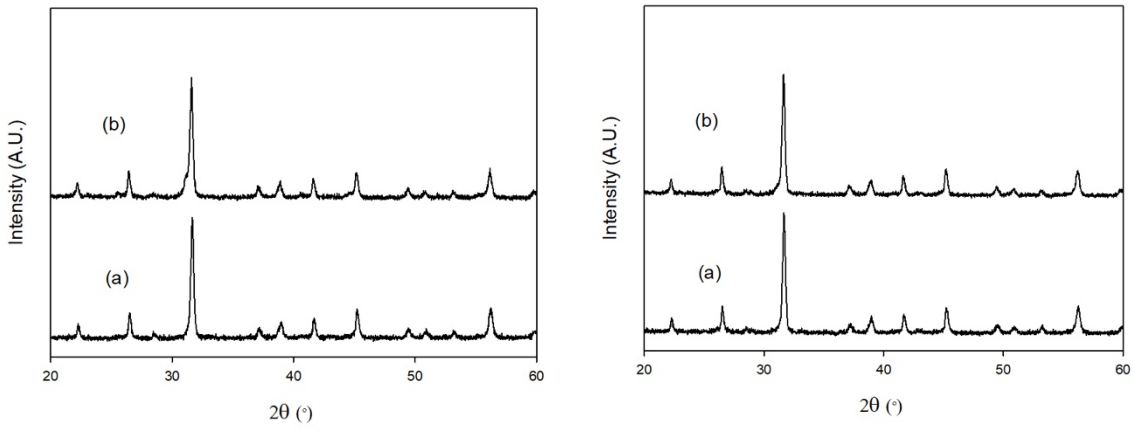

Figure 51. XRD patterns for (a) $BaFe_{0.975}S_{0.025}O_{3-\delta}$ and (b) $BaFe_{0.95}S_{0.05}O_{3-\delta}$ heated in air to a) 800 °C and b) 850 °C for 48 hours

4.4.4 Conclusions

Although the ideal cubic perovskite is difficult to form for $BaFe_{1-x}S_xO_{3-\delta}$, sulfate is found to stabilise the hexagonal perovskite structure. In comparison to the sulfate doped systems, by introducing vacancies in $BaFe_{1-y}O_{3-\delta}$ (y = 0.1) and heating samples to < 1000 °C, the cubic perovskite is predicted to be stabilised by carbonate. Additionally, for $BaFe_{1-y}O_{3-\delta}$ and $BaFe_{1-x}S_xO_{3-\delta}$ heating for longer periods of time is found to stabilise the hexagonal perovskite which is not observed when heating to higher temperatures for shorter times. These materials highlight the importance of temperature and synthesis time. Further work would be needed to further investigate carbonate incorporation in these materials.

4.5 Summary

A summary of all perovskite materials investigated in chapter 4 can be found in Table 10. These systems have shown that not only is the choice of dopant important, but also the synthesis conditions including temperature and time. As reported in Table 10, doping on not only the Sr site, but also the Fe site in $SrFeO_{3-\delta}$ successfully stabilises the cubic perovskite structure. Additionally, this work has highlighted the importance of considering the incorporation of carbonate into these materials, particularly when using a low synthesis temperature.

As perovskite materials have been found to be suitable for use as SOFC cathode materials, conductivity studies were carried out for all phases with the highest conductivity data reported in Table 10. Although the cubic perovskite structure is stabilised for these oxyanion doped materials, a range of conductivities are reported depending on not only the dopant, but also the amount of oxyanion incorporated.

Table 10. Chapter 4 summary table

Sample	**Crystal system (Synthesis temperature)**	**Stability**	**Highest conductivity (Temperature)**
$SrFeO_{3-\delta}$	Tetragonal (1100 °C with anneal at 350 °C)	**Stability in low p(O_2)** - Transforms to oxygen vacancy ordered brownmillerite **Carbonate incorporation/ heat treatment under O_2**	26 S cm^{-1} (400 °C)

		- Cubic perovskite maintained with no loss of carbonate in TGA-MS	
$SrFe_{1-x}S_xO_{3-\delta}$ where x=0.025, 0.05 and 0.075	Cubic (1100 °C with anneal at 350 °C)	**Stability in low p(O_2)** - Cubic cell is maintained when heating under dry N_2 with an increase in lattice parameters **Carbonate incorporation/ heat treatment under O_2** - Cubic cell is maintained - TGA-MS indicates heat treatment in O_2 drives out carbonate from samples synthesised in air	25-30 S cm^{-1} (400-500 °C)
$SrFe_{1-x}B_xO_{3-\delta}$ where x=0.05 and 0.1	Cubic (1200 °C with anneal at 350 °C)	**Stability in low p(O_2)** - Cubic cell is maintained when heating under N_2 with an increase in lattice parameter **Carbonate incorporation** - No loss of carbonate in TGA	30-32 S cm^{-1} (650 °C)
$Sr_{0.5}Ba_{0.5}FeO_{3-\delta}$	Cubic (1100 °C with anneal at 350 °C)	**Stability in low p(O_2)** - Small peaks associated with possible oxygen vacancy ordering **Carbonate incorporation**	45 S cm^{-1} (442 °C)

		- Loss of CO_2 in TGA suggests possible carbonate incorporation	
$Sr_{0.5}Ba_{0.5}Fe_{1-x}S_xO_{3-\delta}$ where x=0.025,0.05,0.075	Cubic (1100 °C with anneal at 350 °C)	**Stability in low p(O_2)** - Cubic cell is maintained with an increase in unit cell - Asymmetry present in XRD data for x=0.025 suggesting multiple similar perovskite phases **Carbonate incorporation** - Loss of CO_2 in TGA suggests possible carbonate incorporation	16-32 S cm^{-1} (420-460 °C)
$Sr_{0.5}Ba_{0.5}Fe_{1-x}P_xO_{3-\delta}$ where x=0.025, 0.05 and 0.075	Cubic (1100 °C with anneal at 350 °C)	**Stability in low p(O_2)** - Cubic cell is maintained with an increase in unit cell - Asymmetry present in XRD data for x=0.075 suggesting multiple similar perovskite phases **Carbonate incorporation** - Loss of CO_2 in TGA suggests possible carbonate incorporation	6-20 S cm^{-1} (442 °C)
$BaFe_{1-y}O_{3-\delta}$ where y=0.8, 0.9 and 1	Cubic (900 °C 12h)	- Synthesis of phases are dependent on temperature and synthesis time	-

	Hexagonal (850 °C 48h)		
$BaFe_{1-x}S_xO_{3-\delta}$ where y=0.025 and 0.05	Hexagonal (800/850 °C 48h)	- Synthesis of phases are dependent on temperature and synthesis time	-

5 Oxyanion incorporation into Ruddlesden-Popper systems

5.1 Introduction

Research into cathode materials for solid oxide fuel cell applications has been dominated by perovskite materials, while perovskite type materials with the Ruddlesden-Popper structure have been less widely studied. More recently, research into Ruddlesden-Popper systems has grown due to the flexible oxide ion defect characteristics of this structure, where the accommodation of either oxide ion vacancies or oxide ion excess is possible. Additionally, Ruddlesden-Popper materials are appealing due to their high mixed oxide and electronic conductivity. The most widely studied systems are the n=1 Ruddlesden-Popper (K_2NiF_4 structure) systems e.g. $La_2NiO_{4+\delta}$.[54–56,75,163] Less widely studied are the n > 1 Ruddlesden-Popper systems as there is generally greater difficulty in synthesising these phases. Although more challenging to synthesise, lanthanum nickelates $La_3Ni_2O_{7-\delta}$ and $La_4Ni_3O_{10-\delta}$ have been prepared by Amow et al.[75] and show improved thermal stability, electrical conductivity and electrode performance compared to $La_2NiO_{4+\delta}$.

In the previous chapter it has been shown that perovskite materials can be successfully synthesised with incorporation of oxyanion groups, where introduction of such groups leads to stabilisation of oxide ion vacancies around the oxyanion dopant. Such doping strategies can be extended to Ruddlesden-Popper type compounds, where previous studies have shown sulfate[164,114], carbonate[112] and combined sulfate/carbonate[115] incorporation into $Sr_4Fe_3O_{10-\delta}$, although in most cases, evacuated sealed tubes were required to allow the high temperature synthesis without loss of the oxyanion group. Such sealed tube synthesis is not practical for applications, and therefore here the possible synthesis of such doped phases in air was investigated.

This work showed that the successful synthesis of oxyanion doped $Sr_4Fe_3O_{10-\delta}$ materials through solid state synthesis in air was possible.[164,165] A structural diagram showing the incorporation of oxyanions is given in Figure 52. A key focus of this work was to extend the doping strategies and synthesis methods highlighted in chapter 4 and apply these to Sr-Fe-O containing Ruddlesden-Popper materials. Again, focusing not only on utilising oxyanion dopants to improve the performance of these materials for SOFC applications, but also investigating the effect on structure.

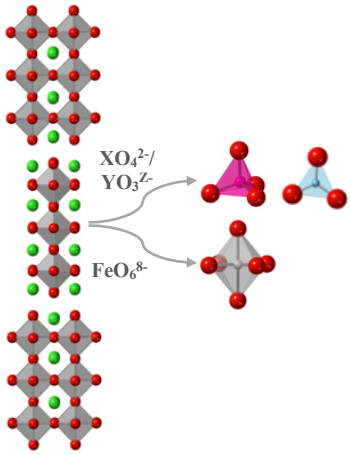

Figure 52. Structure of the n=3 Ruddlesden-Popper system, $Sr_4Fe_3O_{10-\delta}$, showing incorporation of oxyanions XO_4^{2-} (where X=S/ Cr) and YO_3^{z-} (where Y = C/ B and Z= 2/3 respectively)

5.2 Experimental

The $Sr_4Fe_{3-x}(S/Cr/B)_xO_{10-\delta}$ phases were prepared through solid state synthesis using $SrCO_3$, Fe_2O_3 and one of the following: $(NH_4)_2SO_4$, Cr_2O_3 or H_3BO_3. Samples were intimately ground before heating to 950 °C (4 °C/ min) for 12 hours. Samples were then ball milled at 350 rpm for 1h (Fritsch Pulverisette 7 planetary Mill, zirconia balls and container) and reheated to 1000 °C. A further grinding of the samples was carried out before heating to 1050 °C for 12 hours. Samples were finally annealed at 350 °C for 12 h in air in order to ensure

maximum oxygen content. Additionally, samples were heated in dry/ wet N_2 in order to test their stability under lower $p(O_2)$, as well as testing potential suitability for use in proton conducting solid oxide fuel cells. Samples were heated to 800 °C for 12 h with a heating ramp rate of 4 °C/ min for both dry and wet N_2. On cooling dry N_2 samples were cooled at 4 °C/ min and wet N_2 samples cooled at 50 °C/ h.

Powder X-ray diffraction (Panalytical Empyrean diffractometer equipped with a Pixcel 2D detector (Cu Kα radiation)) was used to determine lattice parameters and phase purity. GSAS suite of programs was used to carry out Rietveld refinements [136]. Space group *I*4/*mmm* was used for all Ruddlesden-Popper samples with an additional cubic perovskite phase ($Pm\bar{3}m$) included as a minor impurity. Lattice parameters and sample displacement parameters were refined for all samples. Anisotropic broadening is present in the XRD data, therefore uniaxial strain models were included into the refinements. For all refinements, atom positions and oxygen occupancies were refined. For $Sr_4Fe_{3-x}Cr_xO_{10-\delta}$, Fe/Cr occupancies were fixed and not refined (due to the virtually identical scattering factors of Fe and Cr) where for other Ruddlesden-Popper phases, occupancies were refined. Atomic displacement parameters were constrained for Sr, Fe/Cr/S/B and O sites and fixed at realistic values due to high correlation with site occupancies.

Neutron diffraction data were collected on the HRPD diffractometer at ISIS neutron and muon source.

TGA (Netzch STA 449 F1 Jupiter Thermal Analyser with mass spectrometry attachment) were carried out under N_2 up to 1000 °C.

The ^{57}Fe Mössbauer spectra was carried out at 298 K in constant acceleration mode using approximately 25 mCi Co/Rh source. The ^{57}Fe Mössbauer spectroscopy was performed by Frank Berry and researchers from the Instituto de Química Física “Rocasolano”.

Cr K-edge X-ray absorption spectroscopy (XAS) spectra were collected for standard materials, $LaCrO_3$ and $SrCrO_4$ and $Sr_4Fe_{2.6}Cr_{0.4}O_{10-\delta}$ on beamline B18 at Diamond Light Source (Rutherford Appleton Lab, Harwell, UK). The Athena Software package was used for processing of data.[138]

Four probe dc conductivity measurements were carried out for all samples. Initially, powders were ball milled (350 rpm for 1 h, Fritsch Pulverisette 7 planetary Mill), before pressing into pellets. Pellets were sintered at 1050 °C for 12 h before Pt electrodes were attached to the pellets with Pt paste. Finally, pellets were heated to 900 °C for 1 h to ensure good contact. The pellets were finally annealed at 350 °C for 12 h.

5.3 $Sr_4Fe_{3-x}S_xO_{10-\delta}$

5.3.1 X-ray diffraction results

X-ray diffraction (XRD) studies for the $Sr_4Fe_{3-x}S_xO_{10-\delta}$ systems indicated that upon doping with sulfate, the n = 3 Ruddlesden-Popper structure is formed for x = 0.15 - 0.3 (Figure 53). In comparison when attempting to synthesise the undoped $Sr_4Fe_3O_{10-\delta}$ system, no n=3 phase was obtained, but rather a mixture of $Sr_3Fe_2O_{7-\delta}$ and $SrFeO_{3-\delta}$ was observed. This can be more clearly seen in Figure 53b for the range $2\theta \approx 40 - 45°$, where a significant difference in the XRD patterns can be observed between the undoped (x = 0) and the sulfate doped samples. Thus sulfate is shown to successfully stabilise the n = 3 Ruddlesden-Popper system, further illustrating the potential of oxyanion doping to design new potential SOFC materials.

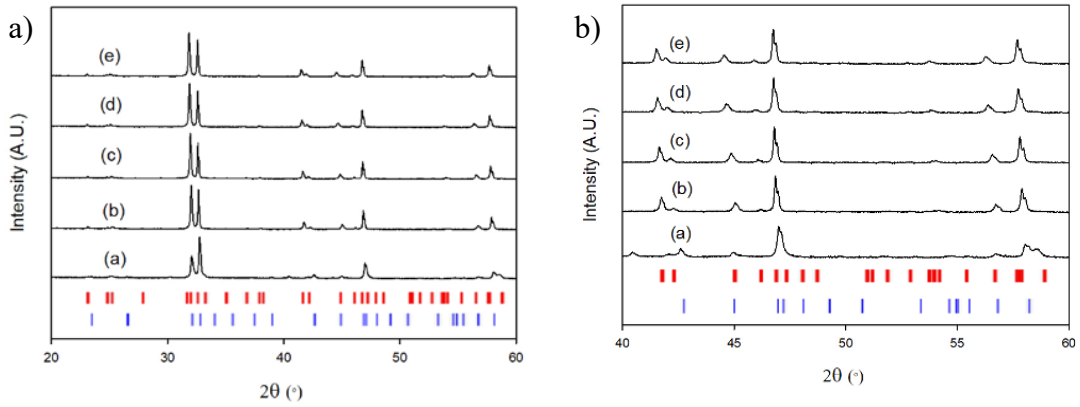

Figure 53. (a) X-ray diffraction patterns for $Sr_4Fe_{3-x}S_xO_{10-\delta}$ where a) x = 0, b) x = 0.15, c) x = 0.2, d) x = 0.25 and e) x = 0.3. (b) Expanded region to illustrate differences between x = 0, and x > 0 samples. The two phases are indicated by red ($Sr_4Fe_{3-x}S_xO_{10-\delta}$, Ruddlesden-Popper n=3) and blue ticks ($Sr_3Fe_2O_{7-x}$, Ruddlesden-Popper n=2)

Using the XRD data, Rietveld refinements were performed on samples, both as prepared and after heating in N_2 (an example fit is shown in Figure 54). The initial refinements indicated a low Fe occupancy in the middle perovskite layer consistent with partial SO_4^{2-} in this layer. Adding S to this site and refining the Fe/S occupancies (with the constraint that the total occupancy was 1) gave good agreement with the expected values (Table 11). Due to asymmetric broadening in the X-ray diffraction data, uniaxial strain was included. A possible explanation for the asymmetric broadening could be the presence of stacking faults along [001], which is common for Ruddlesden-Popper systems [166]. A small amount (< 2.5 wt%) of perovskite impurity was also included in the final refinement.

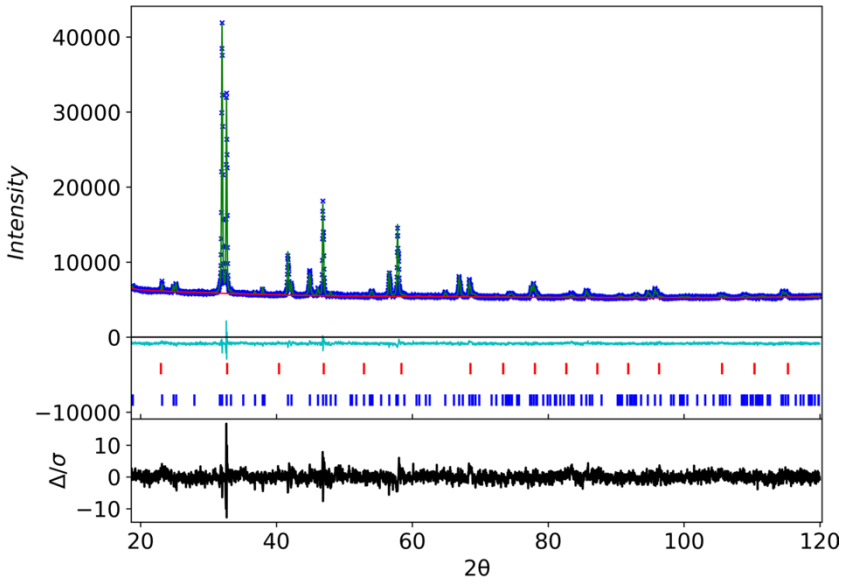

Figure 54. Observed (dark blue), calculated (green) and difference (light blue) XRD profiles for $Sr_4Fe_{2.8}S_{0.2}O_{10-\delta}$. The two phases are indicated by blue (Ruddlesden-Popper, *I*4/*mmm*) and red ticks (perovskite $Pm\bar{3}m$)

From the calculated lattice parameters, it can be seen that there is an approximate linear increase between x = 0.15 - 0.25 (Figure 55). The linear trend does not continue for x = 0.3, suggesting the solubility limit of sulfate in the structure is between x = 0.25 and 0.3. While at first glance this increase in cell volume might be surprising given the smaller size of S^{6+} compared to Fe^{3+}/ Fe^{4+}, it can be correlated with an increase in the proportion of the larger Fe^{3+} upon doping with sulfate (confirmed by ^{57}Fe Mössbauer spectroscopy (see later)). Similar cell expansions due to reduction in the average oxidation state of the transition metal on oxyanion doping has been observed in related perovskite systems [159]. This reduction in average Fe oxidation state can be correlated with the sulfate group helping to stabilise oxide ion vacancy defects.

In addition to sulfate doping, phosphate doping of $Sr_4Fe_3O_{10-\delta}$ was also investigated. However this dopant did not give the desired n = 3 Ruddlesden-Popper system, but rather a mixture of $Sr_3Fe_2O_{7-\delta}$, $SrFeO_{3-\delta}$, $Sr_5(PO_4)_3(OH)$ and $SrCO_3$ was formed.

Table 11. Lattice parameters (space group *I*4/*mmm*) and middle Fe layer site occupancy factors for $Sr_4Fe_{3-x}S_xO_{10-\delta}$ (heating in air). The impurity phase, $SrFeO_{3-\delta}$, was refined in the cubic space group, $Pm\bar{3}m$

		$Sr_4Fe_{3-x}S_xO_{10-\delta}$			
S (x)		0.15	0.2	0.25	0.3
a (Å)		3.8735(1)	3.8768(1)	3.8793(1)	3.8787(1)
c (Å)		28.1682(7)	28.2444(6)	28.3476(7)	28.3682(10)
V (Å^3)		422.64(2)	424.49(2)	426.60(2)	426.77(3)
Rwp (%)		1.80	1.71	1.74	1.97
Rexp (%)		1.30	1.29	1.31	1.30
Fe occupancy (middle perovskite layer)		0.82(3)	0.81(3)	0.73(3)	0.66(4)
S occupancy (middle perovskite layer)		0.18(3)	0.19(3)	0.27(3)	0.34(4)
Perovskite ($SrFeO_3$)	a (Å)	3.8638(4)	3.8659(4)	3.8816(4)	3.8725(3)
	V (Å^3)	57.68(2)	57.78(2)	58.48(2)	58.07(2)
Weight percentage (%)	Ruddlesden-Popper	98.3	98.6	97.9	97.6
	Perovskite	1.7	1.4	2.1	2.4

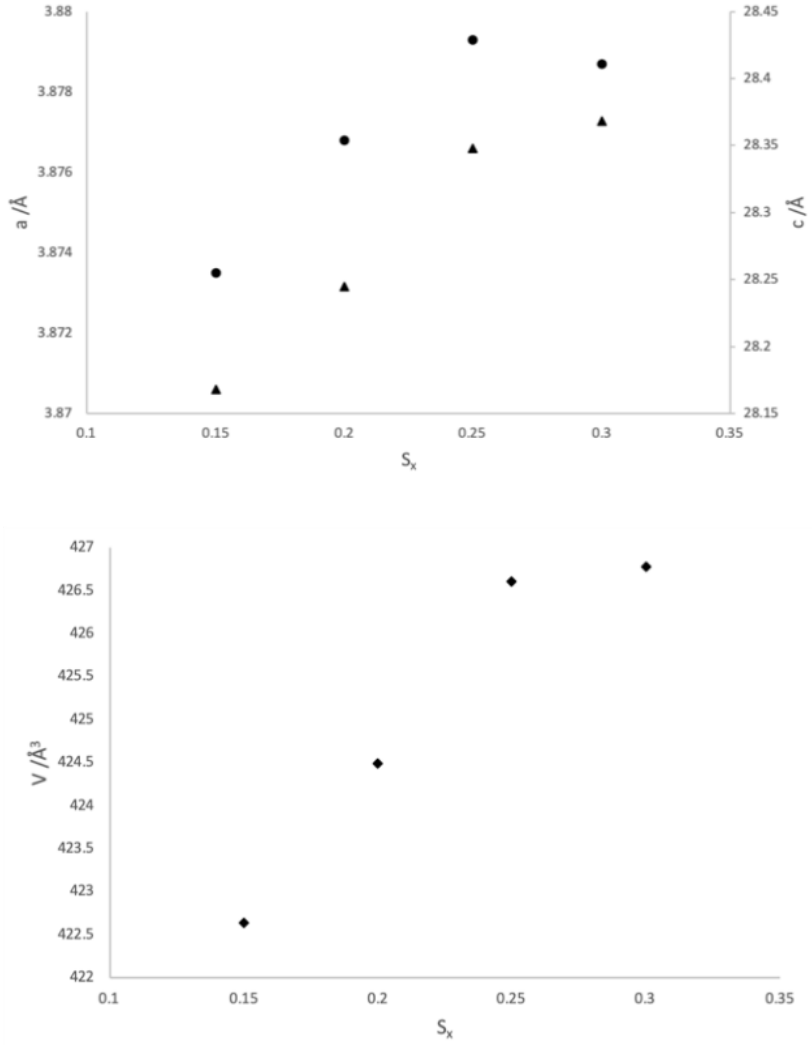

Figure 55. Variation of lattice parameters with sulfate content, x ($Sr_4Fe_{3-x}S_xO_{10-\delta}$), where a = ●, c = ▲ and V = ◆

5.3.2 Neutron diffraction results

$Sr_4Fe_{2.75}S_{0.25}O_{10-\delta}$ and $Sr_4Fe_{2.7}S_{0.3}O_{10-\delta}$ samples were also examined by neutron diffraction (ND). As observed in the XRD data $SrFeO_{3-\delta}$ impurity peaks were present in the ND data with the additional observation of extra peaks due to the n=2 Ruddlesden-Popper phase, $Sr_3Fe_2O_{7-\delta}$. The higher resolution of the ND data suggested the need to include two similar n=3 Ruddlesden-Popper phases to give a good fit to the data. The Ruddlesden-Popper phases were fixed to have the same coordinates, atomic displacement parameters, site occupancies

and strain parameters. The Fe and S occupancies were refined and constrained to a total value of 1. Lattice parameters for the different Ruddlesden-Popper phases were refined separately. Additionally, due to anisotropic reflection broadening in the neutron data, uniaxial strain was included in the refinements. As suggested in section 5.3.1 this could be possibly due to the presence of stacking faults.

Rietveld refinement profiles can be found in Figure 56 and structural data in Table 12 and Table 13. From the ND data the two n=3 Ruddlesden-Popper phases are found to have different lattice parameters, suggesting the presence of phases with a small difference in composition. ND data suggests occupancy of sulfate in the middle perovskite layer as expected, but occupancies for sulfate were found to be higher than the predicted values. Occupancy of sulfate in the middle perovskite layer is also supported by the largest oxygen vacancy located on O1. This suggests oxygen vacancies are predominately located surrounding sulfate. The higher apparent sulfate content may suggest some additional carbonate on this site, with perhaps a carbonate rich shell, which may explain the observation of two n=3 Ruddlesden-Popper phases.

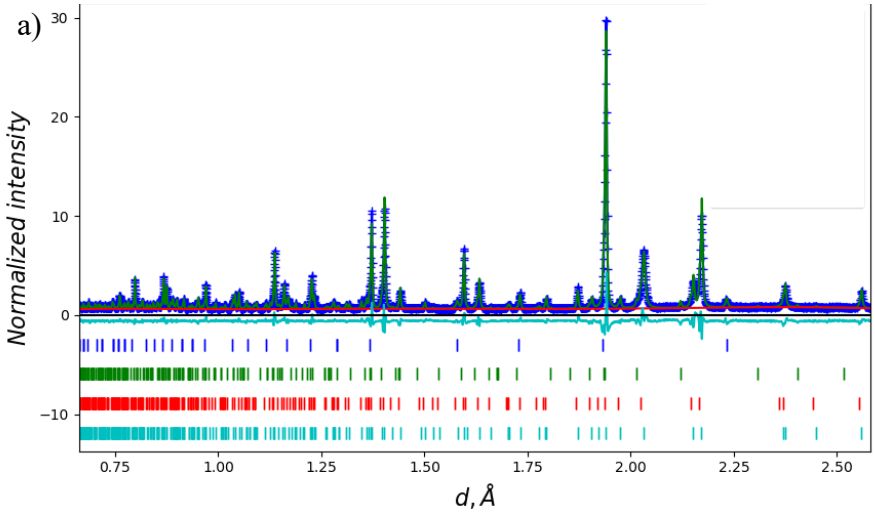
a)
Normalized intensity
30
20
10
0
−10
0.75
1.00
1.25
1.50
1.75
2.00
2.25
2.50
d, Å

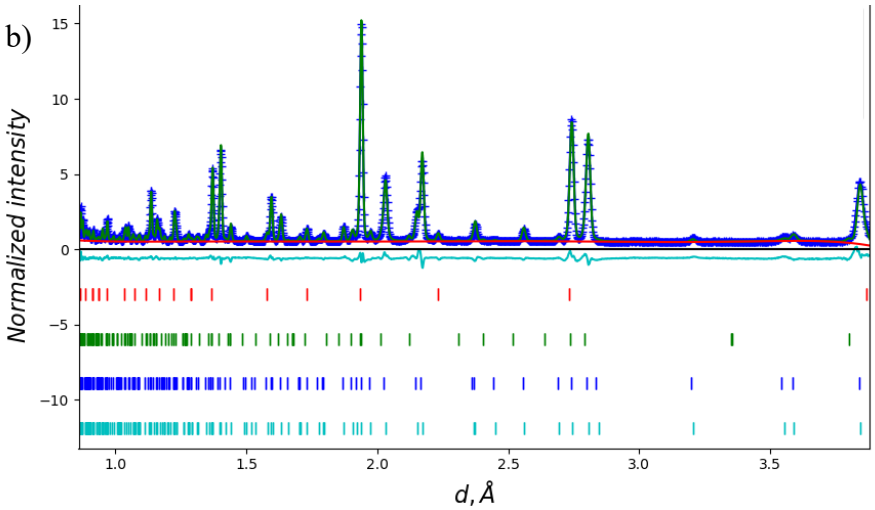
b)
Normalized intensity
15
10
5
0
−5
−10
1.0
1.5
2.0
2.5
3.0
3.5
d, Å

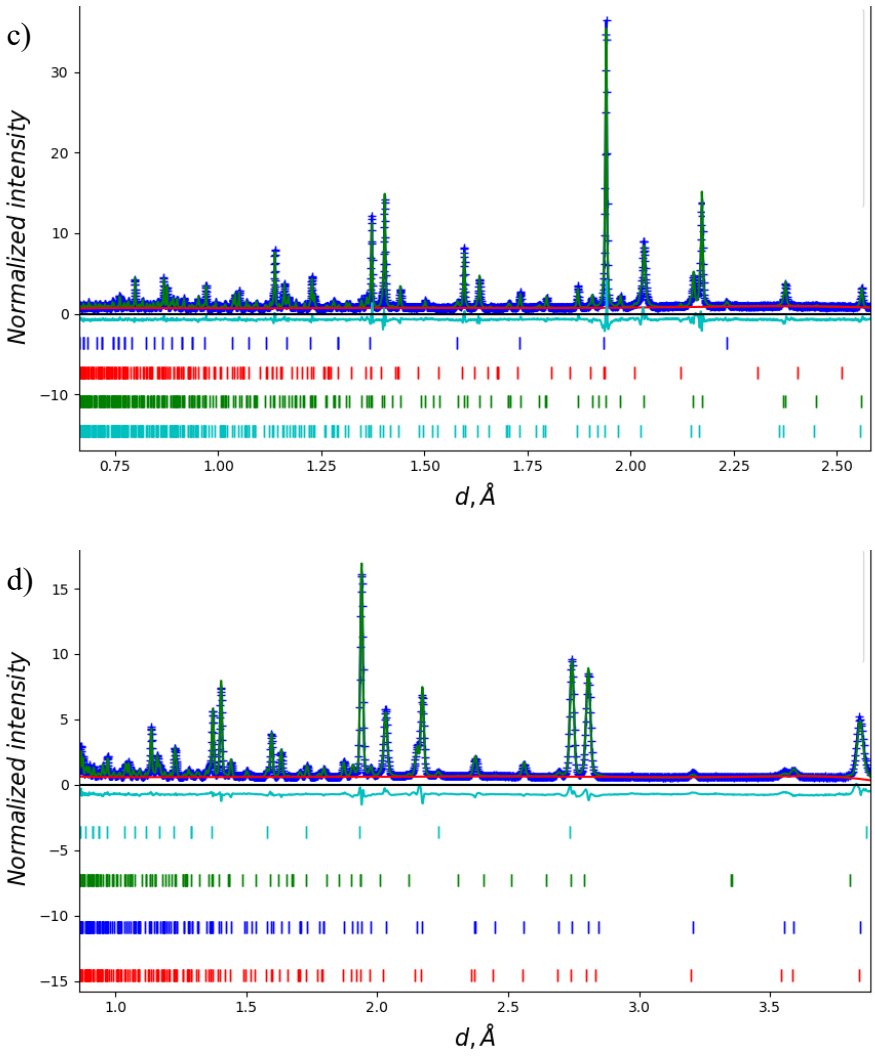

Figure 56. Observed (dark blue), calculated (green) and difference (light blue) neutron diffraction profiles for a) $Sr_4Fe_{2.75}S_{0.25}O_{10-\delta}$ (Bank 1), b) $Sr_4Fe_{2.75}S_{0.25}O_{10-\delta}$ (Bank 2), c) $Sr_4Fe_{2.7}S_{0.3}O_{10-\delta}$ (Bank 1) and d) $Sr_4Fe_{2.7}S_{0.3}O_{10-\delta}$ (Bank 2). Phases (coloured ticks) are presented from top to bottom as $SrFeO_{3-\delta}$, $Sr_3Fe_2O_{7-\delta}$, Ruddlesden-Popper phase 1 and Ruddlesden-Popper phase 2.

Table 12. Refined structural parameters for $Sr_4Fe_{2.62}S_{0.38}O_{8.96}$ with two tetragonal Ruddlesden-Popper phases refined with space group *I*4/*mmm*. Additional impurity phases tetragonal $Sr_3Fe_2O_{7-\delta}$ (*I*4/*mmm*) and $SrFeO_{3-\delta}$ ($Pm\bar{3}m$) were included in the room temperature neutron diffraction data.

	Ruddlesden-Popper Phases		**$Sr_3Fe_2O_7$**	**$SrFeO_3$**
	Phase 1	**Phase 2**		
a (Å)	3.87400(12)	3.87959(4)	3.86870(48)	3.86616(24)
c (Å)	28.33053(154)	28.44151(49)	20.13583(250)	-
V (Å^3)	425.18(3)	428.08(1)	301.37(7)	57.79(1)
Weight Percent (%)	20.0	71.3	3.8	4.9
R_{wp}		**R_{exp}**		**GOF**
6.34%		1.35%		4.72

Ruddlesden-Popper

	x	y	z	Occ	U_{iso}
Sr1	0.0000	0.0000	0.4263(1)	1.00	0.0117(5)
Sr2	0.0000	0.0000	0.2978(1)	1.00	0.0116(5)
Fe1	0.0000	0.0000	0.0000	0.62(1)	0.0089(10)
S1	0.0000	0.0000	0.0000	0.38(1)	0.0089(10)
Fe2	0.0000	0.0000	0.1428(1)	1.00	0.0063(3)
O1	0.0000	0.5000	0.0000	0.64(1)	0.0645(34)
O2	0.0000	0.0000	0.0636(1)	0.91(1)	0.0335(17)
O3	0.0000	0.5000	0.1375(1)	1.00	0.0080(4)
O4	0.0000	0.0000	0.2106(1)	0.93(1)	0.0073(10)

Table 13. Refined structural parameters for $Sr_4Fe_{2.61}S_{0.39}O_{8.92}$ with two tetragonal Ruddlesden-Popper phases refined with space group *I*4/*mmm*. Additional impurity phases tetragonal $Sr_3Fe_2O_7$ (*I*4/*mmm*) and $SrFeO_3$ ($Pm\bar{3}m$) were included in the room temperature neutron diffraction data.

	Ruddlesden-Popper Phases		**$Sr_3Fe_2O_7$**	**$SrFeO_3$**
	Phase 1	**Phase 2**		
a (Å)	3.88009(3)	3.87441(15)	3.87451(100)	3.86684(33)
c (Å)	28.44646(39)	28.33029(168)	20.09681(463)	-
V (Å^3)	428.26(1)	425.27(3)	301.69(14)	57.82(2)
Weight Percent (%)	79.6	15.6	1.7	3.1
R_{wp}		**R_{exp}**	**GOF**	
6.12%		1.31	4.67	

Ruddlesden-Popper

	x	y	z	Occ	U_{iso}
Sr1	0.0000	0.0000	0.4262(1)	1.00	0.0141(5)
Sr2	0.0000	0.0000	0.2978(1)	1.00	0.0121(5)
Fe1	0.0000	0.0000	0.0000	0.61(1)	0.0109(9)
S1	0.0000	0.0000	0.0000	0.39(1)	0.0109(9)
Fe2	0.0000	0.0000	0.1429(1)	1.00	0.0072(3)
O1	0.0000	0.5000	0.0000	0.63(1)	0.0644(32)
O2	0.0000	0.0000	0.0638(1)	0.90(1)	0.0338(16)
O3	0.0000	0.5000	0.1374(1)	1.00	0.0087(4)
O4	0.0000	0.0000	0.2106(1)	0.93(1)	0.0084(9)

5.3.3 Stability in low p(O_2)

The stability of $Sr_4Fe_{3-x}S_xO_{10-\delta}$ samples were tested in N_2 to 800 °C. The results indicated that these n = 3 Ruddlesden-Popper phases appear to remain stable under these conditions (Figure 57) for the sulfate doped phases, x = 0.2 - 0.3. For lower levels of sulfate some small changes are observed in the XRD patterns (Figure 57). This might be due to the partial break down of the structure to produce the n = 2 Ruddlesden-Popper system, $Sr_3Fe_2O_{7-\delta}$, and further work is required to investigate this.

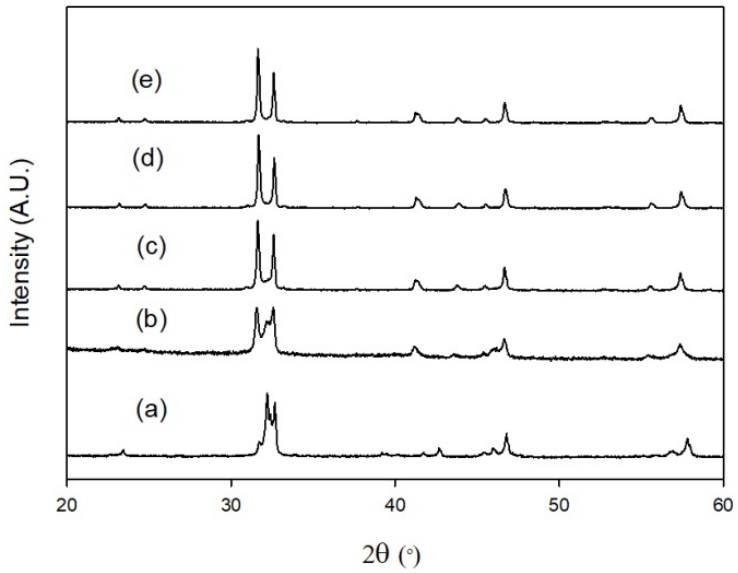

Figure 57. X-ray diffraction patterns for $Sr_4Fe_{3-x}S_xO_{10-\delta}$ after heat treatment in N_2 to 800 °C, where a) x = 0, b) x = 0.15, c) x = 0.2, d) x = 0.25 and e) x = 0.3. Results show significant changes for $x \leq 0.15$.

Overall an increase in lattice parameters is observed for the N_2 treated samples compared to the samples synthesised in air (Figure 58). This is as predicted due to the reduction of Fe^{4+} to the larger Fe^{3+} which can be seen by the change in colour of samples from black to brown. For these N_2 treated samples, we now see the expected general decrease in cell volume with sulfate content (due to the smaller size of S^{6+} versus Fe^{3+}), as the Fe oxidation state is now the same (3+) in each sample.

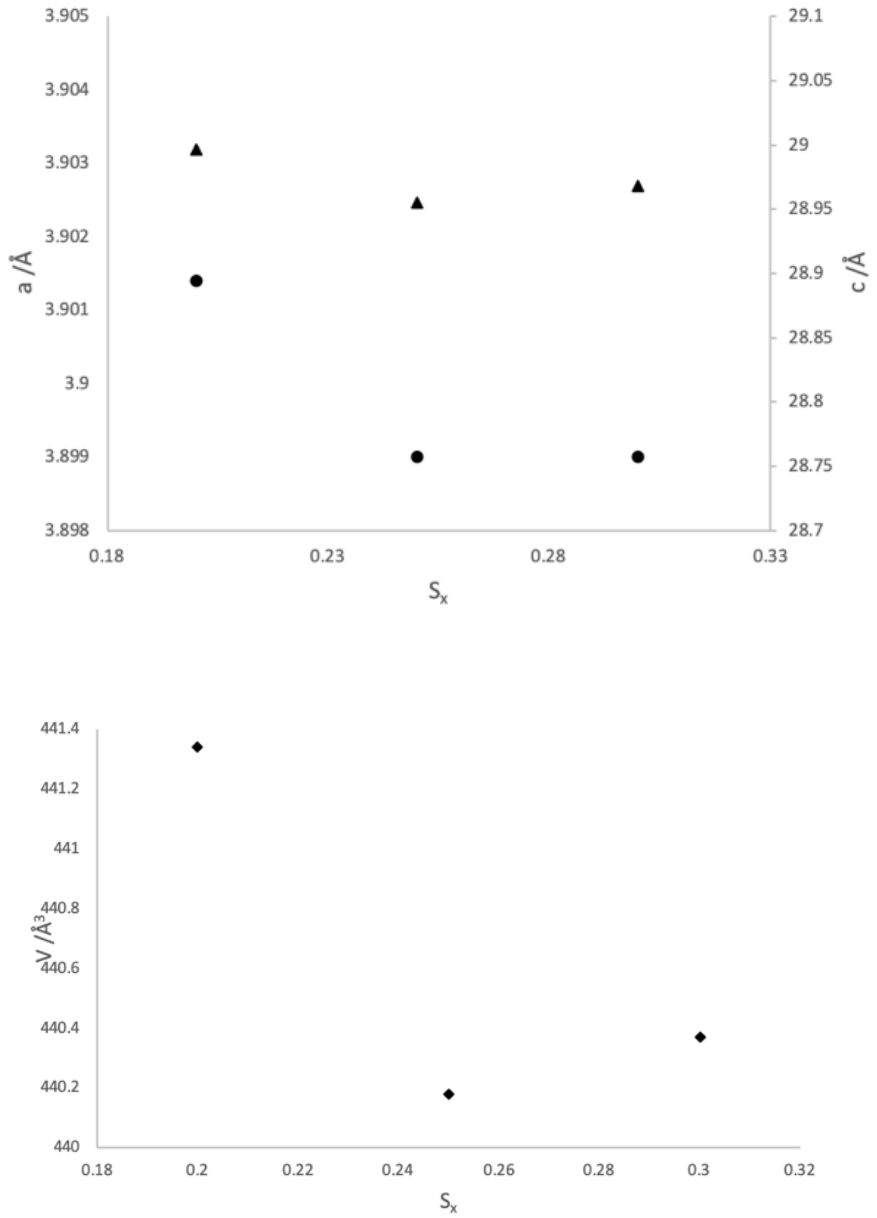

Figure 58. Variation of lattice parameters with sulfate content, x ($Sr_4Fe_{3-x}S_xO_{10-\delta}$ samples N_2 to 800 °C), where a = ●, c = ▲ and V = ◆

5.3.4 Stability in wet N_2

In order to test suitability for potential use in proton conducting solid oxide fuel cells, the stability of $Sr_4Fe_{3-x}S_xO_{10-\delta}$ in wet N_2 was investigated. Upon heating in wet N_2 broad peaks are observed in the XRD patterns (Figure 59). By comparing the air and wet N_2 treated

samples for $Sr_4Fe_{2.75}S_{0.25}O_{10-\delta}$, it can be observed that there is growth of the (002) peak (Figure 60) in the wet N_2 sample. This is in line with previous reports [167–171] of water incorporation into the interstitial sites in Ruddlesden-Popper systems.

Incorporation of water into $Sr_{n+1}Fe_nO_{3n+1}$ systems has previously been reported where $Sr_4Fe_3O_{10-\delta}$ has been shown to absorb water when exposed in ambient air or dipped in distilled water.[171] Water intercalation into $Sr_4Fe_3O_{10-\delta}$ results in a mixture of hydrated phases with different water contents in addition to the original Ruddlesden-Popper phase. Due to the broad peaks observed for the sulfate doped wet N_2 samples (Figure 59), it is predicted a range of hydrated phases, with different water contents, have also formed in the sulfate doped samples studied here.

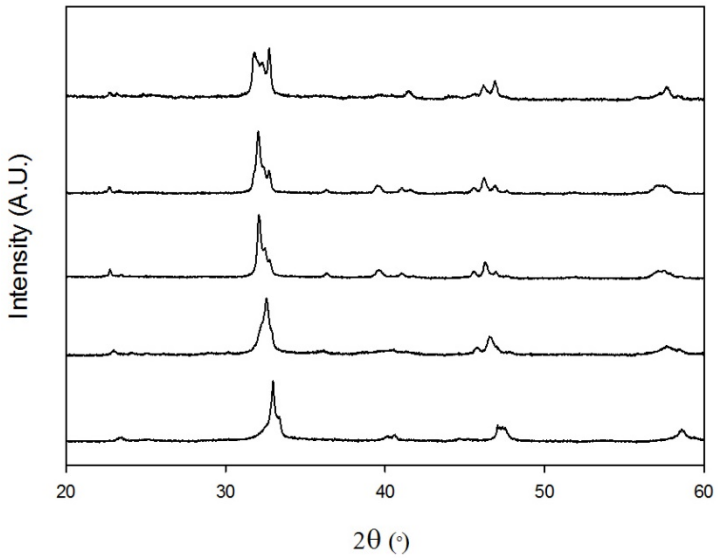

Figure 59. X-ray diffraction patterns for $Sr_4Fe_{3-x}S_xO_{10-\delta}$ after heat treatment in wet N_2 to 800 °C, where a) x=0, b) x=0.15, c) x=0.2, d) x=0.25 and e) x=0.3

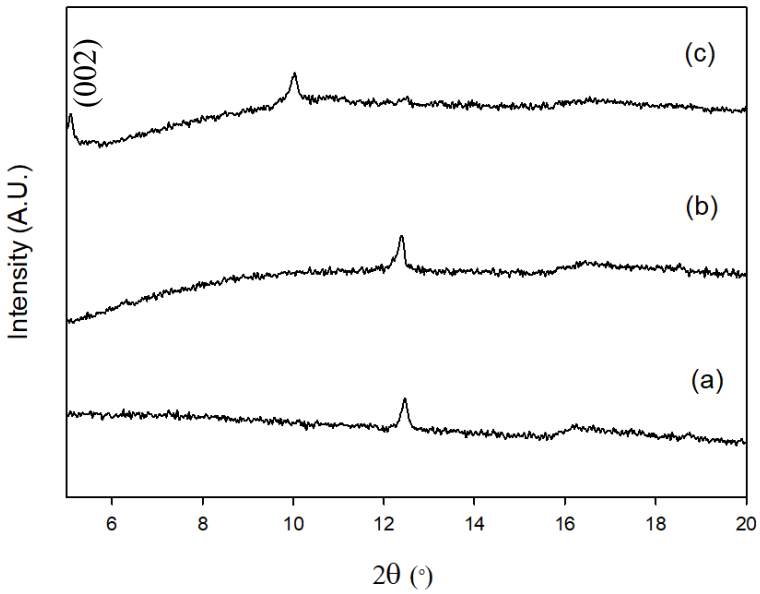

Figure 60. X-ray diffraction patterns for $Sr_4Fe_{2.75}S_{0.25}O_{10-\delta}$ after a) heat treatment in air, b) heat treatment in dry N_2 to 800 °C, c) heat treatment in wet N_2 to 800 °C

After heat treatment in wet N_2, TGA analysis of these hydrated $Sr_4Fe_{2.75}S_{0.25}O_{10-\delta}$ phases was carried out under N_2 up to 1000 °C, which showed that water is released over a range of temperatures in multiple steps (Figure 61). Due to the large temperature range for the loss of water in $Sr_4Fe_{2.75}S_{0.25}O_{10-\delta}$ this suggests water could not only be surface water, but also water incorporated into the structure. Using the %mass loss, the water content can be calculated at ≈ 2.2 moles of water per formula unit for $Sr_4Fe_{2.75}S_{0.25}O_{10-\delta}$. Only a small amount of the calculated water content will be associated with surface water therefore from the calculated water content it is predicted water would be incorporated not only in vacant anion sites, but also in interstitial sites within the layers. Further work would be needed to investigate this.

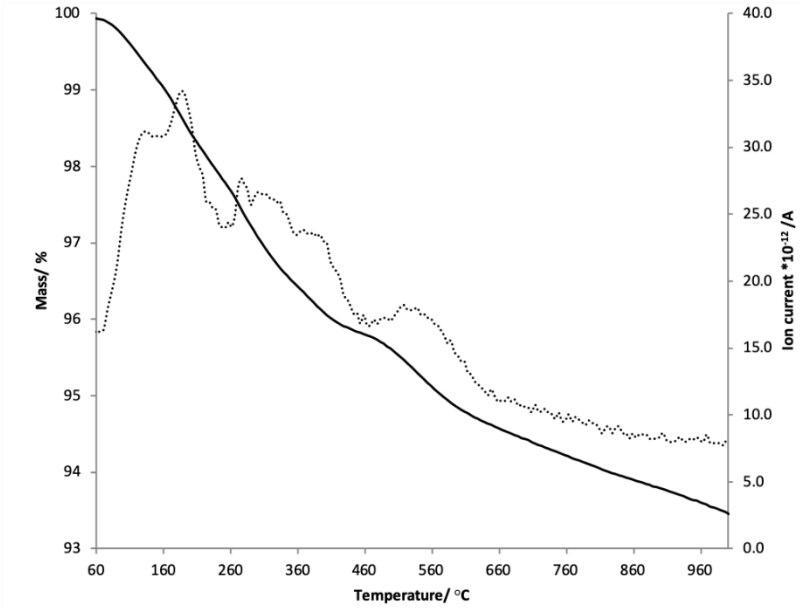

Figure 61. Plot of mass vs. temperature and ion current (for m/z = 18; H_2O) vs. temperature (under N_2) for $Sr_4Fe_{2.75}S_{0.25}O_{10-\delta}$ prepared in wet N_2. Solid lines indicate %mass and dashed lines indicate ion current.

In order to test the reversibility of the incorporation of water, the water incorporated phases were heated to air to 1000 °C where the original Ruddlesden-Popper phase is obtained (Figure 62). This suggests these materials could be potential cathode materials for proton conducting solid oxide fuel cells. Further work would be needed to investigate this.

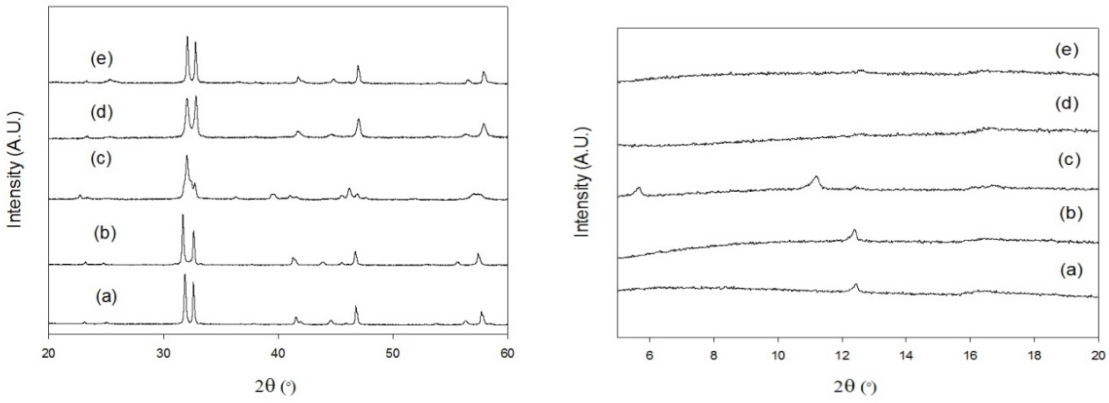

Figure 62. X-ray diffraction patterns for $Sr_4Fe_{2.75}S_{0.25}O_{10-\delta}$ after a) heat treatment in air, b) heat treatment in dry N_2 to 800 °C, c) heat treatment in wet N_2 to 800 °C, d) after TGA to 1000 °C and e) heat treatment in air to 1000 °C for 12 hours after heat treatment in wet N_2.

5.3.5 ^{57}Fe Mössbauer spectroscopy

^{57}Fe Mössbauer spectroscopy was carried out at 298 K for $Sr_4Fe_{2.85}S_{0.15}O_{10-\delta}$ and $Sr_4Fe_{2.7}S_{0.3}O_{10-\delta}$ (Figure 63 & Table 14). Previous studies of the perovskite system, $SrFeO_{3-\delta}$, reported chemical isomer shifts of $\delta \approx 0.15$ and 0.05 mm s^{-1} which are assigned to $Fe^{3.5+}$ and Fe^{4+} respectively [172–174]. In other work disproportionation of Fe^{4+} to $Fe^{3+}$and Fe^{5+} is observed for both Si^{4+} and Sn^{4+} doping of $SrFeO_{3-\delta}$ [111,175]. In the case of silicon doping of $SrFeO_{3-\delta}$, disproportionation of Fe^{4+} to Fe^{3+} ($\delta \approx 0.37$ mm s^{-1}) and Fe^{5+} ($\delta \approx -0.05$ mm s^{-1}) occurs with the addition of some of the Fe^{3+} in lower than octahedral coordination ($\delta \approx 0.18$ mm s^{-1}) [111]. In addition to the perovskite systems, disproportionation of Fe^{4+} is also observed in the Ruddlesden-Popper system, $Sr_4Mn_{3-x}Fe_xO_{10-\delta}$.[176]

Using the assignments described for the above perovskite and Ruddlesden-Popper systems, chemical isomer shifts $\delta \approx$ - 0.02 and 0.28/0.30 mm s^{-1} ($S_{0.15}$/ $S_{0.3}$) can be assigned to Fe^{5+} and Fe^{3+} respectively. Furthermore the chemical isomer shifts $\delta \approx 0.23$ mm s^{-1} ($S_{0.15}$) and 0.24/ 0.16 mm s^{-1} ($S_{0.3}$) can be assigned to Fe^{3+} in lower than octahedral coordination. This has previously been reported in $SrFe_{1-x}Si_xO_{3-\delta}$, where it has been reported that the substitution of the smaller Si^{4+} for Fe^{4+} results in the surrounding of Si^{4+} with the larger Fe^{3+}.[111] As a result it has been suggested that local strain is introduced, which is relieved by incorporating Fe^{5+}. A similar effect therefore appears to be present in these Ruddlesden-Popper systems, $Sr_4Fe_{3-x}S_xO_{10-\delta}$. Overall the data indicate that the amount of Fe^{3+} increases with sulfate content, which can be correlated with increased oxide ion vacancy defect incorporation and the observed increase in lattice parameters with increased sulfate content as previously discussed.

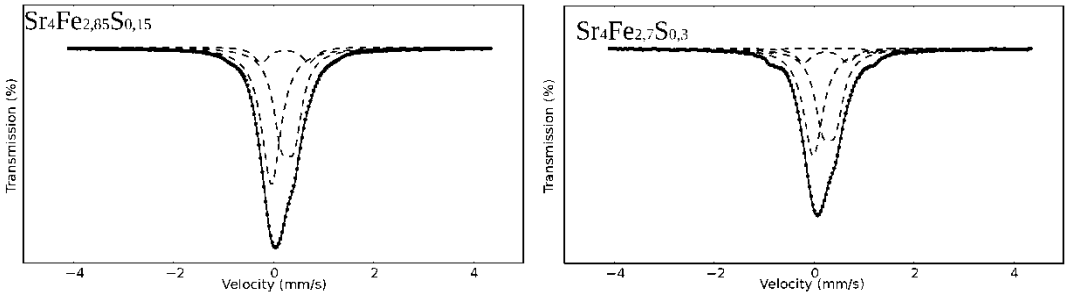

Figure 63. ^{57}Fe Mössbauer spectrum from $Sr_4Fe_{2.85}S_{0.15}O_{10-\delta}$ and $Sr_4Fe_{2.7}S_{0.3}O_{10-\delta}$ at 298 K

Table 14. ^{57}Fe Mössbauer parameters recorded from $Sr_4Fe_{2.85}S_{0.15}O_{10-\delta}$ and $Sr_4Fe_{2.7}S_{0.3}O_{10-\delta}$ at 298 K, where isomer shift and quadrupole splitting are given by δ and Δ respectively.

Compound	**Assignment**	**δ ± 0.01 (mms^{-1})**	**Δ ± 0.05 (mms^{-1})**	**Area ± 5% (%)**
$Sr_4Fe_{2.85}S_{0.15}O_{10-\delta}$	Fe^{5+}	-0.02	X	59
	Fe^{3+}	0.28	0.28	34
	Fe^{3+} in low coordination	0.23	0.91	7
$Sr_4Fe_{2.7}S_{0.3}O_{10-\delta}$	Fe^{5+}	-0.02	0.00	44
	Fe^{3+}	0.30	0.24	45
	Fe^{3+} in low coordination	0.24 0.16	0.90 2.04	9 2

5.3.6 Conductivity studies

The conductivity data for the $Sr_4Fe_{3-x}S_xO_{10-\delta}$ samples showed generally similar values for all samples (Figure 64). When comparing the conductivities of these Ruddlesden-Popper $Sr_4Fe_{3-x}S_xO_{10-\delta}$ samples with our previous results for perovskite-type $SrFe_{1-x}S_xO_{3-\delta}$ [159], the results show that higher conductivities are observed for the latter. This generally low electronic conductivity may be a problem for the utilization of these systems as SOFC cathodes.

However, it is likely that doping with other transition metals, e.g. Co, may lead to an enhancement of the conductivity, which is a future avenue of research.

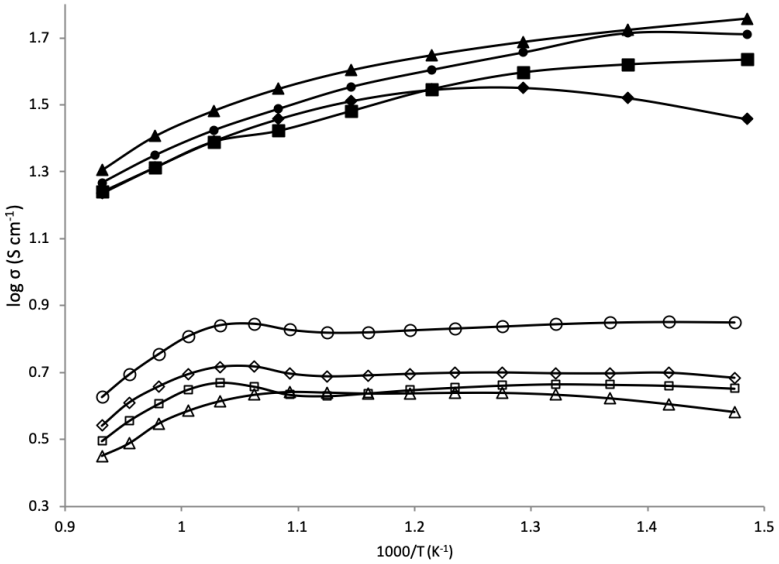

Figure 64. Plot of log σ vs. 1000/T for $Sr_4Fe_{3-x}S_xO_{10-\delta}$ where x = 0.15 (○), 0.2 (□), 0.25 (△), 0.3 (◇) and $SrFe_{1-x}S_xO_{3-\delta}$ [159] where x = 0 (●), 0.025 (■), 0.05 (▲), 0.075 (◆) in air

5.3.7 Conclusions

The present study demonstrates that sulfate can successfully be incorporated into the n = 3 Ruddlesden-Popper structure, $Sr_4Fe_3O_{10-\delta}$, allowing this phase to be successfully stabilised and hence synthesised (without sulfate, a mixture of n = 2 Ruddlesden-Popper and perovskite phases is observed). The successful synthesis is most likely related to the stabilisation of oxide ion vacancies by the sulfate, as previously proposed as key for other oxyanion doping of perovskite and related systems[177]. Sulfate doped materials are found to be stable in dry N_2 ($x \geq 0.2$) and the results indicate that these Ruddlesden-Popper materials can also incorporate water when heating in wet N_2. Although the conductivities are lower than sulfate doped perovskite $SrFeO_{3-\delta}$, the results further highlight the potential of oxyanion doping as a strategy to synthesise new phases of interest for solid oxide fuel cells.

*Work within this chapter has been published in ECS Transactions (A. Jarvis, F. J. Berry, J. F. Marco and P. R. Slater, ECS Trans., 2019, **91**, 1467–1476; DOI: 10.1149/09101.1467ecst)*

5.4 $Sr_4Fe_{3-x}Cr_xO_{10-\delta}$

Following the successful incorporation of sulfate into $Sr_4Fe_3O_{10-\delta}$, further investigation into tetrahedral oxyanion dopants was investigated e.g. chromate. This dopant was chosen due to the same tetrahedral coordination as sulfate, but larger ionic radii of Cr^{6+} compared to S^{6+}.

5.4.1 X-ray diffraction results

The X-ray diffraction data showed that Cr doping was successful in allowing the synthesis of the n=3, $Sr_4Fe_{3-x}Cr_xO_{10-\delta}$, phase. Figure 65 shows the XRD data for x=0, 0.2, 0.25, 0.3, 0.35, 0.4 samples: without Cr doping (x=0), no n=3 phase is obtained, but rather a mixture of $Sr_3Fe_2O_{7-x}$ and $SrFeO_{3-x}$ is obtained. On Cr doping, the successful formation of the n=3 Ruddlesden-Popper phase, $Sr_4Fe_{3-x}Cr_xO_{10-\delta}$, is observed (Figure 65a). The stabilisation of the n=3 phase can be more clearly seen in the 2θ range 40 to 60 ° (Figure 65b), where there is a clear difference in the diffraction data between the undoped and chromate doped phases. At higher Cr contents an extra impurity phase, $SrCrO_4$, is found in addition to the Ruddlesden-Popper type phase, indicating that the Cr solubility in the structure had been exceeded.

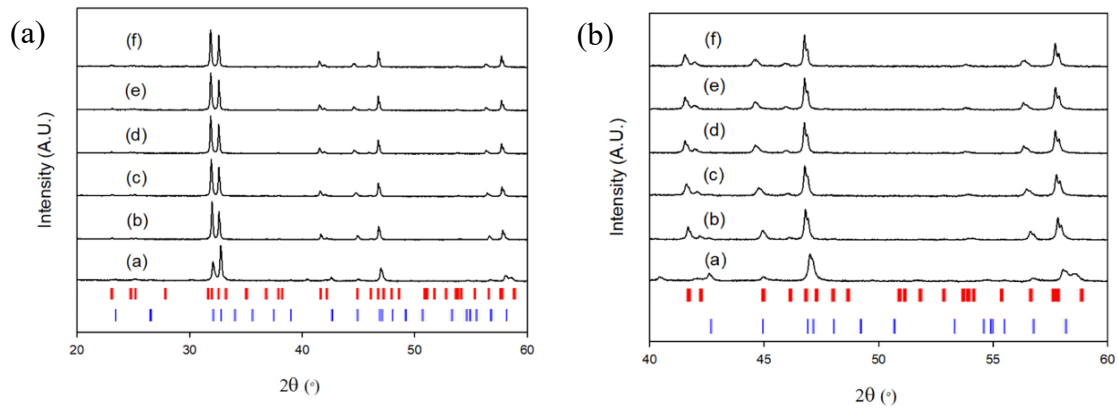

Figure 65. (a) X-ray diffraction patterns for $Sr_4Fe_{3-x}Cr_xO_{10-\delta}$ where a) x=0, b) x=0.2, c) x=0.25, d) x=0.3, e) x=0.35 and f) x=0.4. (b) Expanded region to illustrate differences between x = 0, and x > 0 samples. The two phases are indicated by red ($Sr_4Fe_{3-x}Cr_xO_{10-\delta}$, Ruddlesden-Popper n=3) and blue ticks ($Sr_3Fe_2O_{7-x}$, Ruddlesden-Popper n=2)

The structures of the resultant phases were evaluated through Rietveld refinement using the XRD data. Due to the X-ray scattering factors of chromium and iron being similar, the individual occupancy of these elements cannot be distinguished. Therefore the occupancy of all the transition metal (Fe/Cr) sites were set to 1. The refinements suggested the presence of a small amount of perovskite phase (≈ 3 - 7%), $Sr(Fe/Cr)O_{3-x}$, which was added as a second phase. Further improvements to the Rietveld refinement fits were achieved by including an anisotropic broadening model[178] to the refinements, suggesting the possibility of stacking faults within the structure (an example Rietveld fit is shown in Figure 66). The presence of small perovskite impurities and stacking faults are common for higher order Ruddlesden-Popper systems.[166,179]

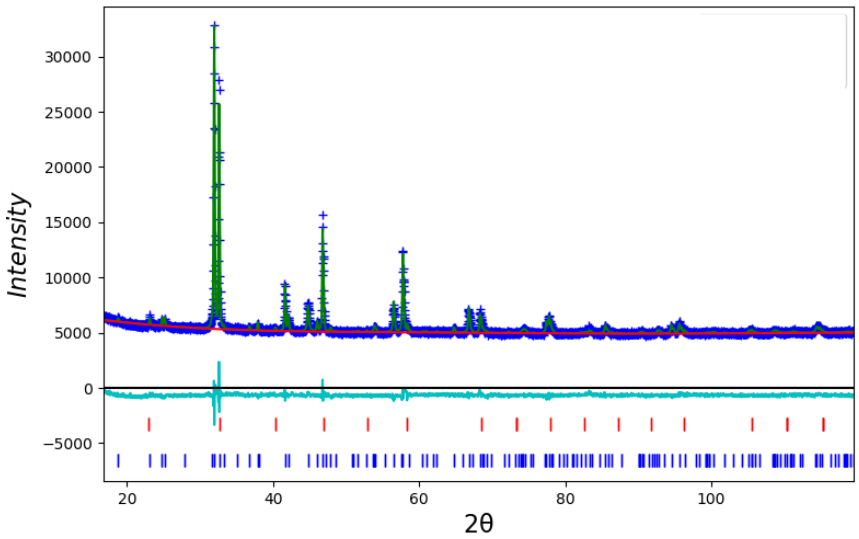

Figure 66. Observed (dark blue), calculated (green) and difference (light blue) XRD profiles for $Sr_4Fe_{2.75}Cr_{0.25}O_{10-\delta}$. The two phases are indicated by blue (Ruddlesden-Popper, *I*4/*mmm*) and red ticks (perovskite $Pm\bar{3}m$)

The final refined structural parameters are shown in Table 15. These data show an increase in unit cell parameters with increasing chromium content up to x=0.35 (Table 15, Figure 67). For x=0.35 and 0.4 a small additional impurity phase, $SrCrO_4$, was shown to also be present, supporting the conclusion from the cell parameter data, that the Cr doping limit is x<0.35.

Table 15. Lattice parameters, O occupancy and U_{iso} values from Rietveld refinement of XRD data for $Sr_4Fe_{3-x}Cr_xO_{10-\delta}$. Ruddlesden-Popper, $Sr_4Fe_{3-x}Cr_xO_{10-\delta}$, was refined with space group *I*4/*mmm*. Additional impurities phases included Perovskite-type $Sr(Fe/Cr)O_{3-\delta}$ and $SrCrO_4$.

		$Sr_4Fe_{3-x}Cr_xO_{10-\delta}$				
Cr (x)		0.2	0.25	0.3	0.35	0.4
a (Å)		3.8767(1)	3.8791(1)	3.8802(1)	3.8795(1)	3.8792(1)
c (Å)		28.2059(7)	28.2919(9)	28.3329(10)	28.3526(8)	28.3542(9)
V ($Å^3$)		423.91(2)	425.72(3)	426.58(3)	426.72(3)	426.67(3)
O occupancy		9.72	9.66	9.80	9.70	9.30
U_{iso}	Sr	0.0163	0.0153	0.0141	0.0149	0.0139
	Fe/Cr	0.0026	0.00241	0.0017	0.0031	0.0023
	O	0.0405	0.0480	0.0473	0.0360	0.0352
Rwp (%)		1.97	2.06	2.26	2.15	2.19
Rexp (%)		1.33	1.33	1.35	1.36	1.36
Perovskite ($SrFeO_3$)	a (Å)	3.8672(3)	3.8696(3)	3.8702(3)	3.8813(2)	3.8812(2)
	V ($Å^3$)	57.84(1)	57.94(1)	57.97(1)	58.47(1)	58.47(1)
Weight percentage (%)	Ruddlesden -Popper	97.2	97.1	96.5	93.1	89.3
	Perovskite	2.8	2.9	3.5	5.5	7.9
	$SrCrO_4$	-	-	-	1.5	2.8

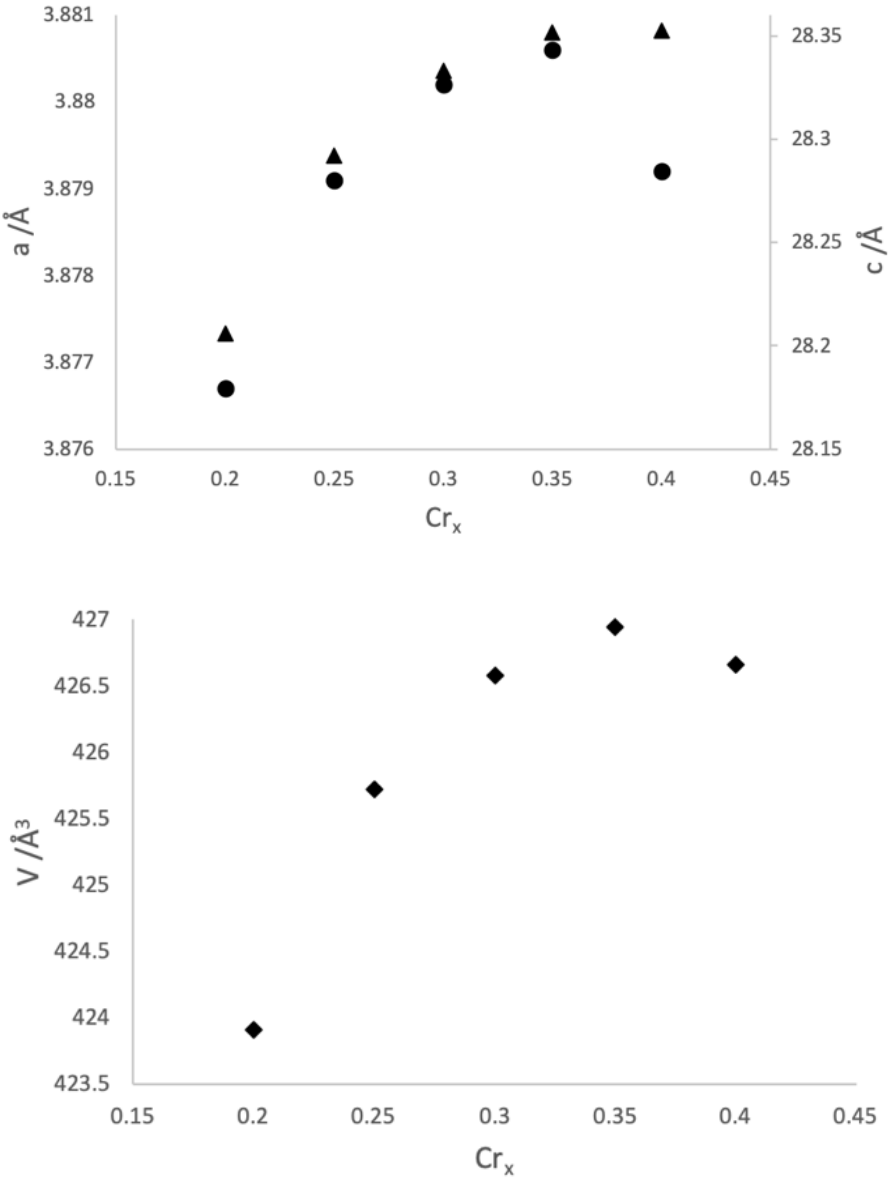

Figure 67. Variation of lattice parameters with Cr content (x) for $Sr_4Fe_{3-x}Cr_xO_{10-\delta}$, where a = ●, c =▲ and V = ◆. Error bars not included due to errors being smaller than the size of the data markers (errors given in Table 15)

5.4.2 Neutron diffraction results

ND data were collected and used for structure refinement as reported for $Sr_4Fe_{3-x}S_xO_{10-\delta}$ (section 5.3.2). A similar observation was observed, where in addition to reflections due to the tetragonal Ruddlesen-Popper phase, impurity phases $SrFeO_{3-\delta}$ and $Sr_3Fe_2O_{7-\delta}$ are present and

are included in the Rietveld refinements (Figure 68). Additionally, the higher resolution of the neutron diffraction data suggested more than one Ruddlesden-Popper phase was required to fit the data, therefore two phases with differing lattice parameters were included in the refinements. ND data suggests occupancy of chromate in the middle perovskite layer as supported by vacancies on the O1 sites as observed for sulfate phases. Higher Cr occupancy for $Sr_4Fe_{2.8}Cr_{0.2}O_{10-\delta}$ and the two phases with differing lattice parameters may suggest some additional carbonate as predicted for $Sr_4Fe_{3-x}S_xO_{10-\delta}$.

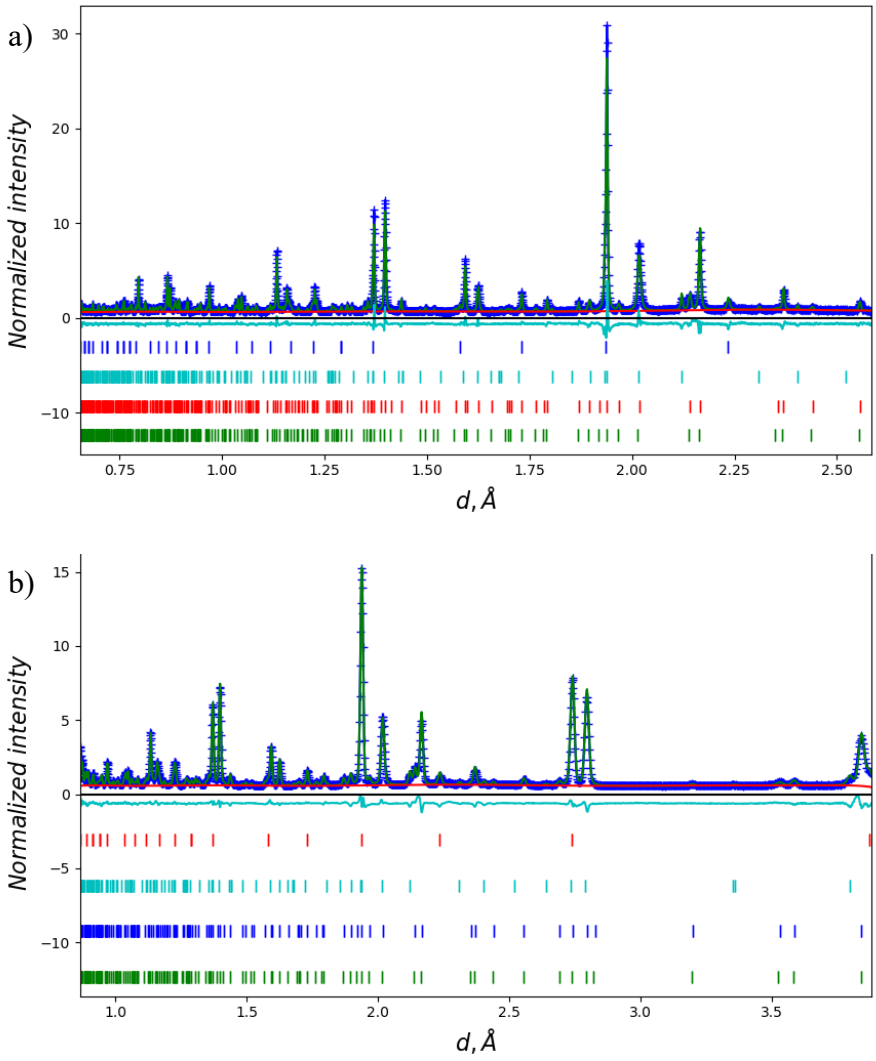

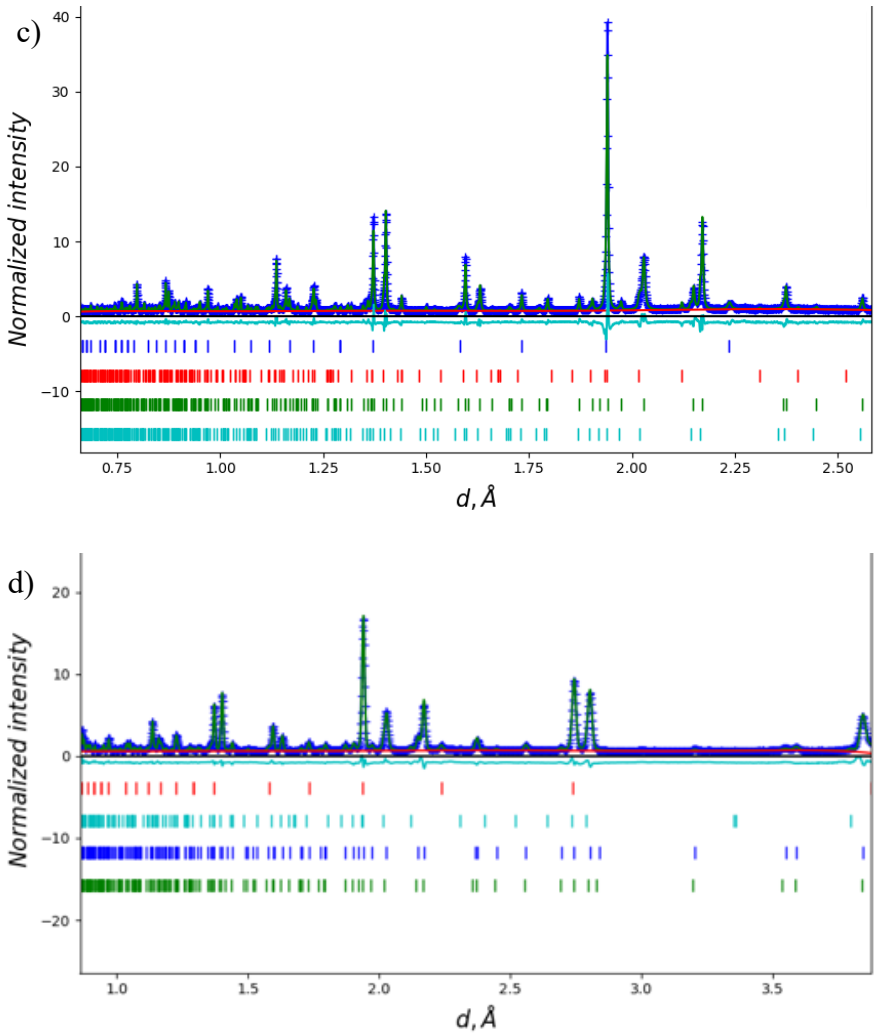

Figure 68. Observed (dark blue), calculated (green) and difference (light blue) neutron diffraction profiles for a) $Sr_4Fe_{2.8}Cr_{0.2}O_{10-\delta}$ (Bank 1), b) $Sr_4Fe_{2.8}Cr_{0.2}O_{10-\delta}$ (Bank 2), c) $Sr_4Fe_{2.7}Cr_{0.3}O_{10-\delta}$ (Bank 1) and d) $Sr_4Fe_{2.7}Cr_{0.3}O_{10-\delta}$ (Bank 2). Phases (coloured ticks) are presented from top to bottom as $SrFeO_{3-\delta}$, $Sr_3Fe_2O_{7-\delta}$, Ruddlesden-Popper phase 1 and Ruddlesden-Popper phase 2.

Table 16. Refined structural parameters for $Sr_4Fe_{2.72}Cr_{0.28}O_{9.16}$ with two tetragonal Ruddlesden-Popper phases refined with space group *I*4/*mmm*. Additional impurity phases tetragonal $Sr_3Fe_2O_7$ (*I*4/*mmm*) and $SrFeO_3$ ($Pm\bar{3}m$) were included in the room temperature neutron diffraction data.

	Ruddlesden-Popper Phases		**$Sr_3Fe_2O_7$**	**$SrFeO_3$**
	Phase 1	**Phase 2**		
a (Å)	3.87750(6)	3.87455(11)	3.86632(18)	3.87052(18)
c (Å)	28.26233(81)	28.19809(149)	20.16129(130)	-
V ($Å^3$)	424.92(2)	423.30(3)	301.38(3)	57.98(1)
Weight Percent (%)	51.2	27.4	11.9	9.5
R_{wp}		**R_{exp}**		**GOF**
5.65%		1.32%		4.30

Ruddlesden-Popper

	x	y	z	Occ	U_{iso}
Sr1	0.0000	0.0000	0.4282(1)	1.00	0.0083(5)
Sr2	0.0000	0.0000	0.2977(1)	1.00	0.0073(6)
Fe1	0.0000	0.0000	0.0000	0.72(1)	0.0029(9)
Cr1	0.0000	0.0000	0.0000	0.28(1)	0.0029(9)
Fe2	0.0000	0.0000	0.1419(1)	1.00	0.0014(4)
O1	0.0000	0.5000	0.0000	0.82(1)	0.0366(21)
O2	0.0000	0.0000	0.0662(1)	0.90(1)	0.0192(14)
O3	0.0000	0.5000	0.1381(1)	0.96(1)	0.0032(6)
O4	0.0000	0.0000	0.2104(1)	0.94(1)	0.0052(11)

Table 17. Refined structural parameters for $Sr_4Fe_{2.68}Cr_{0.32}O_{9.12}$ with two tetragonal Ruddlesden-Popper phases refined with space group *I*4/*mmm*. Additional impurity phases tetragonal $Sr_3Fe_2O_7$ (*I*4/*mmm*) and $SrFeO_3$ ($Pm\bar{3}m$) were included in the room temperature neutron diffraction data.

	Ruddlesden-Popper Phases		**$Sr_3Fe_2O_7$**	**$SrFeO_3$**
	Phase 1	**Phase 2**		
a (Å)	3.87961(4)	3.87500(14)	3.86596(31)	3.87275(30)
c (Å)	28.39055(46)	28.26653(160)	20.15639(211)	-
V (Å^3)	427.32(1)	424.44(3)	30.25(5)	58.08(1)
Weight Percent (%)	70.9	17.4	4.7	7.0
R_{wp}		**R_{exp}**		**GOF**
6.17%		1.29		4.80

Ruddlesden-Popper

	x	y	z	Occ	U_{iso}
Sr1	0.0000	0.0000	0.4274(1)	1.00	0.0129(5)
Sr2	0.0000	0.0000	0.2980(1)	1.00	0.0131(6)
Fe1	0.0000	0.0000	0.0000	0.68(1)	0.0078(9)
Cr1	0.0000	0.0000	0.0000	0.32(1)	0.0078(9)
Fe2	0.0000	0.0000	0.1424(1)	1.00	0.0075(4)
O1	0.0000	0.5000	0.0000	0.77(1)	0.0560(26)
O2	0.0000	0.0000	0.0649(1)	0.92(1)	0.0258(16)
O3	0.0000	0.5000	0.1383(1)	0.96(1)	0.0064(6)
O4	0.0000	0.0000	0.2105(1)	0.95(1)	0.0116(11)

5.4.3 Stability in low p(O_2)

When heating the Cr doped samples in dry N_2 to 800 °C, broadening of reflections in the XRD data is seen in Figure 69. This broadening may indicate that these $Sr_4Fe_{3-x}Cr_xO_{10-\delta}$ phases partially breaks down as suggested for low levels of sulfate doped $Sr_4Fe_3O_{10-\delta}$.

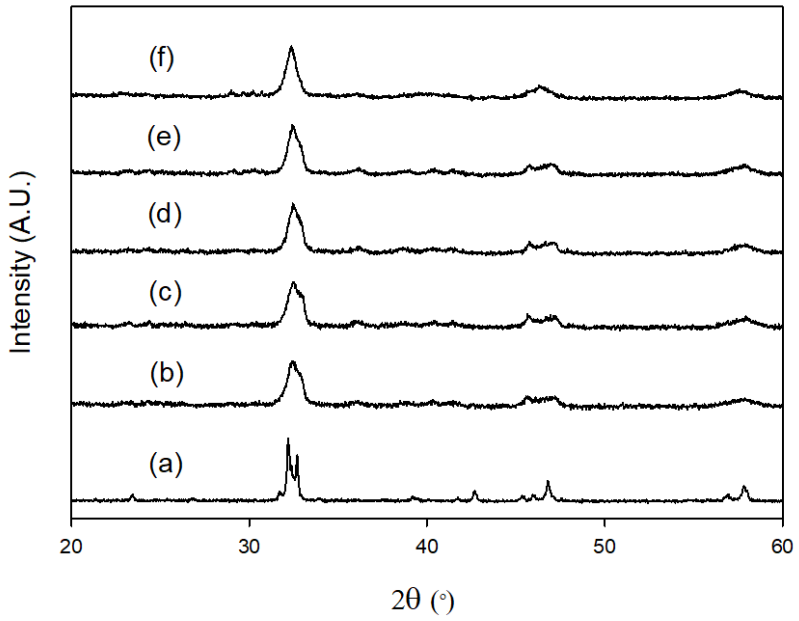

Figure 69. X-ray diffraction patterns for $Sr_4Fe_{3-x}Cr_xO_{10-\delta}$ after heat treatment in dry N_2 to 800 °C, where a) x = 0, b) x = 0.2, c) x = 0.25, d) x = 0.3, e) x = 0.35 and f) x = 0.4

5.4.4 Stability in wet N_2

As discussed for the sulfate doped $Sr_4Fe_3O_{10-\delta}$ materials (section 5.3.4), broadening of XRD data for $Sr_4Fe_{3-x}Cr_xO_{10-\delta}$ (Figure 70) is observed when heating in wet N_2 to 800 °C for 12 h. As previously discussed, multiple hydrated Ruddlesden-Popper phases are expected to form. Further investigation would be needed in order to determine water incorporation into these materials and test the suitability for use in proton conducting solid oxide fuel cells.

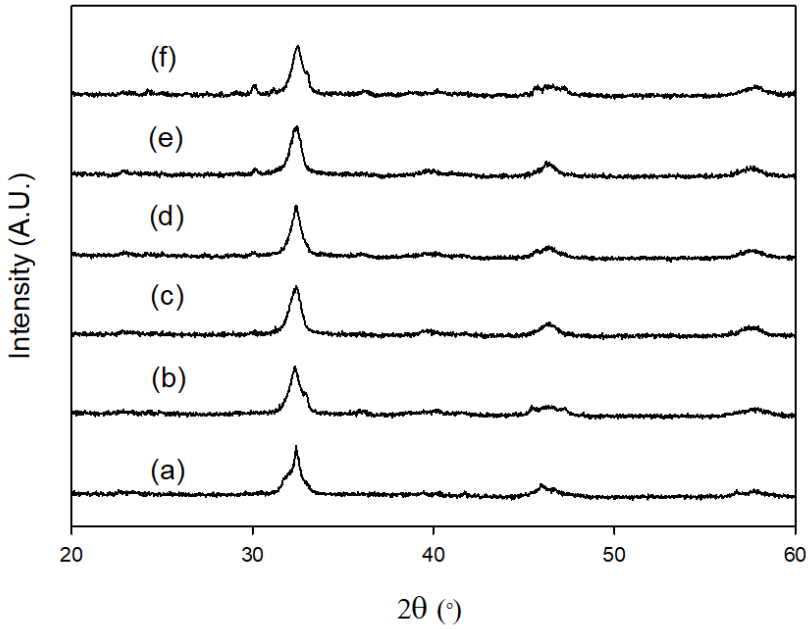

Figure 70. X-ray diffraction patterns for $Sr_4Fe_{3-x}Cr_xO_{10-\delta}$ after heat treatment in wet N_2 to 800 °C, where a) x = 0, b) x = 0.2, c) x = 0.25, d) x = 0.3, e) x = 0.35 and f) x = 0.4

5.4.5 XANES

The XRD data had indicated successful incorporation of Cr into the structure, but the oxidation state and coordination needed further clarification. In order to evaluate this chromium environment/ oxidation state, XAS analysis was carried out on $Sr_4Fe_{2.6}Cr_{0.4}O_{10-\delta}$, and compared with data collected for $LaCrO_3$, $SrCrO_4$ and Cr foil standards. $LaCrO_3$ and $SrCrO_4$ were used as reference materials for octahedral Cr^{3+} and tetrahedral Cr^{6+} (CrO_4^{2-}) respectively, since previous studies have reported the presence of either Cr^{3+} and Cr^{6+} in Cr doped Ruddlesden-Popper systems. In particular, Sousa et al.[180] reported the presence of Cr^{3+} and Cr^{6+} in Cr doped $Ca_4Mn_3O_{10}$, whereas Bréad et al.[181] reported only Cr^{3+} in the $Sr_4FeCrO_6CO_3$ Ruddlesden-Popper system.

The X-ray absorption near edge structure (XANES) data for $Sr_4Fe_{2.6}Cr_{0.4}O_{10-\delta}$ and the $LaCrO_3$ and $SrCrO_4$ standards are shown in Figure 71. The $SrCrO_4$ reference material is found to have a sharp pre edge at 5994 eV which correlates with tetrahedral chromium in the 6+

oxidation state. In comparison a weak pre edge is observed for $LaCrO_3$ which is characteristic of Cr^{3+} in an octahedral coordination. The data for $Sr_4Fe_{2.6}Cr_{0.4}O_{10-\delta}$ are similar to $SrCrO_4$, with a similar sharp pre edge at 5994 eV. Therefore the XANES data support the original proposal that Cr is incorporated as CrO_4^{2-} (tetrahedral Cr^{6+}). The increase in Cr oxidation state during the synthesis from 3+ (Cr_2O_3 precursor) to 6+ in the Ruddlesden-Popper phase is not that surprising given that $SrCrO_4$ being prepared in a similar way using Cr_2O_3. This is additionally supported by the formation of the impurity phase, $SrCrO_4$ (Cr^{6+}) at higher Cr dopant levels.

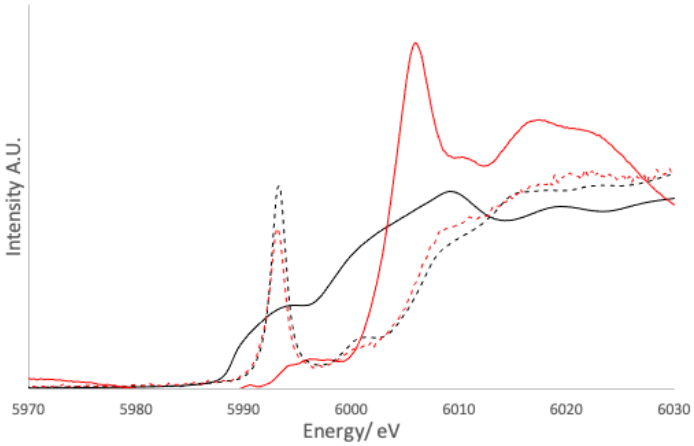

Figure 71. XANES data obtained for Cr foil (black solid line), $LaCrO_3$ (red solid line), $SrCrO_4$ (black dashed line) and $Sr_4Fe_{2.6}Cr_{0.4}O_{10-\delta}$ (red dashed line)

5.4.6 ^{57}Fe Mössbauer spectroscopy

In order to evaluate the Fe environment in these Ruddlesden-Popper phases, ^{57}Fe Mössbauer spectra were recorded from $Sr_4Fe_{2.8}Cr_{0.2}O_{10-\delta}$ and $Sr_4Fe_{2.6}Cr_{0.4}O_{10-\delta}$ (Figure 72). The spectra were fitted considering three different contributions. Their corresponding hyperfine parameters are collected in Table 18. These isomer shifts indicate that both these materials contain Fe^{3+} and Fe^{5+} with at least some of the Fe^{3+} in lower than octahedral coordination. As

reported for oxyanion doped perovskite and Ruddlesden-Popper systems,[111,164] disproportionation of Fe^{4+} to Fe^{3+} and Fe^{5+} can be attributed to the substitution of smaller Cr^{6+} for Fe^{4+}, with the disproportionation process allowing for the release of local strain. This, again, supports the incorporation of higher valence Cr.

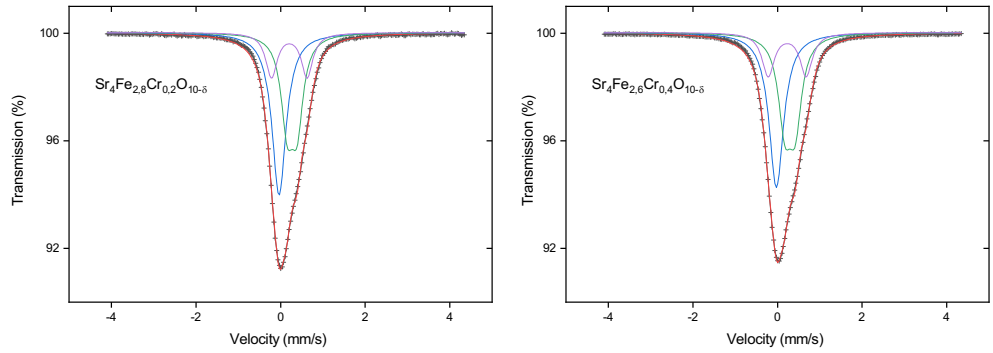

Figure 72. ^{57}Fe Mössbauer spectra recorded from $Sr_4Fe_{2.8}Cr_{0.2}O_{10-\delta}$ and $Sr_4Fe_{2.6}Cr_{0.4}O_{10-\delta}$ at 298K

Table 18. ^{57}Fe Mössbauer parameters recorded from $Sr_4Fe_{2.8}Cr_{0.2}O_{10-\delta}$ and $Sr_4Fe_{2.6}Cr_{0.4}O_{10-\delta}$ at 298K, where isomer shift and quadrupole splitting are given by δ and Δ respectively.

Compound	**Assignment**	**δ ± 0.01 (mms^{-1})**	**Δ ± 0.05 (mms^{-1})**	**Area ± 5%**
$Sr_4Fe_{2.8}Cr_{0.2}O_{10-\delta}$	Fe^{5+}	-0.04	0.00	43
	Fe^{3+}	0.27	0.23	38
	Fe^{3+} in low coordination	0.21	0.84	19
$Sr_4Fe_{2.6}Cr_{0.4}O_{10-\delta}$	Fe^{5+}	-0.03	0.00	41
	Fe^{3+}	0.30	0.24	40
	Fe^{3+} in low coordination	0.23	0.90	19

5.4.7 Conductivity studies

The data for all $Sr_4Fe_{3-x}Cr_xO_{10-\delta}$ samples show three linear regions between 400 – 800 °C (Figure 73), which can be correlated with small changes in composition, and hence Fe oxidation states on heating as indicated by TGA studies. An initial increase in conductivity is observed with increasing temperature, indicative of the expected semiconducting behaviour. Above ≈ 640 - 670 °C a decrease in conductivity is observed which can be correlated with loss of oxygen at higher temperature which reduces the average transition metal oxidation state, as shown in prior work for sulfate doping.[164] In addition to the loss of oxygen in the temperature range 400 – 800 °C, thermogravimetric analysis (TGA-MS) indicated some loss of water at ≈ 640 - 670 °C, suggesting a partial hydration of these systems. Further deviations to the increase in conductivity are observed at the lower temperature in the range ≈ 400 – 460 °C, which can be correlated to an additional loss of oxygen, and hence reduction in average Fe oxidation state, in this temperature range. Upon incorporation of Cr there is an initial increase in conductivity at higher temperatures where x=0.25 with increased Cr incorporation a decrease in conductivity is reported.

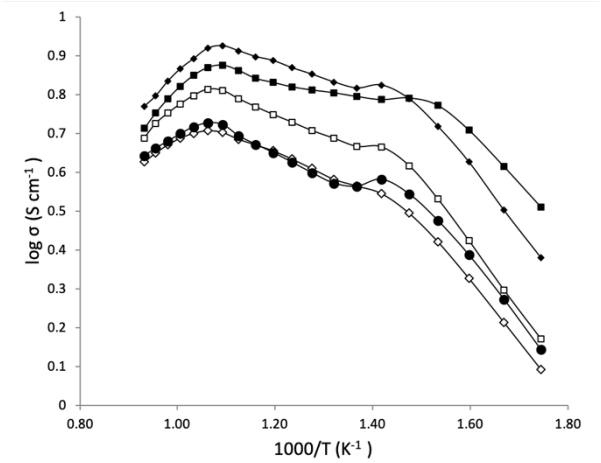

Figure 73. Plot of log σ vs. 1000/T for $Sr_4Fe_{2.8}Cr_{0.2}O_{10-\delta}$ (■), $Sr_4Fe_{2.75}Cr_{0.25}O_{10-\delta}$ (◆), $Sr_4Fe_{2.7}Cr_{0.3}O_{10-\delta}$ (□), $Sr_4Fe_{2.65}Cr_{0.35}O_{10-\delta}$ (◇) and $Sr_4Fe_{2.6}Cr_{0.4}O_{10-\delta}$ (●) in air

5.4.8 Conclusions

This work shows that Cr doping into $Sr_4Fe_3O_{10-\delta}$ successfully stabilised the n=3 Ruddlesden-Popper system. XANES data supports the prediction that Cr is incorporated as CrO_4^{2-} (tetrahedral Cr(VI)). ND data suggests chromate is incorporated into the middle perovskite layer as suggested for sulfate incorporation. In order to test the suitability for use as a solid oxide fuel cell cathode material, samples were heated in dry and wet N_2. Due to the broadening of XRD data observed further, more detailed work would be needed to investigate these materials in terms of understanding the changes observed. By doping with Cr an improvement in the conductivity data is reported compared with S doped equivalents. However, the conductivities still remain comparatively low, and so further work would be needed to enhance these conductivities to compete with common SOFC electrode materials.

Work within this chapter has been published in Journal of Solid State Chemistry (A. Jarvis, F. J. Berry, J. F. Marco, M. Sanchez-Arenillas, G. Cibin, O. Clemens and P. R. Slater, J. Solid State Chem., 2020, 287, 121372; DOI: 10.1016/j.jssc.2020.121372)

5.5 $Sr_4Fe_{3-x}B_xO_{10-\delta}$

Oxyanion doping studies in chapter 5 have shown tetrahedral sulfate and chromate can successfully stabilise the n=3 Ruddlesden-Popper structure. In addition to tetrahedral dopants, in chapter 4 trigonal planar borate resulted in single phase cubic perovskite phases. Therefore, in order to expand the dopants investigated in chapter 5, borate was chosen to further investigate oxyanion incorporation into the n=3 Ruddlesden-Popper system, $Sr_4Fe_3O_{10-\delta}$.

5.5.1 X-ray diffraction results

X-ray diffraction studies for $Sr_4Fe_{3-x}B_xO_{10-\delta}$, indicated stabilisation of the n=3 Ruddlesden-Popper phase upon doping with borate (Figure 74) as observed for the sulfate and chromate systems. This work shows that in addition to sulfate and chromate, borate can also be incorporated into $Sr_4Fe_3O_{10-\delta}$. We assume that the borate is incorporated as trigonal planar BO_3^{3-} as observed for borate doped perovskites.[107,159,182,183]

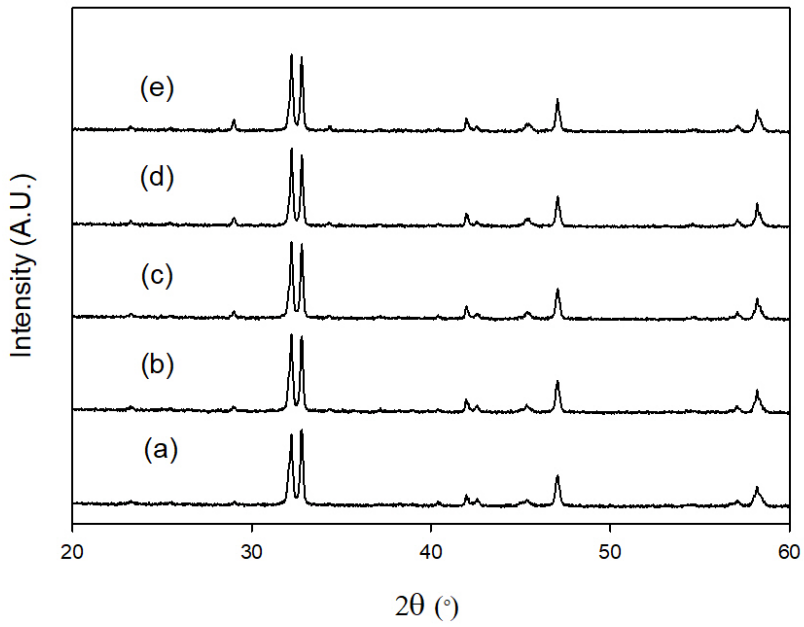

Figure 74. X-ray diffraction patterns for $Sr_4Fe_{3-x}B_xO_{10-\delta}$, where a) x = 0.2, b) x = 0.25, c) x = 0.3, d) x = 0.35 and e) x = 0.4 showing the formation of the n=3 Ruddlesden-Popper phase.

The XRD studies showed an interesting observation of a change in the diffraction data for the borate doped materials when carrying out long scans (overnight) suitable for refinements (Figure 75). In particular it was found that the XRD data changes if samples are left overnight in air.

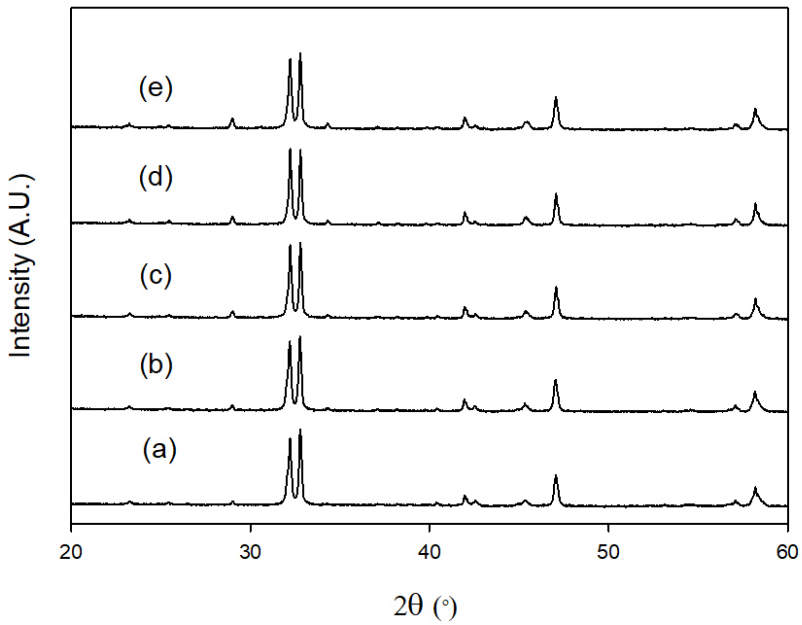

Figure 75. X-ray diffraction patterns for $Sr_4Fe_{3-x}B_xO_{10-\delta}$ left in air overnight, where a) x = 0.2, b) x = 0.25, c) x = 0.3, d) x = 0.35 and e) x = 0.4

In particular, the low angle XRD data (Figure 76) shows a small peak at $2\theta \approx 6$ ° corresponding to the (002) reflection characteristic of hydrated n=3 Ruddlesden-Popper materials. A similar observation was observed for $Sr_4Fe_{3-x}S_xO_{10-\delta}$ heated in wet N_2 (Figure 62). This shows that these borate doped materials are sensitive to moisture and will readily incorporate water when left in air.

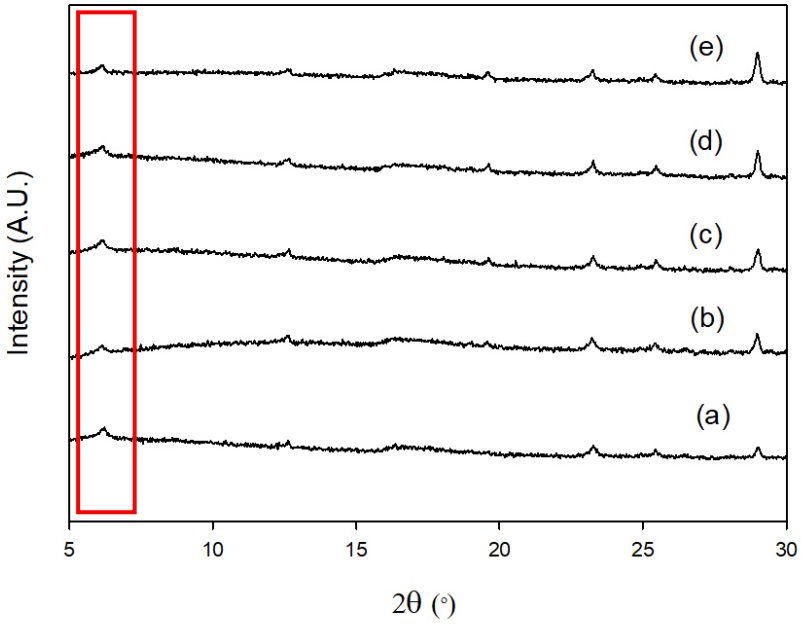

Figure 76. X-ray diffraction patterns for $Sr_4Fe_{3-x}B_xO_{10-\delta}$ left in air overnight, where a) x = 0.2, b) x = 0.25, c) x = 0.3, d) x = 0.35 and e) x = 0.4 showing appearance of the (002) from the hydrated Ruddlesden-Popper phase at $2\theta \approx 6$ ° (highlighted in red)

5.5.2 Stability in low p(O_2)

The stability of the $Sr_4Fe_{3-x}B_xO_{10-\delta}$ materials was examined in low p(O_2) by heating samples to 800 °C for 12 h in dry N_2. The results showed that the tetragonal Ruddlesden-Popper structure was not maintained for the borate doped materials. Here additional reflections, as seen in Figure 77, due to $Sr_3B_2O_6$ and broadening of diffraction data suggests the partial breakdown of the structure.

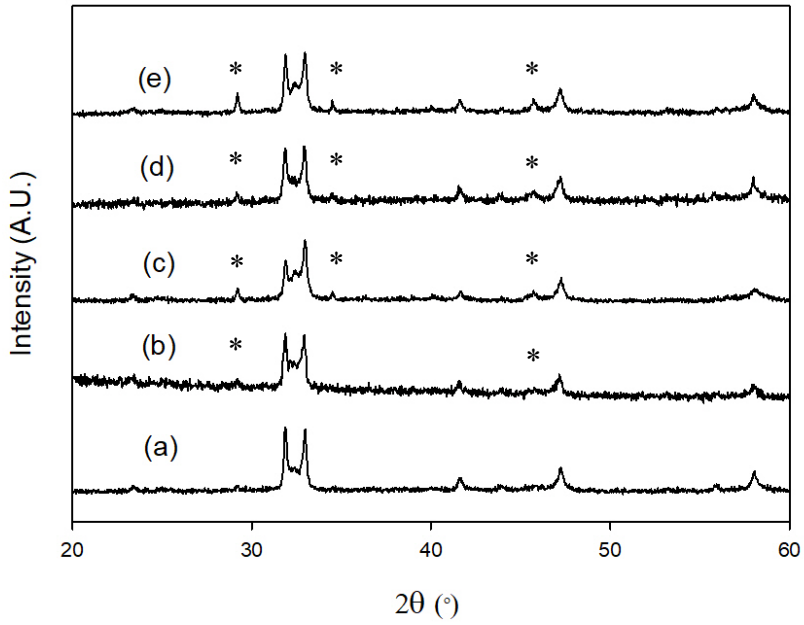

Figure 77. X-ray diffraction patterns for $Sr_4Fe_{3-x}B_xO_{10-\delta}$ after heat treatment in dry N_2 to 800 °C, where a) x = 0.2, b) x = 0.25, c) x = 0.3, d) x = 0.35 and e) x = 0.4 showing partial decomposition with the formation of $Sr_3B_2O_6$ highlighted with an asterisk (*)

5.5.3 Stability in wet N_2

To test the suitability for use in proton conducting SOFCs, $Sr_4Fe_{3-x}B_xO_{10-\delta}$ samples were also heated in wet N_2 to 800 °C for 12 h. As observed for both sulfate and chromate doped materials, broad XRD patterns (Figure 78) are observed for all materials, suggesting the possibility of multiple hydrated phases. Additionally, as observed when heating borate samples in dry N_2, impurities due to $Sr_3B_2O_6$ suggested the partial breakdown of the structure.

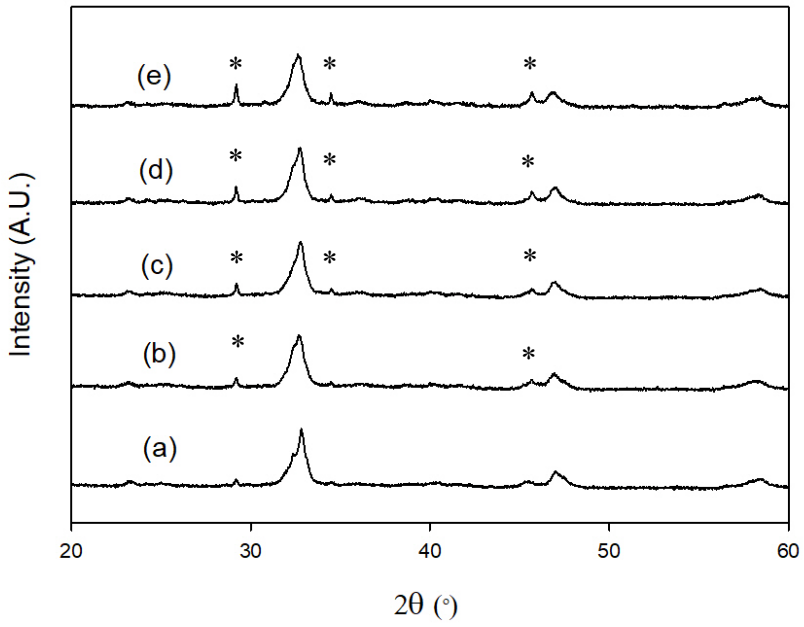

Figure 78. X-ray diffraction patterns for $Sr_4Fe_{3-x}B_xO_{10-\delta}$ after heat treatment in wet N_2 to 800 °C, where a) x = 0, b) x = 0.2, c) x = 0.25, d) x = 0.3, e) x = 0.35 and f) x = 0.4 showing partial decomposition with the formation of $Sr_3B_2O_6$ highlighted with an asterisk (*)

5.5.4 Conductivity studies

At low temperature the conductivity of the borate materials remains essentially constant. At higher temperature (≈ 600 °C) a decrease in conductivity is then observed (Figure 79) which can be associated with the loss of oxygen at high temperature as observed for chromate doping.[165] Comparing borate doped materials a significant increase in conductivity is observed for x = 0.3 and 0.35 compared with x= 0.2, 0.25 and 0.4, although the reasons behind this increase is not clear, and warrants further study.

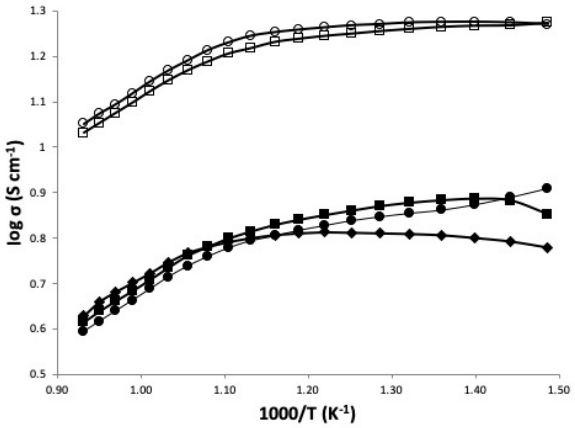

Figure 79. Plot of log σ vs. 1000/T for $Sr_4Fe_{2.8}B_{0.2}O_{10-\delta}$ (■), $Sr_4Fe_{2.75}B_{0.25}O_{10-\delta}$ (●), $Sr_4Fe_{2.7}B_{0.3}O_{10-\delta}$ (□), $Sr_4Fe_{2.65}B_{0.35}O_{10-\delta}$ (○) and $Sr_4Fe_{2.6}B_{0.4}O_{10-\delta}$ (◆) in air

When comparing the conductivities of the sulfate, chromate and borate doped $Sr_4Fe_3O_{10-\delta}$ samples (Figure 80), the lowest conductivity is observed for the sulfate doped materials. At elevated temperatures slightly higher conductivities are observed for $Sr_4Fe_{3-x}Cr_xO_{10-\delta}$ compared with $Sr_4Fe_{3-x}S_xO_{10-\delta}$. The $Sr_4Fe_{3-x}B_xO_{10-\delta}$ samples are found to have conductivities in a similar range to $Sr_4Fe_{3-x}(S/Cr)_xO_{10-\delta}$ samples with the exception of $Sr_4Fe_{2.7}B_{0.3}O_{10-\delta}$ which has significantly higher conductivities over the temperature range 400 – 800 °C. Overall, however, all the oxyanion doped $Sr_4Fe_3O_{10-\delta}$ materials have conductivities that are rather low (8.4 S cm^{-1} at 642 °C for $Sr_4Fe_{2.75}Cr_{0.25}O_{10-\delta}$) compared with common SOFC electrode materials.[145] Further doping studies would therefore be needed to increase these values if these systems were to be employed in SOFCs.

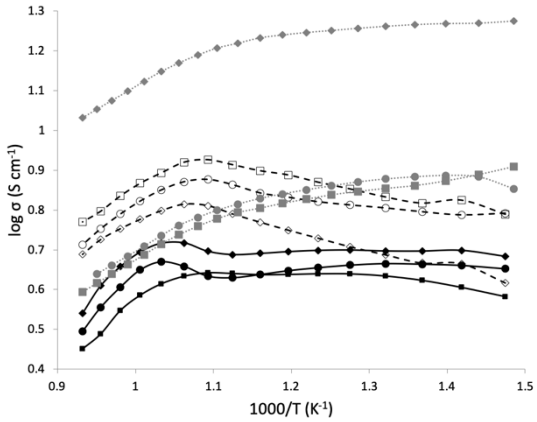

Figure 80. Plot of log σ vs. 1000/T for $Sr_4Fe_{3-x}S_xO_{10-\delta}$[164] (filled black markers), $Sr_4Fe_{3-x}Cr_xO_{10-\delta}$ [165] (empty markers) and $Sr_4Fe_{3-x}B_xO_{10-\delta}$ (filled grey markers) where x = 0.2 (circle), x = 0.25 (square) and x = 0.3 (diamond).

5.5.5 Conclusions

This work has shown that in addition to sulfate and chromate, borate can be incorporated into $Sr_4Fe_3O_{10-\delta}$. However, these $Sr_4Fe_{3-x}B_xO_{10-\delta}$ phases were found to readily incorporate water when left in air at room temperature. Furthermore heating in dry and wet N_2, led to partial break down of materials with the observation of $Sr_3B_2O_6$ impurity. When comparing sulfate, chromate and borate doped $Sr_4Fe_3O_{10-\delta}$, the borate doped materials are generally found to have comparable conductivities to chromate doped materials with the exception of $Sr_4Fe_{2.7}S_{0.3}O_{10-\delta}$ which is found to have a significant improvement in conductivity. Overall this work shows the flexibility of Ruddlesden-Popper structures to incorporate oxyanions as for perovskite systems. However, the generally low conductivities obtained so far limit their potential use in SOFCs.

5.6 Summary

A summary of all Ruddlesden-Popper materials investigated in chapter 5 can be found in Table 19. These systems are found to stabilise the n=3 Ruddlesden-Popper structure when incorporating oxyanion dopants. Without the incorporation of oxyanions, a mixture of the perovskite $SrFeO_{3-\delta}$ structure and the n=2 Ruddlesden-Popper structure, $Sr_3Fe_2O_{7-\delta}$ forms. Neutron diffraction studies of sulfate/ chromate doped phases suggest some additional carbonate as observed in TGA studies of oxyanion doped perovskite materials in chapter 4. Highlighting the importance of investigating the incorporation of carbonate in not only perovskite materials, but perovskite type materials. Compared to the oxyanion doped perovskite materials (chapter 4), low conductivities are reported for the oxyanion doped Ruddlesden-Popper materials. $Sr_4Fe_{3-x}S_xO_{10-\delta}$ materials are found to be the most promising due to stability in low $p(O_2)$ and wet N_2. Further doping strategies are investigated in chapter 6 in order to improve the oxyanion doped Ruddlesden-Popper materials for use in SOFCs.

Table 19. Chapter 5 summary table

Sample	**Crystal system (Synthesis temperature)**	**Stability**	**Highest conductivity (Temperature)**
$Sr_4Fe_{3-x}S_xO_{10-\delta}$ where x= 0.15, 0.2, 0.25 and 0.3	**Undoped** - A mixture of $Sr_3Fe_2O_{7-\delta}$ and $SrFeO_{3-\delta}$ **S doped** - Tetragonal (1050 °C	**Stability in low $p(O_2)$** - Partial breakdown of structure for x= 0.15 - x = 0.2-0.3 remain stable **Stability in wet N_2** - XRD data suggests incorporation of water with	4-7 S cm^{-1} (432-695 °C)

	with anneal at 350 °C)	potential for use in proton conducting SOFCs	
$Sr_4Fe_{3-x}Cr_xO_{10-\delta}$ where x= 0.2, 0.25, 0.3, 0.35 and 0.4	Tetragonal (1050 °C with anneal at 350 °C) Tetragonal Cr^{6+} confirmed via XANES data	**Stability in low p(O_2)** - Broadening in XRD data suggests partial breakdown of structure **Stability in wet N_2** - Broadening in XRD data – further work needed to investigate this	5-8 S cm^{-1} (642-668 °C)
$Sr_4Fe_{3-x}B_xO_{10-\delta}$ where x= 0.2, 0.25, 0.3, 0.35 and 0.4	Tetragonal (1050 °C with anneal at 350 °C) - Sensitive to moisture and readily incorporates water	**Stability in low p(O_2)** - Partial breakdown of structure with additional reflections in XRD due to $Sr_3B_2O_6$ **Stability in wet N_2** - Broadening of XRD data with additional reflections due to $Sr_3B_2O_6$	7-19 S cm^{-1} (400-547 °C)

6 Sulfate incorporation into copper/ cobalt containing n=3 Ruddlesden-Popper systems

6.1 Introduction

Cobalt containing perovskite materials are appealing cathode materials due to good ionic and electronic conductivity which are typically higher than the values observed for cobalt-free materials. A range of cobalt containing perovskite materials have been investigated as SOFC cathode materials. For example $La_{1-x}Sr_xCo_{1-y}Fe_yO_{3-\delta}$ (LSCF) is an appealing material for intermediate temperature SOFCs.[44–47,184,185] In addition, a number of transition metal dopants have been utilised in Co based perovskites, including Ni and Cu in order to lower the valence of sites and as a result introduce oxygen vacancies. For example Cu doped materials $LaCo_{0.5}Cu_{0.5}O_{3-\delta}$ and $La_{0.5}Sr_{0.5}Co_{0.5}Cu_{0.5}O_{3-\delta}$ have been investigated as potential cathode materials for SOFCs where Sr and Cu doping is found to enhance electrochemical performance.[186]

In addition to perovskite materials, Ruddlesden-Popper materials have been investigated as potential cathode materials. $La_{n+1}Ni_nO_{3n+1}$ Ruddlesden-Popper phases are appealing due to the ability for these materials to accommodate either oxide ion excess or oxide ion vacancies.[54,55,74–76,78,187] Doping of Ruddlesden-Popper materials with a range of transition metal dopants has also been investigated, for example cobalt doping of Ruddlesden-Popper material $La_4Ni_3O_{10-\delta}$ has been investigated by Amow et al.[77] showing improved electrode performance compared to the undoped phase.

Although appealing for performance, the high cost and limited availability of cobalt drives the need for alternative materials. Typically, this has been investigated through doping with transition metals of a similar size, but different charge. An alternate doping strategy is to

introduce oxyanions such as sulfate which will also lower the valance of metals and introduce vacancies. Sulfate doping into perovskite and perovskite type materials have been successfully reported for SOFC electrode and electrolyte materials.[101,105,148,159,164] This includes sulfate doped $SrCoO_3$ as reported by Hancock et al.[148] which showed improved conductivity compared with the undoped parent phase. Additionally, Shin et al.[101] has shown by incorporating sulfate into electrolyte material $Ba_2In_2O_5$, conductivity is improved compared with the parent phase with additional enhancement in a wet atmosphere.

Following on from sulfate incorporation into $Sr_4Fe_3O_{10-\delta}$[164], this work investigates sulfate doped materials, $Sr_4Fe_2(Co/Cu)_{1-x}S_xO_{10-\delta}$ with a view to trying to enhance the conductivity and so utilise these materials as SOFC cathode materials.

6.2 Experimental

The $Sr_4Fe_2(Co/Cu)_{1-x}S_xO_{10-\delta}$ phases were prepared through solid state synthesis. Stoichiometric amounts of starting materials ($SrCO_3$, Fe_2O_3, $(NH_4)_2SO_4$ and either Co_3O_4, or CuO) were ground and heated at 4 °C/ min to 950 °C for 12 hours. Resulting powders were then ball milled at 350 rpm for 1 h. A further heat treatment to 1000 °C for 12 hours was carried out before further regrinding and heating the samples to 1050 °C for 12 hours. $Sr_4Fe_2Cu_{1-x}S_xO_{10-\delta}$ phases were reground and further heated to 1075 °C for 12 hours. Finally, to ensure maximum oxygen content, samples were heated to 350 °C for 12 h.

Additionally, in order to test stability under lower $p(O_2)$ as well as testing potential suitability for use in proton conducting solid oxide fuel cells, samples were heated in dry/ wet N_2. Samples were heated to 800 °C for 12 h with a heating ramp rate of 4 °C/ min for both dry and wet N_2. On cooling dry N_2 samples were cooled at 4 °C/ min and wet N_2 samples cooled at 50 °C/ h.

Powder XRD were collected for all samples with Rietveld refinements carried out using the GSAS suite of programs.[136] XRD data was used to determine lattice parameters and phase purity. For all Ruddlesden-Popper samples space group *I*4/*mmm* was used with space group $Pm\bar{3}m$ used for the minor impurity cubic perovskite phase. For all air and dry N_2 refinements atom positions and oxygen occupancies were refined. Due to the virtually identical scattering factors of Fe/Co/Cu, these cannot be distinguished therefore Fe/Co and Fe/Cu sites were constrained with S to equal 1. In order for wet N_2 sample refinements to reach convergence, site occupancies were not refined and fixed with Fe/Cu/Co/S occupancies set as reported for air heated samples. Atomic displacement parameters were constrained for Sr, Fe/Co/Cu/S and O sites and fixed at realistic values due to high correlation with site occupancies.

Neutron diffraction data were collected on the HRPD diffractometer at ISIS neutron and muon source.

In order to test the potential for use as cathode materials for SOFCs, four probe dc conductivity measurements were carried out. Pellets were prepared by ballmilling at 350 rpm for 1 h before pressing into pellets and sintering at 1050 °C ($Sr_4Fe_2Co_{1-x}S_xO_{10-\delta}$) and 1075 °C ($Sr_4Fe_2Cu_{1-x}S_xO_{10-\delta}$) for 12 h. Four Pt electrodes were attached to the pellets with Pt paste and heated to 900 °C for 1 h in air. To ensure full oxygenation, pellets were finally annealed at 350 °C for 12 h.

6.3 X-ray diffraction results

X-ray diffraction (XRD) studies for $Sr_4Fe_2(Co/Cu)_{1-x}S_xO_{10-\delta}$ indicated successful synthesis of the n=3 Ruddlesden-Popper structure (Figure 81). Following from the previous work in this thesis on $Sr_4Fe_{3-x}S_xO_{10-\delta}$[164] which shows successful incorporation of tetrahedral SO_4^{2-}, these

mixed Fe/Co/Cu systems further confirmed successful incorporation of sulfate into the n=3 Ruddlesden Popper structure. As shown previously, at low S dopant levels a mixture of the n=2 Ruddlesden-Popper phase ($Sr_3Fe_2O_{7-\delta}$) and perovskite phase ($SrFeO_{3-\delta}$) form. At higher S dopant levels, additional reflections associated with the formation of $SrSO_4$ is observed for $Sr_4Fe_2(Cu/Co)_{1-x}S_xO_{10-\delta}$ where $x \geq 0.4$, indicating that the S solubility in the structure has been exceeded. This therefore suggests the optimum doping range would be $0.2 < x < 0.4$ ($Sr_4Fe_2Cu_{1-x}S_xO_{10-\delta}$) and $0.2 \leq x < 0.4$ ($Sr_4Fe_2Co_{1-x}S_xO_{10-\delta}$).

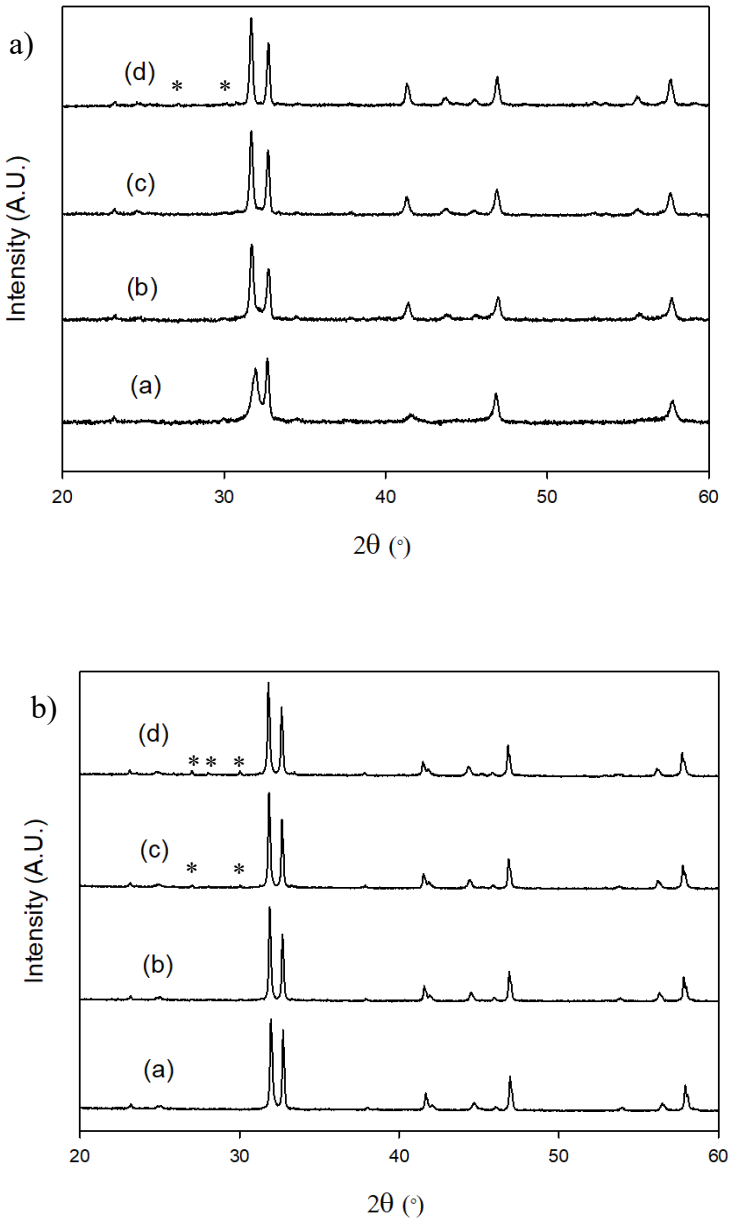

Figure 81. X-ray diffraction patterns for a) $Sr_4Fe_2Cu_{1-x}S_xO_{10-\delta}$ and b) $Sr_4Fe_2Co_{1-x}S_xO_{10-\delta}$ where a) x = 0.2, b) x = 0.3, c) x = 0.4, d) x = 0.5. Where $x \geq 0.4$ $SrSO_4$ impurities form indicating optimum doping ranges of $0.2 < x < 0.4$ ($Sr_4Fe_2Cu_{1-x}S_xO_{10-\delta}$) and $0.2 \leq x < 0.4$ ($Sr_4Fe_2Co_{1-x}S_xO_{10-\delta}$). $SrSO_4$ impurities are highlighted by an asterisk.

Using XRD data, Rietveld refinements were performed on all samples. For all phases there is indication of S occupancy of the middle perovskite layer as observed for previous

Ruddlesden-Popper ($Sr_4Fe_{3-x}(S/Cr/B)_xO_{10-\delta}$) [164,165] systems. Generally, good agreement with expected occupancies were found for Fe/Cu/Co and S sites with the exception of $Sr_4Fe_2Cu_{0.7}S_{0.3}O_{10-\delta}$ where higher than expected occupancies for S are reported.

With increasing sulfate content an increase in unit cell is observed for $Sr_4Fe_2Co_{1-x}S_xO_{10-\delta}$. As reported for $Sr_4Fe_{3-x}S_xO_{10-\delta}$, it is predicted the increase in unit cell is due to the increase in the amount of the larger Fe^{3+} upon doping with sulfate. [164] The Cu doped $Sr_4Fe_2Cu_{1-x}S_xO_{10-\delta}$ phases initially follow a similar trend (Figure 82) where an increase in sulfate from x=0.2 to x=0.3 increases the unit cell volume. On further increasing the sulfate content (x=0.4) a decrease in lattice parameter c and unit cell volume is observed. From the Fe/Cu/S occupancies reported in Table 20 the decrease in unit cell at x=0.4 also corresponds to the incorporation of S not only in the Fe/Cu1 (middle perovskite layer), but also the Fe/Cu2 site. There are a number of factors contributing to the change in lattice parameters for $Sr_4Fe_2Cu_{1-x}S_xO_{10-\delta}$. As highlighted earlier, an increase in cell parameters is likely to be due to an increase in the amount of Fe^{3+}, while a decrease in lattice parameters may be correlated with the incorporation of smaller S^{6+} vs Fe/Cu outweighing any effect of the former.

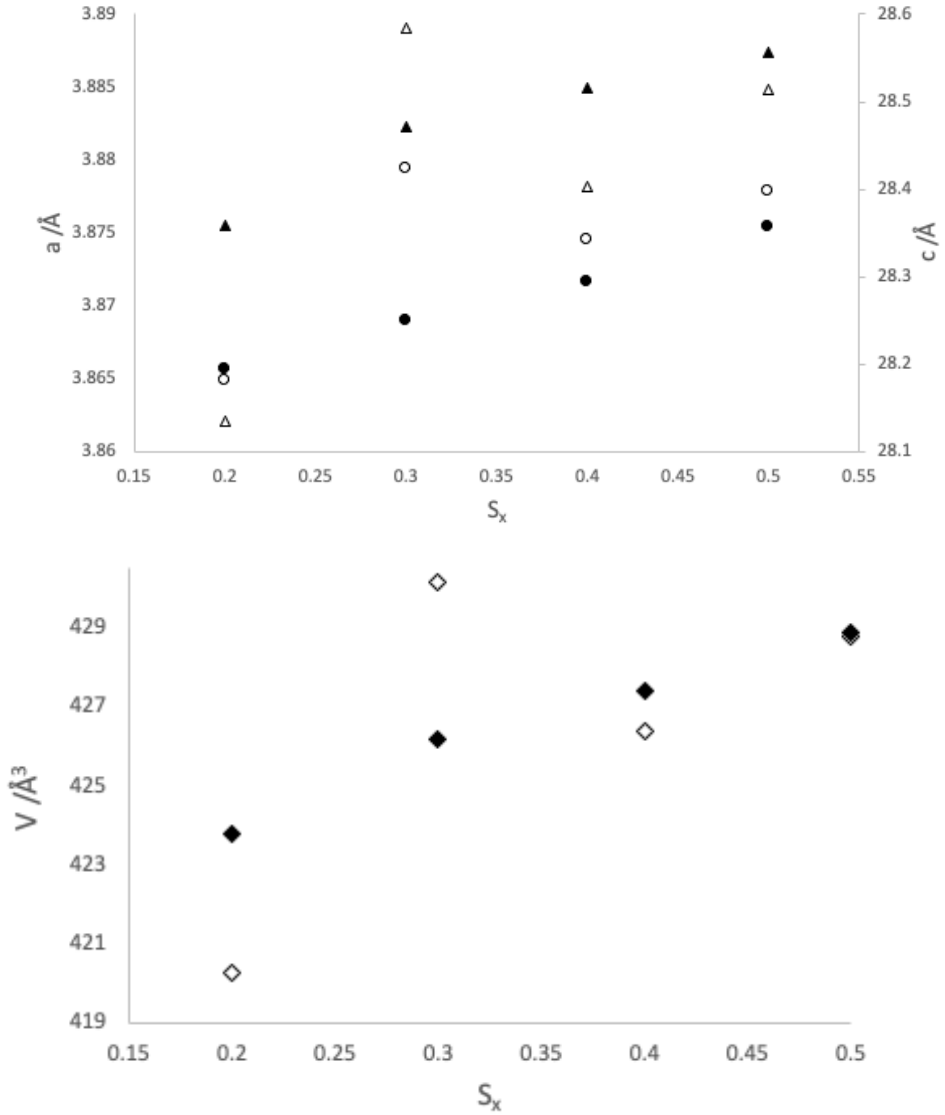

Figure 82. Variation of cell parameters with sulfate content, x for $Sr_4Fe_2Cu_{1-x}S_xO_{10-\delta}$ (empty markers) and $Sr_4Fe_2Co_{1-x}S_xO_{10-\delta}$ (filled markers) where a = ●/○, c = ▲/△ and V = ◆/◇

Table 20. Cell parameters (space group *I*4*/mmm*) and site occupancy factors for $Sr_4Fe_2Cu_{1-x}S_xO_{10-\delta}$ (heating in air). The impurity phases, $SrFeO_{3-\delta}$ and $SrSO_4$ were refined using the cubic space group, $Pm\bar{3}m$ and orthorhombic space group, *Pnma* respectively

$Sr_4Fe_2Cu_{1-x}S_xO_{10-\delta}$					
S (x)		0.2	0.3	0.4	0.5
a (Å)		3.8649(4)	3.8794(1)	3.8745(1)	3.8779(1)
c (Å)		28.1343(28)	28.5838(5)	28.4025(5)	28.5133(4)
V (Å^3)		420.26(10)	430.17(2)	426.38(2)	428.79(1)
Rwp (%)		2.86	2.62	2.23	2.10
Rexp (%)		1.76	1.12	1.15	1.13
Fe/Cu1 occupancy (middle perovskite layer)		0.84(9)	0.62(4)	0.75(3)	0.61(3)
S1 occupancy (middle perovskite layer)		0.16(9)	0.38(4)	0.25(3)	0.39(3)
Fe/Cu2 occupancy		1.00	1.00	0.95(2)	0.97(2)
S2 occupancy		-	-	0.05(2)	0.03(2)
O occupancy		9.56	9.54	9.74	9.64
Weight percentage (%)	Ruddlesden-Popper	100	99.8	98.9	96.6
	Perovskite	-	0.2	-	0.6
	$SrSO_4$	-	-	1.1	2.9

Table 21. Cell parameters (space group *I*4*/mmm*) and site occupancy factors for $Sr_4Fe_2Co_{1-x}S_xO_{10-\delta}$ (heating in air). The impurity phases, $SrFeO_{3-\delta}$ and $SrSO_4$ were refined in the cubic space group, $Pm\bar{3}m$ and orthorhombic space group, *Pnma* respectively

$Sr_4Fe_2Co_{1-x}S_xO_{10-\delta}$					
S (x)		0.2	0.3	0.4	0.5
a (Å)		3.8656(1)	3.8690(1)	3.8716(1)	3.8754(1)
c (Å)		28.3586(9)	28.4710(8)	28.5155(8)	28.5559(9)
V (Å^3)		423.77(3)	426.18(2)	427.43(3)	428.87(3)
Rwp (%)		2.04	1.92	1.90	3.29
Rexp (%)		1.27	1.29	1.28	1.30
Fe/Co1 occupancy (middle perovskite layer)		0.79(5)	0.74(4)	0.55(4)	0.58(8)
S1 occupancy (middle perovskite layer)		0.21(5)	0.26(4)	0.45(4)	0.42(8)
O occupancy		9.30	9.30	9.80	9.66
Weight percentage (%)	Ruddlesden-Popper	99.8	96.8	93.0	85.8
	Perovskite	0.2	3.2	2.8	5.5
	$SrSO_4$	-	-	4.2	8.7

6.4 Neutron diffraction results

$Sr_4Fe_2Co_{0.8}S_{0.2}O_{10-\delta}$ was further examined by neutron diffraction and data analysed using the Rietveld refinement method. Refinement profiles and structural data can be found in Figure 83 and Table 22 respectively. As observed from XRD studies, $SrFeO_{3-\delta}$ impurity peaks were present in ND data with additional peaks due to the n=2 Ruddlesden-Popper phase, $Sr_3Fe_2O_{7-\delta}$. As observed for $Sr_4Fe_{3-x}S/Cr_xO_{10-\delta}$[164,165] the higher resolution of the ND data suggests that the sample is actually composed of two similar n=3 Ruddlesden-Popper phases. The two Ruddlesden-Popper phases were allowed to refine with different cell parameters, whereas atomic coordinates, atomic displacement parameters, site occupancies and strain parameters

were constrained to be equal. Due to S and Co having similar scattering factors, site occupancies for S were fixed at 0.2 with Fe/Co occupancies allowed to refine. For Fe1 and Co1 occupancies were constrained to 0.8 and Fe2 and Co2 constrained to 1.

From the structural data it can be seen that the two Ruddlesden-Popper phases have different cell parameters, suggesting a small difference in composition, as observed for $Sr_4Fe_{3-x}S/Cr_xO_{10-\delta}$. ND suggests Co is incorporated into both iron sites with the overall occupancy being higher than expected. As reported for the other Ruddlesden-Popper phases oxygen vacancies are predominately located surrounding sulfate (O1 and O2).

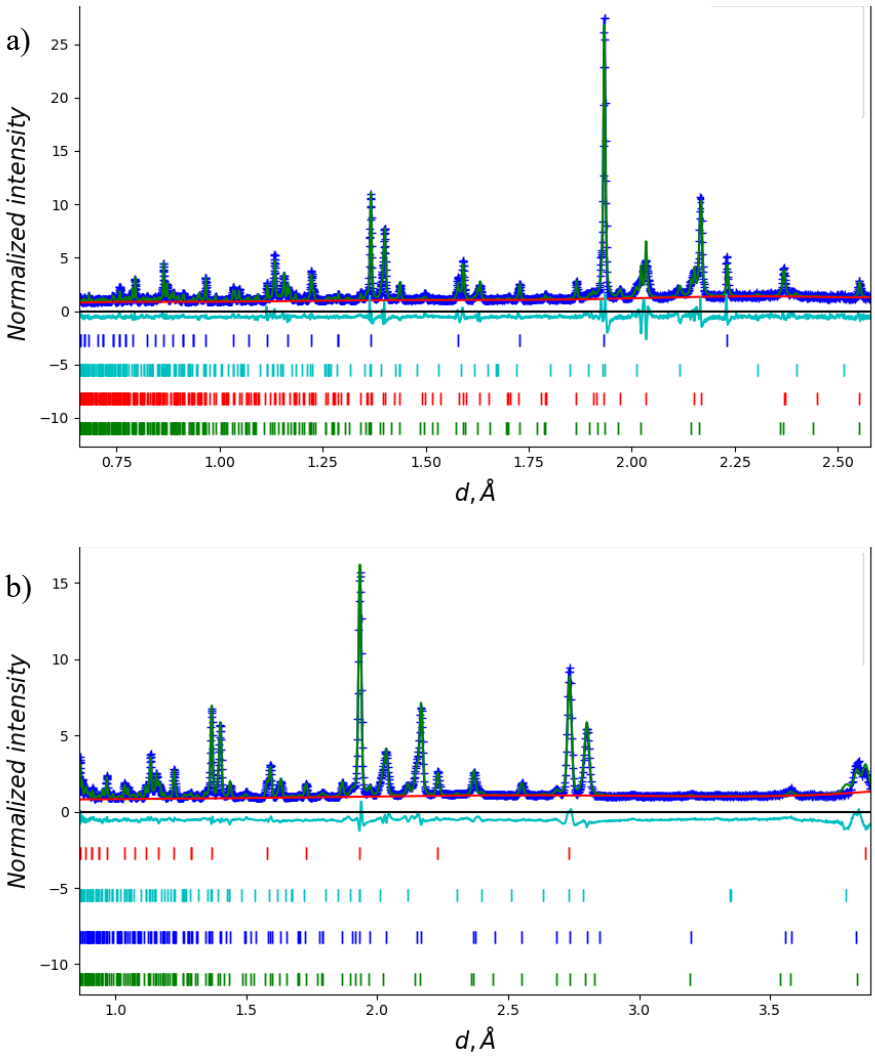

Figure 83. Observed (dark blue), calculated (green) and difference (light blue) neutron diffraction profiles for $Sr_4Fe_{1.75}Co_{1.08}S_{0.16}O_{8.27}$ a) Bank 1 and b) Bank 2. Phases (coloured ticks) are presented from top to bottom as $SrFeO_{3-\delta}$, $Sr_3Fe_2O_{7-\delta}$, Ruddlesden-Popper phase 1 and Ruddlesden-Popper phase 2.

Table 22. Refined structural parameters for $Sr_4Fe_{1.75}Co_{1.08}S_{0.16}O_{8.27}$ with two tetragonal Ruddlesden-Popper phases refined with space group *I*4/*mmm*. Additional impurity phases tetragonal $Sr_3Fe_2O_{7-\delta}$ (*I*4/*mmm*) and $SrFeO_{3-\delta}$ ($Pm\bar{3}m$) were included in the room temperature neutron diffraction data.

	Ruddlesden-Popper Phases		**$Sr_3Fe_2O_{7-\delta}$**	**$SrFeO_{3-\delta}$**
	Phase 1	**Phase 2**		
a (Å)	3.8655(1)	3.8678(2)	3.8598(5)	3.8642(1)
c (Å)	28.4758(9)	28.3084(16)	20.1003(25)	-
V (Å^3)	425.50(3)	423.49(5)	299.46(7)	57.70(1)
Weight Percent (%)	50.8	27.8	10.3	11.1
R_{wp}		**R_{exp}**		**GOF**
6.79%		1.94%		3.52

Ruddlesden Popper

	x	y	z	Occ	U_{iso}
Sr1	0.0000	0.0000	0.4229(2)	1.000	0.0136(6)
Sr2	0.0000	0.0000	0.2967(1)	1.000	
Fe1	0.0000	0.0000	0.0000	0.22(1)	
Co1	0.0000	0.0000	0.0000	0.58(1)	
S1	0.0000	0.0000	0.0000	0.20	0.0050(7)
Fe2	0.0000	0.0000	0.1444(1)	0.78(1)	
Co1	0.0000	0.0000	0.1444(1)	0.22(1)	
O1	0.0000	0.5000	0.0000	0.44(1)	
O2	0.0000	0.0000	0.0641(2)	0.85(1)	0.0146(4)
O3	0.0000	0.5000	0.1366(1)	1.000	
O4	0.0000	0.0000	0.2104(1)	0.85(1)	

6.5 Stability in low p(O_2)

The stability of the $Sr_4Fe_2(Co/Cu)_{1-x}S_xO_{10-\delta}$ samples were tested in N_2 to 800 °C for 12 h. The $Sr_4Fe_2(Co/Cu)_{1-x}S_xO_{10-\delta}$ phases appear to remain stable for x=0.3-0.5, with broadening for x=0.3 suggesting partial breaking down of the structure to produce $Sr_3Fe_2O_{7-\delta}$ (Figure 84). At low dopant levels for both Co/Cu phases, broadening of XRD data also suggests partial break down of the n=3 Ruddlesden-Popper structure as for x=0.3.

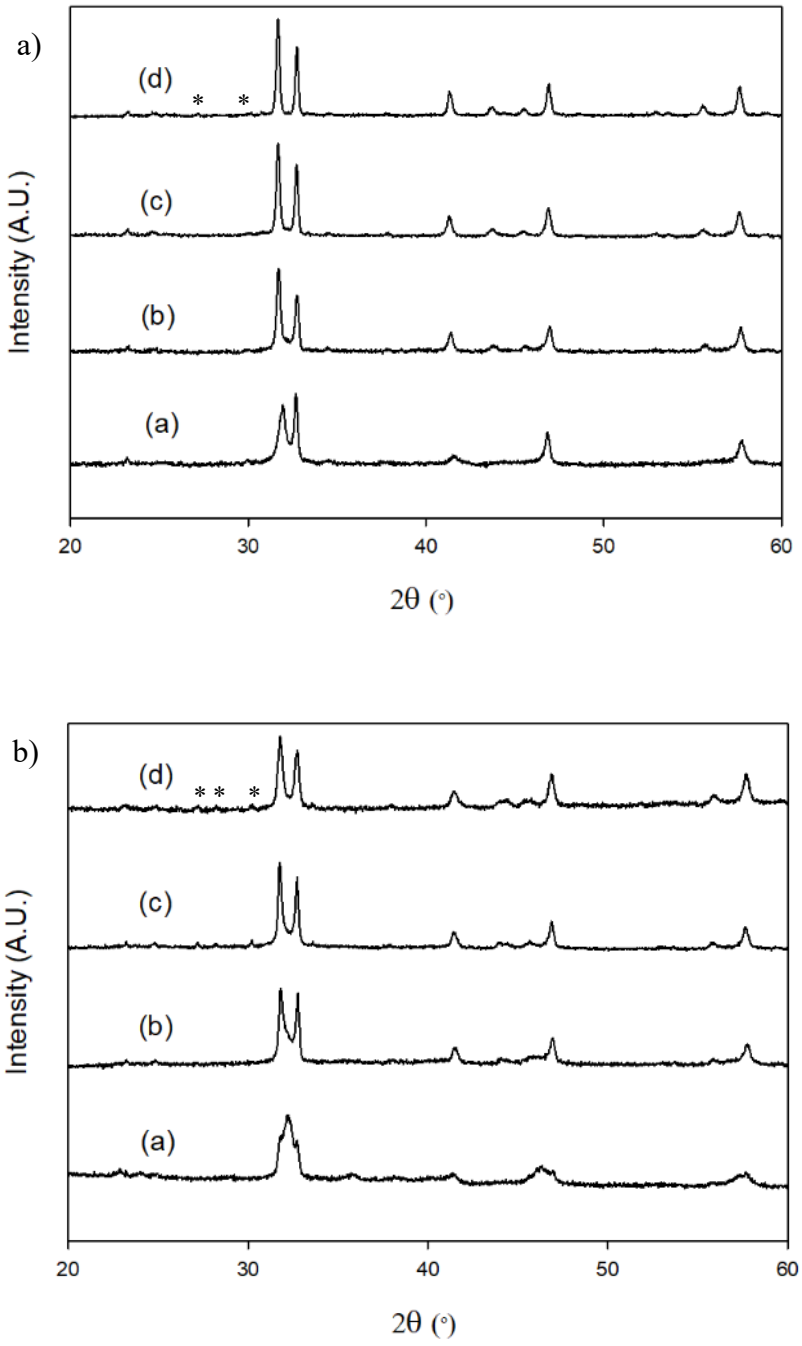

Figure 84. X-ray diffraction patterns for a) $Sr_4Fe_2Cu_{1-x}S_xO_{10-\delta}$ and b) $Sr_4Fe_2Co_{1-x}S_xO_{10-\delta}$ where a) x = 0.2, b) x = 0.3, c) x = 0.4 d) 0.5 after heat treatment in N_2 to 800 °C. $SrSO_4$ impurities are highlighted by an asterisk.

Unit cell parameters were calculated through Rietveld refinements of XRD data. Overall an increase in unit cell volume is observed (Figure 85) when heating in N_2 to 800 °C compared with samples synthesised in air. This is predicted to be due to the reduction of Fe^{4+}/Co^{4+} to Fe^{3+}/Co^{3+}. With increasing S content, a clear trend is not observed for $Sr_4Fe_2Cu_{1-x}S_xO_{10-\delta}$ heated in N_2.

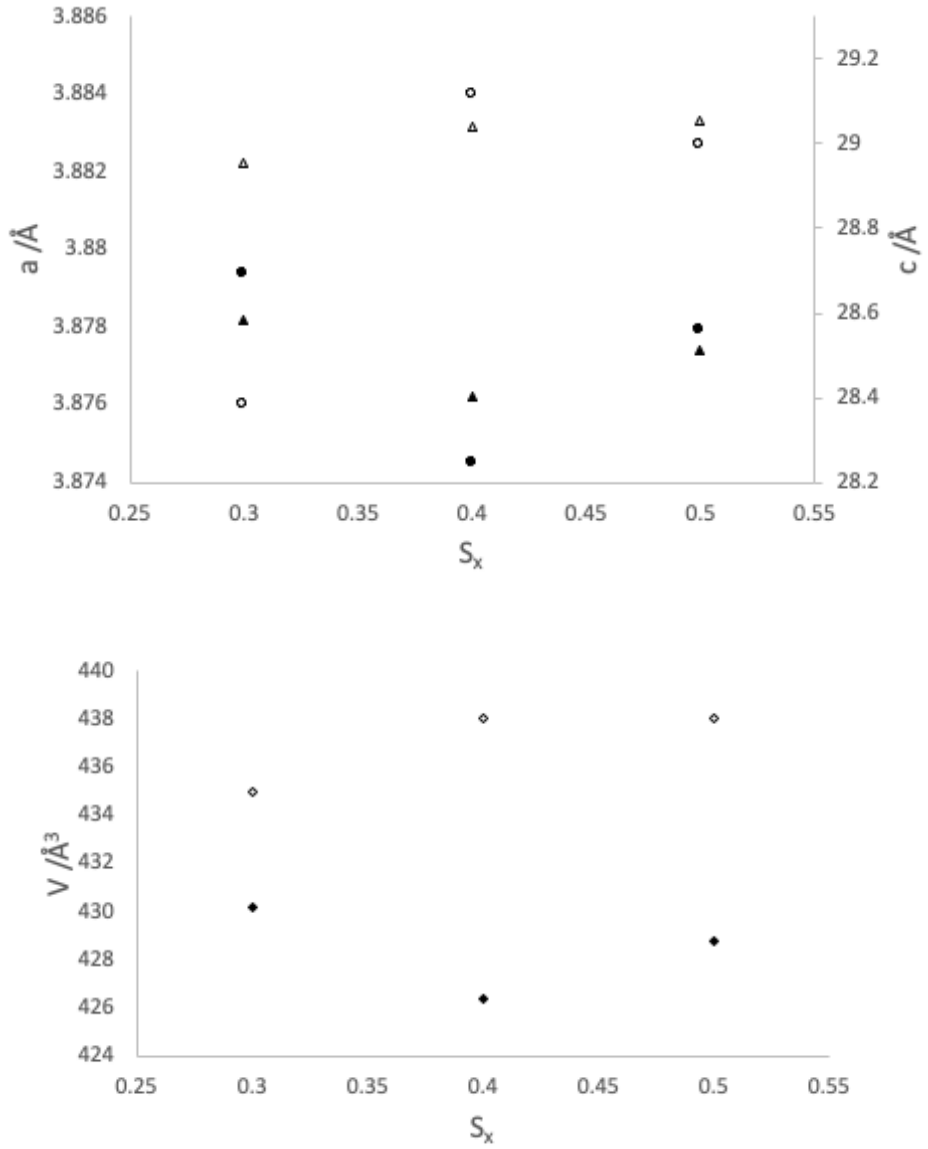

Figure 85. Variation of lattice parameters with sulfate content, x for $Sr_4Fe_2Cu_{1-x}S_xO_{10-\delta}$ heated in air (filled markers) and N_2 to 800 °C (empty markers) where a = ●/○, c = ▲/△ and V = ◆/◇

A similar trend is observed (Figure 86) for $Sr_4Fe_2Co_{1-x}S_xO_{10-\delta}$ where an increase in unit cell volume of samples heated in N_2 compared to air synthesized is expected to be due to the reduction of Fe^{4+}/Co^{4+}.

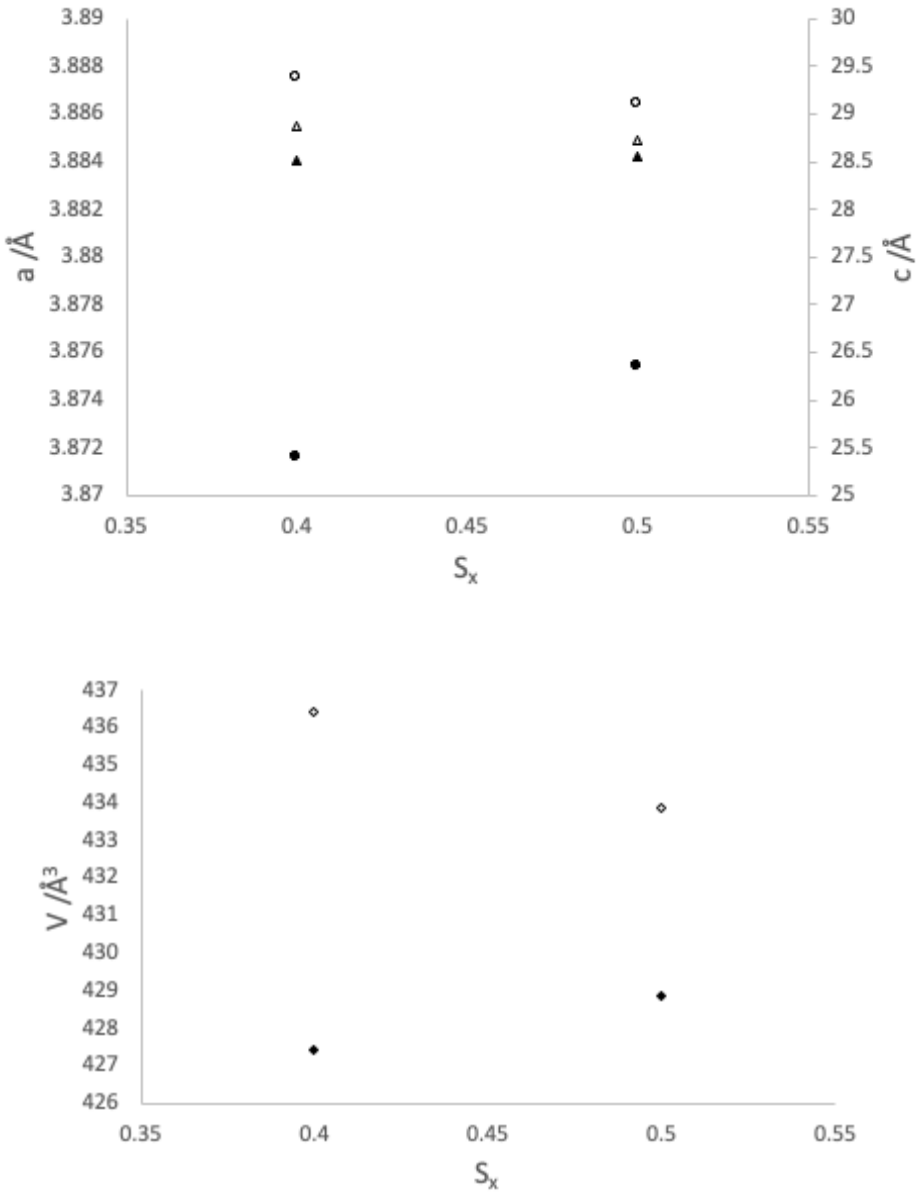

Figure 86. Variation of lattice parameters with sulfate content, x for $Sr_4Fe_2Co_{1-x}S_xO_{10-\delta}$ heated in air (filled markers) and N_2 to 800 °C (empty markers) where a = ●/○, c = ▲/△ and V = ◆/◇

6.6 Stability in wet N_2

In order to test the suitability for use in proton conducting SOFCs, samples were heated in wet N_2 to 800 °C for 12 h. As observed when heating in dry N_2, samples with higher S levels appear to remain stable with peak broadening observed for low dopant levels (Figure 87). As observed for the air treated samples, reflections associated with $SrSO_4$ impurities are present at high dopant levels. Previously, broadening of XRD data for $Sr_4Fe_{3-x}(S/Cr/B)_xO_{10-\delta}$ phases suggest the possibility of water incorporation into the n=3 Ruddlesden-Popper phases. Further work would be needed in order to determine if broadening is due to the partial breakdown of the Ruddlesden-Popper structure or incorporation of water.

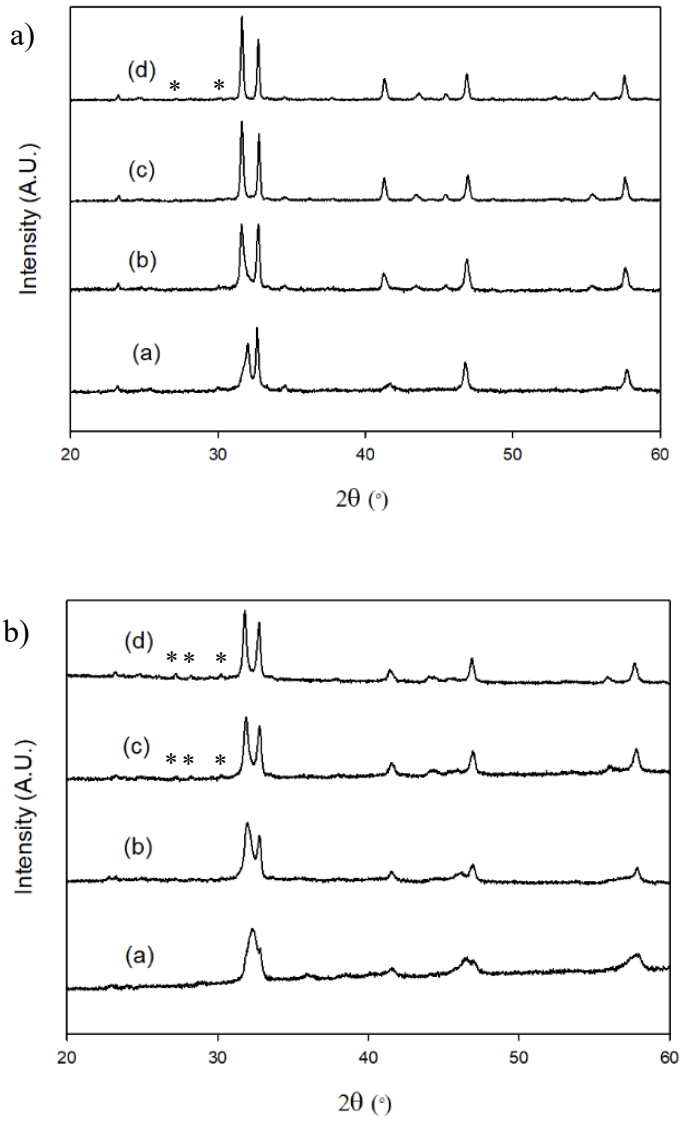

Figure 87. X-ray diffraction patterns for a) $Sr_4Fe_2Cu_{1-x}S_xO_{10-\delta}$ and b) $Sr_4Fe_2Co_{1-x}S_xO_{10-\delta}$ where a) x = 0.2, b) x = 0.3, c) x = 0.4 and d) x = 0.5 after heat treatment in wet N_2 to 800 °C. $SrSO_4$ impurities are highlighted by an asterisk.

Lattice parameters for $Sr_4Fe_2(Cu/Co)_{1-x}S_xO_{10-\delta}$ heated in wet N_2 were calculated through Rietveld refinements of XRD data. An increase in unit cell volume is observed (Figure 88) when heating in wet N_2 compared to dry N_2, supporting the incorporation of water into these Ruddlesden-Popper phases.

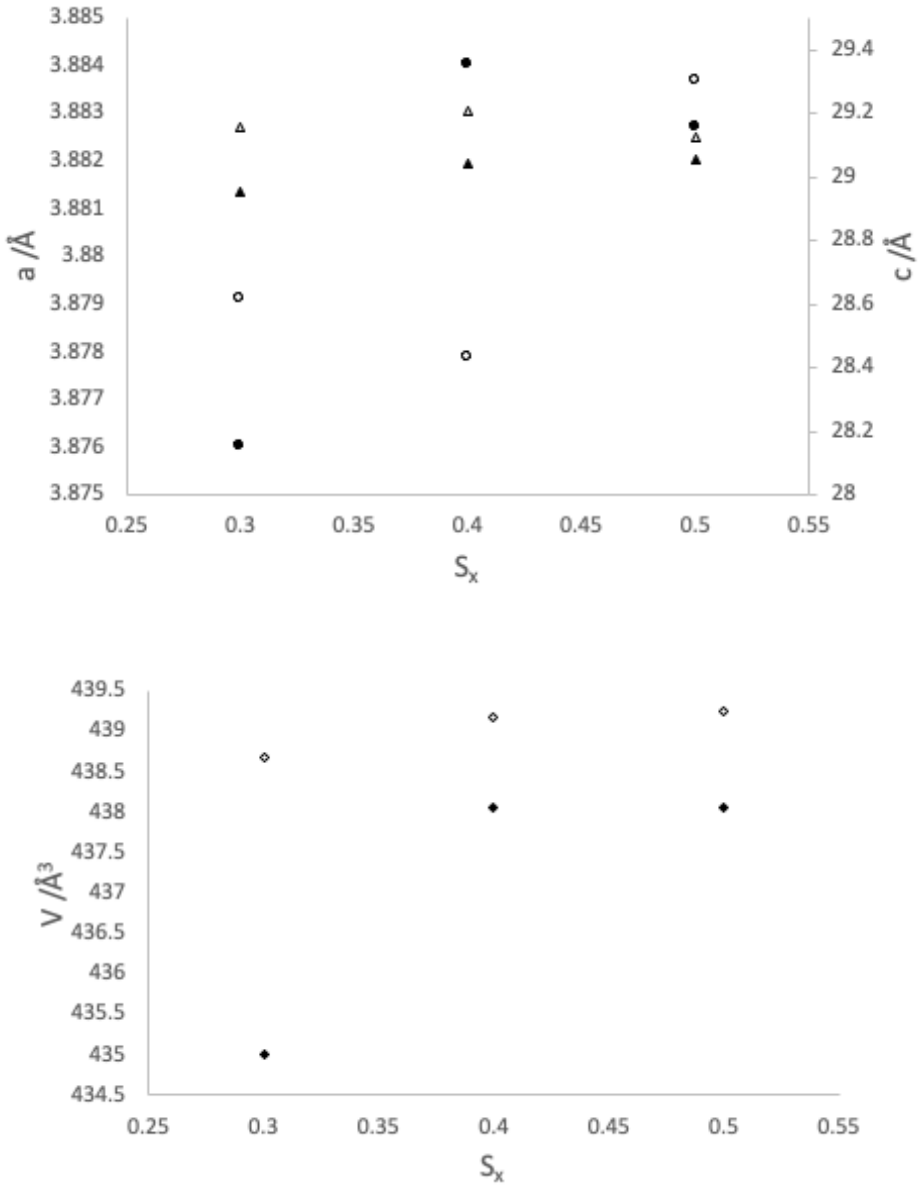

Figure 88. Variation of lattice parameters with sulfate content, x for $Sr_4Fe_2Cu_{1-x}S_xO_{10-\delta}$ heated in dry N_2 (filled markers) and wet N_2 (empty markers) to 800 °C where a = ●/○, c = ▲/△ and V = ◆/◇

In comparison, $Sr_4Fe_2Co_{1-x}S_xO_{10-\delta}$ phases report a decrease in unit cell volume when heating in wet N_2 to 800 °C compared with dry N_2 (Figure 89). This therefore suggests water is not incorporated into the Co phases. Further work would be needed to investigate in more detail the incorporation of water.

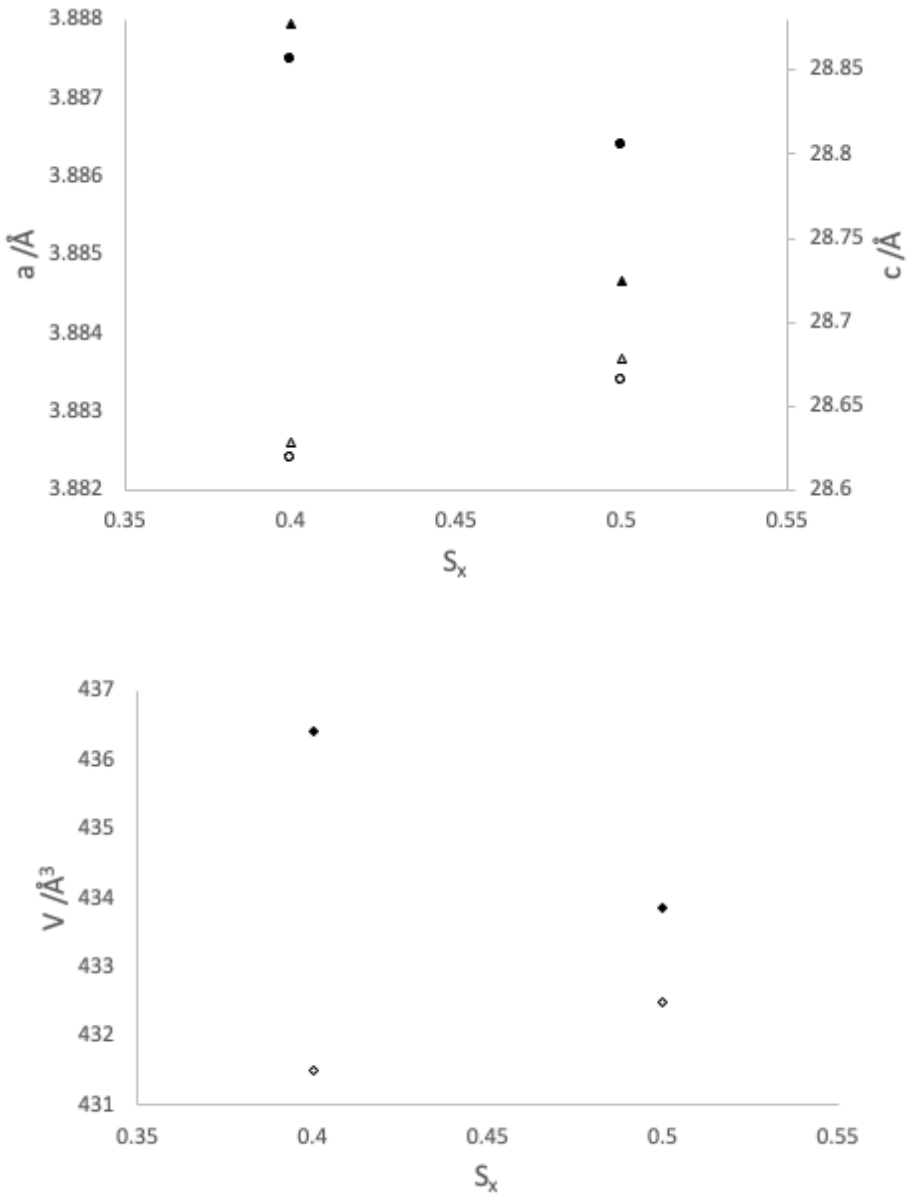

Figure 89. Variation of lattice parameters with sulfate content, x for $Sr_4Fe_2Co_{1-x}S_xO_{10-\delta}$ heated in dry N_2 (filled markers) and wet N_2 (empty markers) to 800 °C where a = ●/○, c = ▲/△ and V = ◆/◇

6.7 Conductivity studies

The conductivity data showed an initial increase in conductivity for the $Sr_4Fe_2Cu_{1-x}S_xO_{10-\delta}$ phases with increasing temperature indicative of the expected semiconducting behaviour

(Figure 90). At higher temperatures (≈550 °C) a decrease in conductivity with increase in temperature is observed. Generally, an increase in sulfate content results in an increase in conductivity up to x=0.4 at low temperatures with the highest conductivity observed for x=0.3 at temperatures greater than ≈ 480 °C.

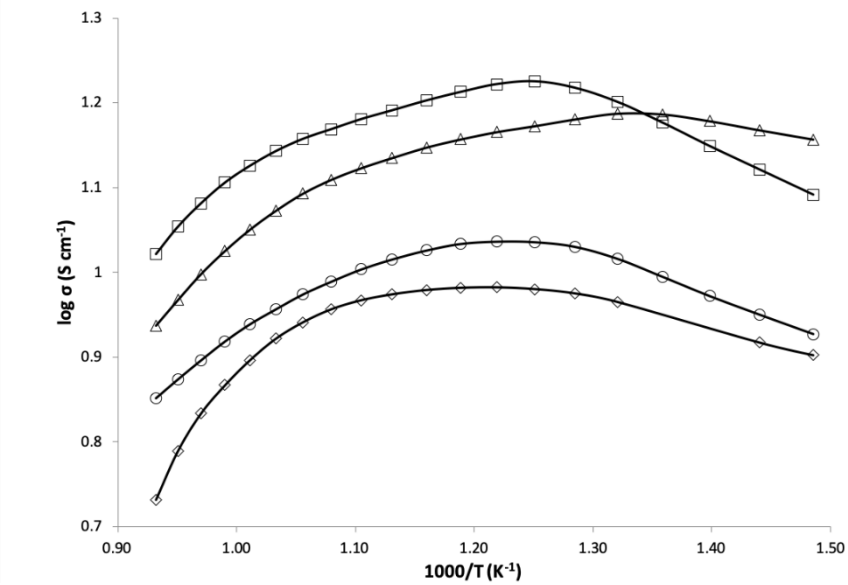

Figure 90. Plot of log σ vs. 1000/T for $Sr_4Fe_2Cu_{1-x}S_xO_{10-\delta}$ where x = 0.2 (○), 0.3 (□), 0.4 (△), 0.5 (◇)

The $Sr_4Fe_2Co_{1-x}S_xO_{10-\delta}$ phases (Figure 91) showed similar conductivity values between ≈ 400 and 650 °C, while at high temperatures all phases show a small decrease in conductivity. This decrease in conductivity at high temperatures is predicted to be due to loss of oxygen. As observed for $Sr_4Fe_2Cu_{1-x}S_xO_{10-\delta}$, an initial increase in conductivity is observed for x=0.3 with a decrease in conductivity with further increases in sulfate content. This is as reported for silicate[111] and sulfate[159] doped $SrFeO_{3-\delta}$ materials, where the decrease in conductivity at higher dopant levels is predicted to be due to disruption of the transition metal-O network.

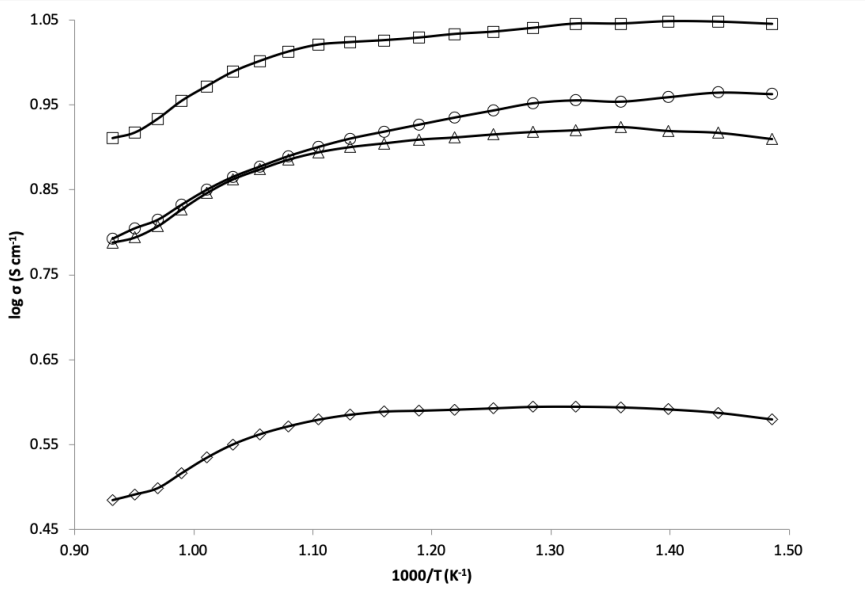

Figure 91. Plot of log σ vs. 1000/T for $Sr_4Fe_2Co_{1-x}S_xO_{10-\delta}$ where x = 0.2 (○), 0.3 (□), 0.4 (△), 0.5 (◇)

Comparing the data for $Sr_4Fe_{3-x}S_xO_{10-\delta}$ and $Sr_4Fe_2(Cu/Co)_{1-x}S_xO_{10-\delta}$ (Figure 92), the results show an improvement in conductivity between 400 – 800 °C for the Co/Cu doped systems. In general, the $Sr_4Fe_2(Cu/Co)_{1-x}S_xO_{10-\delta}$ phases are found to have conductivities in a similar range with the highest conductivity observed for $Sr_4Fe_2Cu_{0.7}S_{0.3}O_{10-\delta}$. Despite the increase in conductivity on Cu/Co doping, these sulfate doped Ruddlesden-Popper phases still have lower conductivities compared with common SOFC materials. Therefore, further work would be needed to further improve this in order for these materials to be used as SOFC cathode materials.

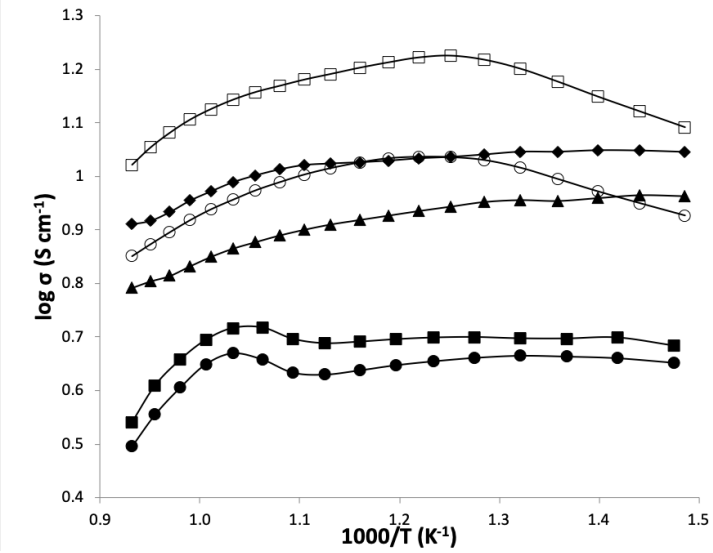

Figure 92. Plot of log σ vs. 1000/T for $Sr_4Fe_{3-x}S_xO_{10-\delta}$[164] (x = 0.2 (●), 0.3 (■)), $Sr_4Fe_{3-x}Cu_{1-x}S_xO_{10-\delta}$ (x = 0.2 (○), 0.3 (□)) and $Sr_4Fe_{3-x}Co_{1-x}S_xO_{10-\delta}$ (x = 0.2 (▲), 0.3 (◆))

6.8 Conclusions

This work has shown that in addition to incorporating sulfate into $Sr_4Fe_3O_{10-\delta}$ as previously shown, improvements in the conductivity can be made by additionally doping with Cu/Co. As reported for $Sr_4Fe_{3-x}S_xO_{10-\delta}$, XRD data for $Sr_4Fe_2(Cu/Co)_{1-x}S_xO_{10-\delta}$ suggests incorporation of sulfate into the middle perovskite layer with potential additional occupancy on Fe2 at higher dopant levels. Although the conductivities and stabilities are improved, the reported conductivities are still lower than traditional perovskite cathode materials, and so further work is needed to optimise these materials for SOFC applications.

Table 23. Chapter 6 summary table

Sample	Crystal system (Synthesis temperature)	Stability	Highest conductivity (Temperature)
$Sr_4Fe_2Cu_{1-x}S_xO_{10-\delta}$ where x= 0.2, 0.3, 0.4 and 0.5	Tetragonal (1075 °C with anneal at 350 °C)	**Stability in low p(O_2)** - Low dopant levels suggest partial breakdown of structure - x=0.3-0.5 appear to remain stable in XRD data **Stability in wet N_2** - Broadening of XRD data at low dopant levels - Higher dopant levels appear to remain stable	10-17 S cm^{-1} (484-547 °C)
$Sr_4Fe_2Co_{1-x}S_xO_{10-\delta}$ where x= 0.2, 0.3, 0.4 and 0.5	Tetragonal (1075 °C with anneal at 350 °C)	**Stability in low p(O_2)** - Low dopant levels suggest partial breakdown of structure - x=0.3-0.5 appear to remain stable in XRD data **Stability in wet N_2** - Broadening of XRD data at low dopant levels - Additional reflections associated with $SrSO_4$ impurities at high dopant levels	4-11 S cm^{-1} (421-484 °C)

7 Synthesis and characterisation of oxyanion doped "0201-1201" type layered oxide, $Sr_{4.5}Fe_2(S/Cr)_{0.5}O_{9\pm\delta}$

7.1 Introduction

Perovskite and perovskite-type materials have attracted considerable interest due to their interesting properties and range of applications. The perovskite structure has the general formula ABX_3, where A and B are cations and X an anion. In addition to the standard perovskite, ABX_3, a number of perovskite-type materials have been investigated including a range of intergrowths of the perovskite structure. An example of the latter is the compound, $TlBa_{2-x}La_{2+x}Cu_2O_9$ which has a structure consisting of a regular intergrowth of "1201" ($TlBa_2CuO_5$) and "0201" (La_2CuO_4) type structures.[188] Cuprate materials commonly use shorthand notation e.g. 1201 and 0201 where each digit is used to define the structure. A more detailed description on the nomenclature used for these materials is discussed by Fisk et al.[189] Subsequently related structures were observed for non-cuprate materials with a new layered oxide structure $Sr_{4.5}Cr_{2.5}O_9$, reported by Pelloquin et al.[190] which is derived from the "0201-1201" type, $TlBa_{2-x}La_{2+x}Cu_2O_9$.[188] This structure has $[(Sr_{0.5}Cr_{0.5})O]$ layers alternating with Cr(III) mixed octahedral-pyramidal layers. Within the structure 3 different chromium sites are observed including tetrahedral Cr^{6+}, octahedral Cr^{3+} and pyramidal Cr^{3+} (Figure 93).

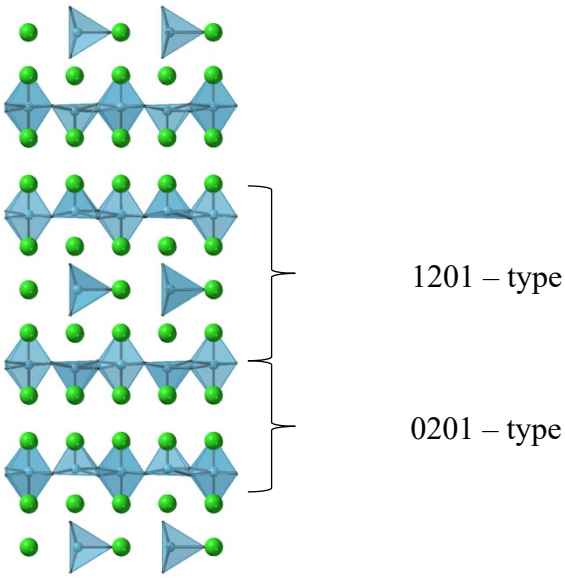

Figure 93. Structure of layered oxide, $Sr_{4.5}Cr_{2.5}O_9$[190], showing chromium polyhedra (blue) and strontium atoms (green)

Oxyanion incorporation has not only been investigated in more recent publications for perovskite type SOFC materials, but has previously been investigated in many perovskite-type cuprate materials.[98,99,150,152–156,191,192] For example sulfate/ phosphate has successfully been incorporated into the superconducting cuprate material, $Y(Ba/Sr)_2Cu_3O_{7-\delta}$ as shown by Slater et al.[99] As shown in this thesis and also by others, successful stabilisation of oxide materials through oxyanion doping has been reported. A key aim of this research was to expand not only oxyanion incorporation into perovskite materials, but also perovskite type materials. Due to the successful incorporation of sulfate and chromate into $Sr_4Fe_3O_{10-\delta}$ materials, these oxyanions were further investigated in chapter 7. In this study we investigate the incorporation of oxyanions (sulfate and chromate) into $Sr_{4.5}Fe_2(Cr/S)_{0.5}O_{9\pm\delta}$ with a view to examining the potential use of these materials for SOFC applications. These phases were identified through unsuccessful attempts to substitute sulfate/chromate into the n=1 Ruddlesden-Popper system, Sr_2FeO_4.

7.2 Experimental

$Sr_{4.5}Fe_2Cr_{0.5}O_{9\pm\delta}$ and $Sr_{4.5}Fe_2S_{0.5}O_{9\pm\delta}$ were prepared through solid state synthesis. Stoichiometric amounts of $SrCO_3$, Fe_2O_3 and either $(NH_4)_2SO_4$ or Cr_2O_3 were ground and heated to 950 °C (4 °C/ min) for 12 h. After the initial heat treatment, $Sr_{4.5}Fe_2Cr_{0.5}O_{9\pm\delta}$ and $Sr_{4.5}Fe_2S_{0.5}O_{9\pm\delta}$ were ball milled for 1 h at 350 rpm (Fritsch Pulverisette 7 planetary Mill). Samples were then reheated to 1000 °C for 12 h before regrinding and heating to 1050 °C for 12 h. Finally, to ensure maximum oxygen content, samples were heated to 350 °C for 12 h.

Powder XRD were collected for all samples with GSAS suite of programs used for structure refinements.[136] XRD data was used to confirm phase purity and to characterise cell parameters. Time of flight neutron powder diffraction (TOF NPD) data were collected for $Sr_{4.5}Fe_2Cr_{0.5}O_{9\pm\delta}$ and $Sr_{4.5}Fe_2S_{0.5}O_{9\pm\delta}$ at room temperature on the HRPD diffractometer at the ISIS pulsed spallation source (Rutherford Appleton Laboratory, UK). Rietveld refinements of the structures using the XRD and NPD data employed the GSAS suite of programs.[136]

TGA experiments were carried out under N_2 up to 800 °C using a Netzch STA 449 F1 Jupiter Thermal Analyser with mass spectrometry attachment.

Cr K-edge X-ray absorption spectroscopy (XAS) spectra were collected on beamline B18 at Diamond Light Source (Rutherford Appleton Lab, Harwell, UK). In addition to standard materials $LaCrO_3$ and $SrCrO_4$, XAS spectra for $Sr_{4.5}Fe_2Cr_{0.5}O_{9\pm\delta}$ was also collected. The Athena Software package was used for data processing.[138]

The ^{57}Fe Mössbauer spectra were recorded at 298 K in constant acceleration mode using approximately 25 mCi Co/Rh source.

In order to test the potential for use as cathode materials for SOFCs, four probe dc conductivity measurements were carried out. Pellets were prepared by ballmilling at 350 rpm for 1 h before pressing into pellets and sintering at 1050 °C for 12 h. Four Pt electrodes were

attached to the pellets with Pt paste and heated to 900 °C for 1 h in air. To ensure full oxygenation, pellets were finally annealed at 350 °C for 12 h.

7.3 Results and discussion

7.3.1 X-ray Diffraction

X-ray diffraction studies indicated successful synthesis of $Sr_{4.5}Fe_2Cr_{0.5}O_{9\pm\delta}$ and $Sr_{4.5}Fe_2S_{0.5}O_{9\pm\delta}$, forming the "0201-1201" type structure as reported for $Sr_{4.5}Cr_{2.5}O_9$.[190] In addition to the "0201-1201" type phase, XRD patterns indicated small impurities of $Sr_3Fe_2O_{7-x}$ present in both samples, and $SrSO_4$ for $Sr_{4.5}Fe_2S_{0.5}O_{9\pm\delta}$ (Figure 94).

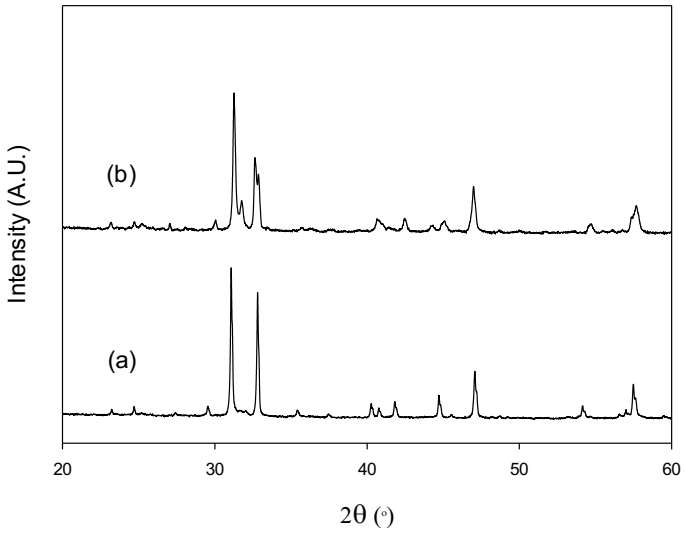

Figure 94. X-ray diffraction patterns for a) $Sr_{4.5}Fe_2Cr_{0.5}O_{9\pm\delta}$ and b) $Sr_{4.5}Fe_2S_{0.5}O_{9\pm\delta}$

Rietveld refinements were carried out using the XRD data where the primary phase was fitted with the space group $A2_1am$. Lattice parameters and sample displacement parameters were refined for all samples. For all sites atom positions and oxygen occupancies were refined. Thermal parameters were constrained for Sr, Fe/Cr/S and O sites and fixed due to the high correlation with site occupancies. For $Sr_{4.5}Fe_2S_{0.5}O_{9\pm\delta}$, Fe/S occupancies were

allowed to refine (with the constraint that the total occupancy was 1) whereas Fe/Cr site occupancies were set at the expected values due to the X-ray scattering factors of chromium and iron being similar. Overall a smaller unit cell volume is observed for the sulfate doped samples, which is as expected due to the smaller ionic radii of S^{6+} compared to Cr^{6+}. Additionally, a higher percentage of $Sr_3Fe_2O_{7-x}$ impurities was observed in the sulfate doped samples.

Table 24 Lattice parameters (space group $A2_1am$) for $Sr_{4.5}Fe_2Cr_{0.5}O_{9\pm\delta}$ and $Sr_{4.5}Fe_2S_{0.5}O_{9\pm\delta}$. Additional impurity phases $Sr_3Fe_2O_{7-x}$ and $SrSO_4$ were included in the refinement.

		$Sr_{4.5}Fe_2Cr_{0.5}O_{9\pm\delta}$	$Sr_{4.5}Fe_2S_{0.5}O_{9\pm\delta}$
a (Å)		10.9095(33)	10.8928(6)
b (Å)		5.4548(17)	5.4815(3)
c (Å)		30.1990(9)	29.7524(20)
V (Å^3)		1797.11(11)	1776.47(25)
R_{wp} (%)		2.24	2.34
R_{exp}(%)		1.33	1.31
Weight percentage (%)	**$Sr_{4.5}Fe_2(S/Cr)_{0.5}O_{9\pm\delta}$**	97.2	85.3
	$Sr_3Fe_2O_7$	2.8	10.7
	$SrSO_4$	-	4.0

In order to gain more information on the structure and iron environments in $Sr_{4.5}Fe_2S_{0.5}O_{9\pm\delta}$ and $Sr_{4.5}Fe_2Cr_{0.5}O_{9\pm\delta}$, larger (5g) samples were prepared for analysis by neutron powder diffraction, XAS and ^{57}Fe Mössbauer spectroscopy. The neutron diffraction refinements for these larger samples suggested higher $Sr_3Fe_2O_{7-x}$ impurities (see later) than for the original smaller sample studied by X-ray diffraction.

7.3.2 X-ray absorption spectroscopy

XAS analysis was carried out on $Sr_{4.5}Fe_2Cr_{0.5}O_{9\pm\delta}$ in order to determine the oxidation state and environment of chromium in this system. In addition to $Sr_{4.5}Fe_2Cr_{0.5}O_{9\pm\delta}$, Cr foil, $LaCrO_3$ and $SrCrO_4$ were measured as reference materials.

From the XANES data (Figure 95) a sharp pre-edge is observed ≈ 5993 eV for $SrCrO_4$ (Cr^{6+}) which is not observed for $LaCrO_3$ (Cr^{3+}). In comparison to the reference materials, $Sr_{4.5}Fe_2Cr_{0.5}O_{9\pm\delta}$ shows a sharp pre-edge as observed for $SrCrO_4$, suggesting Cr^{6+} in a tetrahedral environment. This is as expected due to occupancy of the tetrahedral site reported in the ND refinements (see later). In comparison to $SrCrO_4$, the pre-edge for $Sr_{4.5}Fe_2Cr_{0.5}O_{9\pm\delta}$ shows a decrease in intensity suggesting possible distortions to the Cr geometry. Further work would be needed to investigate this in more detail.

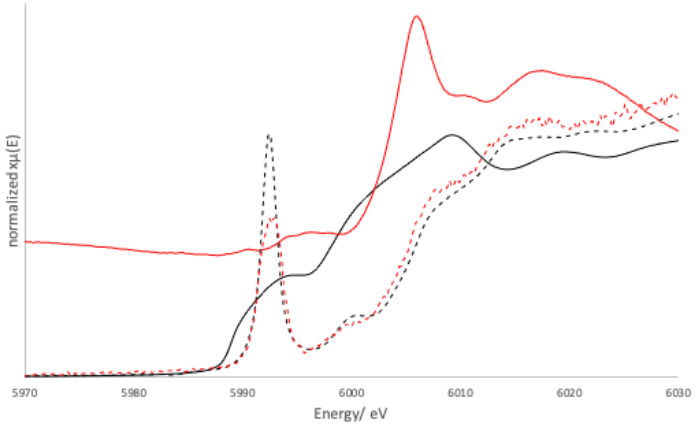

Figure 95. XANES data obtained for Cr foil (black solid line), $LaCrO_3$ (red solid line), $SrCrO_4$ (black dashed line) and $Sr_{4.5}Fe_2Cr_{0.5}O_{9\pm\delta}$ (red dashed line)

7.3.3 ^{57}Fe Mössbauer spectroscopy

The components in the Mössbauer spectra with negative chemical isomer shifts (δ) and that with a value of *ca*. 0.32 mms^{-1} indicate the presence of Fe^{5+} and Fe^{3+} with the component at ca. 0.19-0.29 mms^{-1} indicating that some of Fe^{3+} appears to be in lower than octahedral coordination or be related to $Fe^{3.5+}$. Previous oxyanion doping studies in perovskite and Ruddlesden-Popper materials has shown that by doping with smaller oxyanions, strain is introduced which can be relieved by disproportionation of Fe^{4+} to Fe^{3+} and Fe^{5+}.[111,164,165,175,176] This further supports the incorporation of higher valence S/Cr.

In terms of the Fe^{5+} component this appears to be largest for the Cr-containing material. This is consistent with the higher proportion of $Sr_3Fe_2O_{7-x}$ impurity seen in this larger (5g) sample (see section 7.3.4). Both S and Cr phases have significant $Sr_3Fe_2O_{7-x}$ impurities which are predicted to have an impact on the calculated Fe oxidation state and in turn the calculated oxygen content. Due to this impurity the calculated oxygen contents (≈ 9.4 ($Sr_{4.5}Fe_2S_{0.5}O_{9\pm\delta}$) and ≈ 9.7 ($Sr_{4.5}Fe_2Cr_{0.5}O_{9\pm\delta}$)) are higher than expected. Using neutron diffraction Rietveld refinement data, the fraction of $Sr_3Fe_2O_{7-x}$ impurity can be estimated and therefore the oxygen content recalculated (assuming x=0.3 for $Sr_3Fe_2O_{7-x}$[193]) to be ≈ 9.1 for both phases. The oxygen contents calculated indicate a higher value than observed for $Sr_{4.5}Cr_{2.5}O_9$, suggesting the presence of additional oxygen in interstitial sites; this is further investigated in section 7.3.4.

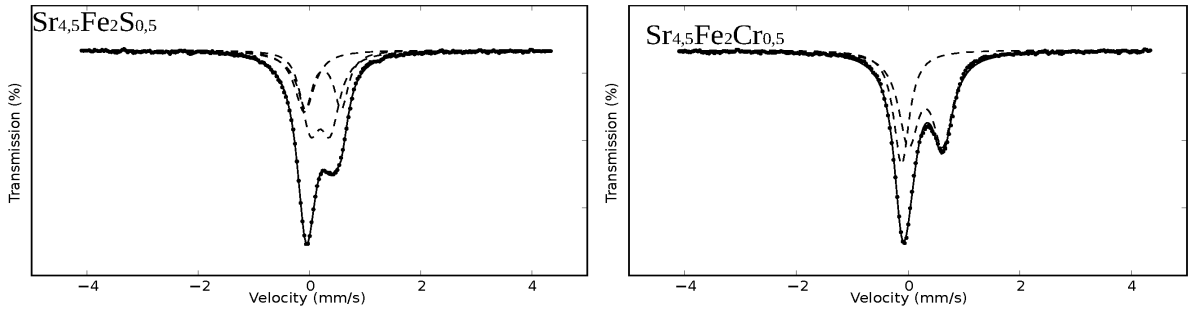

Figure 96. ^{57}Fe Mössbauer spectra recorded from $Sr_{4.5}Fe_2S_{0.5}O_{9\pm\delta}$ and $Sr_{4.5}Fe_2Cr_{0.5}O_{9\pm\delta}$ at 298K

Table 25. ^{57}Fe Mössbauer parameters recorded from $Sr_{4.5}Fe_2S_{0.5}O_{9\pm\delta}$ and $Sr_{4.5}Fe_2Cr_{0.5}O_{9\pm\delta}$ at 298K, where isomer shift and quadrupole splitting are given by δ and Δ respectively.

Compound	**Assignment**	**δ ± 0.01 (mms^{-1})**	**Δ ± 0.05 (mms^{-1})**	**Area ± 5% (%)**
$Sr_{4.5}Fe_2S_{0.5}O_{9\pm\delta}$	Fe^{5+}	-0.09	X	22
	Fe^{3+} in low	0.19	0.36	48
	coordination	0.25	0.65	30
$Sr_{4.5}Fe_2Cr_{0.5}O_{9\pm\delta}$	Fe^{5+}	-0.13	X	34
	Fe^{3+}	0.32	0.71	39
	Fe^{3+} in low coordination	0.29	0.41	27

7.3.4 Neutron diffraction results

Neutron diffraction (ND) studies were carried out in order to determine more detailed structural information of the materials at room temperature. As seen for the XRD data, refinements indicated additional reflections not related to the main phase (Figure 97). Additional impurity phases $Sr_3Fe_2O_{7-x}$ were included for both phases with $SrSO_4$ also included for $Sr_{4.5}Fe_2S_{0.5}O_{9\pm\delta}$. The structure of the main phase was refined with space group

*A*2$_1$*am* as used for the XRD data. For both systems occupancies of Fe, S, Cr and O were refined with atomic displacement parameters grouped for large cation, small cation, and anion sites.

For both sulfate and chromate doped materials, refinements suggested incorporation of oxyanions on the tetrahedral 4a site in the 1201-type stacking. The incorporation of tetrahedral CrO_4^{2-} coordination is further supported by XANES data (as highlighted earlier). For both phases, refinements suggest no occupancy of oxyanions on the Fe1 and Fe2 sites and therefore the occupancies of these Fe sites in both phases were fixed to 1.

Combined XANES and ^{57}Fe Mössbauer spectroscopy data analysis can be used to predict the overall cation oxidation state. Using the oxidation states from these techniques the overall oxygen content is predicted to be ≈ 9.1. For $Sr_{4.5}Cr_{2.5}O_9$[190], 3 Cr sites with oxidation states Cr^{6+} and Cr^{3+} are reported giving a total oxygen content equal to 9. However, for these samples, the ^{57}Fe Mössbauer spectroscopy data suggests a small increase in oxygen content, suggesting additional oxygen in interstitial sites. Previous studies on K_2NiF_4 phases (0201 type layer (see Figure 93)) show additional oxygen can be incorporated into interstitial sites within the rock salt layers.[194–196] Therefore additional interstitial sites were included in the neutron diffraction structure refinements (O11 and O12). For both S and Cr phases a small occupancy was observed for the oxygen interstitials with other oxygen site occupancies fixed to 1. Overall oxygen contents calculated from ND data and ^{57}Fe Mössbauer spectroscopy analysis are in good agreement. Thus the results show that these new systems have the ability to accommodate interstitial anions and warrant further investigation in this regard.

a)

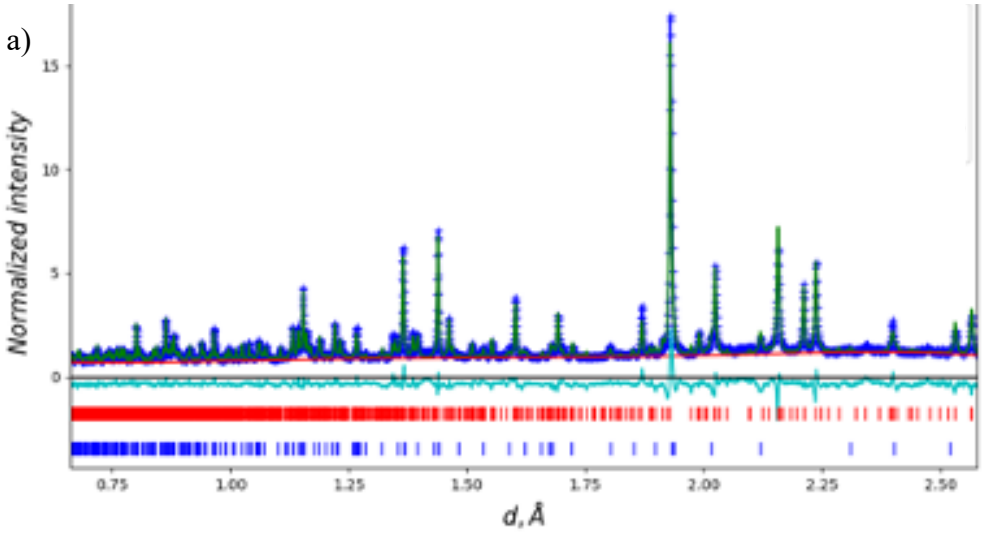
Normalized intensity
15
10
5
0
0.75
1.00
1.25
1.50
1.75
2.00
2.25
2.50
d, Å

b)

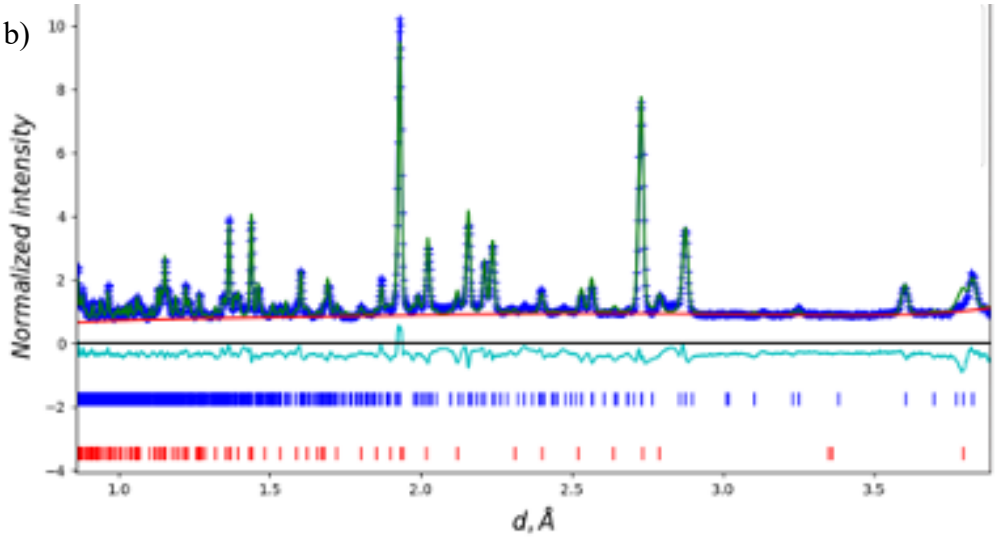
Normalized intensity
10
8
6
4
2
0
−2
−4
1.0
1.5
2.0
2.5
3.0
3.5
d, Å

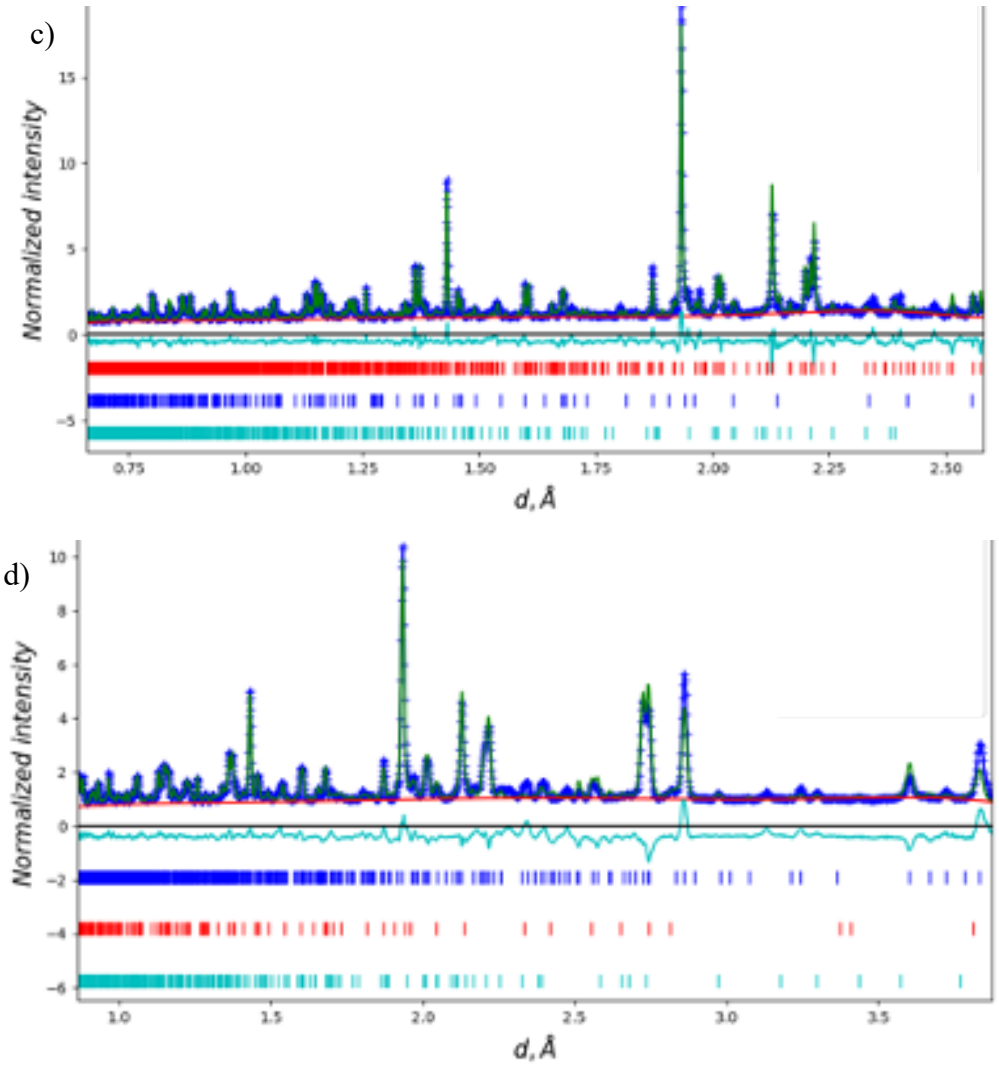

Figure 97. Observed (dark blue), calculated (green) and difference (light blue) neutron diffraction profiles for a) $Sr_{4.5}Fe_2Cr_{0.5}O_{9.13}$ (Bank 1), b) $Sr_{4.5}Fe_2Cr_{0.5}O_{9.13}$ (Bank 2), $Sr_{4.5}Fe_2S_{0.5}O_{9.15}$ (Bank 1) and $Sr_{4.5}Fe_2S_{0.5}O_{9.15}$ (Bank 2). The three phases are indicated by blue ($Sr_{4.5}Fe_2(S/Cr)_{0.5}O_{9\pm\delta}$), red ($Sr_3Fe_2O_7$) and green ($SrSO_4$).

Table 26. Structural parameters from neutron powder diffraction $Sr_{4.5}Fe_2Cr_{0.5}O_{9.13}$

a /Å	**b /Å**	**c /Å**	**V / Å^3**	**GOF**	**Rexp /%**	**Rwp /%**
10.9114(16)	5.4552(8)	30.1856(6)	1796.74(5)	5.90	1.25	7.37
Weight Percent /%						
$Sr_{4.5}Fe_2Cr_{0.5}O_{9.13}$			**$Sr_3Fe_2O_7$**			
85.1			14.9			
	x	**y**	**z**	**Occupancy**	**Uiso**	
Sr1	0.0000	0.0000	0.0000	1.00	0.0016(5)	
Sr2	0.0000	0.5000	0.0836(2)	1.00	0.0016(5)	
Sr3	0.2500	0.0000	0.0860(2)	1.00	0.0016(5)	
Sr4	0.0000	0.5000	0.2041(2)	1.00	0.0016(5)	
Sr5	0.2500	0.0000	0.2067(2)	1.00	0.0016(5)	
Cr1	0.2189(14)	0.4644(7)	0.0000	1.00	0.0027(6)	
Fe2	0.0000	0.0000	0.1461(2)	1.00	0.0027(6)	
Fe3	0.2500	0.5000	0.1515(2)	1.00	0.0027(6)	
O1	0.0429(15)	0.5000	0.0000	1.00	0.0080(5)	
O2	0.2500	0.1363(32)	0.0000	1.00	0.0080(5)	
O3	0.0000	0.0000	0.0799(3)	1.00	0.0080(5)	
O4	0.2424(13)	0.5377(7)	0.0513(3)	1.00	0.0080(5)	
O5	0.0000	0.0000	0.2156(3)	1.00	0.0080(5)	
O6	0.2500	0.5000	0.2117(3)	1.00	0.0080(5)	
O7	0.1250	0.2500	0.1448(13)	1.00	0.0080(5)	
O8	0.1250	0.7500	0.1383(13)	1.00	0.0080(5)	
O9	0.3750	0.2500	0.1431(17)	1.00	0.0080(5)	
O10	0.3750	0.7500	0.1395(18)	1.00	0.0080(5)	
O11	0.3750	0.2500	0.7500	0.00	0.0080(5)	
O12	0.6250	0.2500	0.7500	0.13(1)	0.0080(5)	

Table 27. Structural parameters from neutron powder diffraction $Sr_{4.5}Fe_2S_{0.5}O_{9.15}$

a /Å	**b /Å**	**c /Å**	**V / Å^3**	**GOF**	**Rexp /%**	**Rwp /%**
10.8908(2)	5.4853(1)	29.7785(6)	1778.96(5)	6.61	1.25	7.83

Weight Percent /%		
$Sr_{4.5}Fe_2S_{0.5}O_{9.15}$	**$Sr_3Fe_2O_7$**	**$SrSO_4$**
86.8	7.8	5.4

	x	**y**	**z**	**Occupancy**	**Uiso**
Sr1	0.0000	0.0000	0.0000	1.00	0.0057(6)
Sr2	0.0000	0.5000	0.0815(3)	1.00	0.0057(6)
Sr3	0.2500	0.0000	0.0827(3)	1.00	0.0057(6)
Sr4	0.0000	0.5000	0.2040(2)	1.00	0.0057(6)
Sr5	0.2500	0.0000	0.2056(2)	1.00	0.0057(6)
S1	0.2404(30)	0.4752(15)	0.0000	1.00	0.0001(7)
Fe2	0.0000	0.0000	0.1453(2)	1.00	0.0001(7)
Fe3	0.2500	0.5000	0.1514(2)	1.00	0.0001(7)
O1	0.0641(8)	0.5000	0.0000	1.00	0.0069(5)
O2	0.2500	0.1070(4)	0.0000	1.00	0.0069(5)
O3	0.0000	0.0000	0.0793(3)	1.00	0.0069(5)
O4	0.2569(9)	0.5450(5)	0.0491(3)	1.00	0.0069(5)
O5	0.0000	0.0000	0.2129(4)	1.00	0.0069(5)
O6	0.2500	0.5000	0.2127(3)	1.00	0.0069(5)
O7	0.1250	0.2500	0.1397(14)	1.00	0.0069(5)
O8	0.1250	0.7500	0.1415(13)	1.00	0.0069(5)
O9	0.3750	0.2500	0.1399(14)	1.00	0.0069(5)
O10	0.3750	0.7500	0.1389(12)	1.00	0.0069(5)
O11	0.3750	0.2500	0.7500	0.15(2)	0.0069(5)
O12	0.6250	0.2500	0.7500	0.00	0.0069(5)

7.3.5 Stability in dry and wet N_2

In order to test the suitability for use in solid oxide fuel cells, samples were heated to 800 °C in dry and wet N_2. In both conditions the sulfate and chromate doped phases remain stable and retain the orthorhombic structure (Figure 98 and Figure 99) with a change in unit cell parameters. As these materials remain stable this indicates suitability for solid oxide fuel cell materials with the possibility also for use in proton conducting SOFCs given the stability in wet N_2.

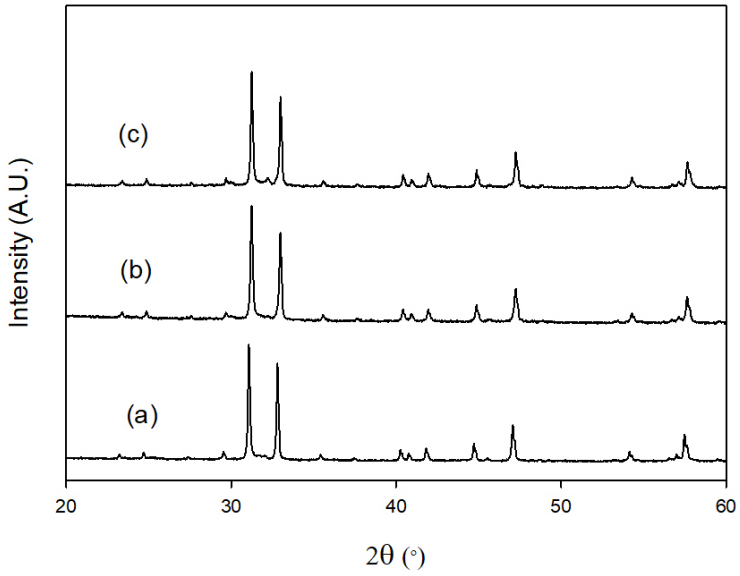

Figure 98. X-ray diffraction patterns for $Sr_{4.5}Fe_2Cr_{0.5}O_{9\pm\delta}$ heated in a) air, b) dry N_2 to 800 °C and c) wet N_2 to 800 °C

Lattice parameters for $Sr_{4.5}Fe_2Cr_{0.5}O_{9\pm\delta}$ heated in air, dry N_2 and wet N_2 are shown in Table 28. For all samples an additional impurity phase, $Sr_3Fe_2O_{7-x}$ phase was included in Rietveld refinements. All cell parameters are relatively similar under the different conditions, with a small increase in unit cell volume for the dry N_2 treated sample, and a small decrease in wet N_2.

Table 28. Lattice parameters (space group $A2_1am$) for $Sr_{4.5}Fe_2Cr_{0.5}O_{9\pm\delta}$. An additional impurity phases $Sr_3Fe_2O_{7-x}$ was included in the refinement for samples heated in air, dry N_2 and wet N_2.

		Air	Dry N_2	Wet N_2
a (Å)		10.9095(33)	10.9053(13)	10.9030(17)
b (Å)		5.4548(17)	5.4557(6)	5.4529(8)
c (Å)		30.1990(9)	30.2165(15)	30.2211(12)
V (Å^3)		1797.11(11)	1797.76(19)	1796.76(15)
R_{wp} (%)		2.24	2.48	2.68
R_{exp} (%)		1.33	1.64	1.60
Weight%	**$Sr_{4.5}Fe_2Cr_{0.5}O_{9\pm\delta}$**	97.2	97.7	94.6
	$Sr_3Fe_2O_7$	2.8	2.3	5.4

As observed for the chromate samples, an additional impurity phase $Sr_3Fe_2O_{7-x}$ is included in the refinement with a further impurity phase $SrSO_4$ included for $Sr_{4.5}Fe_2S_{0.5}O_{9\pm\delta}$. In this case the increase in unit cell when heating $Sr_{4.5}Fe_2S_{0.5}O_{9\pm\delta}$ in dry N_2 was higher, which suggests a greater degree of reduction in this phase. An increase in cell volume is also observed for the wet N_2 treatment, but not as large as the dry N_2 change. The greater degree of reduction for this system is interesting, and it may suggest some reduction of iron to Fe^{2+}, and so further ^{57}Fe Mössbauer spectroscopy studies of the N_2 heated samples would be of interest in this respect. Additionally, the difference in S and Cr doped systems could potentially be due to not only the reduction of iron, but also chromium, therefore further XANES studies would also be of interest.

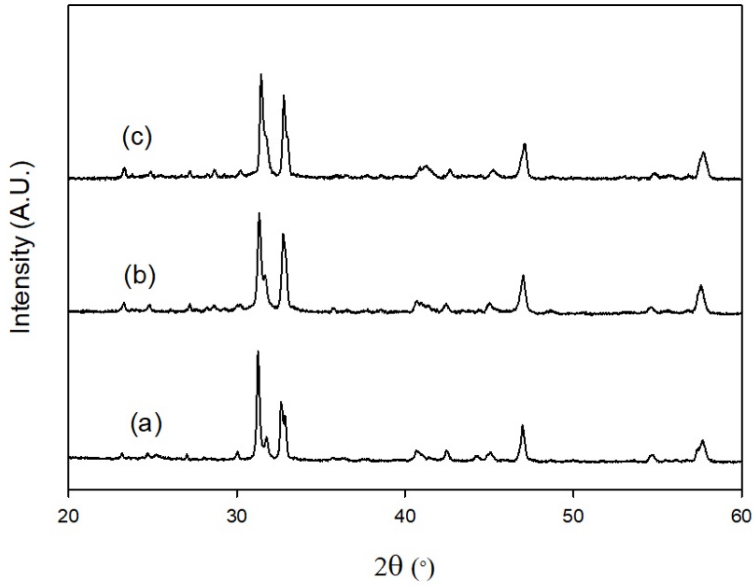

Figure 99. X-ray diffraction patterns for $Sr_{4.5}Fe_2S_{0.5}O_{9\pm\delta}$ heated in a) air, b) dry N_2 to 800 °C and c) wet N_2 to 800 °C

Table 29. Lattice parameters (space group $A2_1am$) for $Sr_{4.5}Fe_2S_{0.5}O_{9\pm\delta}$. Additional impurity phases $Sr_3Fe_2O_{7-x}$ and $SrSO_4$ were included in the refinement for samples heated in air, dry N_2 and wet N_2.

		Air	Dry N_2	Wet N_2
	a (Å)	10.8928(6)	10.9451(11)	10.9196(11)
	b (Å)	5.4815(3)	5.4894(6)	5.4909(6)
	c (Å)	29.7524(20)	29.8746(35)	29.7316(39)
	V (Å^3)	1776.47(25)	1794.91(43)	1782.66(50)
	R_{wp} (%)	2.34	2.90	3.64
	R_{exp} (%)	1.31	1.47	1.49
Weight%	**$Sr_{4.5}Fe_2S_{0.5}O_{9\pm\delta}$**	85.3	87.9	88.9
	$Sr_3Fe_2O_{7-x}$	10.7	8.0	8.6
	$SrSO_4$	4.0	4.1	2.5

In order to investigate the reversibility of the incorporation of water into $Sr_{4.5}Fe_2(Cr/S)_{0.5}O_{9\pm\delta}$, samples were heated in air to 1050 °C for 12 h. Upon heating in air, the original "0201-1201" structure is retained for both sulfate and chromate doped materials (Figure 100). This stability suggests the potential for these materials to be utilised as cathode materials for proton conducting SOFCs.

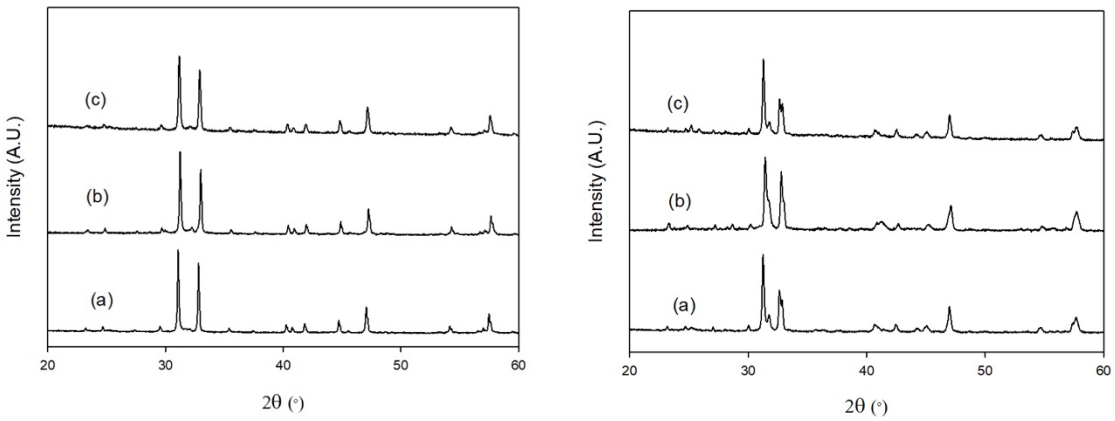

Figure 100. X-ray diffraction patterns for a) $Sr_{4.5}Fe_2Cr_{0.5}O_{9\pm\delta}$ and b) $Sr_{4.5}Fe_2S_{0.5}O_{9\pm\delta}$ heated in a) air, b) wet N_2 to 800 °C and c) air 1050 °C (wet N_2 to 800 °C samples)

7.3.6 Thermogravimetric analysis

Thermogravimetric analysis was performed for the $Sr_{4.5}Fe_2(Cr/S)_{0.5}O_{9\pm\delta}$ samples heated in wet N_2. For this analysis, samples were heated at a heating rate of 10 °C/ min to 1000 °C in N_2. From mass spectrometry data (Figure 101) it is seen water is lost in multiple steps over a temperature range approx. 50 – 800 °C. This suggest water is not only on the surface (≤ 100 °C mass loss), but also incorporated into the structure. Due to the fact that the sample loses both water and oxygen in this temperature range an accurate value for the water content cannot be calculated.

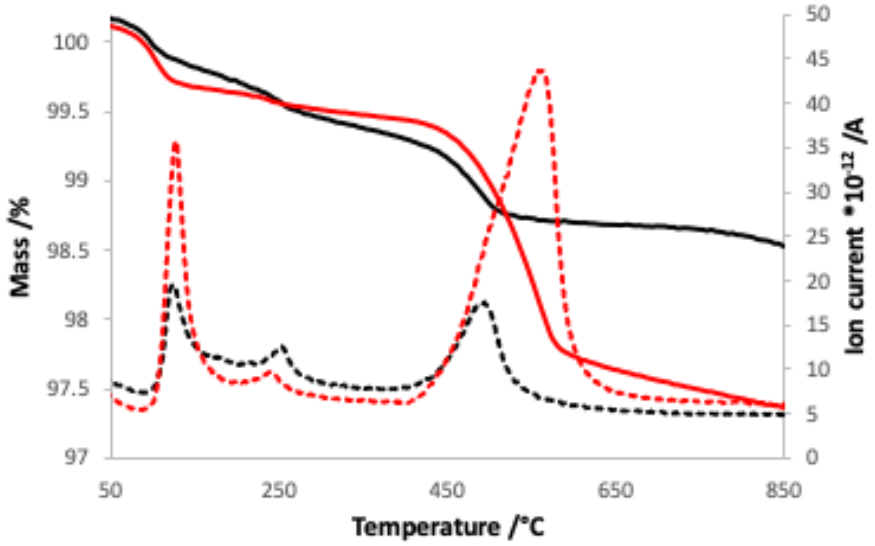

Figure 101. Plot of mass vs temperature and ion current vs temperature for $Sr_{4.5}Fe_2Cr_{0.5}O_{9\pm\delta}$ preheated in wet N_2 (black) and $Sr_{4.5}Fe_2S_{0.5}O_{9\pm\delta}$ preheated in wet N_2 (red). Solid lines indicate %mass and dashed indicate ion current for H_2O

7.3.7 Conductivity studies

Previous work in this thesis examined the conductivities of perovskite and Ruddlesden-Popper type materials for SOFC applications. Here we have carried out 4 probe conductivity measurements to investigate the potential for use of these intergrowth phases as SOFC cathode materials. In general, with increasing temperature an increase in conductivity is observed indicative of semiconducting behaviour. A decrease in conductivity is observed (Figure 102) at ≈ 650 °C for $Sr_{4.5}Fe_2S_{0.5}O_{9\pm\delta}$ and ≈ 740 °C for $Sr_{4.5}Fe_2Cr_{0.5}O_{9\pm\delta}$ which can be correlated with oxygen loss at high temperature. The loss of oxygen at high temperature results in the removal of mixed valency which is predicted to result in a decrease in conductivity. Although in comparison to other perovskite and Ruddlesden-Popper type oxyanion doped systems the conductivity is low, there is potential for these materials to be optimised for SOFC applications through further doping studies.

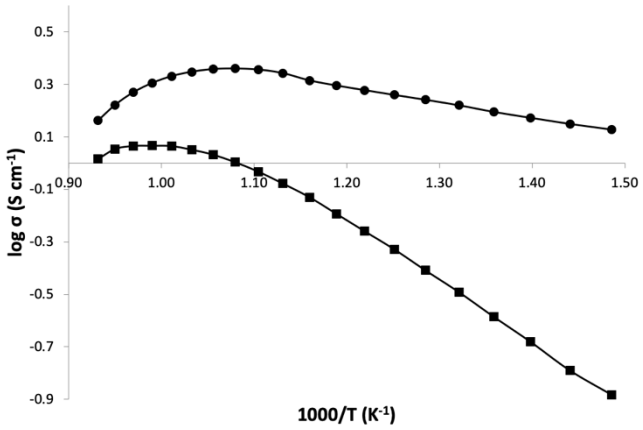

Figure 102. Plot of log σ vs. 1000/T for $Sr_{4.5}Fe_2S_{0.5}O_{9\pm\delta}$ (●) and $Sr_{4.5}Fe_2Cr_{0.5}O_{9\pm\delta}$ (■)

7.4 Conclusions

This work further shows that oxyanions can be successfully incorporated into the oxide materials, leading to the formation of the new phases $Sr_{4.5}Fe_2(S/Cr)_{0.5}O_{9\pm\delta}$. Through neutron diffraction refinements SO_4^{2-} and CrO_4^{2-} were found to be incorporated into the tetrahedral site (S1/Cr1). XANES data further supports the incorporation of tetrahedral Cr^{6+} as suggested by ND refinements. ^{57}Fe Mössbauer spectroscopy studies indicate a higher iron oxidation state than the predicted Fe^{3+}, therefore indicating additional oxygen is incorporated into the structure. ND refinements suggest a small amount of oxygen interstitials are incorporated into the "0201" type layers, with good agreement of oxygen content between ND and ^{57}Fe Mössbauer spectroscopy. Both materials were investigated for use in SOFCs where both were found to be stable when heating in dry and wet N_2. Conductivity data show both materials have low conductivity, and therefore further work would be needed to improve this for SOFC applications. Nevertheless this work highlights the potential of oxyanion doping strategies to form new compounds.

Table 30. Chapter 7 summary table

Sample	Crystal system (Synthesis temperature)	Stability	Highest conductivity (Temperature)
$Sr_{4.5}Fe_2S_{0.5}O_{9\pm\delta}$	Orthorhombic (1050 °C with anneal at 350 °C) - Interstitial oxygen - Impurity phases $Sr_3Fe_2O_{7-x}$ and $SrSO_4$	**Stability in low p(O_2)** - Stable when heating in dry N_2 to 800 °C - Additional impurity phases ($Sr_3Fe_2O_{7-x}$ and $SrSO_4$) as observed for sample heated in air - Increase in cell volume suggests reduction of iron to Fe^{2+} **Stability in wet N_2** - Orthorhombic phase remains stable with additional impurity phases ($Sr_3Fe_2O_{7-x}$ and $SrSO_4$) - TGA studies suggest incorporation of water	10-17 S cm^{-1} (484-547 °C)
$Sr_{4.5}Fe_2Cr_{0.5}O_{9\pm\delta}$	Orthorhombic (1050 °C with anneal at 350 °C) - Impurity phase $Sr_3Fe_2O_7$	**Stability in low p(O_2)** - Stable when heating in dry N_2 to 800 °C - Additional impurity phase ($Sr_3Fe_2O_{7-x}$) as observed for sample heated in air **Stability in wet N_2**	4-11 S cm^{-1} (421-484 °C)

	- Orthorhombic phase remains stable with additional impurity phase ($Sr_3Fe_2O_{7-x}$) - TGA studies suggest incorporation of water

8 Fluorination of oxyanion doped n=3 Ruddlesden-Popper materials

8.1 Introduction

A range of doping strategies have been employed in order to synthesise new oxide materials with useful properties and applications. As previously discussed a number of doping strategies on the cation sites, including oxyanion doping of perovskite and perovskite type materials, have been utilised to stabilise structures and improve properties. Further to this, manipulation of the anion sites, for example synthesis of oxyfluorides, can be applied to modify the structure and properties of materials. An example of this approach includes the Ruddlesden-Popper material, $Sr_2TiO_3F_2$ which is synthesised through low temperature fluorination with PVDF.[197] Wissel et al.[197] found this material to be a potential anode material for fluoride-ion batteries.

Low temperature fluorination with PVDF has been successfully achieved for perovskite materials such as $BaFeO_{3-x}F_x$[198,199], $La_{1-x}Sr_xFeO_{3-y}F_y$[200] and $Ba_{1-x}Sr_xFeO_{3-y}F_y$[201]. In addition to fluorination of perovskite materials, the Ruddlesden-Popper material $Sr_3Fe_2O_{7-\delta}$ has been successfully fluorinated through a range of methods. For example Case et al.[202] successfully synthesised $Sr_3Fe_2O_6F_{0.87}$ at low temperature with gaseous F_2. In comparison Hancock et al.[193] utilised low temperature fluorination with PVDF to successfully synthesise fluorinated $Sr_3Fe_2O_{7-\delta}$ phases with higher F contents. By using PVDF at low temperatures a number of fluorinated phases were synthesised with higher F contents ($Sr_3Fe_2O_{5.28}F_{1.72,}$ $Sr_3Fe_2O_4F_4$ and $Sr_3Fe_2O_3F_6$) compared to other synthesis routes.

Following this earlier work on the successful synthesis of Ruddlesden-Popper phases through low temperature fluorination with PVDF, this method has been used here. Fluorination of these Ruddlesden-Popper phases is predicted to fill oxygen vacancies and in turn remove mixed valency (Fe^{4+}/ Fe^{3+}), therefore in comparison to the undoped Ruddlesden-

Popper materials the fluorinated phases would not be suitable as SOFC cathode materials. Instead, it is predicted these fluorinated Ruddlesden-Popper phases could potentially be used in fluoride-ion batteries. Using X-ray diffraction and ^{57}Fe Mössbauer spectroscopy, this work showed the successful fluorination of the Ruddlesden-Popper materials, $Sr_4Fe_{2.75}(S/Cr)_{0.25}O_{10-\delta}$.

8.2 Experimental

Synthesis of the parent phases, $Sr_4Fe_{2.75}(S/Cr)_{0.25}O_{10-\delta}$, were carried out through standard solid state synthesis as described previously.[164,165] In brief, the parent phases were synthesised through standard solid state synthesis where $SrCO_3$, Fe_2O_3 and either $(NH_4)_2SO_4$ or Cr_2O_3 were intimately ground and heated to 950 °C (4 °C/ min) for 12 hours. $Sr_4Fe_{2.75}(S/Cr)_{0.25}O_{10-\delta}$ was ballmilled (350 rpm for 1 h, Fritsch Pulverisette 7 planetary Mill, zirconia balls and container) and reheated to 1000 °C before further grinding and heating to 1050 °C for 12 hours. Finally, samples were annealed at 350 °C for 12 h in air in order to ensure maximum oxygen content.

Fluorination of materials were carried out by mixing $Sr_4Fe_{2.75}(S/Cr)_{0.25}O_{10-\delta}$ and polyvinylidene fluoride (PVDF) in a 1:1, 1:2 and 1:3 (parent oxide: CH_2CF_2 monomer unit) ratio in order to achieve fluorination of $Sr_4Fe_{2.75}S_{0.25}O_xF_y$ (y = 2, 4 and 6). Additionally, $Sr_4Fe_{2.75}Cr_{0.25}O_{10-\delta}$ and PVDF were mixed in 1:1.5, 1:2.5 and 1:3.5 ratios (corresponding to y=3, 5, 7 respectively) to further examine the effect of varying the amount of PVDF. Samples were synthesised by grinding the mixtures and heating to 350 °C for 12 hours (in a furnace in a fumecupboard; heating and cooling at 50 °C/ h) to achieve $Sr_4Fe_{2.75}S_{0.25}O_xF_y$ where y = 2, 4 and 6. In order to ensure complete reaction, the $Sr_4Fe_{2.75}Cr_{0.25}O_xF_y$ phases were reground and heated to 350 °C for an additional 12 hours.

Powder XRD were collected for all samples with GSAS suite of programs used for structure refinements.[136] XRD data was used to confirm phase purity and to characterise cell parameters for the parent phase and fluorinated materials. Space group *I*4/*mmm* was used for $Sr_4Fe_{2.75}(S/Cr)_{0.25}O_{10-\delta}$, $Sr_4Fe_{2.75}S_{0.25}O_xF_y$ (where y = 2 and 6) and $Sr_4Fe_{2.75}Cr_{0.25}O_xF_y$ (where y = 3 and 7) with an additional cubic perovskite phase, $SrFe(O/F)_{3-x}$ ($Pm\bar{3}m$) included as a minor impurity. For $Sr_4Fe_{2.75}S_{0.25}O_xF_y$ (where y = 2 and 6), SrF_2 was also included as a minor impurity phase. Space group *F*222 was used for $Sr_4Fe_{2.75}S_{0.25}O_xF_4$ and $Sr_4Fe_{2.75}Cr_{0.25}O_xF_5$, which showed peak splitting indicative of a lower symmetry orthorhombic cell. As above, an additional cubic perovskite phase ($Pm\bar{3}m$) was included as a minor impurity.

^{57}Fe Mössbauer spectra were recorded for $Sr_4Fe_{2.75}S_{0.25}O_xF_y$ at 298 K in constant acceleration mode using an approximately 25 mCi Co/Rh source.

8.3 $Sr_4Fe_{2.75}S_{0.25}O_xF_y$

8.3.1 X-ray diffraction results

Fluorination of $Sr_4Fe_{2.75}S_{0.25}O_xF_y$ (y = 2, 4 and 6) by heat treatment with PVDF was shown to be successful through X-ray diffraction studies (Figure 103). For the y = 2, 6 samples the XRD data showed that both samples retained the tetragonal structure of the parent phase, albeit with peaks shifts indicating a larger unit cell consistent with F incorporation increasing the total anion content. For y = 4, peak splitting was observed indicative of a lowering of symmetry from tetragonal to orthorhombic. Furthermore, a noticeable change in colour was observed from black to red/orange with increasing F content, indicating a reduction in the Fe oxidation state towards Fe^{3+} upon fluorination.

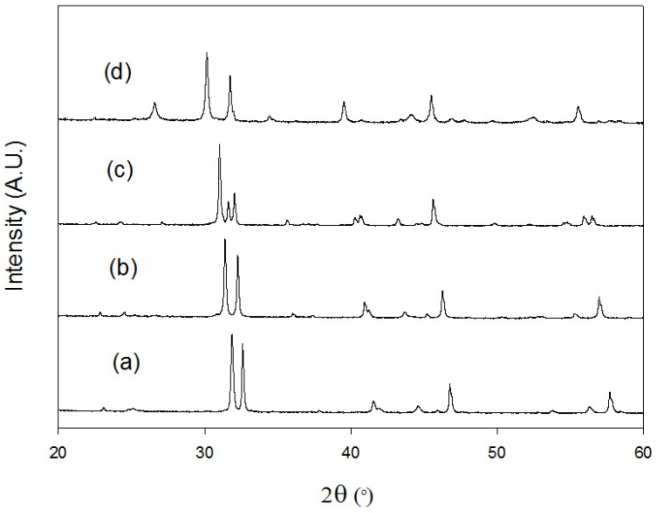

Figure 103. X-ray diffraction patterns for a) $Sr_4Fe_{2.75}S_{0.25}O_{10-\delta}$, b) $Sr_4Fe_{2.75}S_{0.25}O_xF_2$, c) $Sr_4Fe_{2.75}S_{0.25}O_xF_4$ and d) $Sr_4Fe_{2.75}S_{0.25}O_xF_6$

Rietveld refinements using XRD data were carried out on all samples. For all samples a perovskite, $SrFe(O/F)_{3-x}$ (1-4%), phase was included in refinements as observed for the parent phase, $Sr_4Fe_{2.75}S_{0.25}O_{10-\delta}$.[164] Additionally, a small amount of SrF_2 was observed in the y = 2 (0.8%) and 6 (3.4%) samples with no SrF_2 impurity included where y = 4. For all fluorinated phases, Fe/S occupancies were fixed to the predicted values with S located in the middle perovskite layer of the structure. Details of the structure refinement for this parent phase, $Sr_4Fe_{2.75}S_{0.25}O_{10-\delta}$, have been reported in chapter 5. Additionally, the atomic displacement parameters were fixed for Sr, Fe/S and O respectively for the y = 2 and 4 samples, while for the y = 6 sample, all atomic displacement parameters were constrained as equal. The orthorhombic space group, *F*222 was used for the y = 4 sample, whereas for the pure oxide, y = 2 and 6 samples, the tetragonal *I*4/*mmm* space group was used. From Rietveld refinements it can be seen there is an increase in unit cell volume upon incorporation of F (Table 31 & Figure 104) which supports the successful fluorination of $Sr_4Fe_{2.75}S_{0.25}O_{10-\delta}$. This increase in cell volume can be related both to the anion content increase on fluorination, with

the incorporation of F into interstitial sites, as well as the reduction in the average Fe oxidation state and thus increase in the proportion of the larger Fe^{3+}. In order to allow a direct comparison between all 4 samples, Figure 104 plots the variation of equivalent cell volume versus F content for each sample (in this figure, for the y = 4 sample, the average a/b length has been divided by √2 to calculate the equivalent cell volume). This figure shows an approximately linear increase in cell volume with F content across the series. This increase in volume is predicted to be due to an increase in the apical Fe-O/F2 bond as well as the incorporation of F into interstitial sites as observed for Hancock et al.[193]. Neutron diffraction studies would be needed in order to provide more detailed information about anion sites.

Table 31. Lattice parameters for $Sr_4Fe_{2.75}S_{0.25}O_xF_y$ where y = 0, 2 and 6 (space group *I*4/*mmm*) and y = 4 (space group *F*222)

y	0	2	4	6
a (Å)	3.8793(1)	3.9188(1)	5.5771(2)	3.9835(3)
b (Å)	-	-	5.6512(2)	-
c (Å)	28.3476(7)	28.9776(10)	29.2633(13)	30.9916(29)
V ($Å^3$)	426.60(2)	445.01(3)	922.30(9)	491.78(9)
GOF	1.33	1.55	1.56	2.05
Rwp (%)	1.74	2.03	2.04	2.71
Rexp (%)	1.31	1.32	1.32	1.33
Ruddlesden-Popper (%)	97.9	95.6	96.9	95.3
Perovskite (%)	2.1	3.6	3.1	1.3
SrF_2 (%)	-	0.8	-	3.4

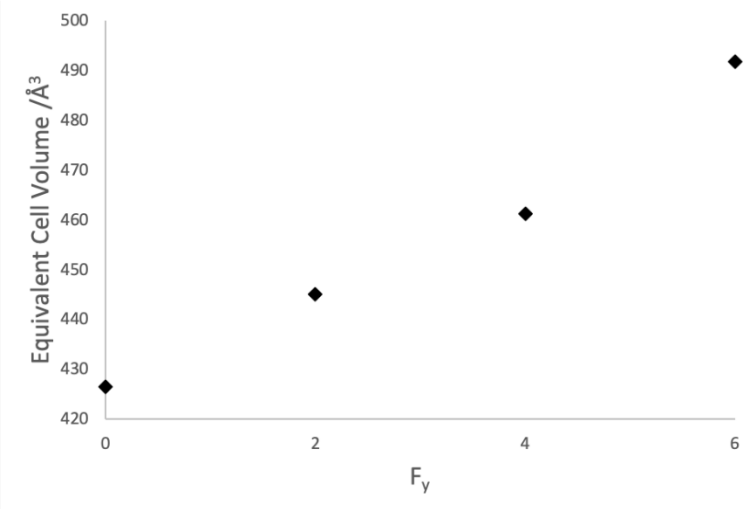

Figure 104. Variation of equivalent cell volume vs fluorine content (F_y) for $Sr_4Fe_{2.75}S_{0.25}O_xF_y$

8.3.2 $Sr_4Fe_{2.75}S_{0.25}O_{10-\delta}$

Details of the Rietveld refinement results for $Sr_4Fe_{2.75}S_{0.25}O_{10-\delta}$ have previously been discussed in Chapter 5, and therefore only a brief discussion on this material is given. XRD data shows sulfate is successfully incorporated into the middle perovskite layer of the n=3 Ruddlesden-Popper structure (tetragonal unit cell: cell parameters found in Table 31).

The Mössbauer spectrum recorded at 198K showed the material to be paramagnetic and was best fitted (Table 32) to three components. The two main spectral features were characterised by chemical isomer shift, $\delta = 0.02$ mms^{-1} characteristic of Fe^{4+} and $\delta = 0.43$mms^{-1} which is typical of Fe^{3+} in octahedral coordination. The small component with chemical isomer shift $\delta = 0.18$mms^{-1} is characteristic of Fe^{3+} in lower than octahedral coordination or to $Fe^{3.5+}$ which corresponds to fast electron sharing between Fe^{3+} and Fe^{4+} ions with a timescale smaller than 10^{-8} seconds at 298K.

Table 32. ^{57}Fe Mössbauer parameters recorded at 298K from $Sr_4Fe_{2.75}S_{0.25}O_{10-\delta}$ (*lc = low coordination)

Sample	Assignment	δ (mms^{-1})	Δ/2ε (mms^{-1})	Area (%)
	Fe^{4+}	0.02	0.20	63
$Sr_4Fe_{2.75}S_{0.25}O_{10-\delta}$	$Fe^{3.5+}$ or Fe^{3+} (lc*)	0.18	2.04	1
	Fe^{3+}	0.43	0.00	36

8.3.3 $Sr_4Fe_{2.75}S_{0.25}O_xF_2$

Fluorination with 1 mole equivalent of CH_2CF_2 to form $Sr_4Fe_{2.75}S_{0.25}O_xF_2$ results in a similar tetragonal unit cell to $Sr_4Fe_{2.75}S_{0.25}O_{10-\delta}$, but with an accompanying expansion in cell volume. Previous studies on the fluorination of n=1 and n=2 Ruddlesden-Popper materials have suggested that incorporation of F occurs in the apical and interstitial anion sites.[193,202–206] The Ruddlesden-Popper structure has the general formula of $Sr_{n+1}Fe_nO_{2n(eq)}O_{n+1(ap)}X_{2(int)}$ where when n=3 a total of 10 normal anion sites (O^{2-}) can incorporate F with the additional possibility to fill interstitial sites. Previous studies by Hancock et al.[7] reported complete filling of normal anion sites when mixing $Sr_3Fe_2O_{7-\delta}$ with PVDF in a 1:1 ratio. Therefore for this sample, it is expected that F will occupy the apical sites O2 and O4 (see Figure 105). It is impossible to distinguish oxygen and fluorine by either X-ray or neutron diffraction therefore using previous studies on Ruddlesden-Popper materials it can be presumed fluorine will initially occupy apical sites labelled in Figure 105 and Table 33.[193,202–206] From Rietveld refinements it can be seen equatorial site O1 and apical site O4 have full occupancy with vacancies still present around the middle perovskite layer on sites O1 and O/F2 supporting the incorporation of SO_4^{2-}. Rietveld refinements also indicate the unexpected occupancy of interstitial sites in the structure. This is due to the expected filling of normal anion sites as previously discussed where $1O^{2-}$ will be replaced by $2F^-$. Instead here additional occupancy of

available interstitial sites are reported with oxygen vacancies on normal anion sites surrounding the sulfate group.

Occupancies for O/F sites were allowed to refine giving a total anion content of 10.06 (±1-2%) which would suggest all anion sites are filled in the structure. By replacing FeO_6^{8-} with SO_4^{2-} an approximate vacancy of $\delta = 0.25$ for $Sr_4Fe_{2.75}S_{0.25}O_{10-\delta}$ can be calculated with Rietveld refinements suggesting vacancies around the middle perovskite layer including on site O1 and O/F2 (Table 33). As we observe oxygen vacancies in the middle perovskite layer for $Sr_4Fe_{2.75}S_{0.25}O_xF_2$ (apical site O/F2) this accounts for the ≈ 0.54 F occupying interstitial anion sites within the structure. Higher oxygen vacancies than expected are observed on sites O1 and O/F2. This could be predicted to be due to the additional reduction of Fe upon incorporation of F.

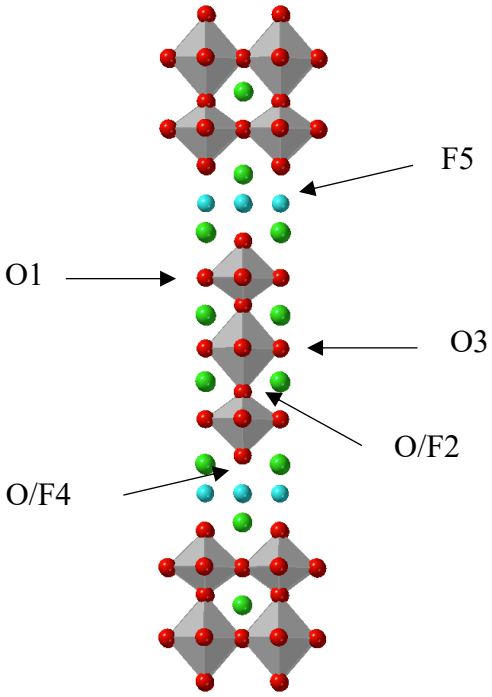

Figure 105. Structure of the tetragonal n=3 Ruddlesden-Popper $Sr_4Fe_{2.75}S_{0.25}O_xF_y$ phase

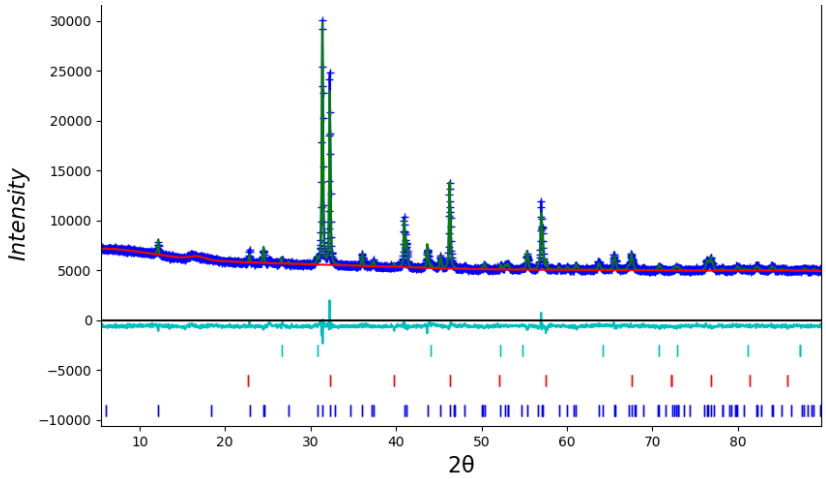

Figure 106. Observed (dark blue), calculated (green) and difference (light blue) XRD profiles for $Sr_4Fe_{2.75}S_{0.25}O_{8.06}F_2$. The respective phases are indicated by blue (Ruddlesden-Popper, *I*4/*mmm*), red ticks (perovskite $Pm\bar{3}m$) and green (SrF_2).

Table 33. Refined structural parameters for $Sr_4Fe_{2.75}S_{0.25}O_{8.06}F_2$ from XRD data

Atom	x	y	z	Occ	Uiso
Sr1	0.0000	0.0000	0.4264(1)	1.00	0.0070
Sr2	0.0000	0.0000	0.3005(1)	1.00	0.0080
Fe1	0.0000	0.0000	0.0000	0.75	0.0173
S1	0.0000	0.0000	0.0000	0.25	0.0173
Fe2	0.0000	0.0000	0.1348(2)	1.00	0.0173
O1	0.0000	0.5000	0.0000	0.83(3)	0.0506
O2/F1	0.0000	0.0000	0.0595(8)	0.94(2)	0.0506
O3	0.0000	0.5000	0.1370(6)	1.00	0.0506
O4/F2	0.0000	0.0000	0.2078(7)	1.00	0.0506
F3	0.0000	0.5000	0.2500	0.27(3)	0.0506

The complex Mössbauer spectrum recorded from $Sr_4Fe_{2.75}S_{0.25}O_xF_2$ showed the material to be predominantly magnetic at 298K and can be associated with the effect of fluorination inducing the reduction of Fe^{4+} to Fe^{3+}. The presence of a low amount (*ca.* 4%) of Fe^{4+} suggests that the reduction is not complete. A significant fraction of the other components (*ca.* 53%) correspond to $Fe^{3.5+}$ or Fe^{3+} in low coordination. Given the small amount of Fe^{4+} we associate the features with chemical isomer shifts 0.14-0.28 mms^{-1} with low coordinate Fe^{3+} consistent with oxide ion deficiency in the middle perovskite layer. The remainder (*ca.* 43%) of the Fe^{3+} ions adopt normal octahedral coordination.

Using the values in Table 34, ratios of Fe^{4+}/Fe^{3+} can be used to calculate the average Fe oxidation state and hence the total anion content, assuming that there are 2 F present in the sample. This calculation gives a total anion content of 9.93 (i.e. a formula of $Sr_4Fe_{2.75}S_{0.25}O_{7.93}F_2$) for this sample, giving a similar value to that determined through Rietveld refinements.

Table 34. ^{57}Fe Mössbauer parameters recorded at 298K from $Sr_4Fe_{2.75}S_{0.25}O_{7.93}F_2$ (*lc = low coordination)

Sample	Assignment	δ (mms^{-1})	Δ/2ε (mms^{-1})	H (T)	Area (%)
$Sr_4Fe_{2.75}S_{0.25}O_yF_2$ (1 PVDF)	Fe^{4+}	0.09	0.00	---	4
	Fe^{3+} (lc*)	0.14	-0.68	27.6	9
		0.28	0.81	---	19
		0.28	-0.27	34.0	25
	Fe^{3+}	0.35	-0.30	37.4	43

8.3.4 $Sr_4Fe_{2.75}S_{0.25}O_xF_4$

Heating with 2 mole equivalent CH_2CF_2 to form $Sr_4Fe_{2.75}S_{0.25}O_xF_4$ results in peak splitting indicating a lowering of symmetry to an orthorhombic cell. In this sample the equatorial site O3 and apical site O4 are still fully occupied. Vacancies are still present on the O/F2 site in the perovskite layer, due to the presence of SO_4^{2-} in this layer. Rietveld refinements also suggests ordered anion occupancy (attributed to F) in the interstitial sites, with half the interstitial sites between the rock salt layers occupied. This is as reported by Hancock et al.[193] where ordered occupancy of half the interstitial sites is reported for the 1:2 $Sr_3Fe_2O_{7-\delta}$:PVDF phase ($Sr_3Fe_2O_4F_4$). In comparison to $Sr_4Fe_{2.75}S_{0.25}O_xF_2$, here we have an orthorhombic structure as shown in Figure 107. With the increased F content an increase in anion occupancy in the interstitial sites occur. In order to ensure there is maximum separation between anions, ordering of these interstitial sites occur resulting in a lower symmetry orthorhombic cell. Using Rietveld refinement, the total anion content can be calculated as 10.86, higher than that for the y = 2 sample, consistent with the increased amount of PVDF used.

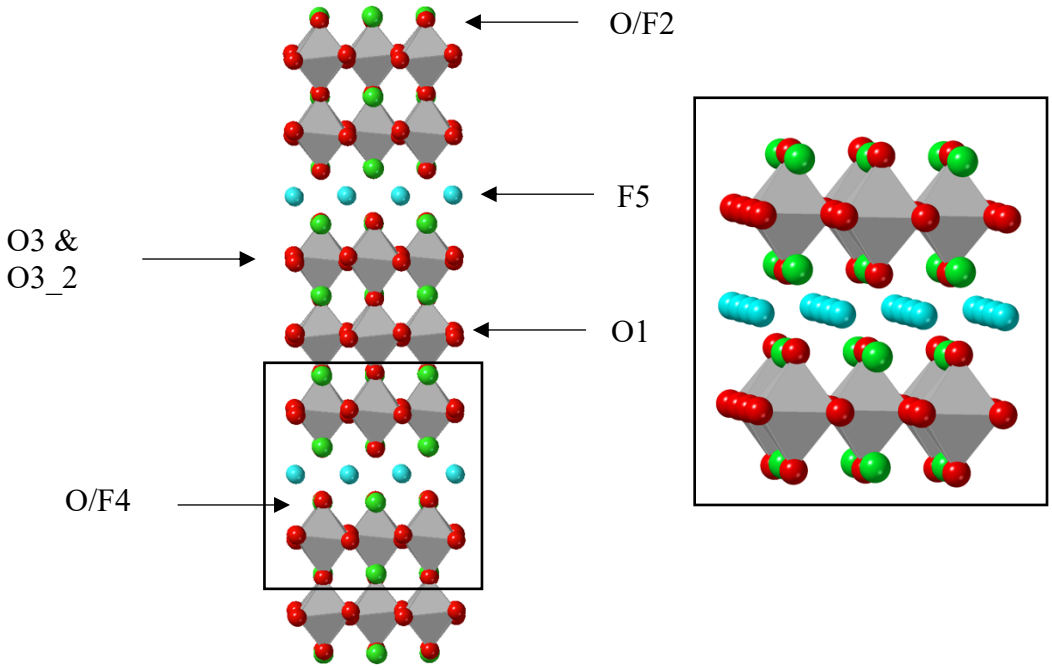

Figure 107. Structure of the orthorhombic n=3 Ruddlesden-Popper $Sr_4Fe_{2.75}S_{0.25}O_xF_4$ showing ordering in interstitial sites

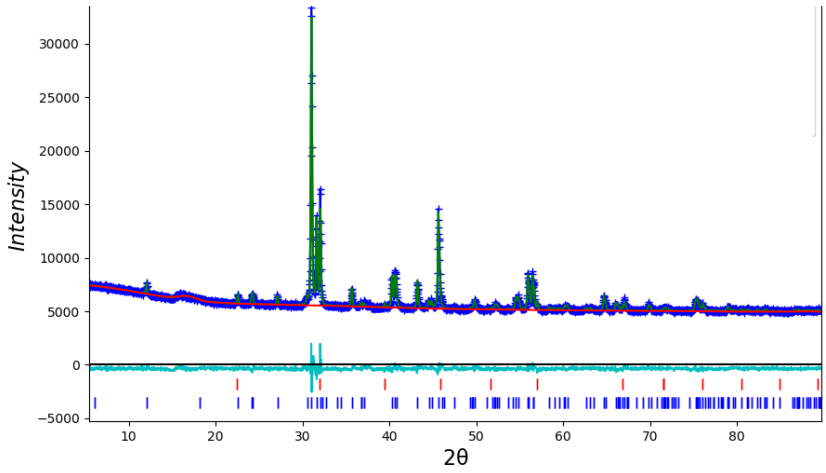

Figure 108. Observed (dark blue), calculated (green) and difference (light blue) XRD profiles for $Sr_4Fe_{2.75}S_{0.25}O_{6.86}F_4$. The two phases are indicated by blue (Ruddlesden-Popper, *I*4/*mmm*) and red ticks (perovskite $Pm\bar{3}m$).

Table 35. Refined structural parameters of $Sr_4Fe_{2.75}S_{0.25}O_{6.86}F_4$ from XRD data

Atom	x	y	z	Occ	Uiso
Sr1	0.0000	0.0000	0.3000(1)	1.00	0.0169
Sr2	0.0000	0.0000	0.4282(1)	1.00	0.0169
Fe1	0.0000	0.0000	0.0000	0.75	0.0211
S1	0.0000	0.0000	0.0000	0.25	0.0211
Fe2	0.0000	0.0000	0.1335(3)	1.00	0.0211
O1	0.7500	0.2500	0.0048(26)	0.99(3)	0.0528
O/F2	0.0000	0.0000	0.0657(9)	0.97(2)	0.0528
O3	0.7500	0.2500	0.1321(15)	1.00	0.0528
O3_2	0.7500	0.7500	0.1422(19)	1.00	0.0528
O/F4	0.0000	0.0000	0.2033(7)	1.00	0.0528
F5	0.2500	0.2500	0.7500	0.94(5)	0.0528

The Mössbauer spectrum of the fluorinated phase, $Sr_4Fe_{2.75}S_{0.25}O_xF_4$, gave three spectral components with chemical isomer shifts characteristic of octahedral Fe^{3+} thereby confirming complete reduction of Fe^{4+} in a predominantly (*ca.* 93%) magnetically ordered material. Additionally, a small haematite impurity was observed. There are three other features which accompany increased fluorination. Firstly, all the chemical isomer shift values for Fe^{3+} are more positive than those observed in the spectrum recorded from $Sr_4Fe_{2.75}S_{0.25}O_xF_2$ indicative of greater ionicity due to the presence of increasing amounts of F. Secondly, the quadrupole interaction tends to larger values suggesting greater distortion around the Fe^{3+} sites. Finally, the magnetic hyperfine fields become increasingly larger indicative of stronger magnetic interactions between the Fe^{3+} ions.

As ^{57}Fe Mössbauer Spectroscopy data for $Sr_4Fe_{2.75}S_{0.25}O_xF_4$ suggests all iron within the structure is present as Fe^{3+}, an overall anion content can be calculated. The total anion content assuming all Fe^{3+} and 4F within the structure can be calculated as 10.88 (i.e. a formula of $Sr_4Fe_{2.75}S_{0.25}O_{6.86}F_4$), giving a similar result to predicted values calculated through Rietveld refinements (10.86 ±1-2%).

Table 36. ^{57}Fe Mössbauer parameters recorded at 298K from $Sr_4Fe_{2.75}S_{0.25}O_{6.86}F_4$ (*lc = low coordination)

Sample	Assignment	δ (mms^{-1})	Δ/2ε (mms^{-1})	H (T)	Area (%)
	Fe^{3+} (hematite)	0.35	-0.20	52.0	1
$Sr_4Fe_{2.75}S_{0.25}O_yF_4$		0.38	-0.24	43.4	66
(2 PVDF)	Fe^{3+}	0.39	0.94	---	6
		0.40	-0.46	39.5	27

8.3.5 $Sr_4Fe_{2.75}S_{0.25}O_xF_6$

Increasing the amount of PVDF used further to give $Sr_4Fe_{2.75}S_{0.25}O_xF_6$ results in a return to the tetragonal *I4/mmm* structure as observed for the y = 0, 2 samples (Figure 105) with the expected increased unit cell volume due to the higher F content. Rietveld refinements suggest full occupancy on equatorial (O3), apical (O/F2 and O/F4) and interstitial sites with oxygen vacancies reported on site O1.

As before, using Rietveld refinements a total anion content can be calculated as 11.68 for $Sr_4Fe_{2.75}S_{0.25}O_xF_6$, showing the expected increase due to the higher F content.

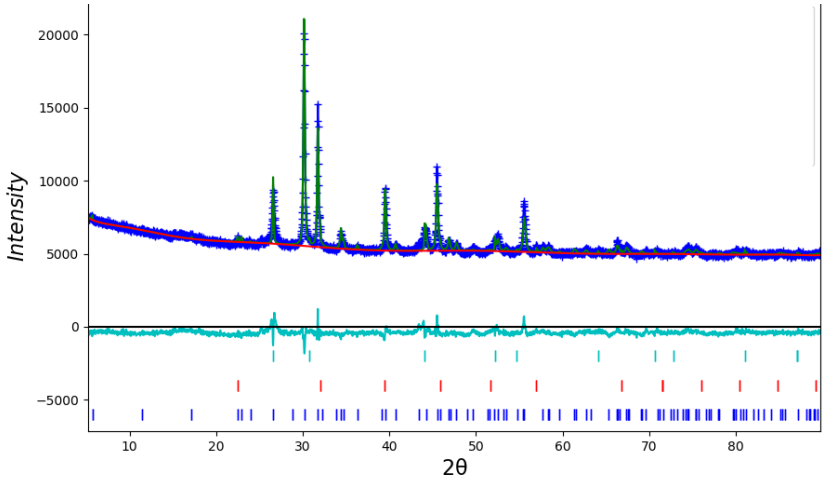

Figure 109. Observed (dark blue), calculated (green) and difference (light blue) XRD profiles for $Sr_4Fe_{2.75}S_{0.25}O_{5.68}F_6$. The phases are indicated by blue (Ruddlesden-Popper, *I4/mmm*), red ticks (perovskite $Pm\bar{3}m$) and green (SrF_2).

Table 37. Refined structural parameters of $Sr_4Fe_{2.75}S_{0.25}O_{5.68}F_6$ from XRD data

Atom	x	y	z	Occ	Uiso
Sr1	0.0000	0.0000	0.4426(2)	1.00	0.0500
Sr2	0.0000	0.0000	0.3001(2)	1.00	0.0500
Fe1	0.0000	0.0000	0.0000	0.75	0.0154
S1	0.0000	0.0000	0.0000	0.25	0.0154
Fe2	0.0000	0.0000	0.1370(3)	1.00	0.0154
O1	0.0000	0.5000	0.0000	0.84(4)	0.0492
O2/F1	0.0000	0.0000	0.0749(15)	1.00	0.0492
O3	0.0000	0.5000	0.1219(10)	1.00	0.0492
O4/F2	0.0000	0.0000	0.1848(12)	1.00	0.0492
F3	0.0000	0.5000	0.2500	1.00	0.0492

^{57}Fe Mössbauer data indicated all spectral components were characteristic of Fe^{3+} with a small haematite impurity present. Some (*ca.* 12%) of Fe^{3+} gives a paramagnetic component characteristic of either $Fe^{3.5+}$ or Fe^{3+} in lower than octahedral coordination. Given the high degree of fluorination and the absence of a discrete Fe^{4+} component, we suggest that the latter assignment is more reasonable. The tendency to higher values of chemical isomer shift and quadrupole interaction of the Fe^{3+} components with increased fluorination is indicative of enhanced ionicity and distortion around the Fe^{3+} sites on increasing the F content.

As observed for $Sr_4Fe_{2.75}S_{0.25}O_xF_4$, the Fe oxidation state for $Sr_4Fe_{2.75}S_{0.25}O_xF_6$ is reported as Fe^{3+}, therefore anion content can be calculated as 11.88 ($\pm$1%) (assuming F_6, this gives a formula of $Sr_4Fe_{2.75}S_{0.25}O_{5.68}F_6$). The total anion content calculated through ^{57}Fe Mössbauer Spectroscopy is found to be similar as that calculated through Rietveld refinement data (11.68) further supporting the successful fluorination of $Sr_4Fe_{2.75}S_{0.25}O_{10-\delta}$.

Table 38. ^{57}Fe Mössbauer parameters recorded at 298K from $Sr_4Fe_{2.75}S_{0.25}O_{5.68}F_6$ (*lc = low coordination)

Sample	Assignment	δ (mms^{-1})	Δ/2ε (mms^{-1})	H (T)	Area (%)
	Fe^{3+} (lc*)	0.17	0.73	---	12
	Fe^{3+} (hematite)	0.38	-0.22	51.1	5
$Sr_4Fe_{2.75}S_{0.25}O_yF_6$		0.46	0.79	---	15
(3 PVDF)		0.35	-0.22	42.7	20
	Fe^{3+}	0.40	-0.42	40.2	34
		0.41	0.56	34.8	13

8.3.6 Conclusions

In this work we have shown the successful fluorination of the n=3 Ruddlesden-Popper structure $Sr_4Fe_{2.75}S_{0.25}O_{10-\delta}$ with ratios of $Sr_4Fe_{2.75}S_{0.25}O_{10-\delta}$:PVDF at 1:1, 1:2 and 1:3 leading to increasing cell volume on increasing F content. Upon increasing fluorination reduction of Fe^{4+} to Fe^{3+} is observed by ^{57}Fe Mössbauer Spectroscopy. Overall this work shows high fluorine contents in the n=3 Ruddlesden-Popper material, $Sr_4Fe_{2.75}S_{0.25}O_{10-\delta}$, can be successfully synthesised through low temperature fluorination. These phases have potential to be utilised as electrode materials in F ion batteries, which will be the subject of future work.

8.4 $Sr_4Fe_{2.75}Cr_{0.25}O_xF_y$

8.4.1 X-ray diffraction results

Following the successful fluorination of $Sr_4Fe_{2.75}S_{0.25}O_x$, the fluorination of the Cr equivalent phases was investigated. Initially, $Sr_4Fe_{2.75}Cr_{0.25}O_xF_y$ phases where y = 2, 4 and 6 were synthesised and X-ray diffraction studies were performed (Figure 110). These F contents were initially investigated due to the prediction that y = 2 and 6 will fully occupy normal anion sites and all anion sites (normal and interstitial) respectively resulting in a tetragonal Ruddlesden-Popper structure. Whereas for y=4 it is predicted half the interstitial sites will be occupied resulting in an orthorhombic Ruddlesden-Popper structure due to ordered anion occupancies. Initial studies were found to be unsuccessful for y = 2, 4 and 6 where mixed phases and SrF_2 impurities are observed. Further studies were carried out for $Sr_4Fe_{2.75}Cr_{0.25}O_{10-\delta}$:PVDF ratios of 1:1.5, 1:2.5 and 1:3.5. Using these modified ratios the successful synthesis of the analogous tetragonal and orthorhombic fluorinated phases was demonstrated. As reported for $Sr_4Fe_{2.75}S_{0.25}O_xF_y$ a change in colour from black to red/orange is observed for $Sr_4Fe_{2.75}Cr_{0.25}O_xF_y$ on fluorination. The need to utilise a higher F content in the

fluorination of the $Sr_4Fe_{2.75}Cr_{0.25}O_{10-\delta}$ samples can be predicted to be due to the additional reducibility of the Cr (most likely from Cr^{6+} to Cr^{3+}). Further work (e.g. Cr XANES) would be needed to confirm this theory.

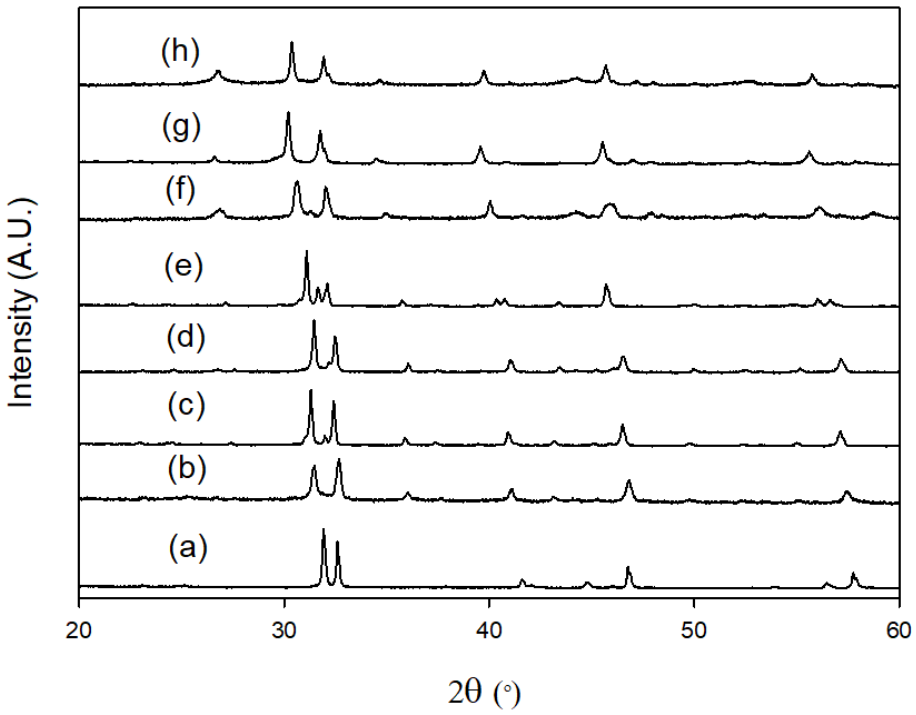

Figure 110. X-ray diffraction patterns for $Sr_4Fe_{2.75}Cr_{0.25}O_xF_y$ where a) y = 0, b) y = 2, c) y = 3, d) y = 4, e) y = 5, f) y = 6, f) y = 7 and h) y = 8

Rietveld refinements were carried out using the XRD data for $Sr_4Fe_{2.75}Cr_{0.25}O_xF_y$ where y = 3, 5 and 7. For all samples a perovskite, $SrFe(O/F)_{3-x}$ (1-4%), impurity phase was included in the refinements as observed for the parent phase, $Sr_4Fe_{2.75}Cr_{0.25}O_{10-\delta}$. Due to the X-ray scattering factors of chromium and iron being similar, individual occupancy of these elements cannot be distinguished. As discussed in chapter 5, it is predicted that Cr is incorporated into the middle perovskite layer. Rietveld refinements were carried out as reported for $Sr_4Fe_{2.75}S_{0.25}O_xF_y$, where atomic displacement parameters were fixed for Sr,

Fe/Cr and O respectively. The Space groups *I*4/*mmm* and *F*222 were used for y = 3/7 and y = 5 respectively.

With increasing F incorporation an overall increase in unit cell volume is observed (Table 39 and Figure 111) for $Sr_4Fe_{2.75}Cr_{0.25}O_xF_y$ (in this figure, the average a/b length for the y = 5 sample has been divided by √2 to calculate the equivalent cell volume). As suggested for $Sr_4Fe_{2.75}S_{0.25}O_xF_y$, the increase in unit cell volume with increasing F content is predicted to be due to the incorporation of F into interstitial sites as well as the increased proportion of the larger Fe^{3+}.

Table 39. Lattice parameters for $Sr_4Fe_{2.75}Cr_{0.25}O_xF_y$ where y = 0, 3, 7 (space group *I*4/*mmm*) and y = 5 $Sr_4Fe_{2.75}Cr_{0.25}O_xF_5$ (space group *F*222)

y	0	3	5	7
a (Å)	3.8791(1)	3.9010(3)	5.6433(3)	3.9822(2)
b (Å)	-	-	5.5683(3)	-
c (Å)	28.2919(9)	29.2650(23)	29.1628(22)	30.9081(25)
V ($Å^3$)	425.72(3)	445.35(7)	916.40(14)	490.13(8)
GOF	1.54	1.95	1.7	1.57
Rwp (%)	2.06	2.68	2.29	2.16
Rexp (%)	1.33	1.38	1.35	1.38
Ruddlesden-Popper (%)	97.1	93.7	93.7	95.1
Perovskite (%)	2.9	6.3	6.3	4.9

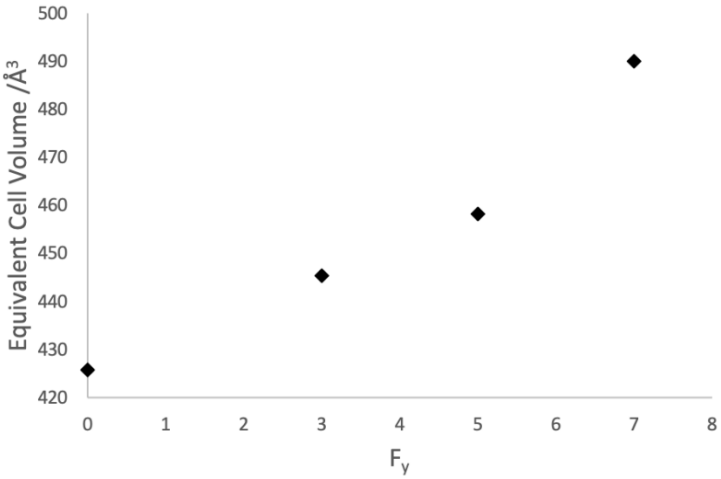

Figure 111. Plots of equivalent cell volume vs fluorine content (F_y) for $Sr_4Fe_{2.75}Cr_{0.25}O_xF_y$

8.4.2 $Sr_4Fe_{2.75}Cr_{0.25}O_xF_3$

Fluorination with 1.5 mole equivalent of CH_2CF_2 to form $Sr_4Fe_{2.75}Cr_{0.25}O_xF_3$ results in a tetragonal unit cell as observed for $Sr_4Fe_{2.75}Cr_{0.25}O_{10-\delta}$. As discussed for $Sr_4Fe_{2.75}S_{0.25}O_xF_y$ phases, it is predicted that the incorporation of F would be on apical sites O2 and O4. Rietveld refinements indicate full occupancy of all apical and equatorial sites (O1-O4). Compared with $Sr_4Fe_{2.75}S_{0.25}O_xF_2$, here we observed no occupancy in the interstitial site F3.

Using anion occupancy data from Rietveld refinements the total anion content can be calculated as 10. Due to the full occupancy of all apical and equatorial sites this would suggest all Fe^{4+} and Cr^{6+} would be reduced to Fe^{3+}/Cr^{3+} giving an overall anion content of 10 (assuming F_3, this would give a formula of $Sr_4Fe_{2.75}Cr_{0.25}O_7F_3$). As shown in chapter 5, the oxidation state of iron is reduced upon incorporation of Cr^{6+} (section 5.4.6 ^{57}Fe Mössbauer Spectroscopy). The incorporation of F is therefore predicted to further reduce the iron oxidation state. Further work (e.g. Cr XANES/ ^{57}Fe Mössbauer Spectroscopy) would be needed to confirm this.

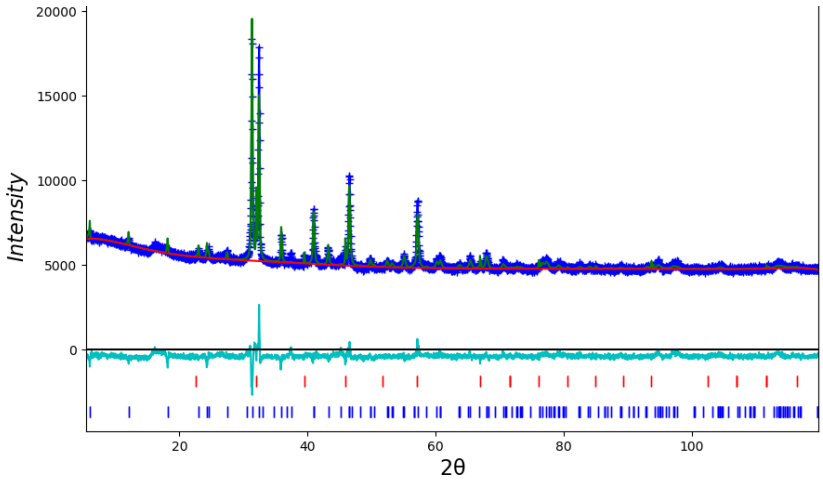

Figure 112. Observed (dark blue), calculated (green) and difference (light blue) XRD diffraction profiles for $Sr_4Fe_{2.75}Cr_{0.25}O_7F_3$. The two phases are indicated by blue (Ruddlesden-Popper, *I*4/*mmm*) and red ticks (perovskite $Pm\bar{3}m$).

Table 40. Refined structural parameters for $Sr_4Fe_{2.75}Cr_{0.25}O_7F_3$ from XRD data

Atom	x	y	z	Occ	Uiso
Sr1	0.0000	0.0000	0.4331(3)	1.00	0.0342
Sr2	0.0000	0.0000	0.3055(2)	1.00	0.0342
Fe/Cr1	0.0000	0.0000	0.0000	1.00	0.0115
Fe/Cr2	0.0000	0.0000	0.1421(4)	1.00	0.0115
O1	0.0000	0.5000	0.0000	1.00	0.0949
O2/F1	0.0000	0.0000	0.0740(11)	1.00	0.0949
O3	0.0000	0.5000	0.1384(7)	1.00	0.0949
O4/F2	0.0000	0.0000	0.2255(15)	1.00	0.0949
F3	0.0000	0.5000	0.2500	0.00	0.0949

8.4.3 $Sr_4Fe_{2.75}Cr_{0.25}O_xF_5$

With further F incorporation peak splitting in the XRD data indicates a lowering of symmetry to an orthorhombic cell (space group *F*222). As observed for $Sr_4Fe_{2.75}Cr_{0.25}O_7F_3$, Rietveld refinements suggests full occupancy of apical sites O2 and O4. Additionally, Rietveld refinements for $Sr_4Fe_{2.75}Cr_{0.25}O_xF_5$ suggest full occupancy of half interstitial sites by F in an ordered manner. As discussed for $Sr_4Fe_{2.75}S_{0.25}O_xF_4$, the ordered anion occupancy observed for these phases is predicted to be due to anions in the interstitials sites having maximum separation which in turn results in a lower symmetry orthorhombic cell (Figure 107).

Using the refined site occupancies the total anion content can be calculated as 10.61. Assuming all iron is reduced to Fe^{3+} as reported for $Sr_4Fe_{2.75}S_{0.25}O_xF_4$ and reduction of Cr^{6+} to Cr^{3+} the total anion content would be expected to be 11 (assuming F_5). Comparing the predicted anion content with the Rietveld refinement data, a lower than expected value is calculated.

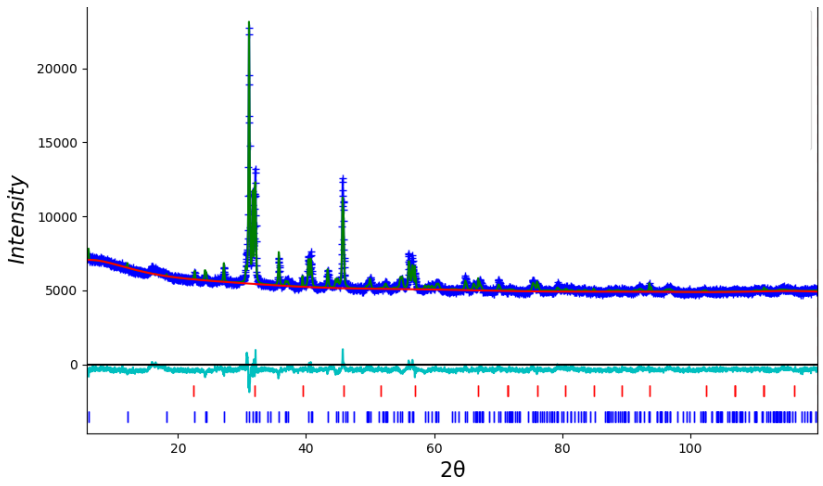

Figure 113. Observed (dark blue), calculated (green) and difference (light blue) XRD profiles for $Sr_4Fe_{2.75}Cr_{0.25}O_{5.62}F_5$. The two phases are indicated by blue (Ruddlesden-Popper, *I*4/*mmm*) and red ticks (perovskite $Pm\bar{3}m$).

Table 41. Refined structural parameters for $Sr_4Fe_{2.75}Cr_{0.25}O_{5.62}F_5$ from XRD data

Atom	x	y	z	Occ	Uiso
Sr1	0.0000	0.0000	0.4300(2)	1.00	0.0304
Sr2	0.0000	0.0000	0.2993(2)	1.00	0.0304
Fe/Cr1	0.0000	0.0000	0.0000	1.00	0.0292
Fe/Cr2	0.0000	0.0000	0.1279(3)	1.00	0.0292
O1	0.7500	0.2500	0.0119(14)	1.00	0.0296
O/F2	0.0000	0.0000	0.0709(9)	1.00	0.0296
O3	0.7500	0.2500	0.1230(11)	1.00	0.0296
O/F4	0.7500	0.7500	0.1469(17)	0.81(4)	0.0296
O5	0.0000	0.0000	0.2050(9)	1.00	0.0296
F3	0.2500	0.2500	0.7500	1.00	0.0296

8.4.4 $Sr_4Fe_{2.75}Cr_{0.25}O_xF_7$

By further increasing the amount of PVDF, the original tetragonal structure is obtained, albeit with anion occupancy of interstitial sites. Rietveld refinements suggest full occupancy of sites O/F2, O3, O/F4 and F5 with vacancies on site O1. A similar observation is reported for $Sr_4Fe_{2.75}S_{0.25}O_xF_6$ where vacancies are present on site O1. Using Rietveld refinements a total anion content can be calculated as 11.74. Assuming all Fe^{4+}/Cr^{6+} is reduced to Fe^{3+}/Cr^{3+} a total anion content can be calculated as 12 (assuming F_7). A lower than predicted anion content is given for $Sr_4Fe_{2.75}S_{0.25}O_xF_6$ therefore further work would be needed to investigate F content and Fe/Cr oxidation states.

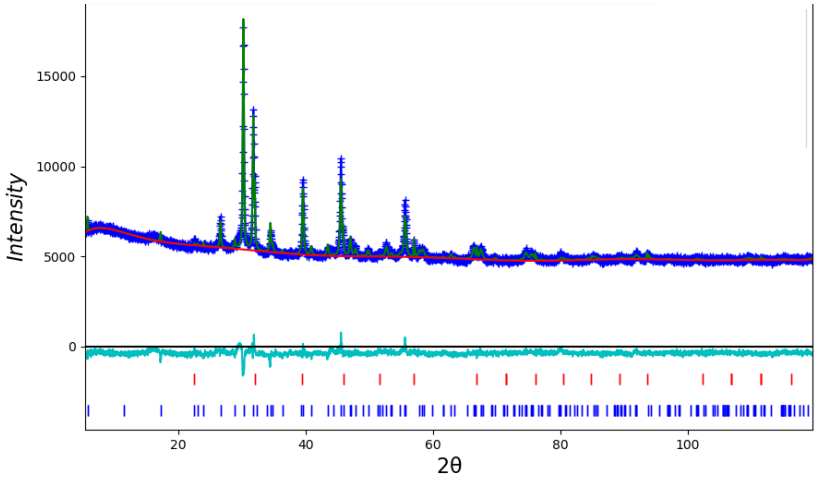

Figure 114. Observed (dark blue), calculated (green) and difference (light blue) XRD profiles for $Sr_4Fe_{2.75}Cr_{0.25}O_{4.74}F_7$. The two phases are indicated by blue (Ruddlesden-Popper, *I*4/*mmm*) and red ticks (perovskite $Pm\bar{3}m$).

Table 42. Rietveld refinement structural parameters of $Sr_4Fe_{2.75}Cr_{0.25}O_{4.74}F_7$ from XRD data

Atom	x	y	z	Occ	Uiso
Sr1	0.0000	0.0000	0.4350(2)	1.00	0.0380
Sr2	0.0000	0.0000	0.2966(2)	1.00	0.0380
Fe1	0.0000	0.0000	0.0000	1.00	0.0168
Fe2	0.0000	0.0000	0.1210(3)	1.00	0.0168
O1	0.0000	0.5000	0.0000	0.87(3)	0.0188
O/F2	0.0000	0.0000	0.0642(10)	1.00	0.0188
O3	0.0000	0.5000	0.1263(6)	1.00	0.0188
O/F4	0.0000	0.0000	0.1872(8)	1.00	0.0188
F5	0.0000	0.5000	0.2500	1.00	0.0188

8.4.5 Conclusions

In addition to the successful fluorination of $Sr_4Fe_{2.75}S_{0.25}O_{10-\delta}$, here we have shown the successful fluorination of $Sr_4Fe_{2.75}Cr_{0.25}O_{10-\delta}$. Initial fluorination studies indicated higher PVDF molar ratios (1:1.5, 1:2.5 and 1:3.5) were needed to successfully synthesise the tetragonal and orthorhombic fluorinated systems. The higher F content required is believed to be due to the reduction of not only Fe but also Cr. Further work is needed to investigate in more detail the iron (Mössbauer spectroscopy) and chromium (XANES) oxidation states and F content for these phases.

Table 43. Chapter 8 summary table

Sample	Crystal system	Synthesis temperature	Purity
$Sr_4Fe_{2.75}S_{0.25}O_{10-\delta}$	Tetragonal	1050 °C with anneal at 350 °C	2 Ruddlesden-Popper phases with $Sr_3Fe_2O_7$ and $SrFeO_3$ impurity phases
$Sr_4Fe_{2.75}S_{0.25}O_xF_2$	Tetragonal	350 °C	$SrFe(O/F)_{3-x}$ and SrF_2 impurity phases
$Sr_4Fe_{2.75}S_{0.25}O_xF_4$	Orthorhombic	350 °C	$SrFe(O/F)_{3-x}$ impurity phase
$Sr_4Fe_{2.75}S_{0.25}O_xF_6$	Tetragonal	350 °C	$SrFe(O/F)_{3-x}$ and SrF_2 impurity phases
$Sr_4Fe_{2.75}Cr_{0.25}O_{10-\delta}$	Tetragonal	1050 °C with anneal at 350 °C	2 Ruddlesden-Popper phases with $Sr_3Fe_2O_7$ and $SrFeO_3$ impurity phases
$Sr_4Fe_{2.75}Cr_{0.25}O_xF_2$	-	350 °C with further regrind and heat treatment	Mixed phase with SrF_2 impurity
$Sr_4Fe_{2.75}Cr_{0.25}O_xF_3$	Tetragonal	350 °C with further regrind and heat treatment	$SrFe(O/F)_{3-x}$ impurity phase
$Sr_4Fe_{2.75}Cr_{0.25}O_xF_4$	-	350 °C with further regrind and heat treatment	Mixed phase with SrF_2 impurity
$Sr_4Fe_{2.75}Cr_{0.25}O_xF_5$	Orthorhombic	350 °C with further regrind and heat treatment	$SrFe(O/F)_{3-x}$ impurity phase

$Sr_4Fe_{2.75}Cr_{0.25}O_xF_6$	-	350 °C with further regrind and heat treatment	Mixed phase with SrF_2 impurity
$Sr_4Fe_{2.75}Cr_{0.25}O_xF_7$	Tetragonal	350 °C with further regrind and heat treatment	$SrFe(O/F)_{3-x}$ impurity phase
$Sr_4Fe_{2.75}Cr_{0.25}O_xF_8$	-	350 °C with further regrind and heat treatment	Mixed phase with SrF_2 impurity

9 Synthesis and characterisation of oxyanion doped solid oxide fuel cell electrolyte materials, $Ba_3(Y/Tm)_2Ti_{1-x}(S/P)_xO_{8+y}$

9.1 Introduction

Solid oxide fuel cell electrolyte materials are typically fluorite and perovskite type materials. This is due to the high oxide ion conductivity typically found for these phases. For example Ishihara et al.[22] reported high ionic conductivity and low electronic conductivity for Sr and La doped $LaGaO_3$. Furthermore, perovskite related $A_3B_3O_8$ phases were found to be of interest as electrolyte materials, e.g. type Ba-In-O phases were investigated by Goodenough et al. [103] These perovskite type $Ba_3In_2MO_8$ (M= Ce, Hf and Zr) materials were found to have enhanced conductivity compared with fluorite-type electrolyte materials Gd-CeO_2 and Y-ZrO_2.[103] These materials are based on the orthorhombic $Ca_3Fe_2TiO_8$ system described as an intermediate between a perovskite and brownmillerite structure.[207,208] Following this work further studies on other $A_3B_3O_8$ phases have been carried out. For example $Ba_3In_{1.4}Y_{0.3}M_{0.3}ZrO_8$ (M= Ga and Gd)[209] and $Ba_3In_{3-x}Zr_xO_{8.5+x/2}$[210] were successfully synthesised with appealing properties suitable for SOFCs.

In previous chapters oxyanion incorporation into electrode materials for SOFCs has been discussed. Here these doping strategies will be applied to potential electrolyte materials for SOFC applications. Previous work by Shin et al.[100,101,104] has shown the successful incorporation of oxyanions (sulfate, phosphate and silicate) into $Ba_2In_2O_5$. By incorporating oxyanions into the ordered brownmillerite structure a disordered cubic perovskite structure is stabilised. As a result an increase in conductivity is observed for these materials. Additionally, conductivity studies carried out on oxyanion doped $Ba_2In_2O_5$ phases indicated not only oxide ion conductivity, but also proton conductivity.

While this work has been also extended to Ba-Sc-O systems[211], investigation on other rare earths have been lacking. Therefore a key motivation for this work was to expand not only oxyanion incorporation of perovskite type materials, but also other rare earth systems for SOFC applications. Following on from oxyanion incorporation into $Ba_2In_2O_5$ phases, in this work we show the successful synthesis of oxyanion doped perovskite type $Ba_3(Y/Tm)_2TiO_8$.

9.2 Experimental

$Ba_3(Y/Tm)_2Ti_{1-x}S_xO_{8+x}$ and $Ba_3(Y/Tm)_2Ti_{1-x}P_xO_{8+(x/2)}$ phases were prepared through solid state synthesis using $BaCO_3$, Y_2O_3/ Tm_2O_3, TiO_2 and $(NH_4)_2SO_4$/ $NH_4H_2PO_4$. For all phases an 8% $BaCO_3$ excess was used due to Ba loss at high temperature. Samples were intimately ground and heated to 950 °C (4 °C/ min) for 12 hours. Finally, samples were pressed into pellets and covered in sacrificial powder to help with Ba loss. Samples were heated to final temperatures of 1200 °C ($Ba_3Y_2Ti_{1-x}S_xO_{8+x}$), 1300 °C ($Ba_3Tm_2Ti_{1-x}S_xO_{8+x}$) and 1400 °C ($Ba_3(Y/Tm)_2TiO_{8+x}$) for 12 hours. $Ba_3(Y/Tm)_2Ti_{1-x}P_xO_{8+(x/2)}$ phases were heated to a final temperature of 1400 °C for 6 hours.

Additionally, samples were heated in dry/ wet N_2 in order to test their stability under lower $p(O_2)$, as well as testing potential suitability for use in proton conducting solid oxide fuel cells. Samples were heated to 800 °C for 12 h with a heating ramp rate of 4 °C/ min for both dry and wet N_2. On cooling dry N_2 samples were cooled at 4 °C/ min and wet N_2 samples cooled at 50 °C/ h.

AC impedance conductivity measurements were carried out by coating pellets with Pt paste and heating to 900 °C for 1 h. Conductivity measurements were carried out in the range of $5x10^{-3}$ to $1x10^4$ kHz in air using a Hewlett Packard 4192A instrument analyser. Data was analysed using Zview software.

Powder XRD (Panalytical Empyrean diffractometer equipped with a Pixcel 2D detector (Cu Kα radiation)) were collected for all samples with GSAS suite of programs used for structure refinements.[136] XRD data was used to confirm phase purity and to characterise cell parameters. For doped phases, space group $Pm\bar{3}m$ was used with occupancies fixed to calculated values. Thermal parameters for the perovskite B-site (Y/Tm/Ti/P/S) were set to be equal and allowed to refine.

Raman spectroscopy measurements (Reinshaw inVia Raman Microscope using the 532 nm laser) were carried out in order to confirm the incorporation of sulfate and phosphate.

TGA were carried out under N_2 up to 1000 °C using a Netzch STA 449 F1 Jupiter Thermal Analyser with mass spectrometry attachment.

9.3 $Ba_3Y_2Ti_{1-x}S_xO_{8+x}$

9.3.1 X-ray diffraction results

X-ray diffraction data for $Ba_3Y_2Ti_{1-x}S_xO_{8+x}$ can be found in Figure 115. For the sulfate doped materials (x=0.2-0.4) it appears cubic perovskite phases are successfully synthesised with additional reflections where x=0.4. For all doped phases broad peaks are observed, which may suggest a possible lowering in symmetry from cubic. It is also possible that more than one perovskite phase with different lattice parameters could be present, or that there is the presence of local inhomogeneities in the sample. Additionally, due to the peak broadening of these materials small impurities due to barium deficient phases cannot be ruled out underneath the main perovskite peaks. In comparison a more complicated pattern is observed for $Ba_3Y_2TiO_{8+x}$ suggesting a lowering of symmetry and possible ordering in this phase. Previous studies on $A_3B_3O_8$ phases such as $Ba_3In_2MO_8$ (M= Ce, Hf and Zr)[103] and $Ca_3Fe_2TiO_8$[207,208] were found to crystallise in the orthorhombic structure. Additional

reflections are observed for $Ba_3Y_2TiO_{8+x}$ suggesting a lower symmetry system, however at present the cell symmetry has not be confirmed. Further work would be needed to investigate this.

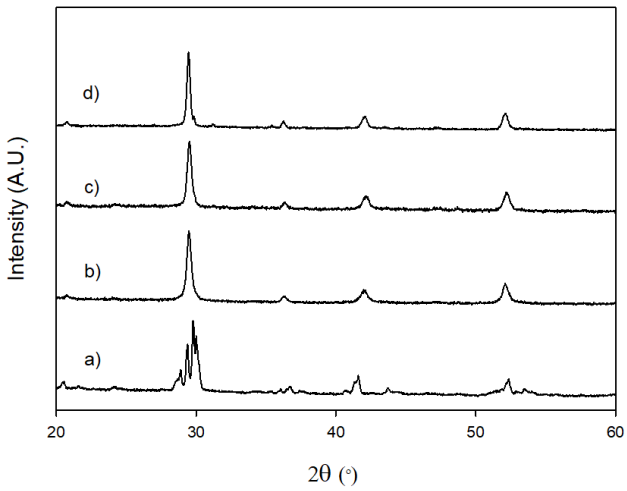

Figure 115. X-ray diffraction patterns for $Ba_3Y_2Ti_{1-x}S_xO_{8+x}$ where a) x=0, b) x=0.2, c) x=0.3 and d) x=0.4

9.3.2 Raman spectroscopy

In order to provide confirmation of sulfate incorporation, Raman spectroscopy data were collected for $Ba_3Y_2Ti_{1-x}S_xO_{8+x}$. With increasing sulfate content growth of the band at ≈ 990 cm^{-1} is seen in Figure 116, which is not observed in the undoped phase. The emerging sulfate peak is as observed in oxyanion doped $Ba_2In_2O_5$ phases by Shin et al.[101] This supports the increasing incorporation of sulfate into $Ba_3Y_2TiO_{8+x}$.

Additional bands are also observed in the Raman data for the doped phases. Assuming a perfect cubic perovskite, no Raman peaks should be seen and so this indicates a lowering of local symmetry from cubic in these systems. Additionally, at higher wavenumber an additional peak (≈ 1060 cm^{-1}) is observed for all phases which is consistent with the presence of carbonate. Carbonate incorporation has previously been reported by Shin et al.[211] where the

undoped $Ba_2Sc_2O_5$ phase is predicted to have partially substituted carbonate on the Sc site. Broad peaks in the Raman data supports the presence of carbonate in this system. For these materials further work would be needed to investigate whether carbonate is due to unreacted $BaCO_3$ or due to carbonate within the perovskite structure.

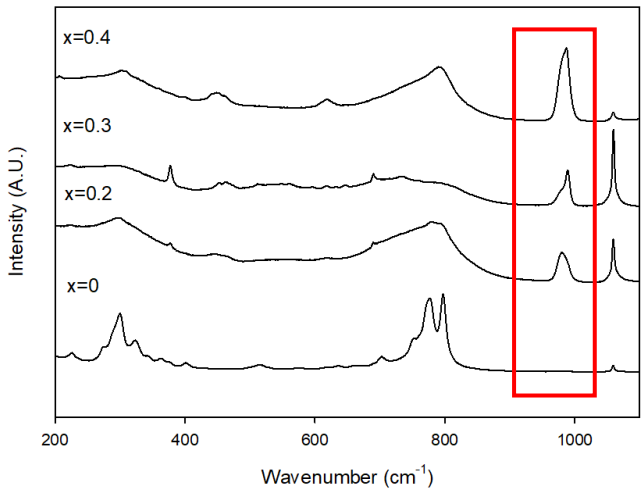

Figure 116. Raman spectra of $Ba_3Y_2Ti_{1-x}S_xO_{8+x}$ with peaks associated with sulfate incorporation highlighted in red

9.3.3 Stability in low p(O_2)

The stabilities of the $Ba_3Y_2Ti_{1-x}S_xO_{8+x}$ samples were tested in N_2 to 800 °C for 12 h. As observed for sulfate doped samples synthesised in air, XRD studies (Figure 117) indicate peak broadening. Additionally, for all doped phases there is growth of impurity peaks for all samples. In comparison the undoped $Ba_3Y_2TiO_8$ has no significant change in the XRD pattern.

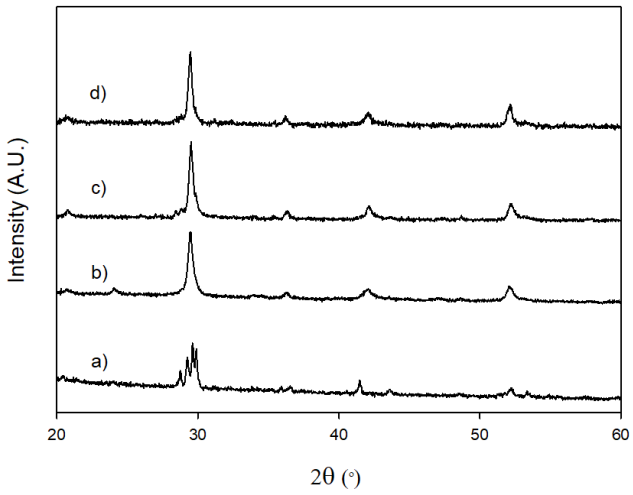

Figure 117. X-ray diffraction patterns for $Ba_3Y_2Ti_{1-x}S_xO_{8+x}$ after heat treatment in N_2 to 800 °C where a) x=0, b) x=0.2, c) x=0.3 and d) x=0.4

9.3.4 Stability in wet N_2

In order to test suitability for use in proton conducting SOFCs, $Ba_3Y_2Ti_{1-x}S_xO_{8+x}$ phases were heated in wet N_2 to 800 °C for 12 h. All phases are found to give more complex XRD patterns suggesting a breakdown into a number of phases (Figure 118). For all doped phases XRD data suggest additional reflections due to the impurity phase $BaSO_4$.

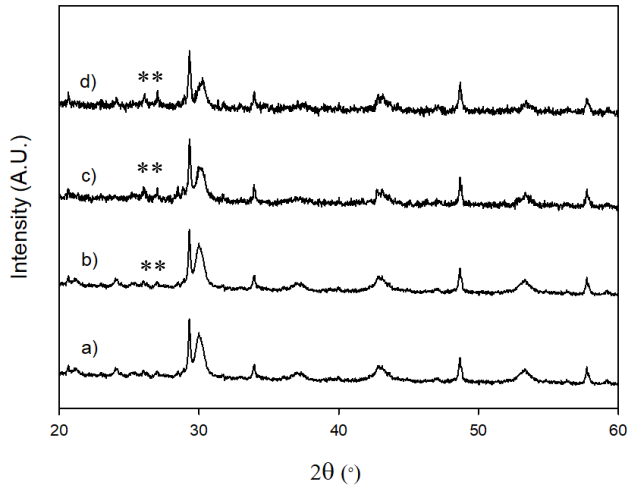

Figure 118. X-ray diffraction patterns for $Ba_3Y_2Ti_{1-x}S_xO_{8+x}$ after heat treatment in wet N_2 to 800 °C where a) x=0, b) x=0.2, c) x=0.3 and d) x=0.4. $BaSO_4$ impurities are highlighted with an asterisk (*).

9.3.5 Conductivity studies

Due to XRD and Raman spectroscopy indicating the successful incorporation of sulfate, impedance spectroscopy was carried out on all phases in air. For all phases, total conductivity is reported due to not being able to reliably separate bulk and grain boundary arcs.

Similar conductivity values are reported for the undoped, x=0.2 and x=0.4 phases with an increase for x=0.3. For all phases a linear relationship is not observed (Figure 119) between 400-800 °C. Instead approximately three straight lines can be seen in the conductivity data suggesting changes in conduction mechanism or cell symmetry on heating. Further work (e.g. variable temperature XRD) would be needed to investigate this. In comparison to typical electrolyte materials, smaller conductivities are reported here (Table 44) therefore further work would be needed to improve these materials for SOFC applications.

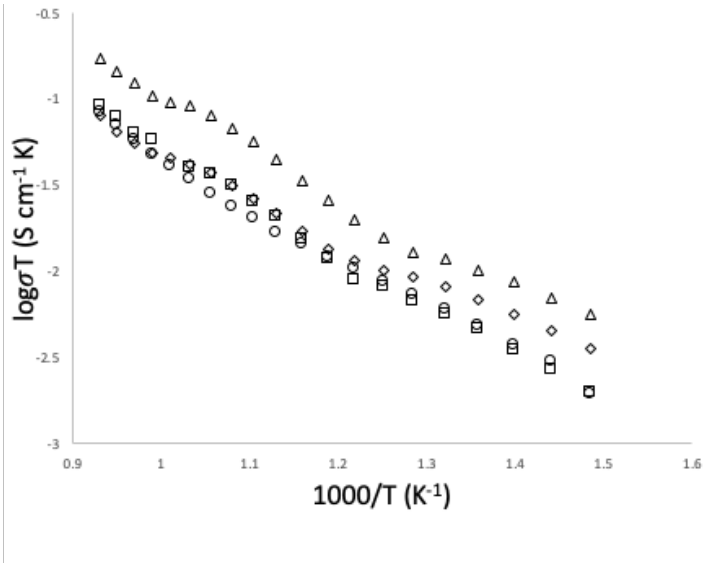

Figure 119. Conductivity data for $Ba_3Y_2Ti_{1-x}S_xO_{8+x}$ where x = 0 (○), 0.2 (□), 0.3 (△), 0.4 (◇)

Table 44. Total conductivity data for $Ba_3Y_2Ti_{1+x}S_xO_{8+x}$ heated in air

$Ba_3Y_2Ti_{1+x}S_xO_{8+x}$

x	Conductivity (S cm^{-1})	
	421 °C	800 °C
0	4.31×10^{-6}	7.94×10^{-5}
0.2	3.89×10^{-6}	8.54×10^{-5}
0.3	1.02×10^{-5}	1.62×10^{-4}
0.4	6.61×10^{-6}	7.46×10^{-5}

9.4 $Ba_3Y_2Ti_{1-x}P_xO_{8+(x/2)}$

9.4.1 X-ray diffraction results

Following on from sulfate doped $Ba_3Y_2TiO_8$ phases, phosphate doping was found to successfully stabilise the cubic perovskite structure. At low dopant levels (x=0.2) additional peaks are found in the XRD data (Figure 120). These additional reflections are assigned to a Ba deficient impurity phase $Ba_3Y_4O_9$. Cubic perovskite phases are successfully synthesised

for x=0.3 and 0.4, with small additional peaks where x=0.3. In comparison to the sulfate doped $Ba_3Y_2TiO_8$ phases, improvements in the XRD can be observed where here we do not have broad peaks in the XRD data.

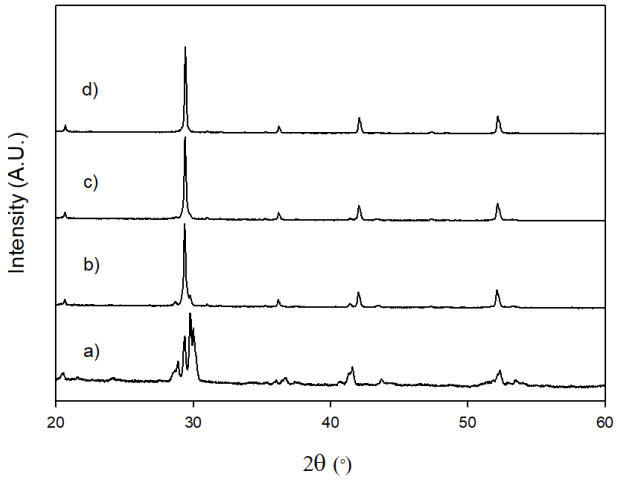

Figure 120. X-ray diffraction patterns for $Ba_3Y_2Ti_{1-x}P_xO_{8+(x/2)}$ where a) x=0, b) x=0.2, c) x=0.3 and d) x=0.4

Table 45. Refined structural parameters for $Ba_3Tm_2Ti_{0.6}P_{0.4}O_{8+(x/2)}$ with space group $Pm\bar{3}m$

$Ba_3Tm_2Ti_{0.6}P_{0.4}O_{8+(x/2)}$					
a (Å)	V (Å^3)	Rwp (%)		Rexp (%)	GOF
4.2882(1)	78.85(1)	3.66		2.08	1.76
	x	y	z	Occ	Uiso
Ba	0.0000	0.0000	0.0000	1.00	0.0371(8)
Y	0.5000	0.5000	0.5000	0.133	0.0274(10)
Ti	0.5000	0.5000	0.5000	0.200	0.0274(10)
P	0.5000	0.5000	0.5000	0.667	0.0274(10)
O	0.5000	0.5000	0.000	0.91	0.1228(41)

Table 46. Lattice parameters (space group $Pm\bar{3}m$) for $Ba_3Y_2Ti_{1-x}P_xO_{8+(x/2)}$ heating in air

$Ba_3Y_2Ti_{1+x}P_xO_{8+(x/2)}$		
	0.3	0.4
a (Å)	4.2871(1)	4.2882(1)
V (Å^3)	78.80(1)	78.85(1)
Rwp (%)	4.11	3.66
Rexp (%)	2.07	2.08
GOF	1.99	1.76

9.4.2 Raman spectroscopy

Raman spectroscopy indicates an emerging band at ≈ 940 cm^{-1} with increasing incorporation of phosphate (Figure 121). A similar observation is reported for $Ba_3Y_2Ti_{1-x}S_xO_{8+x}$ phases. The emerging phosphate peak is as reported for phosphate doped $Ba_2In_2O_5$ phases by Shin et al.[101] In addition to bands associated with phosphate, a number of other bands are present for all doped phases suggesting although the average structure is cubic through XRD, Raman data suggests local distortions away from perfect cubic symmetry. In comparison to $Ba_3Y_2Ti_{1-x}S_xO_{8+x}$ phases, these additional bands are broader and less intense. This could be possibly correlated with the improvements in XRD data. Small additional bands at ≈ 1060 cm^{-1} are consistent with the presence of carbonate.

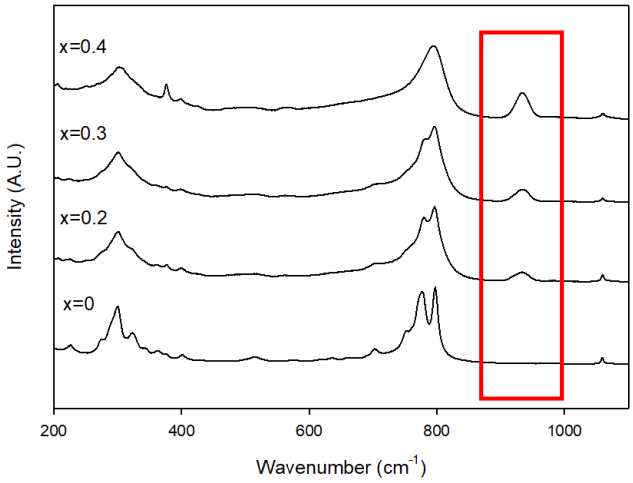

Figure 121. Raman spectra of $Ba_3Y_2Ti_{1-x}P_xO_{8+(x/2)}$ with peaks associated with phosphate incorporation highlighted in red

9.4.3 Stability in low p(O_2)

The stability of $Ba_3Y_2Ti_{1-x}P_xO_{8+(x/2)}$ phases were tested in N_2 to 800 °C. The undoped phase was found to be stable in N_2 with additional peaks for the doped phases. Small additional peaks are observed in the XRD data (Figure 122) for doped phases which suggests either a partial break down of the structure or a change in symmetry in lower p(O_2). Further work would be needed to investigate this.

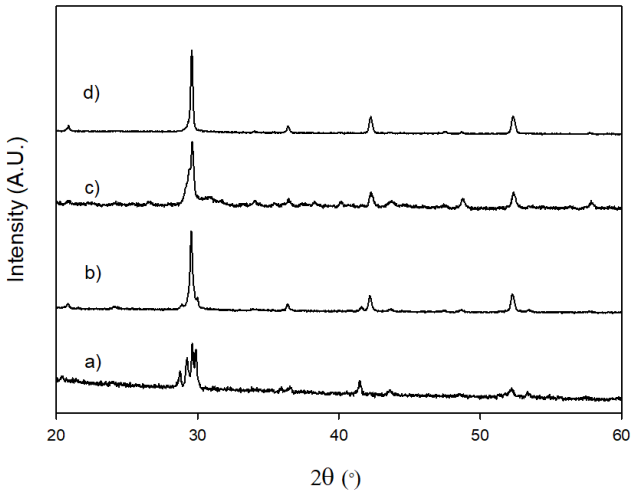

Figure 122. X-ray diffraction patterns for $Ba_3Y_2Ti_{1-x}P_xO_{8+(x/2)}$ after heat treatment in N_2 to 800 °C where a) x=0, b) x=0.2, c) x=0.3 and d) x=0.4

9.4.4 Stability in wet N_2

$Ba_3Y_2Ti_{1-x}P_xO_{8+(x/2)}$ phases were additionally heated in wet N_2 to 800 °C. For the undoped phase XRD data (Figure 123) suggests a breakdown of the structure. For the doped samples, additional reflections are observed suggesting a small impurity phase for all these doped materials.

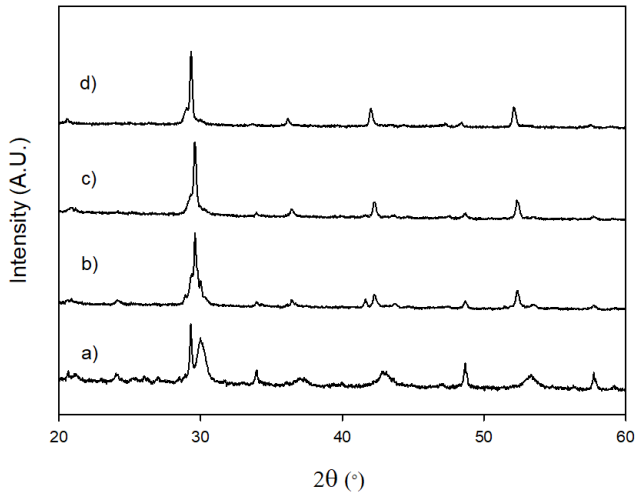

Figure 123. X-ray diffraction patterns for $Ba_3Y_2Ti_{1-x}P_xO_{8+(x/2)}$ after heat treatment in wet N_2 to 800 °C where a) x=0, b) x=0.2, c) x=0.3 and d) x=0.4

9.4.5 Conductivity studies

$Ba_3Y_2Ti_{1-x}P_xO_{8+(x/2)}$ phases show improved conductivity upon doping with phosphate (Figure 124 and Table 47). This is predicted to be due to the disordered oxygen sublattice in the cubic structure of these phases. When comparing the doped phases, similar conductivities are reported for all phases with improvements in conductivity compared to sulfate equivalents. However, in comparison to typical SOFC electrolyte materials, conductivities (0.01-0.1 S cm^{-1}) are low in comparison therefore further work would be needed to improve these materials.

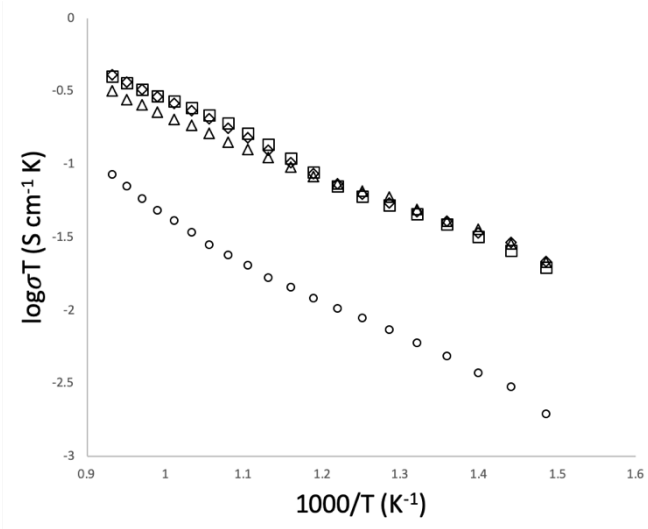

Figure 124. Conductivity data for $Ba_3Y_2Ti_{1-x}P_xO_{8+(x/2)}$ where x = 0 (○), 0.2 (□), 0.3 (△), 0.4 (◇)

Table 47. Total conductivity data for $Ba_3Y_2Ti_{1-x}P_xO_{8+(x/2)}$ heated in air

$Ba_3Y_2Ti_{1+x}P_xO_{8+(x/2)}$

x	Conductivity (S cm^{-1})	
	421 °C	800 °C
0	$4.31x10^{-6}$	$7.94x10^{-5}$
0.2	$3.69x10^{-5}$	$3.72x10^{-4}$
0.3	$4.11x10^{-5}$	$2.96x10^{-4}$
0.4	$4.20x10^{-5}$	$3.81x10^{-4}$

9.5 $Ba_3Tm_2Ti_{1-x}S_xO_{8+x}$

9.5.1 X-ray diffraction results

Due to the successful oxyanion incorporation into $Ba_3Y_2TiO_8$, sulfate and phosphate doped $Ba_3Tm_2TiO_8$ phases have also been investigated. X-ray diffraction studies for sulfate doped phases, $Ba_3Tm_2Ti_{1-x}S_xO_{8+x}$, indicate the stabilisation of the cubic perovskite structure where

x=0.2-0.4 (Figure 125). For x=0.2 and 0.3, small reflections associated with Tm_2O_3 are seen in the XRD data. For the undoped material $Ba_3Tm_2TiO_{8+x}$, a complex diffraction pattern is reported as observed for $Ba_3Y_2TiO_{8+x}$.

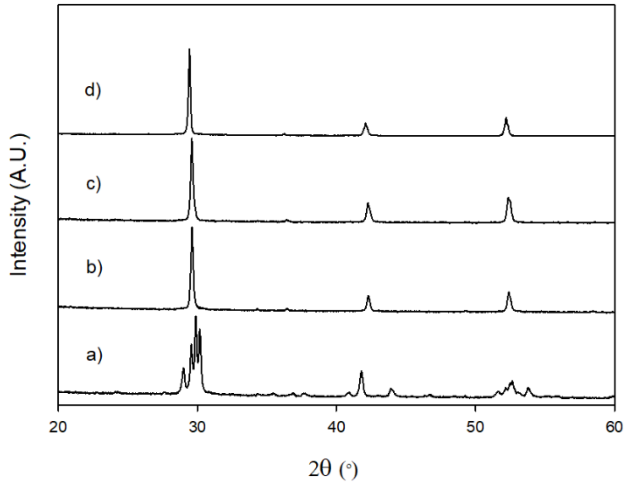

Figure 125. X-ray diffraction patterns for $Ba_3Tm_2Ti_{1-x}S_xO_{8+x}$ where a) x=0, b) x=0.2, c) x=0.3 and d) x=0.4

Rietveld refinements were carried out for all sulfate doped $Ba_3Tm_2TiO_8$ phases with refined structural parameters found in Table 48. Occupancies for Tm/Ti/S/O were fixed to expected values and thermal parameters were allowed to refine.

Table 48. Refined structural parameters for $Ba_3Tm_2Ti_{0.6}S_{0.4}O_{8+x}$ with space group $Pm\bar{3}m$.

$Ba_3Tm_2Ti_{0.6}S_{0.4}O_{8+x}$					
a (Å)	V (Å^3)	Rwp (%)		Rexp (%)	GOF
4.2884(1)	78.87(1)	5.14		2.56	2.01
	x	y	z	Occ	Uiso
Ba	0.0000	0.0000	0.0000	1.00	0.0266(19)
Y	0.5000	0.5000	0.5000	0.133	0.0240(20)
Ti	0.5000	0.5000	0.5000	0.200	0.0240(20)
S	0.5000	0.5000	0.5000	0.667	0.0240(20)
O	0.5000	0.5000	0.000	0.93	0.1626(74)

Lattice parameters for $Ba_3Tm_2Ti_{1-x}S_xO_{8+x}$ phases can be found in Table 49 and Figure 126. With increasing sulfate incorporation an increase in unit cell volume is observed. This is unexpected due to the smaller ionic radii of S^{6+} and Ti^{4+}. Instead here it is predicted the increase in unit cell volume is due to the increased oxygen content with increasing S^{6+}. Additionally, with increasing sulfate content, a decrease in Tm_2O_3 impurity is observed.

Table 49. Lattice parameters (space group $Pm\bar{3}m$) for $Ba_3Tm_2Ti_{1-x}S_xO_{8+x}$ (heating in air)

	$Ba_3Tm_2Ti_{1+x}S_xO_{8+x}$		
	0.2	0.3	0.4
a (Å)	4.2846(1)	4.2866(2)	4.2884(1)
V (Å^3)	78.65(1)	78.77(1)	78.87(1)
Rwp (%)	4.42	5.85	5.14
Rexp (%)	3.60	3.47	2.56
GOF	1.23	1.69	2.01
Tm_2O_3 impurity weight percent (%)	3.1	1.6	0.0

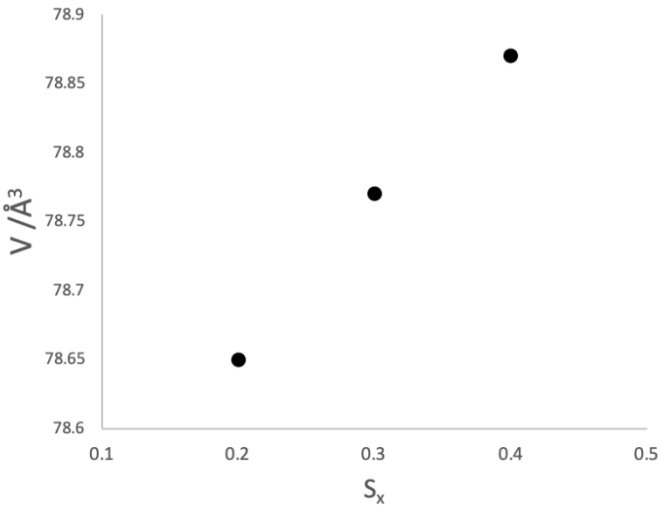

Figure 126. Variation of unit cell volume with sulfate content, x $Ba_3Tm_2Ti_{1-x}S_xO_{8+x}$

9.5.2 Raman spectroscopy

Raman spectroscopy of $Ba_3Tm_2Ti_{1-x}S_xO_{8+x}$ showed a similar trend as for $Ba_3Y_2Ti_{1-x}S_xO_{8+x}$ where appearance of a new band at ≈ 990 cm^{-1} increases with increased sulfate (Figure 127). As previously discussed a perfect cubic perovskite should have no Raman active bands, and

therefore the Raman data suggest local distortions away from the cubic symmetry within the structure. Additionally, at higher wavenumber (≈ 1060 cm^{-1}) all phases have a band associated with carbonate as reported for $Ba_3Y_2Ti_{1-x}S_xO_{8+x}$. Further work would be needed to investigate whether carbonate is due to unreacted $BaCO_3$ or due to carbonate within the perovskite structure.

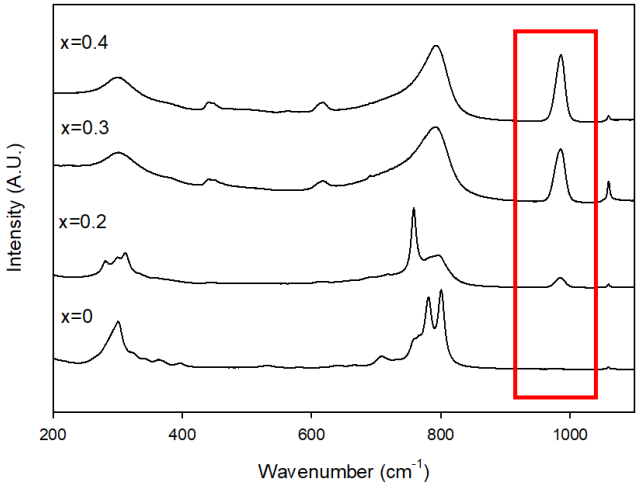

Figure 127. Raman spectra of $Ba_3Tm_2Ti_{1-x}S_xO_{8+x}$ with peaks associated with sulfate incorporation highlighted in red

9.5.3 Stability in low p(O_2)

The stability of $Ba_3Tm_2Ti_{1-x}S_xO_{8+x}$ phases were tested in N_2 to 800 °C. As observed for the undoped phase $Ba_3Y_2TiO_8$, $Ba_3Tm_2TiO_8$ remains stable under N_2 (Figure 128). For the sulfate doped phases, the cubic perovskite structure is also retained under these conditions. As observed when heating in air additional peaks associated with Tm_2O_3 are present for x=0.2 and 0.3.

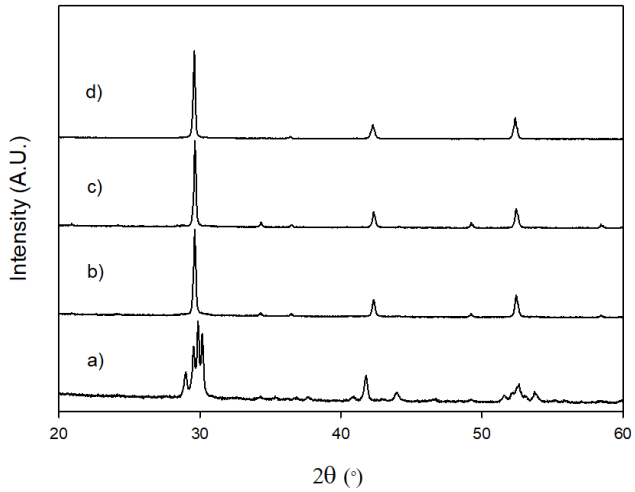

Figure 128. X-ray diffraction patterns for $Ba_3Tm_2Ti_{1-x}S_xO_{8+x}$ after heat treatment in N_2 to 800 °C where a) x=0, b) x=0.2, c) x=0.3 and d) x=0.4

Rietveld refinements were carried out for doped phases heated in N_2 and compared with phases heated in air. A decrease in unit cell volume is observed when comparing equivalent phases in air and N_2. This decrease in unit cell volume is unexpected. This is due to the reduction of Ti^{4+} to give Ti^{3+} which is expected to give an increase in cell volume. Therefore due to the larger unit cell volume for phases synthesised in air, it is predicted these phases are partially hydrated. With increasing sulfate content, an increase in unit cell volume is reported as seen for phases synthesised in air.

Table 50. Lattice parameters (space group $Pm\bar{3}m$) for $Ba_3Tm_2Ti_{1-x}S_xO_{8+x}$ heating in air and N_2 to 800 °C

$Ba_3Tm_2Ti_{1+x}S_xO_{8+x}$						
S (x)		a (Å)	V (Å^3)	R_{wp} (%)	R_{exp} (%)	Tm_2O_3 impurity (%)
0.2	Air	4.2846(1)	78.65(1)	4.42	3.6	3.1
	Dry N_2	4.2812(1)	78.47(1)	4.74	3.29	7.8
0.3	Air	4.2866(2)	78.77(1)	5.85	3.47	1.6
	Dry N_2	4.2817(1)	78.49(1)	4.58	3.14	14.4
0.4	Air	4.2884(1)	78.87(1)	5.14	2.56	0
	Dry N_2	4.2882(1)	78.85(1)	5.56	2.87	0

9.5.4 Stability in wet N_2

As observed for $Ba_3Tm_2Ti_{1-x}S_xO_{8+x}$ phases heated in dry N_2, when heating in wet N_2 all phases remain stable with a shift in the XRD data. For x=0.2 and 0.3, Tm_2O_3 impurity peaks are present with some additional broadening in the XRD data (Figure 129). Further work would be needed to investigate the broadening of these peaks which may related to inhomogeneities in hydration through the sample. Where x=0.4, the cubic perovskite structure remains stable.

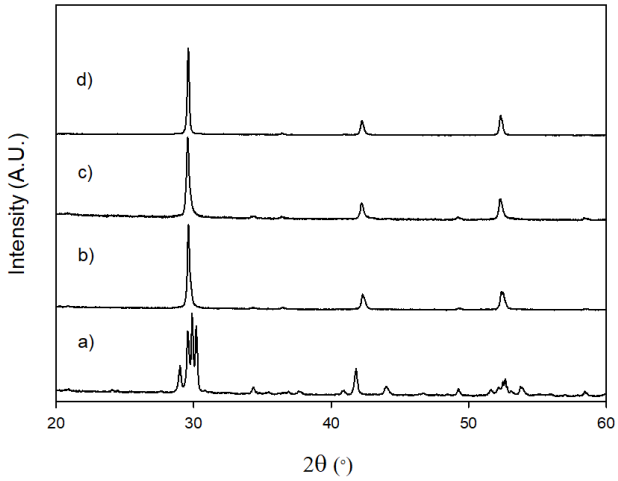

Figure 129. X-ray diffraction patterns for $Ba_3Tm_2Ti_{1-x}S_xO_{8+x}$ after heat treatment in wet N_2 to 800 °C where a) x=0, b) x=0.2, c) x=0.3 and d) x=0.4

Rietveld refinements were carried out for sulfate doped phases and compared with phases heated in N_2 in Table 51 and Figure 130. A larger unit cell volume is reported for phases heated in wet N_2 compared with equivalent dry N_2 phases. This increase in unit cell volume suggests water incorporation into these phases. This theory is further supported by TGA where loss of water over a range of temperatures is observed in Figure 131. This increase in unit cell volume for phases heated in wet N_2 compared with dry N_2 is as observed when comparing phases synthesised in air and heated in dry N_2. This observation additionally supports prior comments that air phases are partially hydrated.

Table 51. Lattice parameters (space group $Pm\bar{3}m$) for $Ba_3Tm_2Ti_{1-x}S_xO_{8+x}$ heating in dry and wet N_2 to 800 °C

$Ba_3Tm_2Ti_{1+x}S_xO_{8+x}$						
S (x)		a (Å)	V (Å^3)	R_{wp} (%)	R_{exp} (%)	Tm_2O_3 impurity (%)
0.2	Dry N_2	4.2812(1)	78.47(1)	4.74	3.29	7.8
	Wet N_2	4.2839(2)	78.62(1)	5.6	3.3	3.4
0.3	Dry N_2	4.2817(1)	78.49(1)	4.58	3.14	14.4
	Wet N_2	4.2930(3)	79.12(1)	5.62	3.36	3.9
0.4	Dry N_2	4.2882(1)	78.85(1)	5.56	2.87	0
	Wet N_2	4.2957(1)	79.27(1)	4.84	2.77	0

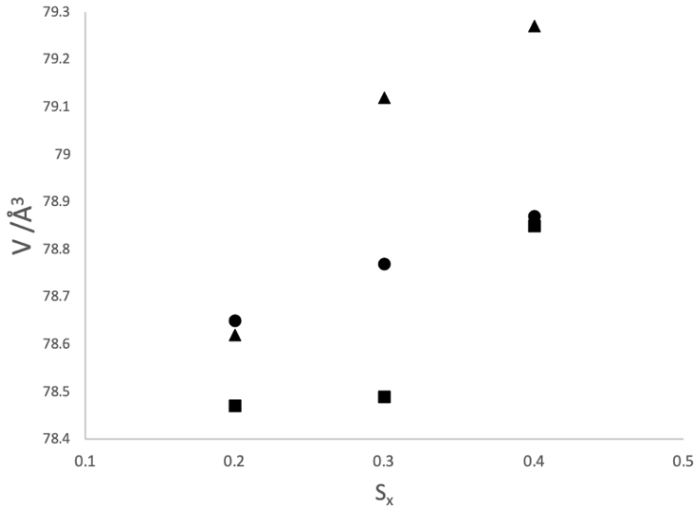

Figure 130. Variation of unit cell volume with sulfate content, x $Ba_3Tm_2Ti_{1-x}S_xO_{8+x}$, where air = ●, N_2 to 800 °C = ■ and wet N_2 to 800 °C = ▲

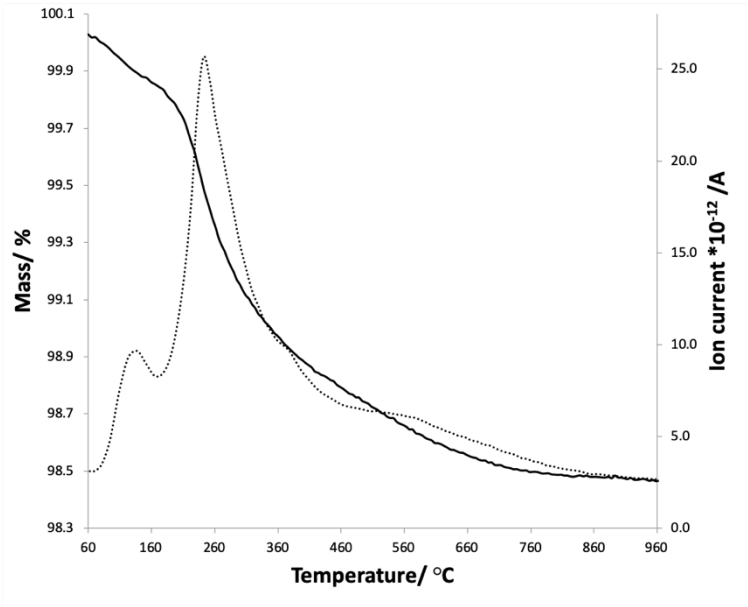

Figure 131. Plot of mass vs. temperature and ion current (for m/z = 18; H_2O) vs. temperature (under N_2) for $Ba_3Tm_2Ti_{0.6}S_{0.4}O_{8+x}$ prepared in wet N_2. Solid lines indicate %mass and dashed lines indicate ion current.

9.5.5 Conductivity studies

Due to the successful incorporation of sulfate into $Ba_3Tm_2Ti_{1-x}S_xO_{8+x}$ conductivity measurements were carried out. Due to the stabilisation of the disordered cubic perovskite structure an increase in conductivity is observed for the sulfate doped phases (Figure 132). Overall an increase in conductivity is reported with increasing temperature. At low temperature, similar conductivities are reported for x=0.2 and 0.4 with the highest conductivity for x=0.4 at high temperatures. Due to the stability of these phases in wet N_2, further work would be needed to investigate the suitability of these materials as proton conducting SOFCs. Further conductivity studies in dry and wet N_2 would be needed to identify any protonic contribution.

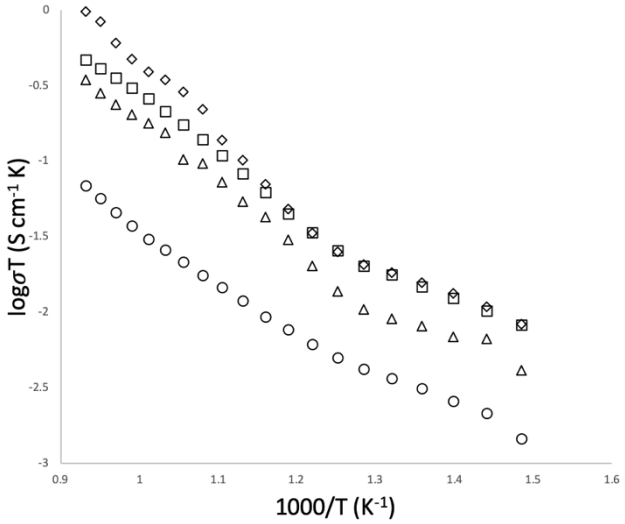

Figure 132. Conductivity data for $Ba_3Tm_2Ti_{1-x}S_xO_{8+x}$ where x = 0 (○), 0.2 (□), 0.3 (△), 0.4 (◇)

Table 52. Total conductivity data for $Ba_3Tm_2Ti_{1+x}S_xO_{8+x}$ heated in air

$Ba_3Tm_2Ti_{1+x}S_xO_{8+x}$

x	Conductivity (S cm^{-1})	
	421 °C	800 °C
0	3.07×10^{-6}	6.44×10^{-5}
0.2	1.47×10^{-5}	4.36×10^{-4}
0.3	9.61×10^{-6}	3.20×10^{-4}
0.4	1.56×10^{-5}	9.15×10^{-4}

9.6 $Ba_3Tm_2Ti_{1-x}P_xO_{8+(x/2)}$

9.6.1 X-ray diffraction results

XRD studies of $Ba_3Tm_2Ti_{1-x}P_xO_{8+(x/2)}$ indicate successful incorporation of phosphate with stabilisation of the cubic perovskite structure (Figure 133). On closer inspection small

additional reflections are observed for the doped phases which can be more clearly seen at low dopant levels. This is associated with a small barium deficient impurity phase, $Ba_3Tm_4O_9$.

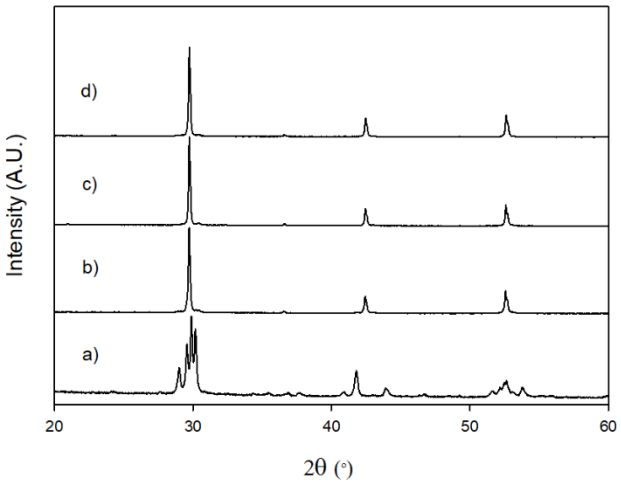

Figure 133. X-ray diffraction patterns for $Ba_3Tm_2Ti_{1-x}P_xO_{8+(x/2)}$ where a) x=0, b) x=0.2, c) x=0.3 and d) x=0.4

Rietveld refinements were carried out for the phosphate doped phases with an additional Tm_2O_3 impurity included. With increasing P content a decrease in unit cell volume is observed (Table 53 and Figure 134). This is predicted to be due to doping with smaller P^{5+} for Ti^{4+}. Here the lower change on P compared to S means less additional oxygen is incorporation, and so the effect of the increase in oxygen content is outweighed likely by the smaller size of P^{5+} verses Ti^{4+}.

Table 53. Lattice parameters (space group $Pm\bar{3}m$) for $Ba_3Tm_2Ti_{1-x}P_xO_{8+(x/2)}$ heating in air

	$Ba_3Tm_2Ti_{1+x}P_xO_{8+(x/2)}$		
	0.2	0.3	0.4
a (Å)	4.2714(1)	4.2706(1)	4.2683(1)
V (Å^3)	77.931(5)	77.886(3)	77.764(4)
Rwp (%)	5.20	4.65	4.90
Rexp (%)	3.06	2.77	2.95
GOF	1.70	1.68	1.66
Tm_2O_3 impurity weight percent (%)	3.3	3.7	2.2

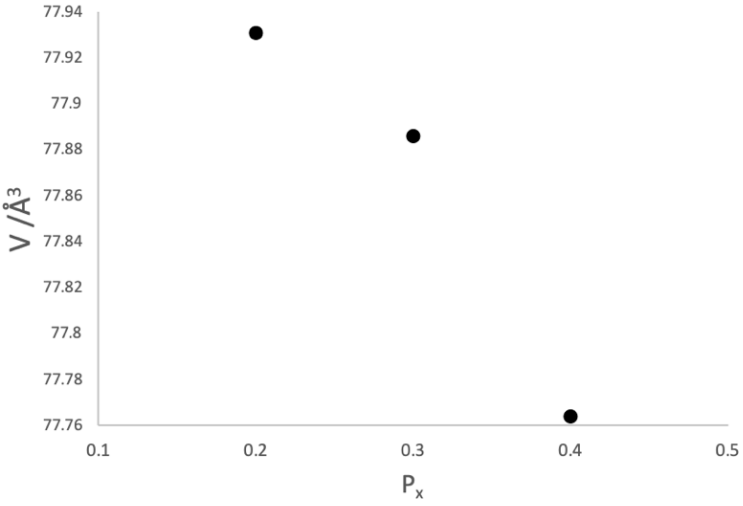

Figure 134. Variation of unit cell volume with sulfate content, x $Ba_3Tm_2Ti_{1-x}P_xO_{8+(x/2)}$

9.6.2 Raman spectroscopy

Raman spectroscopy studies of $Ba_3Tm_2Ti_{1-x}P_xO_{8+(x/2)}$ showed a similar trend as for $Ba_3Y_2Ti_{1-x}P_xO_{8+(x/2)}$ where appearance of a new band at ≈ 940 cm^{-1} (Figure 135) increases with

increased phosphate. As previously discussed, the cubic perovskite has no raman active bands therefore additional bands suggest local distortions within the structure.

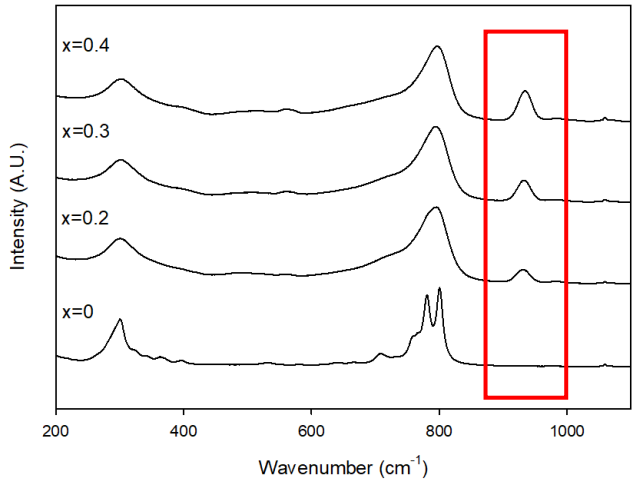

Figure 135. Raman spectra of $Ba_3Tm_2Ti_{1-x}P_xO_{8+(x/2)}$ with peaks associated with phosphate incorporation highlighted in red

9.6.3 Stability in low p(O_2)

The stability of $Ba_3Tm_2Ti_{1-x}P_xO_{8+(x/2)}$ phases were tested in N_2 to 800 °C. For $Ba_3Tm_2Ti_{1-x}P_xO_{8+(x/2)}$ where x=0.2 and 0.4 significant impurities are observed in Figure 136, suggesting a partial breakdown of the structure. $Ba_3Tm_2Ti_{0.7}P_{0.3}O_{8.15}$ remains stable and retains the cubic structure when heating in N_2 to 800 °C.

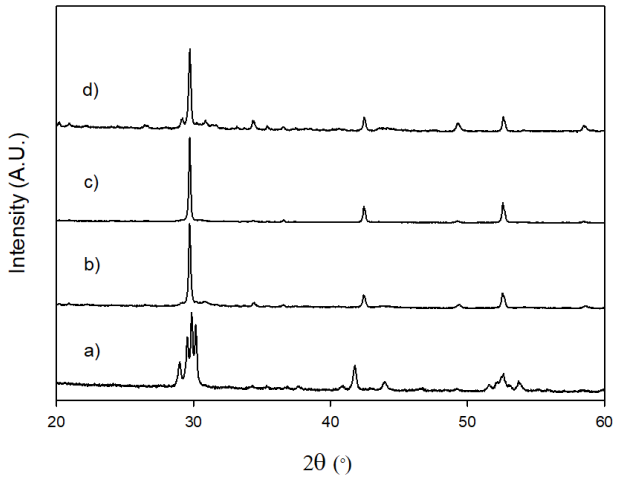

Figure 136. X-ray diffraction patterns for $Ba_3Tm_2Ti_{1-x}P_xO_{8+(x/2)}$ after heat treatment in N_2 to 800 °C where a) x=0, b) x=0.2, c) x=0.3 and d) x=0.4

9.6.4 Stability in wet N_2

In comparison to $Ba_3Tm_2Ti_{1-x}P_xO_{8+(x/2)}$ phases heated in dry N_2 to 800 °C, all phases remained stable when heating in wet N_2 to 800 °C. In Figure 137, a complicated XRD pattern is still observed for $Ba_3Tm_2TiO_8$ with a cubic perovskite structure for all doped phases. In comparison to the sulfate equivalents, no additional broadening is observed for these materials.

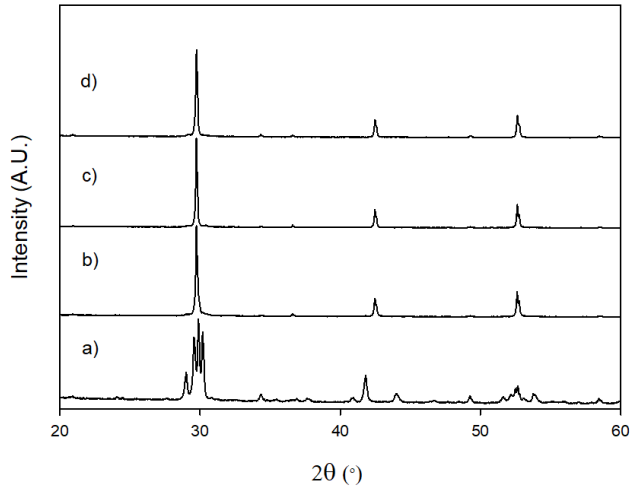

Figure 137. X-ray diffraction patterns for $Ba_3Tm_2Ti_{1-x}P_xO_{8+(x/2)}$ after heat treatment in wet N_2 to 800 °C where a) x=0, b) x=0.2, c) x=0.3 and d) x=0.4

When comparing XRD data for $Ba_3Tm_2Ti_{1-x}P_xO_{8+(x/2)}$ phases heated in wet N_2 to 800 °C and samples synthesised in air, no shift in the XRD data is observed. With no shift in the XRD it is predicted samples synthesised in air are partially hydrated. Further work would be needed to investigate this.

9.6.5 Conductivity studies

As observed for sulfate doped $Ba_3Tm_2TiO_8$ phases, phosphate doped phases (Figure 138) report improved conductivity compared to the undoped $Ba_3Tm_2TiO_8$. Here the highest conductivity is reported for x=0.2 with a reduction in conductivity with increasing phosphate content. As these phases are found to be stable in wet N_2, further conductivity studies would be needed to test suitability for use in proton conducting SOFCs.

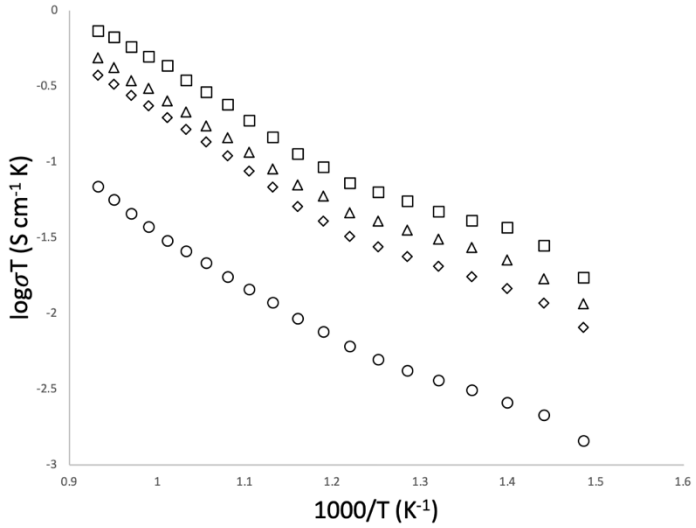

Figure 138. Conductivity data for $Ba_3Tm_2Ti_{1-x}P_xO_{8+(x/2)}$ where x = 0 (○), 0.2 (□), 0.3 (△), 0.4 (◇)

Table 54. Total conductivity data for $Ba_3Tm_2Ti_{1-x}P_xO_{8+(x/2)}$ heated in air

$Ba_3Tm_2Ti_{1+x}P_xO_{8+(x/2)}$

x	Conductivity (S cm^{-1})	
	421 °C	800 °C
0	3.07×10^{-6}	6.44×10^{-5}
0.2	4.06×10^{-5}	6.88×10^{-4}
0.3	2.45×10^{-5}	4.56×10^{-4}
0.4	1.69×10^{-5}	3.49×10^{-4}

9.7 Conclusions

This work has shown oxyanions (sulfate and phosphate) can be successfully incorporated into $Ba_3(Y/Tm)_2TiO_8$ phases with stabilisation of the cubic perovskite structure. For the undoped

phases additional reflections in the XRD data suggests a complex structure most likely related to anion vacancy ordering within the structure. For $Ba_3Y_2Ti_{1-x}(S/P)_xO_{8+y}$ phases XRD analysis indicated impurities in samples synthesised in air and stability issues when heating in dry and wet N_2. These issues were resolved by replacing Y^{3+} with Tm^{3+} which improved purity and stability of the perovskite materials. Thulium was chosen due to the expected similar properties, but smaller ionic radii which is predicted to increase the perovskite tolerance factor. By incorporating oxyanions enhancements to oxide ion conductivity is found. This is predicted to be due stabilisation of the disordered cubic perovskite structure. Although improvements in conductivity have been observed in other systems when doping with oxyanions, in general similar conductivities are reported for these particular materials. Here the effect on conductivity is also predicted to be due to the higher oxidation states (S^{6+}/P^{5+}) and coordination (tetragonal) of the oxyanions which can lead to vacancy trapping and therefore may be limiting an enhancement of the oxide ion conductivity. In order to test suitability for use in proton conducting SOFCs further conductivity studies would be needed. However, it should be noted that given the challenges in obtaining single phase samples in these systems, most likely related to Ba volatility (hence need to add Ba excess in the system) it is unlikely that these phases would be suitable for applications especially since the conductivities are also lower than current perovskite electrolyte materials.

Table 55. Chapter 9 summary table

Sample	**Crystal system (Synthesis temperature)**	**Stability**	**Highest conductivity (Temperature)**
$Ba_3Y_2TiO_8$	Unconfirmed	**Stability in low p(O_2)**	8 x 10^{-5} S cm^{-1}

	- additional reflections suggest lower symmetry system (1400 °C)	- Stable after heat treatment in N_2 to 800 °C **Stability in wet N_2** - Breakdown of structure into a number of phases	(800 °C)
$Ba_3Y_2Ti_{1-x}S_xO_{8+x}$	Cubic - peak broadening suggests possible lowering in symmetry or more than one perovskite phase (1200 °C)	**Stability in low $p(O_2)$** - peak broadening with growth of impurity peaks **Stability in wet N_2** - Breakdown of structure into a number of phases including $BaSO_4$	$7 \times 10^{-5} – 9 \times 10^{-3}$ S cm^{-1} (800 °C)
$Ba_3Y_2Ti_{1-x}P_xO_{8+(x/2)}$	Cubic (1400 °C)	**Stability in low $p(O_2)$** - Small additional peaks suggest partial breakdown of structure **Stability in wet N_2**	$3 \times 10^{-4} – 4 \times 10^{-4}$ S cm^{-1} (800 °C)

		- Additional reflections suggest small impurity phase	
$Ba_3Tm_2TiO_8$	Cubic (1400 °C)	**Stability in low p(O_2)** - Stable after heat treatment in N_2 to 800 °C **Stability in wet N_2** - Stable after heat treatment in wet N_2 to 800 °C	6×10^{-5} S cm^{-1} (800 °C)
$Ba_3Tm_2Ti_{1-x}S_xO_{8+x}$	(1200 °C)	**Stability in low p(O_2)** - Stable after heat treatment in N_2 to 800 °C - Additional peaks associated with Tm_2O_3 where x = 0.2 and 0.3 **Stability in wet N_2** - Stable after heat treatment in wet N_2 to 800 °C - Additional peaks associated with Tm_2O_3	3×10^{-4} – 9×10^{-4} S cm^{-1} (800 °C)

		and additional broadening in the XRD data where x = 0.2 and 0.3	
$Ba_3Tm_2Ti_{1-x}P_xO_{8+(x/2)}$	Cubic (1400 °C)	**Stability in low p(O_2)** - x = 0.3 remains stable - Additional peaks in XRD data suggests a partial breakdown of structure where x=0.2 and 0.4 **Stability in wet N_2** - Stable after heat treatment in wet N_2 to 800 °C	3 x 10^{-4} – 7 x 10^{-4} S cm^{-1} (800 °C)

10 Synthesis and characterisation of apatite materials with exsolution of copper

10.1 Introduction

The apatite structure has the general formulae $A_{10-x}(MO_4)_6X_{2\pm y}$ where A is commonly La/Sr/Ca and M= Si/Ge/P. The apatite structure has attracted interest for a number of applications including bioceramics and solid oxide fuel cells. The apatite structure is appealing for SOFC applications due to high oxide ion interstitial conductivity. $La_{9.33+z}(SiO_4)_6O_2$ materials attract considerable interest due to conductivity of the apatite phases being better than SOFC electrolyte material yttria-stabilised zirconia, YSZ.[86,94,212–214] In addition to La-Si-O apatite phases, $La_{10-x}(GeO_4)_6O_2$ phases have also been investigated due to high oxide ion conductivity. In comparison to Si phases, issues due to Ge volatility can occur in $La_{10-x}(GeO_4)_6O_2$ phases having a negative effect on conductivity.[87,215]

Typical doping strategies for SOFC materials include doping with different cations to improve the structure and properties of materials. In this work we have already discussed an alternate doping strategy where oxyanion doping has been applied to a range of perovskite and perovskite type phases. Here we investigate an alternate strategy where materials are doped with Cu which is in turn exsolved from the apatite phases using H_2 (Figure 139).

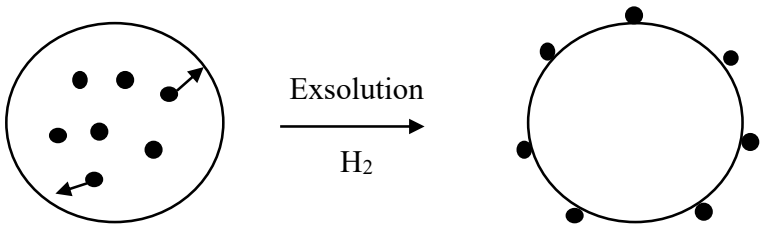

Figure 139. Diagram illustrating the exsolution process

By exsolving metal nanoparticles on the surface improvements can be made to the catalytic performance of materials. Additionally, exsolution offers more control over the

distribution and size of nanoparticles on the surface compared to other approaches.[116] Perovskite-type materials have been of particular interest for exsolution due to the flexibility of these structures. The perovskite structure is found to accommodate a range of metal dopants with exsolution on both the A and B site.[116,122,125,126,216] Exsolved nanoparticles on perovskite oxide lattices have been found to be suitable for energy applications where previous studies by Neagu et al.[116] and Tsekouras et al.[11] investigated exsolution of perovskite materials for solid oxide electrolysis cell cathode applications. A site deficient perovskite, $La_{0.4}Sr_{0.4}M_xTi_{1-x}O_{3-\delta}$ (where M=Fe/Ni) has been successfully shown to exsolve Fe/Ni with improvements to steam electrolysis for solid oxide electrolysis cell applications.[11] Perovskite materials doped with a range of metal dopants have been further investigated for SOFC applications where a particular interest has been in exsolution of Ni nanoparticles.[117–120,123,128,129,217,218]

In this work we report Cu doping in a range of apatite materials with synthesis and characterisation of materials before and after exsolution of Cu. Previous studies have also reported the successful incorporation of Cu into a range of apatite materials. A number of A-P-O apatite phases where A = Ca, Sr and Ba have been reported to incorporate copper where hexagonal tunnels, which are typically occupied by anions, are found to be occupied by copper. [219–221] This observation is not only reported for phosphate apatite phases, but also the apatite-like $Sr_5(CrO_4)(Cu_{0.586}O)$ reports the incorporation of copper into the tunnels parallel to the hexagonal c axis.[222] In relation to SOFC materials, apatite materials are of interest due to their appealing oxide ion conductivity. By doping with Cu, Yang et al.[96] found improvements in densification and a decrease in activation energy for La-Si-O apatite phases. This improvement in activation energy is predicted to be due to the enlarged lattice resulting in a bigger conduction channel.[96] These previous studies have shown that apatite materials can

accommodate copper with appealing properties for SOFC applications. As previously discussed for perovskite materials, exsolution of metal nanoparticles is found to improve the electrode performance for SOFC anode materials. Therefore, this work concentrates on incorporating copper into the apatite structure with a view to exsolve nanoparticles on the apatite surface. This in turn is predicted to improve properties for SOFC electrode materials.

10.2 Experimental

$(Ca/Sr)_{10}(PO_4)_6(OH)_{1-2x}(CuO_2)_x$ phases were synthesised by grinding stoichiometric amounts of $CaCO_3$/ $SrCO_3$, $NH_4H_2PO_4$ and CuO. The method described has been adapted from synthesis methods described by Kazin et al.[221] Samples heated to 400 °C for 12 h before regrinding and heated to 600 °C for 12 h. This was repeated with heating at 800 °C for 12 h. All phases were then pressed into pellets and heated to 1100 °C for 24 h followed by quenching of samples. All pellets were ground and samples were heated in dry N_2 to 950 °C (4 °C/ min) for 24 h.

$(Ca/Sr)_{10}(CrO_4)_6CuO_2$ phases were synthesised by grinding stoichiometric amounts of $CaCO_3$/ $SrCO_3$, Cr_2O_3 and CuO. Samples were heated to 850 °C for 12 h before regrinding and heated to 900 °C for 12 h. This was repeated with heating at 950 °C for 12 h.

$La_{10-x}Cu_xGe_{6-y}Cu_yO_{26+z}$ phases were synthesised by grinding stoichiometric amounts of La_2O_3, GeO_2 and CuO. Samples were heated to 950 °C for 12 h before regrinding and heating to 1000 °C for 12 h. This was repeated with heating at 1050 and 1100 °C for 12 h. The sample $La_{10}Ge_{5.5}Cu_{0.5}O_z$ was reground and heated for a further 12 h at 1150 °C.

Exsolution of $(Ca/Sr)_{10}(PO_4)_6(OH)_{1-2x}(CuO_2)_x$, $(Ca/Sr)_{10}(CrO_4)_6CuO_2$ and $La_{10-x}Cu_xGe_{6-y}Cu_yO_{26+z}$ was carried out by heating samples in 10% H_2/ 90% N_2 for 12 h with heating and cooling at 5 °C/ min. Final heating temperatures were 900 °C ($Ca_{10}(PO_4)_6(OH)_{1-}$

$_{2x}(CuO_2)_x$), 950 °C ($Sr_{10}(PO_4)_6(OH)_{1-2x}(CuO_2)_x$) 900 °C ($(Ca/Sr)_{10}(CrO_4)_6CuO_2$) and 700 °C ($La_{10-x}Cu_xGe_{6-y}Cu_yO_z$).

In order to determine the purity and lattice parameters of samples, powder X-ray diffraction (Panalytical Empyrean diffractometer equipped with a Pixcel 2D detector (Cu Kα radiation)) data was collected. For $(Ca/Sr)_{10}(CrO_4)_6CuO_2$ phases heated in 10% H_2/ 90% N_2, a Bruker D8 diffractometer with Cu Kα radiation was used. Topas software was used in order to determine lattice parameters through Pawley refinement.

Scanning electron microscopy images and energy dispersive X-ray spectroscopy (Philips XL-30 with EDS) data were collected for $(Ca/Sr)_{10}(CrO_4)_6CuO_2$ and $La_{10-x}Cu_xGe_{6-y}Cu_yO_{26+z}$ phases heated in 10% H_2/ 90% N_2. For $(Ca/Sr)_{10}(PO_4)_6(OH)_{1-2x}(CuO_2)_x$ phases heated in 10% H_2/ 90% N_2 the TM4000 microscope was used.

10.3 $(Ca/Sr)_{10}(PO_4)_6(OH)_{1-2x}(CuO_2)_x$

10.3.1 X-ray diffraction results

Figure 140 shows the XRD patterns for $(Ca/Sr)_{10}(PO_4)_6(OH)_{1-2x}(CuO_2)_x$ phases heated in air. All phases show formation of the hexagonal apatite structure with successful synthesis where copper is incorporated. The successful incorporation of Cu is also supported by the change in colour from white to purple for all phases. Small $Ca_3(PO4)_2$ impurities were found to be present for $Ca_{10}(PO_4)_6(OH)_{1-2x}(CuO_2)_x$ phases with additional $Sr_3(PO4)_2$ impurities for $Sr_{10}(PO_4)_6(OH)_{1-2x}(CuO_2)_x$.

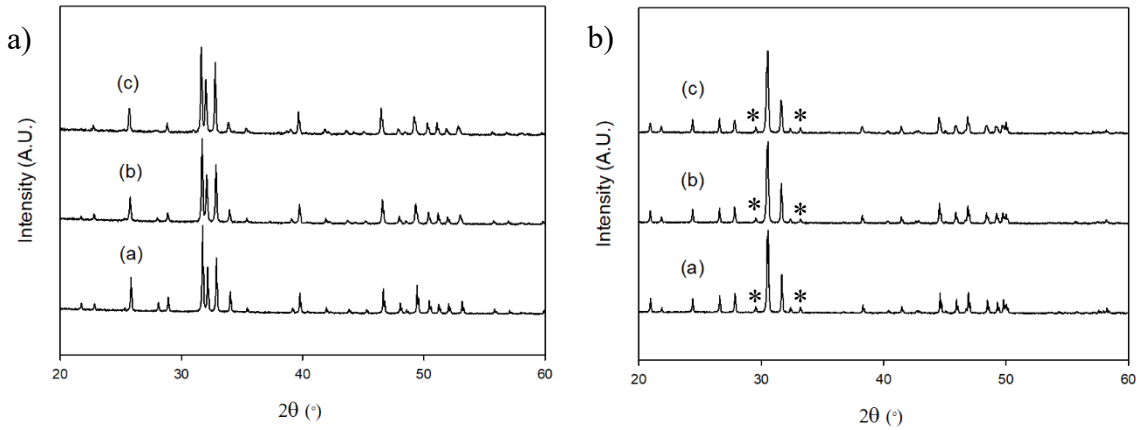

Figure 140. X-ray diffraction patterns for a) $Ca_{10}(PO_4)_6(OH)_{1-2x}(CuO_2)_x$ and b) $Sr_{10}(PO_4)_6(OH)_{1-2x}(CuO_2)_x$ heated in air, where a) x=0, b) x=0.5 and c) x=1. Peaks associated with $Sr_3(PO4)_2$ impurities are highlighted with an asterisk (*).

Previous studies on copper doped strontium phosphate apatite phases by Kazin et al.[221] found that by annealing in argon a higher copper occupancy could be obtained. Due to the higher occupancy obtained when heating in argon, $(Ca/Sr)_{10}(PO_4)_6(OH)_{1-2x}(CuO_2)_x$ phases were further investigated by heating in N_2 to 950 °C. For $(Ca/Sr)_{10}(PO_4)_6(OH)_{1-2x}(CuO_2)_x$ phases where x=0.5 and 1, small impurities were still found to be present in the XRD data (Figure 141). An increase in $Sr_3(PO4)_2$ impurities was found for $Sr_{10}(PO_4)_6(OH)(CuO_2)_{0.5,}$ but XRD data suggests a small improvement in purity for $Sr_{10}(PO_4)_6CuO_2$.

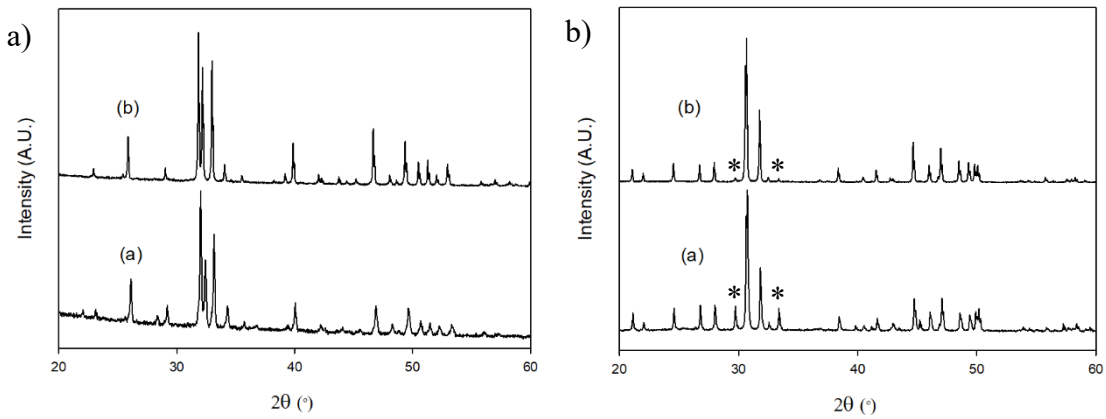

Figure 141. X-ray diffraction patterns for a) $Ca_{10}(PO_4)_6(OH)_{1-2x}(CuO_2)_x$ and b) $Sr_{10}(PO_4)_6(OH)_{1-2x}(CuO_2)_x$ heated in N_2, where a) x=0.5 and b) x=1. Peaks associated with $Sr_3(PO4)_2$ impurities are highlighted with an asterisk (*).

For both Ca/Sr phases an increase in unit cell volume is observed with increased Cu content. This is expected due to incorporating Cu in place of protons. Additionally, an overall larger unit cell volume is observed for Sr phases due to the larger size of Sr^{2+} vs Ca^{2+}.

Table 56. Lattice parameters for $(Ca/Sr)_{10}(PO_4)_6(OH)_{1-2x}(CuO_2)_x$ heated in 10% H_2/ 90% N_2 to 700 °C

	a (Å)	c (Å)	V (Å^3)	R_{wp} (%)	R_{exp} (%)
$Ca_{10}(PO_4)_6(OH)(CuO_2)_{0.5}$	9.4376(2)	6.8998(2)	532.2164(281)	5.89	3.58
$Ca_{10}(PO_4)_6CuO_2$	9.4464(1)	6.9292(1)	535.4829(98)	5.70	2.91
$Sr_{10}(PO_4)_6(OH)(CuO_2)_{0.5}$	9.7827(2)	7.2855(1)	603.8243(216)	4.78	1.37
$Sr_{10}(PO_4)_6CuO_2$	9.7962(1)	7.2969(1)	606.4302(181)	4.05	1.38

In order to investigate exsolution of Cu nanoparticles from $(Ca/Sr)_{10}(PO_4)_6(OH)_{1-2x}(CuO_2)_x$ apatite phases, samples were heated in 10% H_2/ 90% N_2. After heat treatment in 10% H_2/ 90% N_2, XRD data (Figure 142) confirmed that the apatite structure was retained with additional reflections associated with Cu. These additional reflections indicate the successful exsolution of Cu. Furthermore, when comparing the apatite materials when heating in N_2 to 10% H_2/ 90% N_2 a decrease in unit cell volume is observed for all phases again supporting the exsolution of Cu.

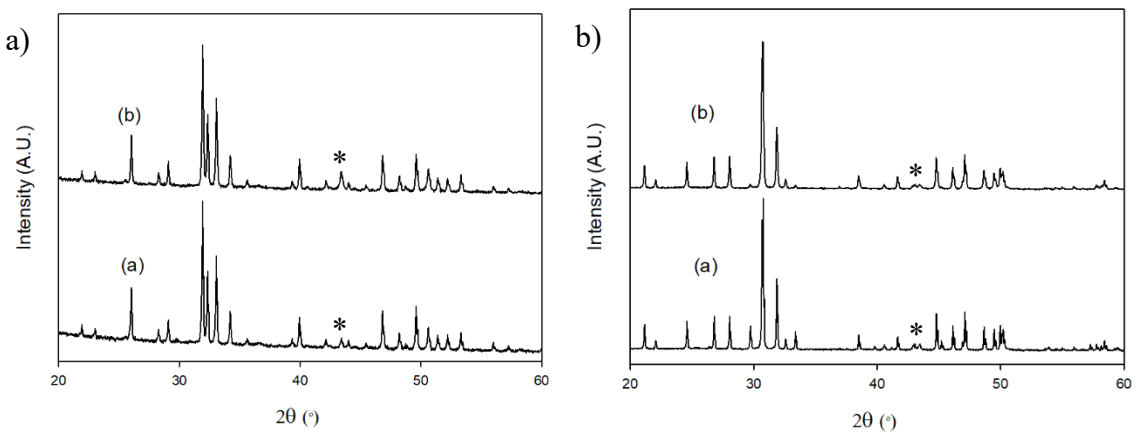

Figure 142. X-ray diffraction patterns for a) $Ca_{10}(PO_4)_6(OH)_{1-2x}(CuO_2)_x$ and b) $Sr_{10}(PO_4)_6(OH)_{1-2x}(CuO_2)_x$ heated in 10% H_2/ 90% N_2, where a) x=0.5 and b) x=1. Peaks associated with Cu are highlighted with an asterisk (*).

Table 57. Lattice parameters for $(Ca/Sr)_{10}(PO_4)_6(OH)_{1-2x}(CuO_2)_x$ heated in 10% H_2/ 90% N_2 to 700 °C

		a (Å)	c (Å)	V (Å^3)	R_{wp} (%)	R_{exp} (%)
$Ca_{10}(PO_4)_6(OH)(CuO_2)_{0.5}$	Dry N_2	9.4376(2)	6.8998(2)	532.2164(281)	5.89	3.58
	H_2	9.4246(1)	6.8848(1)	529.5986(195)	4.77	3.50
$Ca_{10}(PO_4)_6CuO_2$	Dry N_2	9.4464(1)	6.9292(1)	535.4829(98)	5.70	2.91
	H_2	9.4248(2)	6.8849(1)	529.6321(202)	6.59	3.34
$Sr_{10}(PO_4)_6(OH)(CuO_2)_{0.5}$	Dry N_2	9.7827(2)	7.2855(1)	603.8243(216)	4.78	1.37
	H_2	9.7667(1)	7.2815(1)	601.5122(129)	3.38	1.34
$Sr_{10}(PO_4)_6CuO_2$	Dry N_2	9.7962(1)	7.2969(1)	606.4302(181)	4.05	1.38
	H_2	9.7659(2)	7.2820(1)	601.4494(218)	2.80	1.31

10.3.2 Scanning electron microscopy

Due to the successful synthesis of Cu doped apatite phases, $(Ca/Sr)_{10}(PO_4)_6(OH)_{1-2x}(CuO_2)_x$ with indication of Cu exsolution through XRD, scanning electron microscopy was carried out.

$Ca_{10}(PO_4)_6(OH)_{1-2x}(CuO_2)_x$ heated in 10% H_2/ 90% N_2 to 900 °C

SEM analysis was carried out for both Cu doped phases, $Ca_{10}(PO_4)_6(OH)(CuO_2)_{0.5}$ and $Ca_{10}(PO_4)_6CuO_2$ after heating in 10% H_2/ 90% N_2. SEM data show spherical particles on the surface of the apatite structure with EDX analysis supporting the conclusion of copper exsolution. This can be seen in Figure 143 and Figure 144 where SEM indicates small particles (estimated as nanoparticles) on the surface with EDX showing a higher proportion of copper in these areas. This therefore supports the successful exsolution of copper from $Ca_{10}(PO_4)_6(OH)_{1-2x}(CuO_2)_x$ phases.

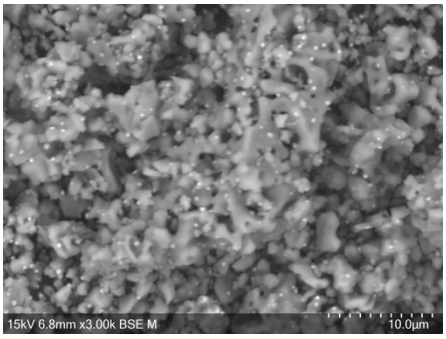

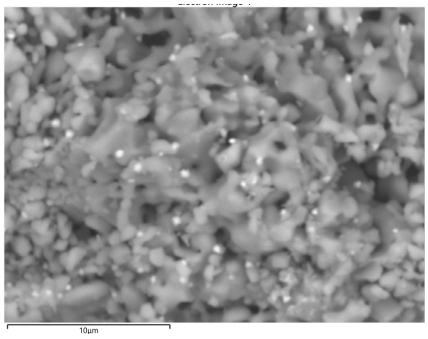

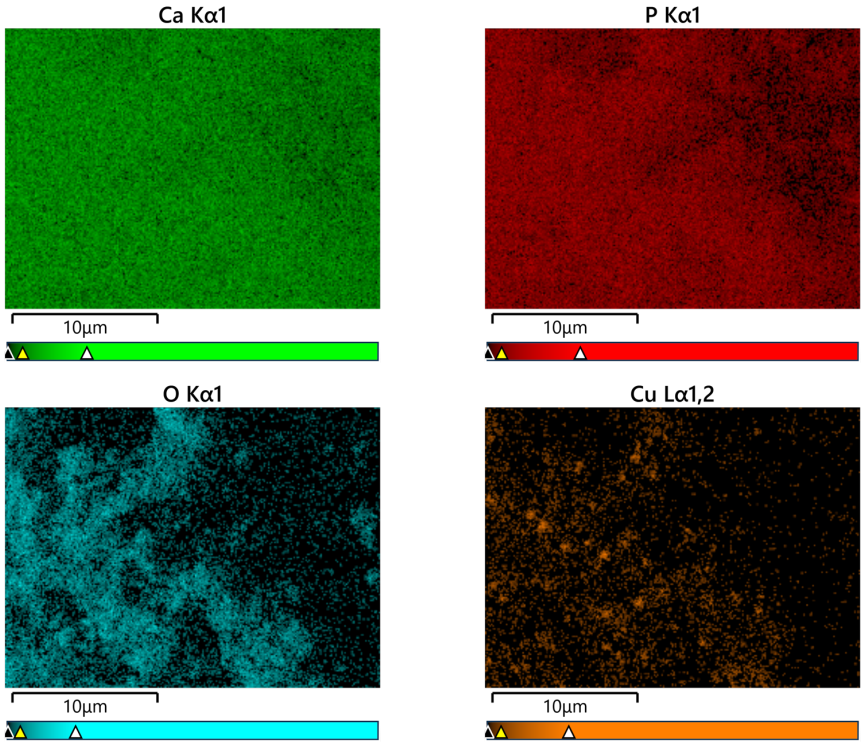

Figure 143. Scanning electron microscopy with energy dispersive X-ray spectroscopy of exsolved $Ca_{10}(PO_4)_6(OH)(CuO_2)_{0.5}$

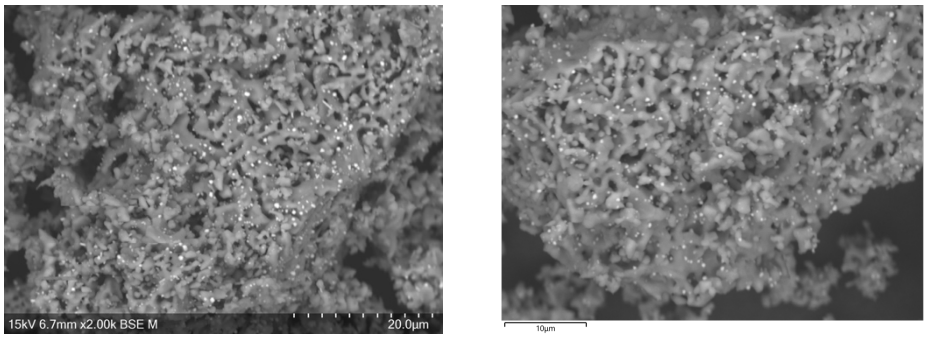

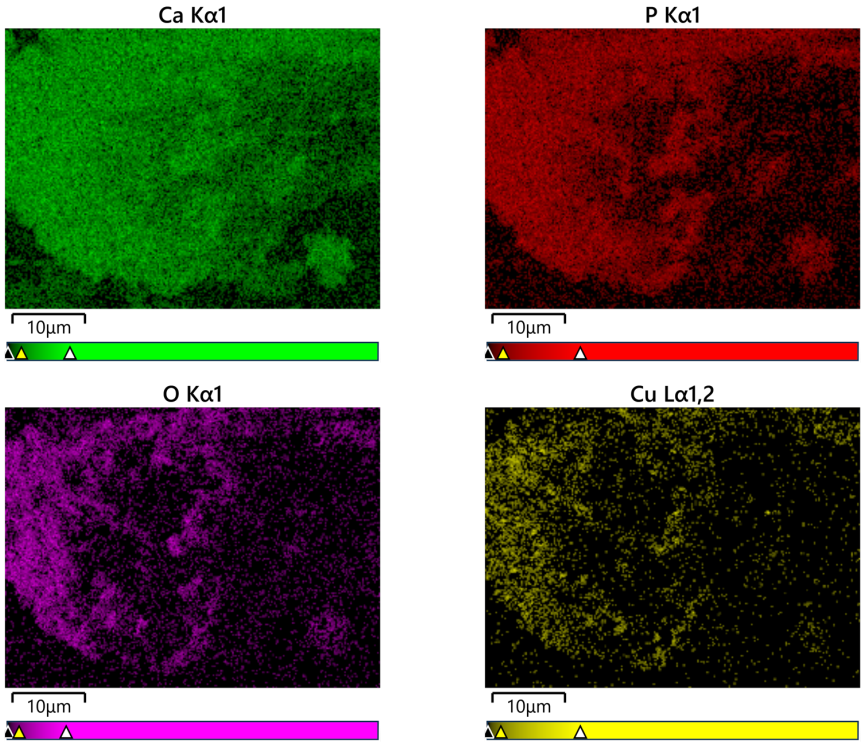

Figure 144. Scanning electron microscopy with energy dispersive X-ray spectroscopy of exsolved $Ca_{10}(PO_4)_6CuO_2$

$Sr_{10}(PO_4)_6(OH)_{1-2x}(CuO_2)_x$ heated in 10% H_2/ 90% N_2 to 950 °C

$Sr_{10}(PO_4)_6(OH)_{1-2x}(CuO_2)_x$ phases heated in 10% H_2/ 90% N_2 were also analysed by SEM with EDX analysis. As observed for the calcium equivalent phases, lighter spots (spherical particles) on the surface can be seen in SEM images in Figure 145 and Figure 146. EDX analysis of both $Sr_{10}(PO_4)_6(OH)(CuO_2)_{0.5}$ and $Sr_{10}(PO_4)_6CuO_2$ phases show a higher concentration of copper in these areas where the spherical particles are exsolved onto the surface, in support of the conclusion that these are due to Cu exsolution.

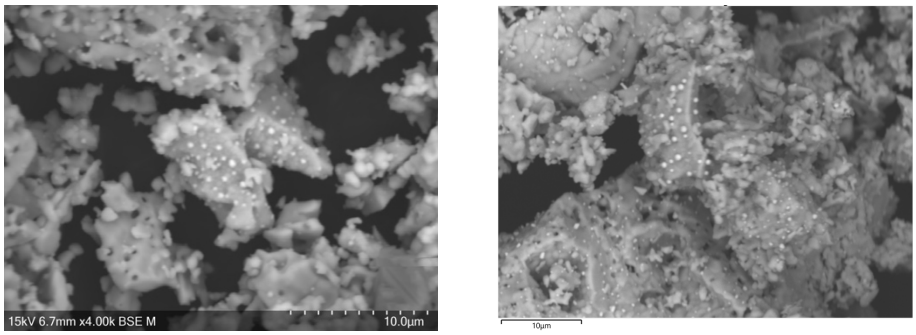

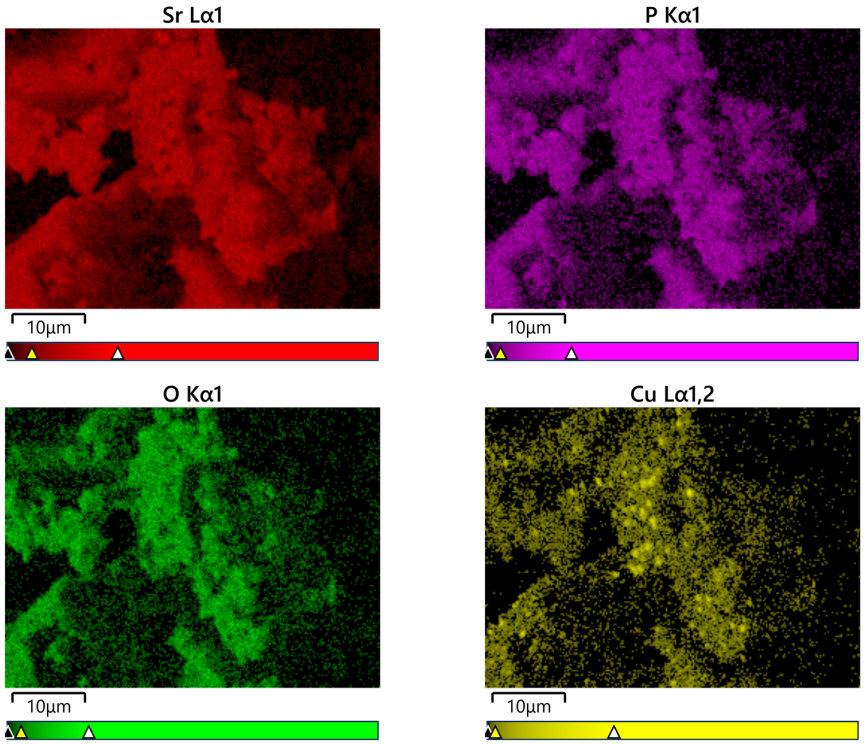

Figure 145. Scanning electron microscopy with energy dispersive X-ray spectroscopy of exsolved $Sr_{10}(PO_4)_6(OH)(CuO_2)_{0.5}$

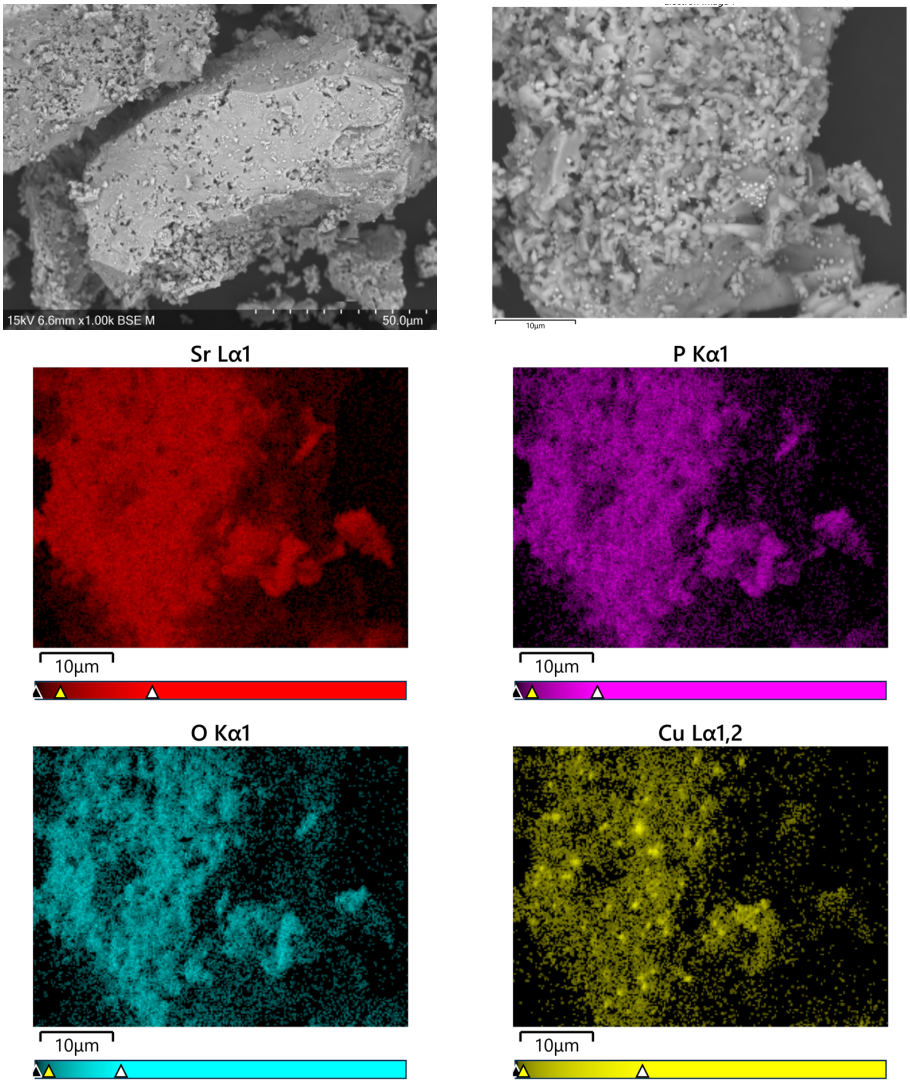

Figure 146. Scanning electron microscopy with energy dispersive X-ray spectroscopy of exsolved $Sr_{10}(PO_4)_6CuO_2$

10.4 $(Sr/Ca)_{10}(CrO_4)_6(OH)_x(CuO2)_y$

10.4.1 X-ray diffraction results

Due to the successful synthesis of $(Ca/Sr)_{10}(PO_4)_6(OH)_x(CuO_2)_y$ phases, specifically where y=1, $(Ca/Sr)_{10}(CrO_4)_6CuO_2$ phases were synthesised. Both Ca and Sr apatite phases successfully incorporate copper in the apatite structure as shown by the XRD data in Figure 147.

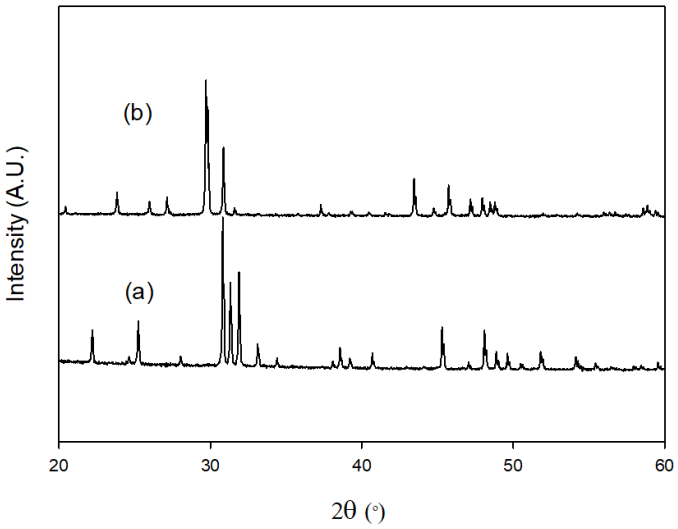

Figure 147. X-ray diffraction patterns for a) $Ca_{10}(CrO_4)_6CuO_2$ and b) $Sr_{10}(CrO_4)_6CuO_2$ heated in air

In order to investigate exsolution of copper nanoparticles from $(Ca/Sr)_{10}(CrO_4)_6CuO_2$ phases, these materials were heated in 10% H_2/ 90% N_2 to 900 °C for 12h. In comparison to the phosphate doped materials both $(Ca/Sr)_{10}(CrO_4)_6CuO_2$ apatite phases decompose and do not retain the apatite structure in contrast to the phosphate equivalent samples. Instead a mixture of phases are formed including reflections associated with Cu (Figure 148). For $(Ca/Sr)_{10}(CrO_4)_6CuO_2$ phases heated in 10% H_2/ 90% N_2, Cr could be reduced to Cr^{3+} whereas in comparison this would not occur for $(Ca/Sr)_{10}(PO_4)_6CuO_2$ phases. Therefore, it could be predicted when heating under 10% H_2/ 90% N_2, reduction of Cr to Cr^{3+} occurs resulting in a breakdown of the apatite structure.

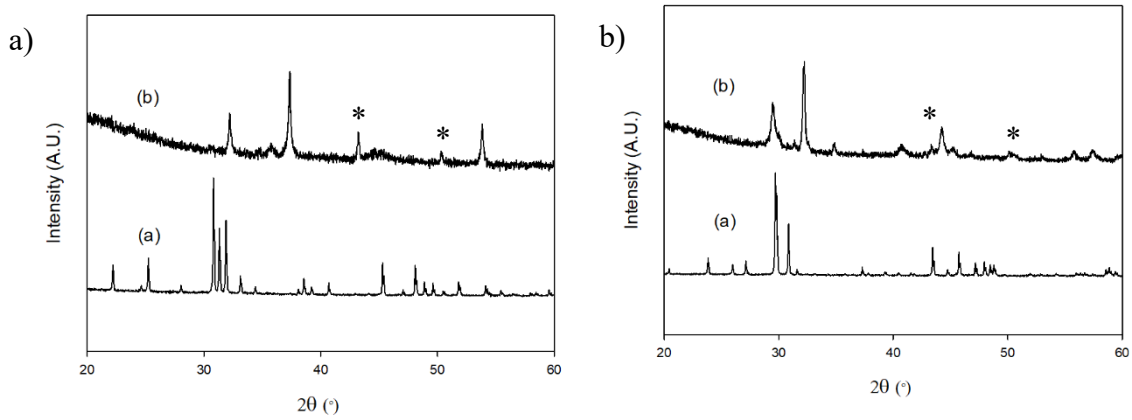

Figure 148. X-ray diffraction patterns for a) $Ca_{10}(CrO_4)_6CuO_2$ and b) $Sr_{10}(CrO_4)_6CuO_2$ heated in a) air and b) 10% H_2/ 90% N_2 to 900 °C. Peaks associated with Cu are highlighted with an asterisk (*).

10.4.2 Scanning electron microscopy

In order to investigate exsolution of copper nanoparticles from $Ca_{10}(CrO_4)_6CuO_2$ and $Sr_{10}(CrO_4)_6CuO_2$**,** SEM analysis was carried out. SEM images (Figure 149) for $Ca_{10}(CrO_4)_6CuO_2$, show lighter areas of spherical particles on the surface. EDX analysis was carried out on the spherical nanoparticles with a higher percentage of copper found at these points (Figure 150 and Table 58) supporting the conclusion that they are due to Cu.

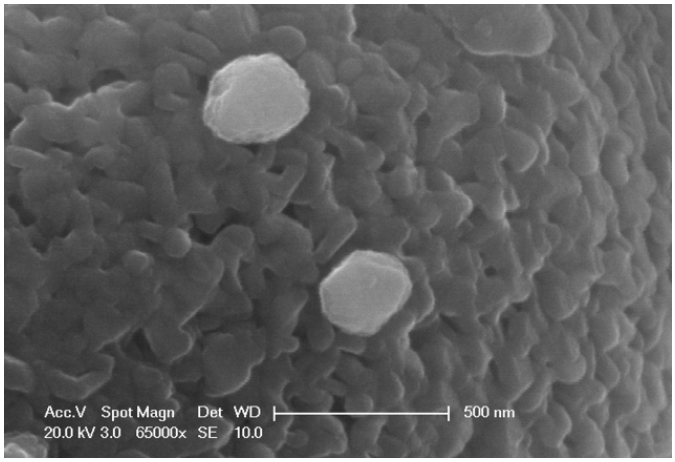

Figure 149. Scanning electron microscopy images of $Ca_{10}(CrO_4)_6CuO_2$

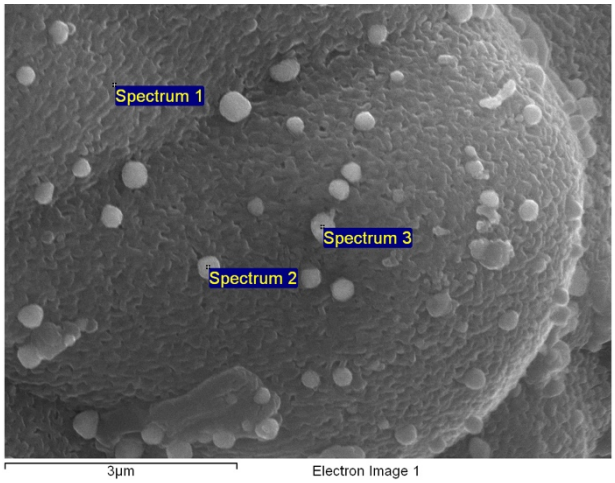

Figure 150. Scanning electron microscopy with energy dispersive X-ray spectroscopy of exsolved $Ca_{10}(CrO_4)_6CuO_2$

Table 58. Elemental analysis of $Ca_{10}(CrO_4)_6CuO_2$ through energy dispersive X-ray spectroscopy

	$Ca_{10}(CrO_4)_6CuO_2$			
	O	Ca	Cr	Cu
Spectrum 1	42.92 %	27.41 %	24.32 %	5.35 %
Spectrum 2	33.44 %	26.81 %	22.14 %	17.62 %
Spectrum 3	32.15 %	32.16 %	25.94 %	9.75 %

Additionally, SEM images of $Sr_{10}(CrO_4)_6CuO_2$ indicate light spots on the surface (Figure 151 and Figure 152). EDX analysis of $Sr_{10}(CrO_4)_6CuO_2$ also suggests a higher percentage of copper in these lighter areas, therefore suggesting successful exsolution of copper from $Sr_{10}(CrO_4)_6CuO_2$. In comparison to $Ca_{10}(CrO_4)_6CuO_2$, lighter spots are observed on the surface of $Sr_{10}(CrO_4)_6CuO_2$ where as more defined spherical particles are observed in Figure 150. Further SEM with EDX analysis would be needed to investigate this.

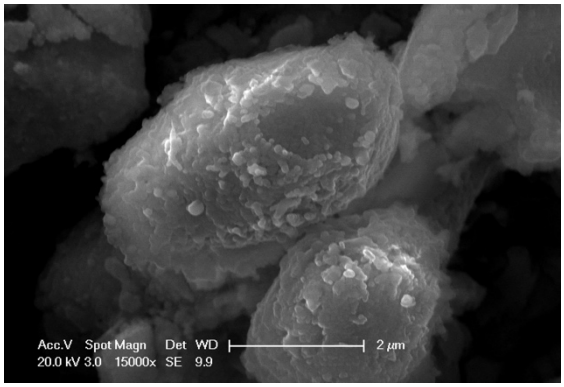

Figure 151. Scanning electron microscopy images of $Sr_{10}(CrO_4)_6CuO_2$

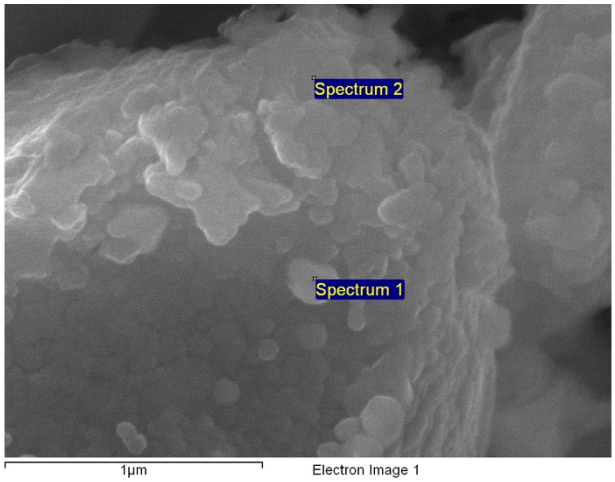

Figure 152. Scanning electron microscopy with energy dispersive X-ray spectroscopy of exsolved $Sr_{10}(CrO_4)_6CuO_2$

Table 59. Elemental analysis of $Sr_{10}(CrO_4)_6CuO_2$ through energy dispersive X-ray spectroscopy

	$Sr_{10}(CrO_4)_6CuO_2$				
	C	O	Cr	Cu	Sr
Spectrum 1	22.12%	20.18%	10.14%	15.90%	31.66%
Spectrum 2	26.35%	27.90%	12.48%	2.31%	30.95%

10.5 $La_{10-x}Cu_xGe_{6-y}Cu_yO_z$

10.5.1 X-ray diffraction results

Phosphate and chromate apatite phases successfully incorporate Cu into the apatite structure with exsolution of Cu under 10% H_2/ 90% N_2. Due to this, this method was extended to La-Ge-O apatite phases due to their appealing properties for SOFC applications.

In addition to phosphate and chromate apatite phases, Cu doped lanthanum germanate apatite phases have also been synthesised in air with a view to investigate copper exsolution. In addition to doping on the M site in $A_{10}(MO_4)_6O_2$, here copper doping on both the La and Ge site has been investigated. A total of 6 samples have been investigated including $La_{10}Ge_{5.5}Cu_{0.5}O_z$, $La_{9.5}Cu_{0.5}Ge_6O_z$, $La_{9.5}Cu_{0.5}Ge_{5.5}Cu_{0.5}O_z$, $La_9CuGe_{5.5}Cu_{0.5}O_z$, $La_{9.33}Ge_{5.7}Cu_{0.3}O_z$ and $La_{9.8}Cu_{0.2}Ge_6O_z$. The first three samples ($La_{10}Ge_{5.5}Cu_{0.5}O_z$, $La_{9.5}Cu_{0.5}Ge_6O_z$ and $La_{9.5}Cu_{0.5}Ge_{5.5}Cu_{0.5}O_z$) have all cation sites filled and therefore doping on and/or La/Ge is investigated. The remaining three samples ($La_9CuGe_{5.5}Cu_{0.5}O_z$, $La_{9.33}Ge_{5.7}Cu_{0.3}O_z$ and $La_{9.8}Cu_{0.2}Ge_6O_z$) have been investigated due to the predicted same stoichiometry for the apatite structure after heating in 10% H_2/ 90% N_2 (see Equation 27).

Equation 27.

$$\left.\begin{array}{l} La_9CuGe_{5.5}Cu_{0.5}O_z \\ La_{9.33}Ge_{5.7}Cu_{0.3}O_z \\ La_{9.8}Cu_{0.2}Ge_6O_z) \end{array}\right\} \xrightarrow{10\%\ H_2/\ 90\%\ N_2} La_{9.8}Ge_6O_x + Cu$$

XRD studies were carried out on all phases synthesised in air. XRD data (Figure 153) for $La_{9.5}Cu_{0.5}Ge_{5.5}Cu_{0.5}O_z$ and $La_{9.8}Cu_{0.2}Ge_6O_z$ indicated peak broadening which suggests the triclinic apatite structure is formed as previously observed for oxygen rich La-Ge-O

apatites.[88–90] For the remaining phases ($La_{10}Ge_{5.5}Cu_{0.5}O_z$, $La_{9.5}Cu_{0.5}Ge_6O_z$, $La_9CuGe_{5.5}Cu_{0.5}O_z$ and $La_{9.33}Ge_{5.7}Cu_{0.3}O_z$) the hexagonal apatite structure was stabilised with additional reflections associated with extra peaks due to a La_2GeO_5 impurity phase for $La_{10}Ge_{5.5}Cu_{0.5}O_z$.

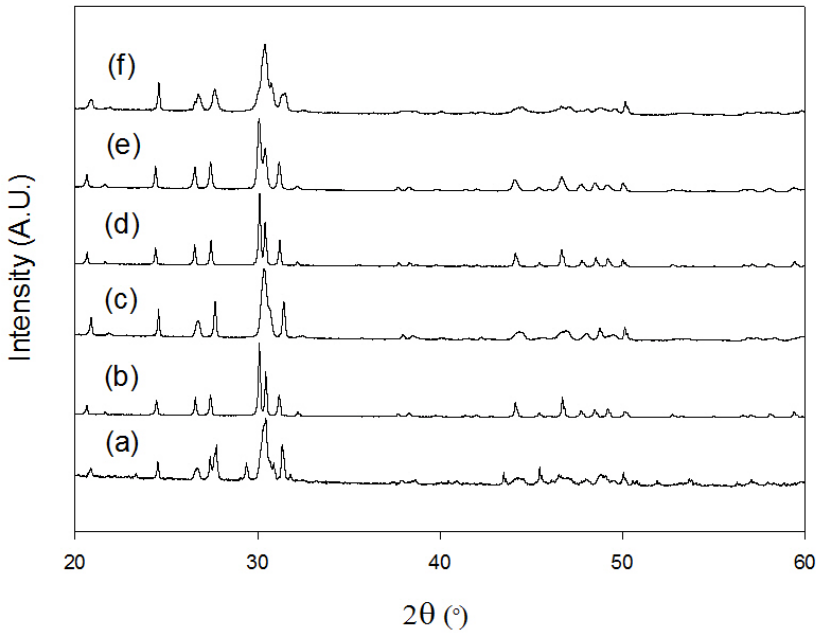

Figure 153. X-ray diffraction patterns for a) $La_{10}Ge_{5.5}Cu_{0.5}O_z$, b) $La_{9.5}Cu_{0.5}Ge_6O_z$, c) $La_{9.5}Cu_{0.5}Ge_{5.5}Cu_{0.5}O_z$, d) $La_9CuGe_{5.5}Cu_{0.5}O_z$, e) $La_{9.33}Ge_{5.7}Cu_{0.3}O_z$ and f) $La_{9.8}Cu_{0.2}Ge_6O_z$

For all phases Pawley refinements were carried out using TOPAS software in order to determine lattice parameters (Table 60).

Table 60. Lattice parameters for $La_{10-x}Cu_xGe_{6-y}Cu_yO_z$ heated in air

	$La_{10}Ge_{5.5}Cu_{0.5}O_z$	$La_{9.5}Cu_{0.5}Ge_6O_z$	$La_9CuGe_{5.5}Cu_{0.5}O_z$	$La_{9.33}Ge_{5.7}Cu_{0.3}O_z$
a (Å)	9.8725(4)	9.9231(1)	9.9144(2)	9.9261(3)
c (Å)	7.2669(6)	7.2709(1)	7.2853(2)	7.2855(3)
Volume ($Å^3$)	613.3885(692)	620.0273(205)	620.1602(234)	621.6476(397)
R_{wp} (%)	2.61	10.32	10.98	14.27
R_{exp} (%)	6.37	2.66	2.67	2.68

	$La_{9.5}Cu_{0.5}Ge_{5.5}Cu_{0.5}O_z$	$La_{9.8}Cu_{0.2}Ge_6O_z$
a (Å)	9.9582(5)	9.9376(5)
b (Å)	9.9107(4)	9.8805(4)
c (Å)	7.2386(3)	7.2947(3)
α (°)	90.6295(30)	90.7897(30)
β (°)	88.2005(40)	87.8976(59)
γ (°)	120.6949(36)	119.9737(38)
V ($Å^3$)	613.9947(510)	620.0356(540)
R_{wp} (%)	8.47	8.06
R_{exp} (%)	2.38	2.29

10.5.2 Exsolution

In order to investigate Cu exsolution, the $La_{10-x}Cu_xGe_{6-y}Cu_yO_z$ phases were heated in 10% H_2/ 90% N_2 to 700 °C for 12 h. For all phases broadening of XRD data is observed suggesting a lowering of symmetry for these phases most likely to the triclinic cell. Further details for each sample is given below.

$La_{10}Ge_{5.5}Cu_{0.5}O_z$

After heating in 10% H_2/ 90% N_2 broadening in the XRD is observed with additional reflections due to Cu and a further La_2GeO_5 impurity phase (Figure 154). SEM images indicate brighter spots on the surface of the apatite structure. In order to investigate if Cu is exsolved on these brighter spots, EDX analysis was carried out. Figure 155 and Table 61 show that the spherical particles on the surface of the apatite structure contain a higher percentage of Cu on the surface compared with areas where spherical particles are not present. These results support the conclusion that Cu is exsolved onto the surface of the apatite structure.

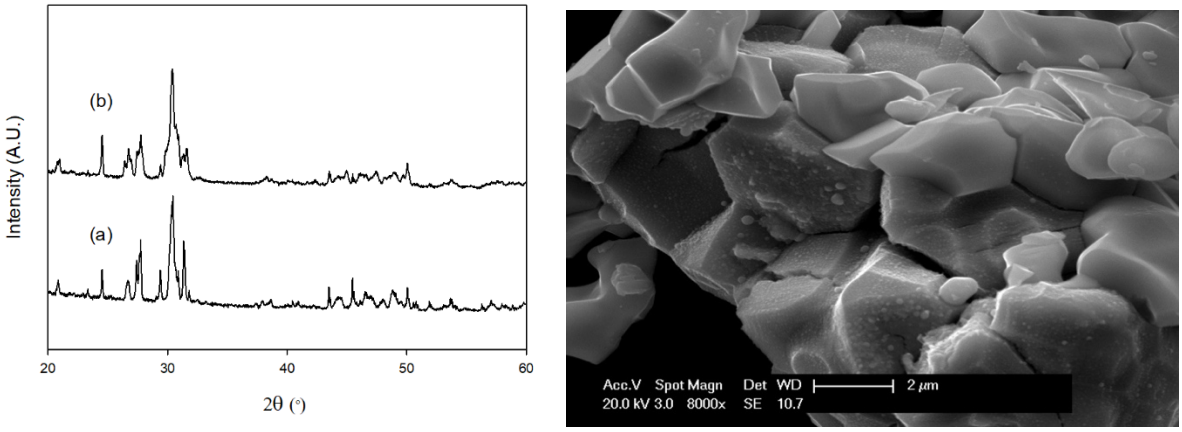

Figure 154. X-ray diffraction patterns for $La_{10}Ge_{5.5}Cu_{0.5}O_z$ a) heated in air and b) heated in 10% H_2/ 90% N_2 to 700 °C (left) and scanning electron microscopy image of $La_{10}Ge_{5.5}Cu_{0.5}O_z$ heated in 10% H_2/ 90% N_2 to 700 °C (right)

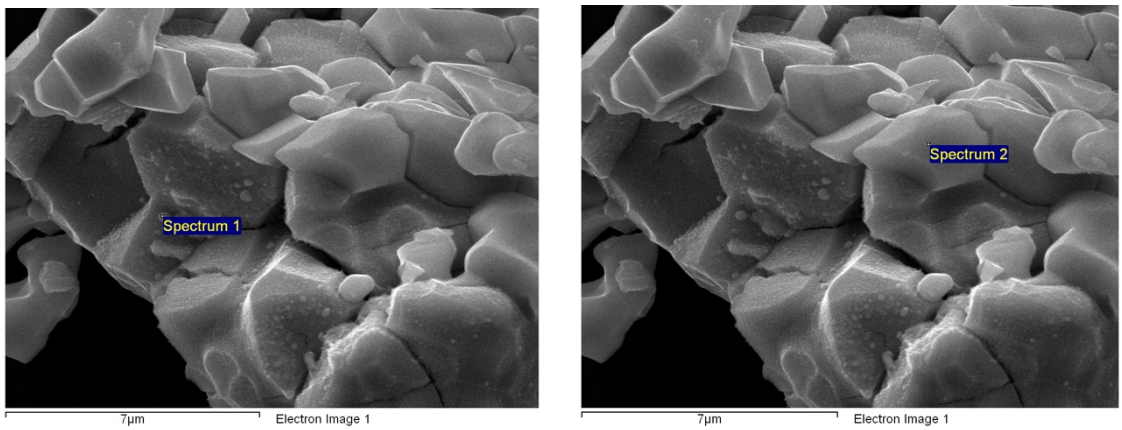

Figure 155. Scanning electron microscopy images of $La_{10}Ge_{5.5}Cu_{0.5}O_z$ heated in 10% H_2/ 90% N_2 to 700 °C with energy dispersive X-ray spectroscopy

Table 61. Elemental analysis of $La_{10}Ge_{5.5}Cu_{0.5}O_z$ through energy dispersive X-ray spectroscopy

	$La_{10}Ge_{5.5}Cu_{0.5}O_z$ - Weight %			
	La	Ge	Cu	O
Spectrum 1	64.29	2.03	30.47	3.30
Spectrum 2	69.13	3.28	-	27.60

$La_{9.5}Cu_{0.5}Ge_6O_z$

As observed for $La_{10}Ge_{5.5}Cu_{0.5}O_z$, peak broadening in the XRD data is reported for $La_{9.5}Cu_{0.5}Ge_6O_z$. The peak broadening in the XRD data indicates lowering of symmetry to a triclinic apatite phase (Figure 156). Additionally, SEM with EDX analysis was used in order to investigate exsolution of Cu. Figure 156 shows an SEM image of $La_{9.5}Cu_{0.5}Ge_6O_z$ with brighter spots on the surface of the apatite structure. EDX analysis (Figure 157) of

$La_{9.5}Cu_{0.5}Ge_6O_z$ reported no copper present in the dark regions in the SEM image with a significant weight percentage of Cu on brighter spots. This provides support for the conclusion that when heating in 10% H_2/ 90% N_2, Cu is exsolved onto the surface of the apatite structure.

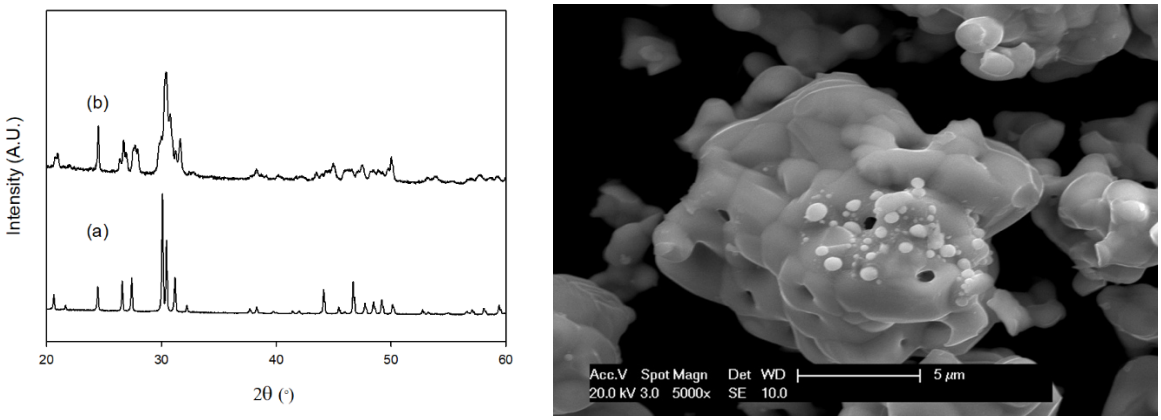

Figure 156. X-ray diffraction patterns for $La_{9.5}Cu_{0.5}Ge_6O_z$ a) heated in air and b) heated in 10% H_2/ 90% N_2 to 700 °C (left) and scanning electron microscopy images of $La_{9.5}Cu_{0.5}Ge_6O_z$ heated in 10% H_2/ 90% N_2 to 700 °C (right)

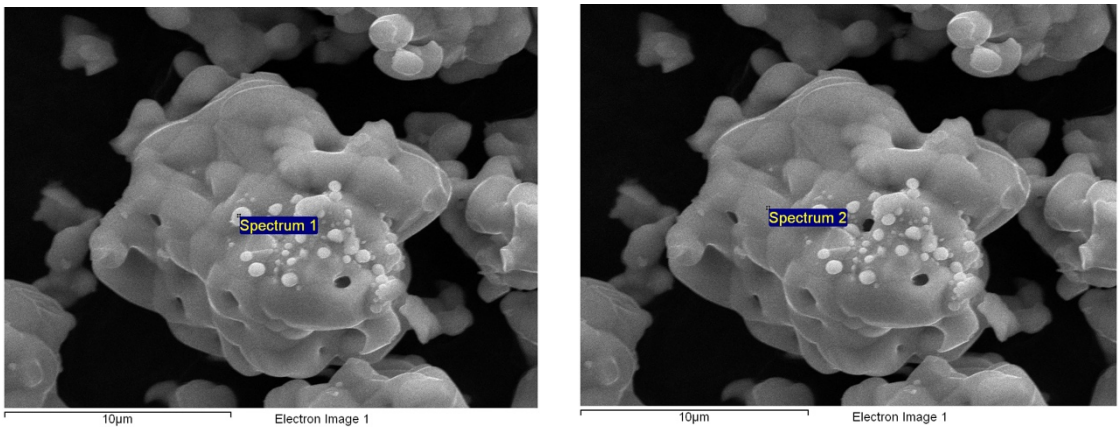

Figure 157. Scanning electron microscopy images with energy dispersive X-ray spectroscopy of $La_{9.5}Cu_{0.5}Ge_6O_z$ heated in 10% H_2/ 90% N_2 to 700 °C

Table 62. Elemental analysis of $La_{9.5}Cu_{0.5}Ge_6O_z$ through energy dispersive X-ray spectroscopy

	$La_{9.5}Cu_{0.5}Ge_6O_z$ - Weight %			
	La	Ge	Cu	O
Spectrum 1	27.07	12.02	46.87	14.03
Spectrum 2	69.75	5.16	-	25.80

$La_{9.5}Cu_{0.5}Ge_{5.5}Cu_{0.5}O_z$

The previous phases $La_{10}Ge_{5.5}Cu_{0.5}O_z$ and $La_{9.5}Cu_{0.5}Ge_6O_z$ have investigated Cu doping on Ge and La respectively. Here Cu doping on both La and Ge sites has been investigated. XRD data shows peak broadening with a lowering of symmetry to a triclinic apatite structure as reported for $La_{9.5}Cu_{0.5}Ge_6O_z$. As observed for previous La-Ge-Cu-O phases, brighter spherical particles are found on the surface (Figure 158). EDX analysis (Figure 159) of these brighter spots indicate a significant weight percent of copper on these spots with only a small percentage of Cu found on darker areas. This therefore supports the conclusion that Cu doping on La and/or Ge sites results in the successful exsolution of Cu onto the surface of the apatite structure.

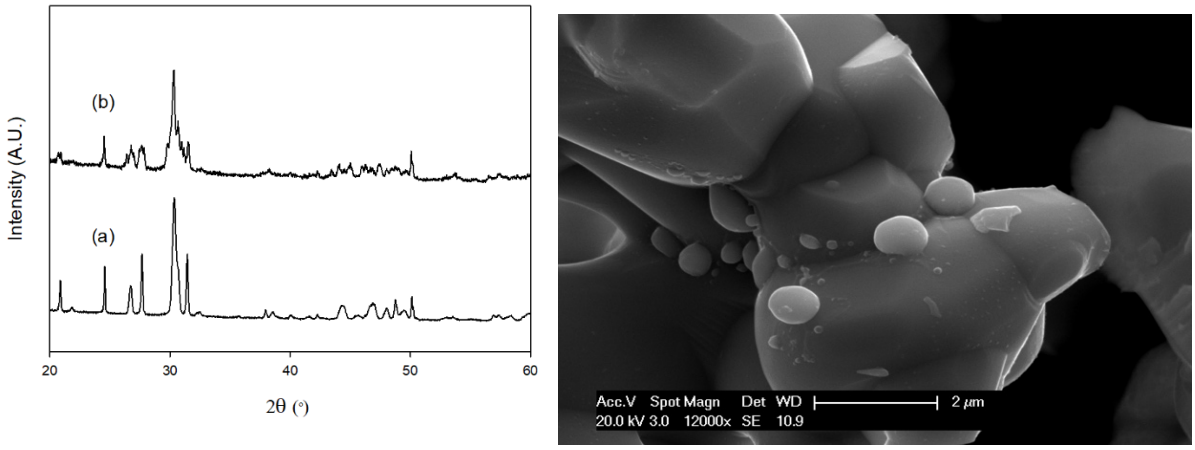

Figure 158. X-ray diffraction patterns for $La_{9.5}Cu_{0.5}Ge_{5.5}Cu_{0.5}O_z$ a) heated in air and b) heated in 10% H_2/ 90% N_2 to 700 °C (left) and scanning electron microscopy images of $La_{9.5}Cu_{0.5}Ge_{5.5}Cu_{0.5}O_z$ (right)

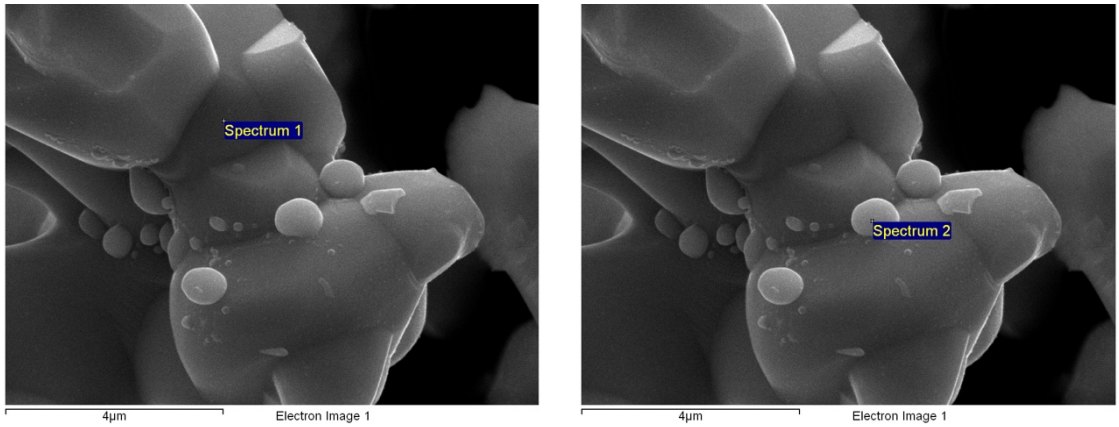

Figure 159. Scanning electron microscopy images with energy dispersive X-ray spectroscopy of $La_{9.5}Cu_{0.5}Ge_{5.5}Cu_{0.5}O_z$ heated in 10% H_2/ 90% N_2 to 700 °C

Table 63. Elemental analysis of $La_{9.5}Cu_{0.5}Ge_{5.5}Cu_{0.5}O_z$ through energy dispersive X-ray spectroscopy

	$La_{9.5}Cu_{0.5}Ge_{5.5}Cu_{0.5}O_z$ - Weight %			
	La	Ge	Cu	O
Spectrum 1	67.94	5.94	1.78	24.35
Spectrum 2	22.89	5.52	58.17	13.42

$La_9CuGe_{5.5}Cu_{0.5}O_z$

Following promising results from the initial Cu doping, three further compositions ($La_9CuGe_{5.5}Cu_{0.5}O_z$, $La_{9.33}Ge_{5.7}Cu_{0.3}O_z$ and $La_{9.8}Cu_{0.2}Ge_6O_z$) were investigated. These remaining phases have been investigated due to the expected formation of the same La:Ge ratio on exsolution when heating in 10% H_2/ 90% N_2 as described previously (Equation 27). Compared with the previously studied $La_{9.5}Cu_{0.5}Ge_{5.5}Cu_{0.5}O_z$, here a higher proportion of Cu is doped on the La site while still stabilising the hexagonal apatite structure.

After heat treatment in 10% H_2/ 90% N_2 peak broadening in the XRD data is reported as seen for other phases. SEM with EDX (Figure 161 and Table 64) show brighter spherical particles on the surface. EDX analysis shows a small percentage of Cu on the surface (darker areas) with a significantly higher percentage of Cu on the brighter spherical areas in the SEM image (Figure 160). Therefore the results show that not only is the hexagonal apatite structure stabilised with a higher proportion of Cu, but the Cu can also be exsolved onto the surface of the apatite structure by the reductive heat treatment.

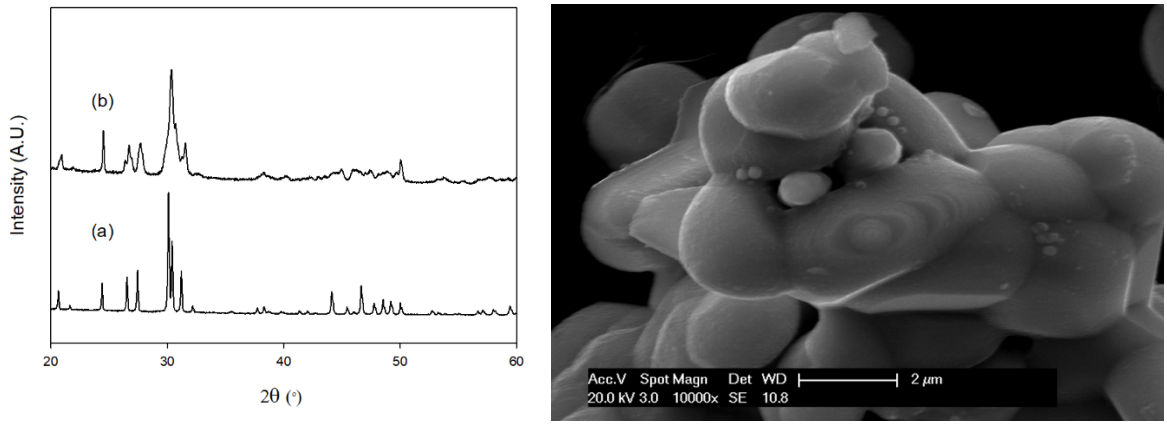

Figure 160. X-ray diffraction patterns for $La_9CuGe_{5.5}Cu_{0.5}O_z$ a) heated in air and b) heated in 10% H_2/ 90% N_2 to 700 °C (left) and scanning electron microscopy images of $La_9CuGe_{5.5}Cu_{0.5}O_z$ heated in 10% H_2/ 90% N_2 to 700 °C (right)

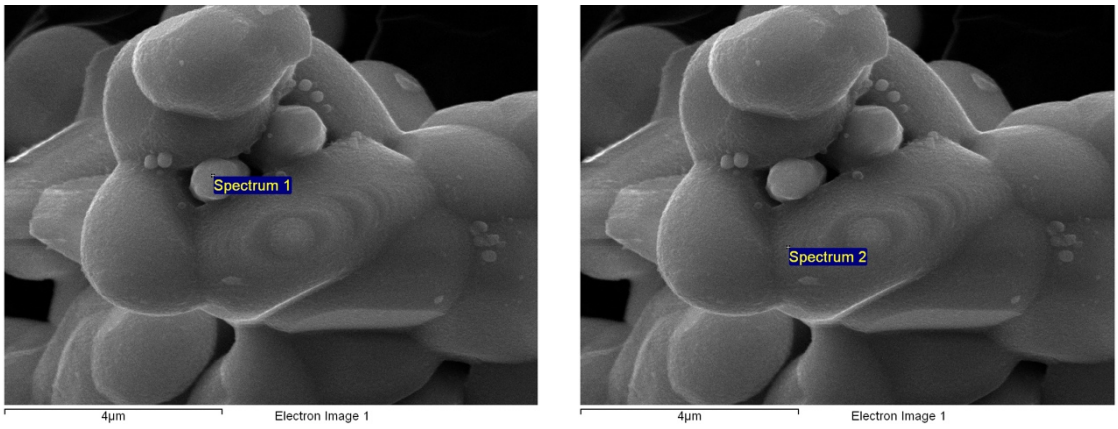

Figure 161. Scanning electron microscopy images with energy dispersive X-ray spectroscopy of $La_9CuGe_{5.5}Cu_{0.5}O_z$ heated in 10% H_2/ 90% N_2 to 700 °C

Table 64. Elemental analysis of $La_9CuGe_{5.5}Cu_{0.5}O_z$ through energy dispersive X-ray spectroscopy

	$La_9CuGe_{5.5}Cu_{0.5}O_z$ - Weight %			
	La	Ge	Cu	O
Spectrum 1	16.24	2.99	72.16	8.62
Spectrum 2	71.09	4.80	2.56	21.54

$La_{9.33}Ge_{5.7}Cu_{0.3}O_z$

As observed for other La-Ge-O phases heating in 10% H_2/ 90% N_2 lends to broadening of the XRD data suggesting a lowering of symmetry to a triclinic cell. Although some brighter areas are observed in the SEM images (Figure 162), EDX analysis did not indicate a higher percentage of Cu in these areas in contrast to the results reported for the other phases.

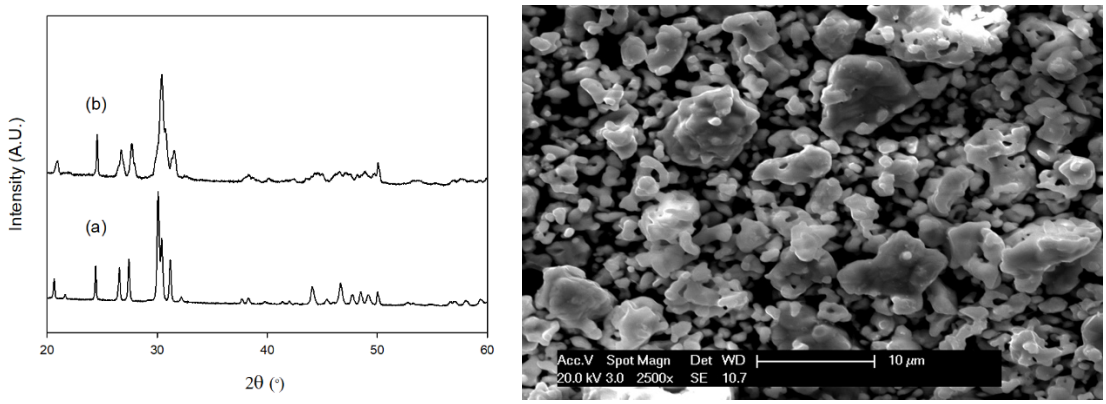

Figure 162. X-ray diffraction patterns for $La_{9.33}Ge_{5.7}Cu_{0.3}O_z$ a) heated in air and b) heated in 10% H_2/ 90% N_2 to 700 °C (left) and scanning electron microscopy images of $La_{9.33}Ge_{5.7}Cu_{0.3}O_z$ heated in 10% H_2/ 90% N_2 to 700 °C (right)

$La_{9.8}Cu_{0.2}Ge_6O_z$

The final sample investigated is $La_{9.8}Cu_{0.2}Ge_6O_z$ which is also predicted to exsolve Cu on the surface of $La_{9.8}Ge_6O_x$ after heating in 10% H_2/ 90% N_2. As for the other samples, peak broadening is observed in the XRD data. SEM was carried out in order to investigate Cu exsolution from $La_{9.8}Cu_{0.2}Ge_6O_z$ (Figure 163). Initially, spherical spots on the surface suggest exsolution of Cu on the surface. Further investigation with EDX analysis suggests lighter areas do not have a higher percentage of Cu as reported for other phases. SEM with EDX for both $La_{9.33}Ge_{5.7}Cu_{0.3}O_z$ and $La_{9.8}Cu_{0.2}Ge_6O_z$ suggest no exsolution of Cu. This therefore suggests lower levels of Cu doping effects exsolution from La-Ge-O apatite phases.

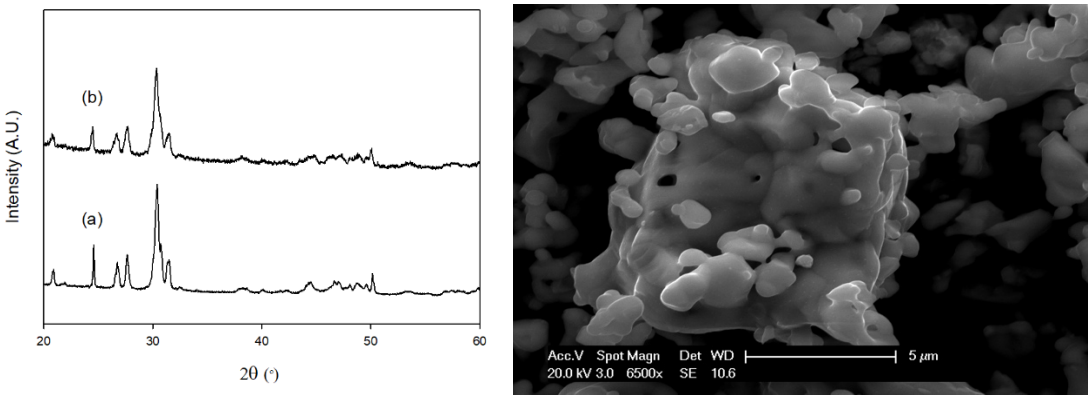

Figure 163. X-ray diffraction patterns for $La_{9.8}Cu_{0.2}Ge_6O_z$ a) heated in air and b) heated in 10% H_2/ 90% N_2 to 700 °C (left) and scanning electron microscopy images of $La_{9.8}Cu_{0.2}Ge_6O_z$ heated in 10% H_2/ 90% N_2 to 700 °C (right)

10.6 Conclusions

This work has shown the successful incorporation of copper into a range of apatite materials with successful exsolution of nanoparticles on the surface. $(Ca/Sr)_{10}(PO_4)_6(OH)_{1-2x}(CuO_2)_x$ phases are found to remain stable and retain the hexagonal apatite structure when heating in 10% H_2/ 90% N_2. SEM analysis show the successful exsolution of Cu on the surface of the

apatite structure. A similar observation is found for $(Ca/Sr)_{10}(PO_4)_6(OH)_x(CuO_2)_y$ phases where Cu particles are found on the surface. Although Cu exsolution is successful for $(Ca/Sr)_{10}(CrO_4)_6(OH)_x(CuO_2)_y$ phases, the apatite structure breaks down when heating in 10% H_2/ 90% N_2 indicating phosphate equivalents are more stable.

In addition to the above apatite phases, La-Ge-O apatite phases were investigated showing successful exsolution of Cu on the surface of the apatite structure. For all phases peak broadening in the XRD data is observed suggesting lowering of all symmetry with additional reflections associated with La_2GeO_5 impurity for $La_{10}Ge_{5.5}Cu_{0.5}O_z$. Phases with lower Cu doping levels ($La_{9.33}Ge_{5.7}Cu_{0.3}O_z$ and $La_{9.8}Cu_{0.2}Ge_6O_z$) were found to not exsolve Cu on the surface. Further research would be needed to investigate the effect of Cu dopant levels on exsolution.

Additionally, further work would be needed in order to test the effect on properties of these materials after exsolution. Particularly the effect on properties with a view to utilise these materials as SOFC electrode materials, or as catalysts in other applications.

Table 65. Chapter 10 summary table

Sample	**Crystal system (Synthesis temperature)**	**Exsolution in 10% H_2/ 90% N_2**
$Ca_{10}(PO_4)_6(OH)_{1-2x}(CuO_2)_x$	Hexagonal (1100 °C, additional treatment in dry N_2 to 950 °C)	900 °C - Apatite structure retained with additional reflections associated with Cu - Cu nanoparticles on surface
$Sr_{10}(PO_4)_6(OH)_{1-2x}(CuO_2)_x$	Hexagonal (1100 °C, additional treatment in dry N_2 to 950 °C)	950 °C - Apatite structure retained with additional reflections associated with Cu - Cu nanoparticles on surface

$Ca_{10}(CrO_4)_6CuO_2$	Hexagonal (950 °C)	900 °C - Samples decompose into a mixture of phases including Cu - Cu nanoparticles on surface
$Sr_{10}(CrO_4)_6CuO_2$	Hexagonal (950 °C)	900 °C - Samples decompose into a mixture of phases including Cu - Cu nanoparticles on surface
$La_{10-x}Cu_xGe_{6-y}Cu_yO_{26+z}$	Hexagonal (1100 °C, La10Ge5.5Cu0.5Oz (1150 °C))	700 °C - Broadening of XRD data suggests lowering of symmetry for all phases - SEM with EDX shows brighter spherical areas with a higher percentage of Cu for $La_{10}Ge_{5.5}Cu_{0.5}O_z$, $La_{9.5}Cu_{0.5}Ge_6O_z$, $La_{9.5}Cu_{0.5}Ge_6O_z$ and $La_9CuGe_{5.5}Cu_{0.5}O_z$ - SEM with EDX suggests no exsolution of Cu for $La_{9.33}Ge_{5.7}Cu_{0.3}O_z$ and $La_{9.8}Cu_{0.2}Ge_6O_z$

11 Conclusions

The aim of the project was to use a number of doping strategies to synthesise novel materials for energy applications. A range of novel materials have been successfully prepared through oxyanion incorporation, fluorination and exsolution. Materials investigated have included perovskite, perovskite type and apatite materials and have been synthesised through solid state synthesis. A range of characterisation techniques have been used to analyse these materials including XRD, ND, TGA, XANES, ^{57}Fe Mössbauer spectroscopy, SEM, 4 probe conductivity and AC impedance spectroscopy.

Oxyanion doping in perovskite phases

A range of iron containing perovskite phases were synthesised with a number of oxyanions (borate, sulfate and phosphate). Incorporation of oxyanions resulted in stabilisation of the cubic perovskite structure. In addition under reducing conditions the cubic perovskite structure was maintained for these doped phases. Initial conductivity studies indicated comparable conductivity to the undoped $SrFeO_{3-\delta}$ perovskite phases with lower conductivities for $Sr_{0.5}Ba_{0.5}FeO_{3-\delta}$ phases. With these initial promising results, further investigation would be needed to test the suitability of these materials as solid oxide fuel cell cathode materials. In addition to sulfate, phosphate and borate doped perovskite phases, carbonate incorporation was reported for $BaFeO_{3-\delta}$. Although traditionally carbonate incorporation is overlooked, the results here suggest that carbonate incorporation stabilises the cubic perovskite structure with this synthesis of the cubic phase dependent on the temperature and time. The work therefore suggests carbonate incorporation should be considered for other perovskite materials, especially phases synthesised via low temperature (e.g. solgel) routes.

Oxyanion doping and fluorination of Ruddlesden-Popper phases

Following the successful incorporation of oxyanions into perovskite materials, these methods were extended to a range of Ruddlesden-Popper phases. Using the synthesis strategies developed for perovskite materials, a range of n=3 Ruddlesden-Popper phases were stabilised through oxyanion incorporation. Without oxyanion incorporation (borate, chromate and sulfate) a mixture of the n=2 Ruddlesden-Popper phase and $SrFeO_{3-\delta}$ perovskite phase is obtained. High resolution neutron diffraction experiments showed a complex situation with multiple closely related n=3 Ruddlesden-Popper phases with additional broadening due to potential stacking faults within the structure. In order to investigate suitability for use in SOFCs, these Ruddlesden-Popper phases were heated in dry and wet N_2. XRD studies of sulfate doped $Sr_4Fe_3O_{10-\delta}$ phases heated in dry N_2 showed good stability at high dopant levels. In comparison XRD studies of borate and chromate doped phases heated in dry N_2 suggested the partial break down of these systems. These $Sr_4Fe_{3-x}(S/Cr)_xO_{10-\delta}$ phases show additional broadening in the XRD data when heated in wet N_2 indicating multiple hydrated Ruddlesden-Popper phases. This observation of significant water incorporation is promising for the potential for these materials to be used in proton conducting SOFCs. Further work would be needed to investigate this in more detail. In comparison to the oxyanion doped perovskite phases, poorer conductivity is reported for these Ruddlesden-Popper phases therefore further work was needed to improve this. In order to improve conductivity Co/ Cu were additionally doped into the Ruddlesden-Popper phases which not only also stabilised the n=3 Ruddlesden-Popper phase, but also resulted in improved conductivity. Doping with Co/ Cu were initially carried out for $Sr_4Fe_{3-x}S_xO_{10-\delta}$ phases due to these being the most promising for SOFC applications. However given that the conductivities were still lower than the related

perovskite systems, oxyanion doped perovskite phases appear to be the most appealing as solid oxide fuel cell cathode materials.

These oxyanion doped Ruddlesden-Popper phases, $Sr_4Fe_{2.75}(S/Cr)_{0.25}O_{10-\delta}$, were also investigated to see whether they would incorporate fluorine. As previously reported for fluorination of $Sr_3Fe_2O_7$, high levels of fluorine can be incorporated into these n=3 Ruddlesden-popper phases.[193] Not only is F incorporated into normal anion sites, but at higher F levels interstitial sites are filled. These phases have potential interest as electrode materials for F ion batteries, and further work would be of interest to examine these phases in this application.

Oxyanion incorporation into other perovskite related phases

In order to expand on oxyanion incorporation, further potential SOFC electrode materials were investigated including the perovskite type "0201-1201" type layered oxide. The n=3 Ruddlesden-Popper structure was successfully synthesised by incorporating sulfate and chromate, therefore these dopants were further researched for perovskite type materials. $Sr_{4.5}Fe_2(S/Cr)_{0.5}O_{9\pm\delta}$ phases show the successful incorporation of oxyanions to allow the synthesis of these new oxide materials. Sulfate and chromate incorporation is supported by a range of techniques including XRD, ND, XANES and ^{57}Fe Mössbauer spectroscopy. Cr XANES data for $Sr_{4.5}Fe_2Cr_{0.5}O_{9\pm\delta}$ shows a characteristic sharp pre-edge associated with Cr^{6+} with a reduction in intensity of this peak suggesting some distortion in geometry. Additionally, the presence of Fe^{5+} in the ^{57}Fe Mössbauer spectra is as reported for other oxyanion doped perovskite materials. [111,175] In order to test stability for use in SOFCs, $Sr_{4.5}Fe_2(S/Cr)_{0.5}O_{9\pm\delta}$ phases were heated in dry and wet N_2. Promising results are observed with phases remaining stable when heated to 800 °C, with TGA analysis supporting the

incorporation of water. Conductivity tests for these phases, however, showed low conductivity in comparison to other oxyanion doped materials investigated in this thesis and also for typical SOFC materials. Therefore further work would be needed to improve these phases for SOFC applications.

The investigation of oxyanion doped $Ba_3(Y/Tm)_2TiO_8$ phases as possible SOFC electrolyte materials was performed. XRD studies of undoped $Ba_3(Y/Tm)_2TiO_8$ phases were found to display complex patterns with additional reflections compared with oxyanion doped phases. These additional reflections indicate a complex structure most likely due to ordering of anion vacancies, and further work would be required to clarify this. Incorporation of oxyanions (sulfate and phosphate) resulted in stabilisation of the cubic perovskite structure as observed for previously discussed perovskite materials. Improved purity and stability when heating in dry and wet N_2 were observed for $Ba_3Tm_2Ti_{1-x}(S/P)_xO_{8+y}$ phases in comparison to equivalent $Ba_3Y_2Ti_{1-x}(S/P)_xO_{8+y}$ phases. The incorporation of sulfate and phosphate into these phases is supported by Raman spectroscopy where growth in the sulfate/ phosphate bands with increased dopant is observed. AC impedance spectroscopy was used to investigate these materials as potential SOFC electrolyte materials. Although on oxyanion incorporation improvements to conductivity were observed the conductivity values are still lower than current electrolyte materials.

Exsolution of Cu in apatite materials

Finally, a range of apatite materials including $(Ca/Sr)_{10}(PO_4)_6(OH)_{1-2x}(CuO_2)_x$, $(Ca/Sr)_{10}(CrO_4)_6(OH)_x(CuO_2)_y$ and $La_{10-x}Cu_xGe_{6-y}Cu_yO_z$ were successfully synthesised. Under reducing conditions exsolution of Cu nanoparticles on the surface was observed by SEM analysis. X-ray diffraction studies showed stability of $(Ca/Sr)_{10}(PO_4)_6(OH)_{1-2x}(CuO_2)_x$

phases with a change in lattice parameters due to the Cu exsolution. In comparison $(Ca/Sr)_{10}(CrO_4)_6(OH)_x(CuO_2)_y$ phases decompose under reducing conditions producing a mixture of phases including reflections associated with Cu. Finally, successful Cu exsolution from La-Ge-Cu-O apatite phases was shown, resulting in a lowering of symmetry with additional reflections associated with La_2GeO_5. Given the initial promising exsolution results further studies are warranted with a particular focus on potential applications of these materials; e.g. as fuel cell anodes.

12 Further work

This work has shown new materials can be successfully synthesised using a range of doping strategies with the potential for use in SOFCs. A number of techniques have been used in order to characterise and test the properties of these materials.

A range of perovskite and perovskite related phases have been successfully synthesised through the incorporation of oxyanions. In order to characterise these materials XRD, ND, XANES and ^{57}Fe Mössbauer spectroscopy has been carried out. Although initial studies support the successful incorporation of oxyanions, further neutron diffraction studies could be performed to investigate in more detail the oxygen positions and the incorporation of carbonate in perovskite materials. Additionally, stability studies of Ruddlesden-Popper phases when heated in wet N_2 show broadening in the XRD data and ND experiments could be used to investigate deuterated analogues of these phases.

^{57}Fe Mössbauer spectroscopy data provided information regarding the Fe environment for Ruddlesden-Popper and "0201-1201" type oxide materials. This information was useful to investigate the effect on the iron environment upon incorporation of oxyanions and further supporting the successful incorporation. Further Mössbauer studies on iron oxide perovskite systems, particularly carbonate doped $BaFeO_{3-\delta}$ phases would be of interest combined with neutron diffraction to investigate the effect of carbonate incorporation.

Due to work in this thesis focusing on the investigation of materials for SOFCs further testing of materials is needed with a particular focus on testing in dry and wet N_2. Specifically the stability of Ruddlesden-Popper phases in wet N_2 warrant further investigation for proton conducting SOFCs. Also, although improvements to conductivity data has been made by incorporating oxyanions, further doping strategies are needed to improve conductivities further, so as to ensure values that are comparable with common electrode materials. This has

initially been improved in this work by doping with Co/Cu into the Ruddlesden-Popper phases.

The oxyanion doped n=3 Ruddlesden-Popper phases, $Sr_4Fe_{2.75}(S/Cr)_{0.25}O_{10-\delta}$, were successfully synthesised through low temperature fluorination. Due to the successful fluorination of the n=3 Ruddlesden-Popper phases with high fluorine contents, further studies are warranted for these phases with the need to investigate as possible fluoride ion battery electrodes.

For a number of systems more complex patterns are observed when investigating materials through XRD/ ND. Ruddlesden-Popper materials are found to have not only multiple closely related phases present, but additional broadening attributed to stacking faults. Transmission electron microscopy would be of interest in order to investigate these features further. Additionally, $Ba_3(Y/Tm)_2TiO_8$ phases were found to have complex XRD patterns attributed to anion vacancy ordering. Additional investigation of these materials is warranted to explain this, for example single crystal growth to allow single crystal XRD to be performed.

Finally, initial studies on metal exsolution of apatite phases highlighted an alternate synthesis method which can be used to change the properties of materials. There is a wide range of further work that could be carried out in order to investigate metal exsolution from these and other potential SOFC materials. From the work carried out here further investigation into the effect of the levels of Cu on the exsolution process would be of interest. Furthermore, as these materials are predicted to be suitable SOFC materials, testing of these materials should be undertaken in order to test their suitability.

13 Publication List

Jarvis, A., Slater, P. R., *Investigation into the Effect of Sulfate and Borate Incorporation on the Structure and Properties of $SrFeO_{3-\delta}$.,* Crystals, 2017, **7**, 169–181, DOI: 10.3390/cryst7060169.

Mcsloy, A. J., Trussov, I., Jarvis, A., Cooke, D. J., Slater, P. R., Panchmatia, P. M., *Mechanism of Carbon Dioxide and Water Incorporation in Ba_2TiO_4:A Joint Computational and Experimental Study.*, J. Phys. Chem. C, 2018, **122**, 1061–1069, DOI: 10.1021/acs.jpcc.7b10330.

Jarvis, A., Berry, F. J., Marco, J. F., Slater, P. R., *Introduction of Sulfate to Stabilize the n = 3 Ruddlesden-Popper System $Sr_4Fe_3O_{10-\delta}$, as a Potential SOFC Cathode*. ECS Trans., 2019, **91**, 1467–1476, DOI: 10.1149/09101.1467ecst.

Jarvis, A., Berry, F. J., Marco, J. F., Sanchez-Arenillas, M., Cibin, G., Slater, P. R., *Synthesis and Characterisation of $Sr_4Fe_{3-x}Cr_xO_{10-\delta}$: Stabilisation of n=3 Ruddlesden-Popper Phases through Cr Doping.*, J. Solid State Chem., 2020, **287**, 121372, DOI: 10.1016/j.jssc.2020.121372.

Jarvis, A., Berry, F. J., Marco, J. F., Sanchez-Arenillas, M., Slater, P. R., *Fluorination of oxyanion doped n=3 Ruddlesden-Popper materials.*, In preparation.

Jarvis, A., Berry, F. J., Marco, J. F., Sanchez-Arenillas, M., Cibin, G., Gibbs, A., Slater, P. R., *Synthesis and characterisation of oxyanion doped "0201-1201" type layered oxide,* $Sr_{4.5}Fe_2(S/Cr)_{0.5}O_{9\pm\delta}$., In preparation

14 Conference List

EPS research conference	October 2016	Poster
36th Solid state chemistry group meeting	December 2016	Poster
STFC batteries early career researcher conference	March 2017	Poster
BCA spring meeting	April 2017	Talk
FCH2 technical conference	May/June 2017	Poster
ISIS crystallography user meeting	October 2017	Poster
CCSHFC “Hydrogen and fuel cells- gearing up for commercialisation”	March 2018	Poster
Winter crystallography meeting	November 2018	Poster
CCSHFC “Hydrogen and Fuel Cells – Powering the future March 2019”	March 2019	Poster
SOFC-XVI	September 2019	Poster
3rd Annual MISE Workshop	October 2019	Poster

15 References

1 T. M. Gür, *Prog. Energy Combust. Sci.*, 2016, **54**, 1–64.

2 F. Baldi, L. Wang, M. Pérez-Fortes and F. Maréchal, *Front. Energy Res.*, , DOI:10.3389/fenrg.2018.00139.

3 E. Baur and H. Preis, *Z. Elktrochem. Angew. P.*, 1937, **43**, 727–732.

4 T. Takahshi, H. Iwahara and T. Arao, *J. Appl. Electrochem.*, 1975, **5**, 187–195.

5 H. A. Harwig, *J. Inorg. Gen. Chem.*, 1978, **444**, 151–166.

6 P. Shuk, *Solid State Ionics*, 1996, **89**, 179–196.

7 H. A. Harwig and A. G. Gerards, *Thermochim. Acta*, 1979, **28**, 121–131.

8 H. G. Scott, *J. Mater. Sci.*, 1975, **10**, 1527–1535.

9 R. F. Geller and P. J. Yaborsky, *J. Res. Natl. Bur. Stand. (1934).*, 1945, **35**, 87–110.

10 V. V. Kharton, E. N. Naumovich and A. A. Vecher, *J. Solid State Electrochem.*, 1999, **3**, 61–81.

11 O. H. Kwon and G. M. Choi, *Solid State Ionics*, 2006, **177**, 3057–3062.

12 N. Q. Minh, *J. Am. Ceram. Soc.*, 1993, **76**, 563–588.

13 B. C. Steele and A. Heinzel, *Nature*, 2001, **414**, 345–352.

14 T. H. Etsell and S. N. Flengas, *Chem. Rev.*, 1970, **70**, 339–376.

15 J. Van Herle, T. Horita, T. Kawada, N. Sakai, H. Yokokawa and M. Dokiya, *J. Eur. Ceram. Soc.*, 1996, **16**, 961–973.

16 H. Inaba and H. Tagawa, *Solid State Ionics*, 1996, **83**, 1–16.

17 M. Mogensen, N. M. Sammes and G. A. Tompsett, *Solid State Ionics*, 2000, **129**, 63–94.

18 T. Inoue, T. Setoguchi, K. Eguchi and H. Arai, *Solid State Ionics*, 1989, **35**, 285–291.

19 C. J. Kevane, E. L. Holverson and R. D. Watson, *J. Appl. Phys.*, 1963, **34**, 2083–2087.

20 B. Steele, *Solid State Ionics*, 2000, **129**, 95–110.

21 R. Doshi, V. L. Richards, J. D. Carter, X. P. Wang and M. Krumpelt, *J. Electrochem. Soc.*, 1999, **146**, 1273–1278.

22 T. Ishihara, H. Matsuda and Y. Takita, *J. Am. Chem. Soc.*, 1994, **116**, 3801–3803.

23 H. Iwahara, H. Uchida, K. Ono and K. Ogaki, *J. Electrochem. Soc.*, 1988, **135**, 529–533.

24 H. Iwahara, *Solid State Ionics*, 1988, **28**–**30**, 573–578.

25 H. Iwahara, T. Yajima, T. Hibino, K. Ozaki and H. Suzuki, *Solid State Ionics*, 1993, **61**, 65–69.

26 H. Iwahara, *Solid State Ionics*, 1996, **86**–**88**, 9–15.

27 K. Katahira, Y. Kohchi, T. Shimura and H. Iwahara, *Solid State Ionics*, 2000, **138**, 91–98.

28 T. Yajima, H. Kazeoka, T. Yogo and H. Iwahara, *Solid State Ionics*, 1991, **47**, 271–275.

29 T. Yajima, H. Suzuki, T. Yogo and H. Iwahara, *Solid State Ionics*, 1992, **51**, 101–107.

30 H. Iwahara, *Solid State Ionics*, 1992, **52**, 99–104.

31 N. Agmon, *Chem. Phys. Lett.*, 1995, **244**, 456–462.

32 S. V. Bhide, *J. Electrochem. Soc.*, 1999, **146**, 2038–2044.

33 M. J. Scholten, J. Schoonman, J. C. van Miltenburg and H. A. J. Oonk, *Solid State Ionics*, 1993, **61**, 83–91.

34 Y. Wang, H. Wang, T. Liu, F. Chen and C. Xia, *Electrochem. commun.*, 2013, **28**, 87–90.

35 F. Su, C. Xia and R. Peng, *J. Eur. Ceram. Soc.*, 2015, **35**, 3553–3558.

36 H. Zhou, L. Dai, L. Jia, J. Zhu, Y. Li and L. Wang, *Int. J. Hydrogen Energy*, 2015, **40**,

8980–8988.

37 K. H. Ryu and S. M. Haile, *Solid State Ionics*, 1999, **125**, 355–367.

38 H. U. Anderson, D. M. Sparlin, T. Lamno and S. Lamno, *J. Solid State Chem.*, 1990, **87**, 55–63.

39 J. Mizusaki, *Solid State Ionics*, 2000, **132**, 167–180.

40 H. Kamata, Y. Yonemura, J. Mizusaki, H. Tagawa, K. Naraya and T. i. Sasamoto, *J. Phys. Chem. Solids*, 1995, **56**, 943–950.

41 C. S. Tedmon, H. S. Spacil and S. P. Mitoff, *J. Electrochem. Soc.*, 1969, **116**, 1170–1175.

42 O. Yamamoto, Y. Takeda, R. Kanno and M. Noda, *Solid State Ionics*, 1987, **22**, 241–246.

43 M. Gödickemeier, K. Sasaki, L. J. Gaucklet and I. Riess, *Solid State Ionics*, 1996, **86**–**88**, 691–701.

44 V. Dusastre and J. A. Kilner, *Solid State Ionics*, 1999, **126**, 163–174.

45 Y. Teraoka, H. M. Zhang, K. Okamoto and N. Yamazoe, *Mater. Res. Bull.*, 1988, **23**, 51–58.

46 L. W. Tai, M. M. Nasrallah, H. U. Anderson, D. M. Sparlin and S. R. Sehlin, *Solid State Ionics*, 1995, **76**, 273–283.

47 Y. Teraoka, T. Nobunaga, K. Okamoto, N. Miura and N. Yamazoe, *Solid State Ionics*, 1991, **48**, 207–212.

48 J. Mizusaki and T. Sasamoto, *J. Am. Ceram. Soc.*, 1983, **66**, 247–252.

49 A. Mai, V. A. C. Haanappel, S. Uhlenbruck, F. Tietz and D. Stöver, *Solid State Ionics*, 2005, **176**, 1341–1350.

50 Z. Shao and S. M. Haile, *Nature*, 2004, **431**, 170–173.

51 Z. Shao, G. Xiong, J. Tong, H. Dong and W. Yang, *Sep. Purif. Technol.*, 2001, **25**, 419–429.

52 B. Wei, Z. Lü, X. Huang, J. Miao, X. Sha, X. Xin and W. Su, *J. Eur. Ceram. Soc.*, 2006, **26**, 2827–2832.

53 Z. Chen, R. Ran, W. Zhou, Z. Shao and S. Liu, *Electrochim. Acta*, 2007, **52**, 7343–7351.

54 S. J. Skinner and J. A. Kilner, *Solid State Ionics*, 2000, **135**, 709–712.

55 V. V. Kharton, A. P. Viskup, E. N. Naumovich and F. M. B. Marques, *J. Mater. Chem.*, 1999, **9**, 2623–2629.

56 J. A. Kilner and C. K. M. Shaw, *Solid State Ionics*, 2002, **154**–**155**, 523–527.

57 J. M. Bassat, P. Odier and J. P. Loup, *J. Solid State Chem.*, 1994, **110**, 124–135.

58 A. Montenegro-Hernández, J. Vega-Castillo, L. Mogni and A. Caneiro, *Int. J. Hydrogen Energy*, 2011, **36**, 15704–15714.

59 M. Mogensen and K. Kammer, *Annu. Rev. Mater. Res.*, 2003, **33**, 321–331.

60 P. R. Slater, D. P. Fagg and J. T. S. Irvine, *J. Mater. Chem.*, 1997, **7**, 2495–2498.

61 O. A. Marina, N. L. Canfield and J. W. Stevenson, *Solid State Ionics*, 2002, **149**, 21–28.

62 B. Riegel, M. Gazda, P. Jasinski, B. Kusz, J. Karczewski, B. Riegel, M. Gazda, P. Jasinski and B. Kusz, *J. electroceramics*, 2010, **24**, 326–330.

63 D. Neagu and J. T. S. Irvine, *Chem. Mater.*, 2010, **22**, 5042–5053.

64 P. R. Slater, P. A. Wright, J. T. S. Irvine, P. R. Slater and P. A. Wright, *Ionics.*, 1996, **2**, 213–216.

65 S. Tao and J. T. S. Irvine, *Nat. Mater.*, 2003, **2**, 320–323.

66 S. Tao and J. T. S. Irvine, *Chem. Mater.*, 2004, **16**, 4116–4121.

67 J. Sfeir, P. A. Buffat, P. Möckli, N. Xanthopoulos, R. Vasquez, H. Joerg Mathieu, J. Van herle and K. Ravindranathan Thampi, *J. Catal.*, 2001, **202**, 229–244.

68 V. M. Goldschmidt, *Naturwissenschaften*, 1926, **14**, 477–485.

69 R. D. Shannon, *Acta Crystallogr. Sect. A*, 1976, **32**, 751–767.

70 S. Hui and A. Petric, *J. Eur. Ceram. Soc.*, 2002, **22**, 1673–1681.

71 S. Hui and A. Petric, *J. Electrochem. Soc.*, 2002, **149**, J1–J10.

72 S. N. Ruddlesden and P. Popper, *Acta Crystallogr.*, 1957, **10**, 538–539.

73 S. N. Ruddlesden and P. Popper, *Acta Crystallogr.*, 1958, **11**, 54–55.

74 P. Ganguly and C. Rao, *Mater. Res. Bull.*, 1973, **8**, 405–412.

75 G. Amow and S. J. Skinner, *J. Solid State Electrochem.*, 2006, **10**, 538–546.

76 S. Takahashi, S. Nishimoto, M. Matsuda and M. Miyake, *J. Am. Ceram. Soc.*, 2010, **93**, 2329–2333.

77 G. Amow, J. Au and I. Davidson, *Solid State Ionics*, 2006, **177**, 1837–1841.

78 R. J. Woolley and S. J. Skinner, *Solid State Ionics*, 2014, **255**, 1–5.

79 K. T. Lee and A. Manthiram, *Chem. Mater.*, 2006, **18**, 1621–1626.

80 K. T. Lee, D. M. Bierschenk and A. Manthiram, *J. Electrochem. Soc.*, 2006, **153**, 1255–1260.

81 T. Armstrong, F. Prado and A. Manthiram, *Solid State Ionics*, 2001, **140**, 89–96.

82 S. Nakayama, H. Aono and Y. Sadaoka, *Chem. Lett.*, 1995, **24**, 431–432.

83 S. Nakayama, M. Sakamoto, M. Highchi and K. Kodaira, *J. Mater. Sci. Lett.*, 2000, **19**, 91–93.

84 J. E. H. Sansom, D. Richings and P. R. Slater, *Solid State Ionics*, 2001, **139**, 205–210.

85 A. Najib, J. E. H. Sansom, J. R. Tolchard, P. R. Slater and M. S. Islam, *Dalt. Trans.*, 2004, 3106–3109.

86 J. McFarlane, S. Barth, M. Swaffer, J. E. H. Sansom and P. R. Slater, *Ionics (Kiel).*, 2002, **8**, 149–154.

87 J. E. H. Sansom, L. Hildebrandt and P. R. Slater, *Ionics (Kiel).*, 2002, **8**, 155–160.

88 L. León-Reina, M. C. Martín-Sedeño, E. R. Losilla, A. Cabeza, M. Martínez-Lara, S. Bruque, F. M. B. Marques, D. V Sheptyakov and M. A. G. Aranda, *Chem. Mater.*, 2003, **15**, 2099–2108.

89 L. León-Reina, J. M. Porras-Vázquez, E. R. Losilla and M. A. G. Aranda, *J. Solid State Chem.*, 2007, **180**, 1250–1258.

90 E. J. Abram, C. A. Kirk, D. C. Sinclair and A. R. West, *Solid State Ionics*, 2005, **176**, 1941–1947.

91 J. E. H. Sansom, A. Najib and P. R. Slater, *Solid State Ionics*, 2004, **175**, 353–355.

92 A. Orera, T. Baikie, P. Panchmatia, T. J. White, J. Hanna, M. E. Smith, M. S. Islam, E. Kendrick and P. R. Slater, *Fuel Cells*, 2011, **11**, 10–16.

93 H. Arikawa, H. Nishiguchi, T. Ishihara and Y. Takita, *Solid State Ionics*, 2000, **136**–**137**, 31–37.

94 H. Yoshioka and S. Tanase, *Solid State Ionics*, 2005, **176**, 2395–2398.

95 S. Ide, H. Takahashi, I. Yashima, K. Suematsu, K. Watanabe and K. Shimanoe, *J. Phys. Chem. C*, 2020, **124**, 2879–2885.

96 T. Yang, H. Zhao, M. Fang, K. Świerczek, J. Wang and Z. Du, *J. Eur. Ceram. Soc.*, 2019, **39**, 424–431.

97 C. A. Hancock, J. M. Porras-Vazquez, P. J. Keenan and P. R. Slater, *Dalt. Trans.*, 2015, **44**, 10559–10569.

98 M. G. Francesconi and C. Greaves, *Supercond. Sci. Technol.*, 1997, **10**, A29–A37.

99 P. R. Slater, C. Greaves, M. Slaski and C. M. Muirhead, *Phys. C Supercond. its Appl.*,

1993, **208**, 193–196.

100 J. F. Shin, D. C. Apperley and P. R. Slater, *Chem. Mater.*, 2010, **22**, 5945–5948.

101 J. F. Shin, A. Orera, D. C. Apperley and P. R. Slater, *J. Mater. Chem.*, 2011, **21**, 874–879.

102 S. A. Speakman, J. W. Richardson, B. J. Mitchell and S. T. Misture, *Solid State Ionics*, 2002, **149**, 247–259.

103 J. B. Goodenough, J. E. Ruiz-Diaz and Y. S. Zhen, *Solid State Ionics*, 1990, **44**, 21–31.

104 J. F. Shin, L. Hussey, A. Orera and P. R. Slater, *Chem. Commun.*, 2010, **46**, 4613–4615.

105 D. Pérez-Coll, J. C. Pérez-Flores, N. Nasani, P. R. Slater and D. P. Fagg, *J. Mater. Chem. A*, 2016, **4**, 11069–11076.

106 C. A. Hancock and P. R. Slater, *Dalton Trans.*, 2011, **40**, 5599–5603.

107 J. M. Porras-Vazquez, T. F. Kemp, J. V. Hanna and P. R. Slater, *J. Mater. Chem.*, 2012, **22**, 8287–8293.

108 C. A. Hancock, R. C. T. Slade, J. R. Varcoe and P. R. Slater, *J. Solid State Chem.*, 2011, **184**, 2972–2977.

109 Y. Zhu, W. Zhou, J. Sunarso, Y. Zhong and Z. Shao, *Adv. Funct. Mater.*, 2016, **26**, 5862–5872.

110 Y. Liu, X. Zhu and W. Yang, *J. Memb. Sci.*, 2016, **501**, 53–59.

111 J. M. Porras-Vazquez, T. Pike, C. A. Hancock, J. F. Marco, F. J. Berry and P. R. Slater, *J. Mater. Chem. A*, 2013, **1**, 11834–11841.

112 K. Yamaura, Q. Huang, J. W. Lynn, R. W. Erwin and R. J. Cava, *J. Solid State Chem.*, 2000, **152**, 374–380.

113 Y. Breard, C. Michel, M. Hervieu and B. Raveau, *J. Mater. Chem.*, 2000, **10**, 1043–

1045.

114 B. Gonano, Y. Bréard, D. Pelloquin, V. Caignaert, O. Perez, A. Pautrat, P. Boullay, P. Bazin and J. M. Le Breton, *Inorg. Chem.*, 2017, **56**, 15241–15250.

115 B. Gonano, Y. Bréard, D. Pelloquin, V. Caignaert, O. Pérez, A. Pautrat, P. Bazin, E. Suard and P. Boullay, *Dalt. Trans.*, 2018, **47**, 13088–13093.

116 D. Neagu, G. Tsekouras, D. N. Miller, H. Ménard and J. T. S. Irvine, *Nat. Chem.*, 2013, **5**, 916–923.

117 B. D. Madsen, W. Kobsiriphat, Y. Wang, L. D. Marks and S. A. Barnett, *J. Power Sources*, 2007, **166**, 64–67.

118 W. Kobsiriphat, B. D. Madsen, Y. Wang, L. D. Marks and S. A. Barnett, *Solid State Ionics*, 2009, **180**, 257–264.

119 W. Kobsiriphat, B. D. Madsen, Y. Wang, M. Shah, L. D. Marks and S. A. Barnett, *J. Electrochem. Soc.*, 2010, **157**, B279–B284.

120 T. Jardiel, M. T. Caldes, F. Moser, J. Hamon, G. Gauthier and O. Joubert, *Solid State Ionics*, 2010, **181**, 894–901.

121 E. Konysheva and J. T. S. Irvine, *Chem. Mater.*, 2011, **23**, 1841–1850.

122 G. Tsekouras, D. Neagu and J. T. S. Irvine, *Energy Environ. Sci.*, 2013, **6**, 256–266.

123 Y. Sun, J. Li, Y. Zeng, B. S. Amirkhiz, M. Wang, Y. Behnamian and J. Luo, *J. Mater. Chem. A*, 2015, **3**, 11048–11056.

124 D. Neagu, T. S. Oh, D. N. Miller, H. Ménard, S. M. Bukhari, S. R. Gamble, R. J. Gorte, J. M. Vohs and J. T. S. Irvine, *Nat. Commun.*, 2015, **6**, 8120.

125 J. H. Myung, D. Neagu, D. N. Miller and J. T. S. Irvine, *Nature*, 2016, **537**, 528–531.

126 J. G. Lee, J. H. Myung, A. B. Naden, O. S. Jeon, Y. G. Shul and J. T. S. Irvine, *Adv. Energy Mater.*, 2020, **10**, 1–6.

127 J. Lu, C. Zhu, C. Pan, W. Lin, J. P. Lemmon, F. Chen, C. Li and K. Xie, *Sci. Adv.*

128 R. Glaser, T. Zhu, H. E. Troiani, A. Caneiro, L. V. Mogni and S. Barnett, *J. Mater. Chem. A*, 2018, **6**, 5193–5201.

129 T. Zhu, H. E. Troiani, L. V Mogni, M. Han and S. A. Barnett, *Joule*, 2018, **2**, 478–496.

130 M. Ai-Mamouri, P. P. Edwards, C. Greaves and M. Slaski, *Nature*, 1994, **369**, 382–384.

131 P. R. Slater, P. P. Edwards, C. Greaves, I. Gameson, M. G. Francesconi, J. P. Hodges, M. Al-Mamouri and M. Slaski, *Phys. C Supercond. its Appl.*, 1995, **241**, 151–157.

132 P. R. Slater, *J. Fluor. Chem.*, 2002, **117**, 43–45.

133 The High Resolution Powder Diffractometer (HRPD), ISIS, https://www.isis.stfc.ac.uk/Pages/hrpd.aspx, (accessed 28 August 2020).

134 H. M. Rietveld, *Acta Crystallogr. Sect. A*, 1966, S 21, A228.

135 H. Rietveld, *Acta Crystallogr.*, 1967, **22**, 151–152.

136 B. H. Toby and R. B. Von Dreele, *J. Appl. Crystallogr.*, 2013, **46**, 544–549.

137 G. S. Pawley, *J. Appl. Crystallogr.*, 1981, **14**, 357–361.

138 B. Ravel and M. Newville, *J. Synchrotron Radiat.*, 2005, **12**, 537–541.

139 R. L. Mössbauer, *Zeitschrift für Phys.*, 1958, **151**, 124–143.

140 P. W. Atkins and D. F. Shriver, *Shriver Atkin's Inorg. Chem.*, 2010.

141 C. V. Raman and K. S. Krishnan, *Nature*, 1928, **121**, 501–502.

142 L. J. van der Pauw, *Philips Res. Reports*, 1958, **13**, 1–9.

143 Y. SINGH, *Int. J. Mod. Phys. Conf. Ser.*, 2013, **22**, 745–756.

144 J. T. S. Irvine, D. C. Sinclair and A. R. West, *Adv. Mater.*, 1990, **2**, 132–138.

145 A. Orera and P. R. Slater, *Chem. Mater.*, 2010, **22**, 675–690.

146 A. J. Jacobson, *Chem. Mater.*, 2010, **22**, 660–674.

147 H. H. Möbius, *J. Solid State Electrochem.*, 1997, **1**, 2–16.

148 C. A. Hancock, R. C. T. Slade, J. R. Varcoe and P. R. Slater, *J. Solid State Chem.*, 2011, **184**, 2972–2977.

149 M. Li, W. Zhou, X. Xu and Z. Zhu, *J. Mater. Chem. A*, 2013, **1**, 13632–13639.

150 K. Kinoshita and T. Yamada, *Nature*, 1992, **357**, 313–315.

151 T. G. N. Babu, D. J. Fish and C. Greaves, *J. Mater. Chem.*, 1991, **1**, 677–679.

152 A. Maignan, D. Pelloquin, S. Malo, C. Michel, M. Hervieu and B. Raveau, *Phys. C Supercond.*, 1995, **249**, 220–233.

153 F. Letouzé, C. Martin, A. Maignan, C. Michel, M. Hervieu and B. Raveau, *Phys. C Supercond.*, 1995, **254**, 33–43.

154 F. Goutenoire, M. Hervieu, A. Maignan, C. Michel, C. Martin and B. Raveau, *Phys. C Supercond.*, 1993, **210**, 359–366.

155 M. Huvé, C. Michel, A. Maignan, M. Hervieu, C. Martin and B. Raveau, *Phys. C Supercond. its Appl.*, 1993, **205**, 219–224.

156 H. G. von Schnering, L. Walz, M. Schwarz, W. Becker, M. Hartweg, T. Popp, B. Hettich, P. Müller and G. Kämpf, *Angew. Chemie Int. Ed. English*, 1988, **27**, 574–576.

157 J. Deakin, I. Trussov, A. Gibbs, E. Kendrick and P. R. Slater, *Dalt. Trans.*, 2018, **47**, 12901–12906.

158 A. J. McSloy, I. Trussov, A. Jarvis, D. J. Cooke, P. R. Slater and P. M. Panchmatia, *J. Phys. Chem. C*, 2018, **122**, 1061–1069.

159 A. Jarvis and P. R. Slater, *Crystals*, 2017, **7**, 169–181.

160 I. Starkov, S. Bychkov, A. Matvienko and A. Nemudry, *Phys. Chem. Chem. Phys.*, 2014, **16**, 5527–5535.

161 E. V. Tsipis and V. V. Kharton, *J. Solid State Electrochem.*, 2008, **12**, 1367–1391.

162 D. Rembelski, J. P. Viricelle, L. Combemale and M. Rieu, *Fuel Cells*, 2012, **12**, 256–264.

163 B. Guan, W. Li, H. Zhang and X. Liu, *J. Electrochem. Soc.*, 2015, **162**, F707–F712.

164 A. Jarvis, F. J. Berry, J. F. Marco and P. R. Slater, *ECS Trans.*, 2019, **91**, 1467–1476.

165 A. Jarvis, F. J. Berry, J. F. Marco, M. Sanchez-Arenillas, G. Cibin, O. Clemens and P. R. Slater, *J. Solid State Chem.*, 2020, **287**, 121372.

166 R. Seshadri, M. Hervieu, C. Martin, A. Maignan, B. Domenges, B. Raveau and A. N. Fitch, *Chem. Mater.*, 1997, **9**, 1778–1787.

167 L. Jantsky, H. Okamoto, A. Demont and H. Fjellvåg, *Inorg. Chem.*, 2012, **51**, 9181–9191.

168 M. Matvejeff, M. Lehtimäki, A. Hirasa, Y. H. Huang, H. Yamauchi and M. Karppinen, *Chem. Mater.*, 2005, **17**, 2775–2779.

169 D. Pelloquin, J. Hadermann, M. Giot, V. Caignaert, C. Michel, M. Hervieu and B. Raveau, *Chem. Mater.*, 2004, **16**, 1715–1724.

170 V. Øygarden, H. Fjellvåg, M. H. Sørby and A. O. Sjåstad, *Inorg. Chem.*, 2016, **55**, 7630–7636.

171 M. Lehtimäki, A. Hirasa, M. Matvejeff, H. Yamauchi and M. Karppinen, *J. Solid State Chem.*, 2007, **180**, 3247–3252.

172 F. J. Berry, X. Ren, R. Heap, P. Slater and M. F. Thomas, *Solid State Commun.*, 2005, **134**, 621–624.

173 F. J. Berry, R. Heap, Ö. Helgason, E. A. Moore, S. Shim, P. R. Slater and M. F. Thomas, *J. Phys. Condens. Matter*, 2008, **20**, 215207.

174 P. Adler, A. Lebon, V. Damljanović, C. Ulrich, C. Bernhard, A. V. Boris, A. Maljuk, C. T. Lin and B. Keimer, *Phys. Rev. B*, 2006, **73**, 094451.

175 F. J. Berry, A. F. Bowfield, F. C. Coomer, S. D. Jackson, E. A. Moore, P. R. Slater, M. F. Thomas, A. J. Wright and X. Ren, *J. Phys. Condens. Matter*, 2009, **21**, 256001.

176 I. D. Fawcett, G. M. Veith, M. Greenblatt, M. Croft and I. Nowik, *J. Solid State Chem.*, 2000, **155**, 96–104.

177 C. A. Hancock, J. M. Porras-Vazquez, P. J. Keenan and P. R. Slater, *Dalt. Trans.*, 2015, **44**, 10559–10569.

178 P. W. Stephens, *J. Appl. Crystallogr.*, 1999, **32**, 281–289.

179 J. Grins, D. Wardecki, K. Jansson, S. Carlson, J. J. Biendicho and G. Svensson, *J. Mater. Chem. A*, 2018, **6**, 5313–5323.

180 P. M. Sousa, A. V. Girão, M. E. M. Jorge, M. D. Carvalho, P. M. Costa, R. P. Borges, M. M. Cruz and M. Godinho, *J. Phys. Chem. Solids*, 2004, **65**, 1823–1829.

181 Y. Bréard, C. Michel, M. Hervieu, A. Ducouret, N. Nguyen, F. Studer, A. Maignan, B. Raveau and E. Suard, *Chem. Mater.*, 2001, **13**, 2423–2429.

182 J. M. Porras-Vazquez and P. R. Slater, *Fuel Cells*, 2012, **12**, 1056–1063.

183 J. M. Porras-Vazquez and P. R. Slater, *J. Power Sources*, 2012, **209**, 180–183.

184 A. Esquirol, N. P. Brandon, J. A. Kilner and M. Mogensen, *J. Electrochem. Soc.*, 2004, **151**, A1847.

185 E. Perry Murray, M. J. Sever and S. A. Barnett, *Solid State Ionics*, 2002, **148**, 27–34.

186 M. M. Natile, G. Eger, P. Batocchi, F. Mauvy and A. Glisenti, *Int. J. Hydrogen Energy*, 2017, **42**, 1724–1735.

187 J. M. Bassat, P. Odier and J. P. Loup, *J. Solid State Chem.*, 1994, **110**, 124–135.

188 C. Martin, A. Maignan, M. Huve, M. Hervieu, C. Michel and B. Raveau, *Phys. C Supercond. its Appl.*, 1991, **179**, 1–8.

189 Z. Fisk and J. L. Sarrao, *Annu. Rev. Mater. Res.*, 1997, **27**, 35–67.

190 D. Pelloquin, A. Wahl, A. C. Masset, A. Maignan, C. Michel and B. Raveau, *J. Solid State Chem.*, 2000, **154**, 375–383.

191 C. Greaves and P. R. Slater, *Phys. C Supercond. its Appl.*, 1991, **175**, 172–178.

192 C. Greaves and P. R. Slater, *J. Mater. Chem.*, 1991, **1**, 17–21.

193 C. A. Hancock, T. Herranz, J. F. Marco, F. J. Berry and P. R. Slater, *J. Solid State Chem.*, 2012, **186**, 195–203.

194 J. D. Jorgensen, B. Dabrowski, S. Pei, D. R. Richards and D. G. Hinks, *Phys. Rev. B*, 1989, **40**, 2187–2199.

195 A. Mehta and P. J. Heaney, *Phys. Rev. B*, 1994, **49**, 563–571.

196 V. V Kharton, A. P. Viskup, A. V Kovalevsky, E. N. Naumovich and F. M. B. Marques, *Solid State Ionics*, 2001, **143**, 337–353.

197 K. Wissel, S. Dasgupta, A. Benes, R. Schoch, M. Bauer, R. Witte, A. D. Fortes, E. Erdem, J. Rohrer and O. Clemens, *J. Mater. Chem. A*, 2018, **6**, 22013–22026.

198 O. Clemens, F. J. Berry, J. Bauer, A. J. Wright, K. S. Knight and P. R. Slater, *J. Solid State Chem.*, 2013, **203**, 218–226.

199 O. Clemens, A. J. Wright, F. J. Berry, R. I. Smith and P. R. Slater, *J. Solid State Chem.*, 2013, **198**, 262–269.

200 O. Clemens, M. Kuhn and R. Haberkorn, *J. Solid State Chem.*, 2011, **184**, 2870–2876.

201 O. Clemens, R. Haberkorn, P. R. Slater and H. P. Beck, *Solid State Sci.*, 2010, **12**, 1455–1463.

202 G. S. Case, A. L. Hector, W. Levason, R. L. Needs, M. F. Thomas and M. T. Weller, *J. Mater. Chem.*, 1999, **9**, 2821–2827.

203 Y. Tsujimoto, K. Yamaura, N. Hayashi, K. Kodama, N. Igawa, Y. Matsushita, Y. Katsuya, Y. Shirako, M. Akaogi and E. Takayama-Muromachi, *Chem. Mater.*, 2011,

23, 3652–3658.

204 R. Li and C. Greaves, *Phys. Rev. B - Condens. Matter Mater. Phys.*, 2000, **62**, 3811–3815.

205 M. S. Islam and S. D'Arco, *Chem. Commun.*, 1996, 2291–2292.

206 P. R. Slater and R. K. B. Gover, *J. Mater. Chem.*, 2002, **12**, 291–294.

207 J.-C. Grenier, J. Darriet, M. Pouchard and P. Hagenmuller, *Mater. Res. Bull.*, 1976, **11**, 1219–1225.

208 J. Rodríguez-Carvajal, M. Vallet-Regí and J. M. G. Calbet, *Mater. Res. Bull.*, 1989, **24**, 423–430.

209 F. G. Kinyanjui, S. T. Norberg, C. S. Knee and S.-G. Eriksson, *J. Alloys Compd.*, 2014, **605**, 56–62.

210 I. Kontoulis, C. P. Ftikos and B. C. H. Steele, *Mater. Sci. Eng. B*, 1994, **22**, 313–316.

211 J. F. Shin, K. Joubel, D. C. Apperley and P. R. Slater, *J. Chem. Soc. Dalt. Trans.*, 2012, **41**, 261–266.

212 S. Nakayama and M. Sakamoto, *J. Eur. Ceram. Soc.*, 1998, **18**, 1413–1418.

213 E. J. Abram, D. C. Sinclair and A. R. West, *J. Mater. Chem.*, 2001, **11**, 1978–1979.

214 P. J. Panteix, I. Julien, D. Bernache-Assollant and P. Abélard, *Mater. Chem. Phys.*, 2006, **95**, 313–320.

215 H. Arikawa, H. Nishiguchi, T. Ishihara and Y. Takita, *Solid State Ionics*, 2000, **136**–**137**, 31–37.

216 C. Arrivé, T. Delahaye, O. Joubert and G. Gauthier, *J. Power Sources*, 2013, **223**, 341–348.

217 S. Liu, Q. Liu and J. L. Luo, *ACS Catal.*, 2016, **6**, 6219–6228.

218 B. D. Madsen, W. Kobsiriphat, Y. Wang, L. D. Marks and S. Barnett, *ECS Trans.*,

2007, **7**, 1339–1348.

219 F. E Imrie and J. M. Skakle, *Bioceram. Dev. Appl.*, 2013, **3**, 5–6.

220 T. Baikie, G. M. H. Ng, S. Madhavi, S. S. Pramana, K. Blake, M. Elcombe and T. J. White, *Dalt. Trans.*, 2009, **10**, 6722–6726.

221 P. E. Kazin, A. S. Karpov, M. Jansen, J. Nuss and Y. D. Tretyakov, *Zeitschrift fur Anorg. und Allg. Chemie*, 2003, **629**, 344–352.

222 A. P. Tyutyunnik and G. V Bazuev, *J. Alloys Compd.*, 2012, **522**, 141–143.